



Università degli Studi di Napoli Federico II

SCUOLA POLITECNICA E DELLE SCIENZE DI BASE
Department of Industrial Engineering
Aerospace Division

DOCTORAL THESIS
IN
INDUSTRIAL ENGINEERING

**High lift and stability issues for innovative
transport aircraft configurations in
aerodynamic design**

Author:
Manuela Ruocco
Matricola DR992749

Coordinator:
Prof. Michele Grassi
Supervisor:
Prof. Fabrizio Nicolosi

Month xx 2020

Declaration of Authorship

I, Manuela RUOCCO, declare that this thesis titled, High lift and stability issues for innovative transport aircraft configurations in aerodynamic design and the work presented in it are my own. I confirm that:

- This work was done wholly or mainly while in candidature for a research degree at this University.
- Where any part of this thesis has previously been submitted for a degree or any other qualification at this University or any other institution, this has been clearly stated.
- Where I have consulted the published work of others, this is always clearly attributed.
- Where I have quoted from the work of others, the source is always given. With the exception of such quotations, this thesis is entirely my own work.
- I have acknowledged all main sources of help.
- Where the thesis is based on work done by myself jointly with others, I have made clear exactly what was done by others and what I have contributed myself.

Signed:

Date: *March 15, 2020 (revised)*

La fatica non è mai sprecata. Soffri, ma sogni.

Pietro Mennea

An italian legend of running



UNIVERSITÀ DEGLI STUDI DI NAPOLI
FEDERICO II

Doctor of Philosophy in Industrial Engineering

Abstract

High lift and stability issues for innovative transport aircraft configurations in aerodynamic design

Manuela Ruocco

Performing fast and reliable analyses is a crucial issue during the first phases of Aircraft Design, in particular during the conceptual and preliminary ones. This study aims to be a self-explanatory work as regards the innovative methodologies introduced in the Aerodynamic design of transport aircraft, their integration in a comprehensive java-based tool and the following applications concerning the European *IRON* (Innovative turbopROp configuratioN) project.

Priority identified within the aircraft marketplace are constantly pursuing climate and environmentally friendly goals. Meeting these priorities will have tangible impacts in the aircraft design as a whole, from the implementation of new technologies to the design process itself.

Based on these observations, this work is motivated by the following research question:

How is it possible to enhance the current state of art of aerodynamic parameters estimation within the aircraft design, coupling aeronautical and software competencies, focusing mainly on an innovative configuration for regional turboprop?

This study is collocated in this scenario, offering innovative methodologies that allow to perform preliminary analyses useful in the design process

of modern and future aircraft. In this context is collocated the *IRON* project, whose design process has been followed during the development of this work, which is part of the Clean Sky 2 program for Horizon 2020, aiming at reducing noise and emissions for future aircraft. This work can be divided in four main topics: *i*) development of a java-based framework for *MDAO* analyses, focusing on the software structure and on all the aerodynamic aspects, *ii*) improved methodologies for aerodynamic high lift prediction, *iii*) validation of developed methodologies, *iv*) innovative regional turboprop application. The author had chosen this work organization to best clarify the global scenario in which the research has been conducted, starting from a brief introduction and moving on the computer framework built up for preliminary design, *JPAD* (Java API for Aircraft Design), completely designed and developed within the *DAF* (Design of Aircraft and Flight technologies) research group from University of Study of Naples Federico II. Then the improved methodologies are presented developed and integrated within *JPAD*, coming up beside the semi-empirical methodologies. To come with the reader through the explanation of the work, the following chapter illustrates the methodology validation by means of CFD analyses and wind tunnel test. Finally all the methodologies implemented in *JPAD* are used to analyse the reference aircraft. Particular emphasis is posed on aircraft aerodynamic, to highlight how the introduced methodology can improve the results leading to better performance output.



UNIVERSITÀ DEGLI STUDI DI NAPOLI
FEDERICO II

Dottorato di Ricerca in Ingegneria Industriale

Abstract

High lift and stability issues for innovative transport aircraft configurations in aerodynamic design

Manuela Ruocco

Nell'ambito dell'*Aircraft Design*, soprattutto nelle prime fasi di progettazione concettuale e preliminare, svolge un ruolo cruciale la possibilità di svolgere analisi accurate e affidabili nel più breve tempo possibile. Lo scopo del presente lavoro è quello di introdurre metodologie innovative per la stima dei parametri aerodinamici di un velivolo e dei suoi componenti, integrate in un unico ambiente software dalle notevoli prestazioni, e di presentare le relative applicazioni con particolare riferimento al progetto europeo *IRON*.

Il mercato aeronautico spinge verso obiettivi ambientali sempre più ambiziosi, e ciò ha un notevole impatto su tutto il processo di progettazione. Basandosi su tali osservazioni, la domanda a cui nel presente testo si è cercato di dare una risposta, può essere riassunta nelle seguenti righe:

In che modo risulta essere possibile migliorare l'attuale stato dell'arte nell'ambito della stima dei parametri aerodinamici di un velivolo, integrando le competenze sviluppate dall'autore nel campo *Aircraft Design* e in quello della *Software Engineering*, con particolare attenzione a nuovi e innovativi turboprop regionali?

In tale scenario si colloca questo studio mirando ad offrire metodologie aerodinamiche innovative per le analisi preliminari utili nel processo

di design di velivoli moderni. Il presente lavoro nasce nell'ambito del progetto *IRON* (Innovative turbopROp configuratioN), che si configura all'interno dello scenario europeo come parte di Clean Sky 2, in Horizon 2020, il Programma Quadro europeo per la Ricerca e l'Innovazione, che mira a ridurre rumore ed emissioni nei futuri velivoli. Questo lavoro tratta quattro principali aspetti: *i*) Progettazione e sviluppo di un software scritto in java per analisi e ottimizzazione multidisciplinare, *ii*) Sviluppo di metodologie innovative per la stima di parametri aerodinamici, *iii*) Validazione di tali metodologie, *iv*) Applicazione dei metodi introdotti al turboprop regionale in configurazione innovativa nell'ambito del progetto *IRON*. Benchè questo descritto non rispetti l'effettivo ordine di sviluppo del lavoro, l'autore ha scelto tale organizzazione per chiarire, nel modo che esso ritiene migliore, il flusso logico del lavoro svolto che parte dal contesto nel quale nasce la domanda di ricerca, fino all'effettiva applicazione delle metodologie sviluppate in un ambiente software. Le metodologie innovative oggetto di tale tesi, insieme ad una collezione di metodi tradizionali, sono state implementate all'interno di un ambiente software integrato per l'analisi e l'ottimizzazione multidisciplinare di velivoli: *JPAD* (Java API for Aircraft Design). Esso è un framework interamente scritto in java e completamente progettato e sviluppato all'interno del gruppo di ricerca DAF (Design of Aircraft and Flight technologies) dell'Università degli Studi di Napoli Federico II.

Summary

Declaration	iii
Abstract	vii
1 Introduction	1
1.1 Introduction	1
1.2 Research scenario	2
1.3 European Framework Programme - Clean Sky 2	7
1.4 The <i>IRON</i> project	8
1.5 Thesis objective and layout	21
2 A java framework for aircraft design and optimization	25
2.1 Introduction	25
2.2 Software for aircraft MDAO	26
2.3 The software structure	32
2.4 Aerodynamic and stability module	41
2.5 Result validation	42
2.5.1 Case study: Airbus A220-300	42
3 Aerodynamic methodologies for aircraft preliminary design	67
3.1 Introduction	67
3.2 Aerodynamic conventional methodologies	68
3.2.1 Airfoil database	68
3.2.2 Downwash evaluation for two lifting surfaces	74
3.2.3 Downwash evaluation for three lifting surfaces	80
3.2.4 Longitudinal static stability	83
3.2.5 Lateral and Directional stability	91

3.2.6	VMU	93
3.3	Improved methodology for Lift estimation	97
3.3.1	Pre-analysis	97
3.3.2	Analysis	97
3.4	Drag estimation	99
3.5	Improved methodology for high lift devices	102
4	Methodologies validation	107
5	Aerodynamic analysis of innovative regional turboprop	119
5.1	Introduction	119
5.2	IRON LOOP1 analyses	120
5.3	Three surfaces configuration	133
5.4	IRON LOOP2 aerodynamic assessment	153
5.4.1	Nacelle positioning	155
5.4.2	Longitudinal static stability assessment	157
6	Conclusions	171

List of Figures

1.1	Accessibility of air travel [45].	3
1.2	Monthly average Brent crude spot price (Jan 2016 - Dec 2020) [4].	4
1.3	Difference in fuel price between main airports and regional ones. [6].	5
1.4	Future turboprop routes [6].	6
1.5	Clean sky 2 infographic.	8
1.6	<i>IRON</i> project Loops.	10
1.7	<i>IRON</i> project, baseline configuration provided by Leonardo Company.	11
1.8	<i>IRON</i> project, baseline configuration provided by Leonardo Company, three views.	11
1.9	<i>IRON</i> project, baseline configuration technical drawing.	12
1.10	<i>IRON</i> project, cabin configuration layout.	12
1.11	Rendering of <i>IRON</i> model manufactured to ILA Berlin Air Show 2018.	16
1.12	<i>IRON</i> project, Loop 2 configuration.	18
1.13	Complete Aircraft high-lift configurations in take off and landing condition	20
1.14	<i>IRON</i> Loop 3 configuration.	21
1.15	Test flow chart and work organization.	24
2.1	JPAD <i>Graphical User Interface</i>	31
2.2	<i>Programming Language popularity trade ranked by TIOBE tiobe</i>	33
2.3	JPAD <i>input data infographic</i>	34
2.4	JPAD <i>Graphical User Interface, CAD generator</i>	35

2.5	<i>Blended wing body CAD, generated by JPAD.</i>	36
2.6	<i>JPAD structure infographic.</i>	36
2.7	<i>JPAD input manager perspective for weights analysis.</i>	40
2.8	<i>JPAD core modules dependencies.</i>	40
2.9	<i>JPAD core modules structure and dependencies.</i>	43
2.10	<i>JPAD aerodynamic and stability module flow chart.</i>	44
2.11	<i>A220 family (former Bombardier CSeries) 3-views.</i>	45
2.12	<i>A220-300 root and kink airfoil SC(2)-0714 considered for analyses in JPAD, data from [23].</i>	45
2.13	<i>A220-300 tip airfoil SC(2)-0710 considered for analyses in JPAD, data from [23].</i>	46
2.14	<i>A220-300 CAD model representation in JPAD GUI.</i>	48
2.15	<i>A220-300 3-view and wing representation made by JPAD.</i>	49
2.16	<i>JPAD airfoil input data GUI. A220-300 root airfoil.</i>	50
2.17	<i>JPAD airfoil input data GUI. A220-300 root airfoil, lift coefficient curve $M=0.2$, $Re=1e6$.</i>	50
2.18	<i>Comparison between the A220-300 wing [2] and the JPAD wing.</i>	51
2.19	<i>Boarding diagram of the A220-300 parametric model - JPAD</i>	51
2.20	<i>A220-300 aerodynamic assessment with JPAD software. Wing lift coefficient curves calculated with improved method in different operating conditions summarized in Tab.2.5 and Tab. 2.6.</i>	53
2.21	<i>A220-300 Wing lift coefficient curves comparison calculated with improved method and with OpenVSP.</i>	54
2.22	<i>A220-300 aerodynamic assessment with JPAD software. cC_l distribution along semispan calculated with improved method explained in Chap. 3, in configuration with high lift devices deflected, in different operating conditions summarized in Tab.2.5 and Tab. 2.6, at $\alpha_w = 2^\circ$.</i>	55
2.23	<i>A220-300 aerodynamic assessment with JPAD software. Nacelle pitching moment, for each nacelle, landing condition.</i>	55
2.24	<i>A220-300 aerodynamic assessment with JPAD software. Fuselage pitching moment in different operating conditions.</i>	56
2.25	<i>A220-300 aerodynamic assessment with JPAD software. Downwash angle in various operating conditions.</i>	57

2.26	A220-300 aerodynamic assessment with <i>JPAD</i> software. Total moment coefficient breakdown at take off condition, $X_{cg} = 34\%$ MAC.	58
2.27	A220-300 aerodynamic assessment with <i>JPAD</i> software. Total moment coefficient breakdown at climb condition, $X_{cg} =$ 34% MAC.	58
2.28	A220-300 aerodynamic assessment with <i>JPAD</i> software. Total moment coefficient breakdown at cruise condition, $X_{cg} = 34\%$ MAC.	59
2.29	A220-300 aerodynamic assessment with <i>JPAD</i> software. Total moment coefficient breakdown at landing condition, $X_{cg} = 34\%$ MAC.	59
2.30	A220-300 aerodynamic assessment with <i>JPAD</i> software. Moment coefficient for different angles of elevator deflec- tion, landing condition, $X_{cg} = 34\%$ MAC.	60
2.31	A220-300 aerodynamic assessment with <i>JPAD</i> software. Horizontal tail lift coefficient for different angles of elevator deflection and equilibrium lift coefficient curve, take off condition, $X_{cg} = 24.3\%$ MAC.	60
2.32	A220-300 aerodynamic assessment with <i>JPAD</i> software. Horizontal tail lift coefficient for different angles of eleva- tor deflection and equilibrium lift coefficient curve, climb condition, $X_{cg} = 24.3\%$ MAC.	61
2.33	A220-300 aerodynamic assessment with <i>JPAD</i> software. Horizontal tail lift coefficient for different angles of eleva- tor deflection and equilibrium lift coefficient curve, cruise condition, $X_{cg} = 24.3\%$ MAC.	61
2.34	A220-300 aerodynamic assessment with <i>JPAD</i> software. Horizontal tail lift coefficient for different angles of eleva- tor deflection and equilibrium lift coefficient curve, landing condition, $X_{cg} = 24.3\%$ MAC.	62
2.35	A220-300 aerodynamic assessment with <i>JPAD</i> software. Angle of elevator equilibrium deflection in various conditions.	63
2.36	A220-300 aerodynamic assessment with <i>JPAD</i> software. Total yawing coefficient breakdown at landing condition. .	64

2.37 A220-300 aerodynamic assessment with *JPAD* software.
Rudder deflection required for equilibrium vs angle of sideslip.
Landing condition. 64

2.38 A220-300 aerodynamic assessment with *JPAD* software.
Aerodynamic efficiency in equilibrium conditions vs lift co-
efficient in different operative conditions summarized in
Tab.2.5. 65

2.39 A220-300 aerodynamic assessment with *JPAD* software.
Total equilibrium polar curves calculated with improved
method in different operative conditions summarized in
Tab.2.5. 65

2.40 A220-300 aerodynamic assessment with *JPAD* software.
Total equilibrium efficiency curves calculated with improved
method in different operative conditions summarized in
Tab.2.5. 66

2.41 *A220-300 CAD model automatically produced by JPAD.* . . . 66

3.1 Infographics for *JPAD* airfoil data input. 69

3.2 α_{0_l} of airfoil families varying on thickness ratio.[3] 70

3.3 C_{l_α} of airfoil families varying on thickness ratio.[3] 70

3.4 C_l^* of airfoil families varying on thickness ratio.[3] 71

3.5 α_S of airfoil families varying on thickness ratio.[3] 71

3.6 $C_{l_{max}}$ of airfoil families varying on thickness ratio.[3] 71

3.7 $C_{l_{max}}/C_{l_{max}}^{(ref)}$ varying on thickness ratio and parameterized
for Reynolds number.[3] 72

3.8 $C_{l_{max}}/C_{l_{max}}^{(ref)}$ varying on thickness ratio and parameterized
for Reynolds number.[3] 72

3.9 Lift coefficient curve for NACA 64-215, $Re = 3e6$, incom-
pressible flow. Comparison between *xfoil* result and recon-
struction from database values. 73

3.10 The wing vortex sheet. 74

3.11 Upwash and Downwash in a finite lifting surface. 75

3.12 Dimensions for determination of Downwash Gradient, con-
sidering constant distances. 76

3.13 Definition of wing angles. 77

3.14 Arm definitions for downwash gradient evaluation. 79

3.15	Comparison between downwash distributions in both aft-tail and canard configuration.	82
3.16	Forces and moment acting on an aircraft with three lifting surfaces for longitudinal static stability.	84
3.17	Qualitative effect of vertical location of c.g. on pitching moment.	86
3.18	Characteristic angles of the horizontal tail.	87
3.19	Qualitative behaviour of elevator efficiency index vs elevator deflection.	87
3.20	Efficiency correction factor for plain flap.	88
3.21	Interpolating function of ΔC_{D_0} built by CFD-RANS analyses on <i>IRON</i> aircraft performed by software Star-CCM+.	90
3.22	FlowChart of optimum angle of incidence of horizontal tail calculation.	92
3.23	Interpolating function of τ_r built by CF analyses on <i>IRON</i> aircraft.	93
3.24	Takeoff configuration for the assessment of VMU	94
3.25	Ground effect on 55° delta configuration	95
3.26	Ground effect on a jet transport configuration	96
3.27	Notation for improved methodology for lift coefficient estimation.	98
3.28	Coordinate transformation used in the reduction of the lifting line equation.	99
3.29	Infographic for improved methodology for lift coefficient estimation.	100
3.30	Flow chart of improved methodology for lift coefficient estimation.	101
3.31	C_l distribution comparison for $\alpha_w = 4^\circ$ with and without high lift devices performed by a <i>CFD</i> analysis for a wing with $S=105 \text{ m}^2$, $\mathcal{R}= 12$, and with two fowler flaps deflected of 15° . Complete data and analyses results are reported in Chap. 5.	104
3.32	Flow chart of improved methodology for lift coefficient estimation with high lift devices.	106
4.1	<i>Wing planform in clean configuration, whose data are in 4.4.</i>	108
4.2	3D lift coefficient curve comparison	109

4.3	<i>Wing planform modelling with high lift devices, whose data are in 4.4.</i>	110
4.4	Chord distribution comparison between the real and the one with high lift devices deflected of $\delta_f = 48.85^\circ$, wing from [49].	111
4.5	C_l distribution in clean configuration from Nasa-Blackwell method [12] and from experimental data from [49], and in configuration with high lift devices deflected of $\delta_f = 48.85^\circ$ calculated with improved method at angle of attack of 18.7°	111
4.6	3D lift coefficient curve comparison with high lift devices deflected $\delta_f = 48.84^\circ$. Experimental data from [49]	112
4.7	<i>IRON</i> Loop 1 configuration wing planform with high lift devices.	113
4.8	<i>IRON</i> Loop 1 chord distribution comparison. Real configuration compared with the one due to the high lift devices deflection.	114
4.9	<i>IRON</i> Loop 1 zero lift angle distribution comparison. Real configuration compared with the one due to the high lift devices deflection.	114
4.10	<i>IRON</i> Loop 1 configuration. Lift coefficient distribution for configuration with two fowler flaps deflected of $\delta_f = 15^\circ$. Comparison between improved method and <i>CFD</i> . $\alpha = 2^\circ$	115
4.11	<i>IRON</i> Loop 1 configuration. Lift coefficient distribution for configuration with two fowler flaps deflected of $\delta_f = 15^\circ$. Comparison between improved method and <i>CFD</i> . $\alpha = 14^\circ$	115
4.12	<i>IRON</i> Loop 1 configuration. Lift coefficient distribution for configuration with two fowler flaps deflected of $\delta_f = 15^\circ$. Comparison between improved method and <i>CFD</i> . $\alpha = 16^\circ$	116
4.13	<i>IRON</i> Loop1 configuration. 3D lift coefficient curve comparison in clean configuration and with high lift devices deflected in take off, $\delta_f = 15^\circ$	117
5.1	<i>IRON</i> Loop 1 and Loop 2 configuration comparison. . . .	120

5.2	Airfoil target from <i>TLAR</i> , useful for its design.	122
5.3	Kink airfoil: comparison with the reference <i>NACA</i> laminar airfoil.	123
5.4	Kink airfoil: Lift coefficient comparison of CFD vs. MSES results, stall conditions $M=0.28$ $Re=13.6e6$	124
5.5	Kink airfoil: Polar comparison of Star-CCM+ CFD vs. MSES results, stall conditions $M=0.28$ $Re=13.6e6$	125
5.6	Kink airfoil: Moment coefficient comparison of Star-CCM+ CFD vs. MSES results, stall conditions $M=0.28$ $Re=13.6e6$	125
5.7	<i>IRON</i> Loop 1 aerodynamic assessment. Wing centre of pressure location along semi span calculated for zero lift angle of attack. Climb condition: $M = 0.288$, $Re = 1.3e7$	127
5.8	<i>IRON</i> Loop 1 aerodynamic assessment. Wing construction used to verify the calculated C_{M_0} . Climb condition: $M = 0.288$, $Re = 1.3e7$	128
5.9	<i>IRON</i> Loop 1 aerodynamic assessment. Wing lift coefficient distribution calculated with Nasa-Blackwell method and for zero lift angle of attack. Climb condition: $M = 0.288$, $Re = 1.3e7$	129
5.10	<i>IRON</i> Loop 1 aerodynamic assessment. Wing induced angle distribution calculated for zero lift angle of attack. Climb condition: $M = 0.288$, $Re = 1.3e7$	130
5.11	<i>IRON</i> Loop 1 aerodynamic assessment. Wing stall path method. Lift coefficient distribution calculated with Nasa-Blackwell method corresponding to the angle of attack for which the first station reaches the local airfoil maximum lift coefficient. Climb condition: $M = 0.288$, $Re = 1.3e7$	130
5.12	<i>IRON</i> Loop 1 aerodynamic assessment. Wing 3D lift coefficient calculated with Nasa-Blackwell method coupled with stall path method. Climb condition: $M = 0.288$, $Re = 1.3e7$	131
5.13	<i>IRON</i> Loop 1 aerodynamic assessment. Wing 3D polar breakdown. Climb condition: $M = 0.288$, $Re = 1.3e7$	131
5.14	<i>IRON</i> Loop 1 aerodynamic assessment. Wing 3D moment coefficient curve. Climb condition: $M = 0.288$, $Re = 1.3e7$	132

5.15	<i>IRON</i> Loop 1 aerodynamic assessment. Fuselage effect on 3D wing lift coefficient curve. Climb condition: $M = 0.288$, $Re = 1.3e7$	132
5.16	<i>IRON</i> Loop 1 aerodynamic assessment. Local angle of attack variation due to component angle of incidence and local downwash calculated with Slingerland method [84], in four different operating condition summarized in Tab. 5.1.	134
5.17	<i>IRON</i> Loop 1 aerodynamic assessment. Horizontal tail 3D lift coefficient for different angles of elevator deflection. Climb condition : $M = 0.288$, $Re = 1.3e7$	135
5.18	<i>IRON</i> Loop 1 aerodynamic assessment. Elevator effectiveness. Climb condition : $M = 0.288$, $Re = 1.3e7$	135
5.19	<i>IRON</i> Loop 1 aerodynamic assessment. Total lift coefficient for different angles of elevator deflection. Climb condition : $M = 0.288$, $Re = 1.3e7$	136
5.20	<i>IRON</i> Loop 1 aerodynamic assessment. Total moment coefficient breakdown with respect to the centre of gravity $CG = 15\%$ of MAC. Climb condition : $M = 0.288$, $Re = 1.3e7$	136
5.21	<i>IRON</i> Loop 1 aerodynamic assessment. Total moment coefficient with respect to the centre of gravity $CG = 15\%$ of MAC, for different angles of elevator deflection. Climb condition : $M = 0.288$, $Re = 1.3e7$	137
5.22	<i>IRON</i> Loop 1 aerodynamic assessment. Total equilibrium lift coefficient calculated for $CG = 15\%$ MAC. Climb condition : $M = 0.288$, $Re = 1.3e7$	137
5.23	<i>IRON</i> Loop 1 aerodynamic assessment. Angle of equilibrium of elevator deflection calculated for $CG = 15\%$ MAC. Climb condition : $M = 0.288$, $Re = 1.3e7$	138
5.24	<i>IRON</i> Loop 1 aerodynamic assessment. Total moment coefficient with respect to the centre of gravity $CG = 33\%$ MAC , for different angles of elevator deflection . Climb condition : $M = 0.288$, $Re = 1.3e7$	138
5.25	<i>IRON</i> Loop 1 aerodynamic assessment. Total equilibrium lift coefficient calculated for $CG = 33\%$ MAC. Climb condition : $M = 0.288$, $Re = 1.3e7$	139

5.26	<i>IRON</i> Loop 1 aerodynamic assessment. Total moment coefficient with respect to the centre of gravity. Climb condition : $M = 0.288$, $Re = 1.3e7$	139
5.27	<i>IRON</i> Loop 1 aerodynamic assessment. Angle of equilibrium of elevator deflection calculated with respect to the centre of gravity. Climb condition : $M = 0.288$, $Re = 1.3e7$.	140
5.28	<i>IRON</i> Loop 1 aerodynamic assessment. Aircraft polar breakdown. Climb condition : $M = 0.288$, $Re = 1.3e7$. . .	140
5.29	<i>IRON</i> Loop 1 aerodynamic assessment. Equilibrium polar curve calculated at different centre of gravity location. Climb condition : $M = 0.288$, $Re = 1.3e7$	141
5.30	<i>IRON</i> Loop 1 aerodynamic assessment. Efficiency curve calculated at different centre of gravity location. Climb condition : $M = 0.288$, $Re = 1.3e7$	141
5.31	<i>IRON</i> Loop 1 aerodynamic assessment. Angle of equilibrium of elevator deflection calculated with respect to the centre of gravity $CG=15\%$ MAC. Landing condition : $M = 0.154$, $Re = 1.1e7$	142
5.32	<i>IRON</i> Loop 1 aerodynamic assessment. Total moment coefficient breakdown with respect to the centre of gravity $CG = 15\%$ MAC. Landing condition : $M = 0.154$, $Re = 1.1e7$	142
5.33	<i>IRON</i> Loop 1 aerodynamic assessment. Total moment coefficient breakdown with respect to the centre of gravity $CG = 15\%$ MAC. Cruise condition : $M = 0.62$, $Re = 1.1e7$.	143
5.34	<i>IRON</i> Loop 1 aerodynamic assessment. Equilibrium lift coefficient curve in different condition calculated for $CG = 15\%$ MAC. Operating conditions are summarized in Tab. 5.1.	143
5.35	<i>IRON</i> Loop 1 aerodynamic assessment. Equilibrium lift coefficient curve in different condition calculated for $CG = 25\%$ MAC. Operating conditions are summarized in Tab. 5.1.	144
5.36	<i>IRON</i> Loop 1 aerodynamic assessment. Equilibrium lift coefficient curve in different condition calculated for $CG = 33\%$ MAC. Operating conditions are summarized in Tab. 5.1.	144

5.37	<i>IRON</i> Loop 1 aerodynamic assessment. Efficiency curve in different condition calculated for CG = 15% MAC. Operating conditions are summarized in Tab. 5.1.	145
5.38	<i>IRON</i> Loop 1 aerodynamic assessment. Efficiency curve in different condition calculated for CG = 25% MAC. Operating conditions are summarized in Tab. 5.1.	145
5.39	<i>IRON</i> Loop 1 aerodynamic assessment. Efficiency curve in different condition calculated for CG = 33% MAC. Operating conditions are summarized in Tab. 5.1.	146
5.40	<i>IRON</i> Loop 1 aerodynamic assessment. Polar curve in different condition calculated for CG = 15% MAC. Operating conditions are summarized in Tab. 5.1.	146
5.41	<i>IRON</i> Loop 1 aerodynamic assessment. Polar curve in different condition calculated for CG = 25% MAC. Operating conditions are summarized in Tab. 5.1.	147
5.42	<i>IRON</i> Loop 1 aerodynamic assessment. Polar curve in different condition calculated for CG = 33% MAC. Operating conditions are summarized in Tab. 5.1.	147
5.43	<i>IRON</i> Loop 1 centre of gravity excursion problems.	148
5.44	<i>IRON</i> boarding diagram - Loop 1 ending.	148
5.45	<i>IRON</i> boarding diagram limitations - Loop 1 ending.	148
5.46	<i>IRON</i> configurations comparison before Loop 2 - Top views	150
5.47	<i>IRON</i> efficiency curves comparison for the three different configuration.	152
5.48	Example of Pareto front for the optimization of Configuration 1 - <i>IRON</i> Loop 2.	153
5.49	<i>IRON</i> boarding diagram - Loop 2 configuration.	154
5.50	<i>IRON</i> Loop2, Wind tunnel test results. Nacelle effect on longitudinal stability, Re=315000	156
5.51	<i>IRON</i> Loop2, alternative engine positions.	157
5.52	<i>IRON</i> Loop2 revised configuration.	158
5.53	<i>IRON</i> Loop2, Wind tunnel test results. Nacelle effect on longitudinal stability with canard, Re = 315000.	159
5.54	<i>IRON</i> Loop 2 aerodynamic assessment. Wing lift characteristics: comparison between wing lift distribution of canard on and canard off at $AoA = 0^\circ$. <i>CFD-RANS</i> analysis, $\delta_{f_w} = 35^\circ$ and $\delta_{f_c} = 25^\circ$	161

5.55	<i>IRON</i> Loop 2 aerodynamic assessment, WWB configuration. Wing lift distribution till the stall occurrence, <i>CFD-RANS</i> analysis, $\delta_{fw} = 35^\circ$	161
5.56	<i>IRON</i> Loop 2 configuration, wind tunnel tests. Moment coefficient curve for different configurations, $Re=315000$. .	163
5.57	<i>IRON</i> Loop 2 aerodynamic assessment. Wing-body-canard configuration, lift coefficient characteristics comparison between Loop 2 configuration and Loop 2 revised configuration with different wing twist. Landing condition, $\delta_{fw} = 35^\circ$, $\delta_c = 25^\circ$	164
5.58	<i>IRON</i> Loop 2 revised aerodynamic assessment. Total equilibrium lift coefficient in landing condition, $\delta_{fw} = 35^\circ$, $\delta_c = 25^\circ$ with $i_h = -5^\circ$	165
5.59	<i>IRON</i> Loop 2 revised configuration, polar curve in various operating conditions, $X_{cg} = -22\%$ MAC. Component curves calculated with <i>CFD</i> in fully turbulent condition and riblets off.	166
5.60	<i>IRON</i> Loop 2 revised configuration, efficiency in various operating conditions, $X_{cg} = -22\%$ MAC. Component curves calculated with <i>CFD</i> in fully turbulent condition and riblets off.	167
5.61	<i>IRON</i> Loop 2 revised configuration, comparison efficiency in cruise, components curve calculated in fully turbulent condition, riblet off. Comparison at different centre of gravity position.	167
5.62	<i>IRON</i> Loop 2 revised configuration, comparison polar curve in cruise, $X_{cg} = -22\%$ MAC, using 3D component curves calculated for different conditions with high-fidelity methods.	168
5.63	<i>IRON</i> Loop 2 revised configuration, comparison polar curve in climb, $X_{cg} = -22\%$ MAC, using 3D component curves calculated for different conditions with high-fidelity methods.	168
5.64	<i>IRON</i> Loop 2 revised configuration, comparison efficiency in cruise, $X_{cg} = -22\%$ MAC, using 3D component curves calculated for different conditions with high-fidelity methods.	169
5.65	<i>IRON</i> Loop 2 revised configuration, comparison efficiency in climb, $X_{cg} = -22\%$ MAC, using 3D component curves calculated for different conditions with high-fidelity methods.	169

List of Tables

1.1	IRON TLAR	13
1.2	IRON Loop 1 aerodynamic target of innovative configuration	13
1.3	IRON Loop 1 weights assumption	13
1.4	IRON reference aircraft major geometric characteristics . .	14
1.5	IRON Loop2 aircraft major geometric characteristics . . .	19
1.6	IRON Loop 2 weights assumption	19
2.1	Component reference mass percentages with respect to the MTOW.	38
2.2	A220-300 main geometrical data and interior arrangements.	46
2.3	A220-300 main weights data.	46
2.4	A220-300 airfoil input data	47
2.5	A220-300 operating conditions.	48
2.6	A220-300, control surface setting in different conditions. . .	48
2.7	A220-300, control surface geometry.	52
2.8	Main output data concerning JPAD weights analysis of the A220-300 parametric model.	52
2.9	A220-300 operating conditions.	54
3.1	Lift and pitching moment contributions in x - z plane	85
3.2	Output of longitudinal static stability module in <i>JPAD</i> . . .	91
3.3	Output of lateral stability module in <i>JPAD</i>	93
4.1	Main wing geometrical characteristics from [49]	108
4.2	Main wing geometrical characteristics from [49]	108
4.3	Results comparison from Improved method and experimen- tal data in clean configuration, from [49]	109
4.4	Main wing high lift devices data from [49].	110

4.5	Results comparison from Improved method and experimental data in configuration with high lift devices deflected ($\delta_f = 48.84^\circ$), experimental data from [49]	112
4.6	Main wing flap data of <i>IRON</i> Loop 1 data.	113
4.7	Main wing geometrical characteristics of <i>IRON</i> Loop 1 data.	114
4.8	Results comparison between wing span lift coefficient calculated with improved method and with <i>CFD</i> analyses, for <i>IRON</i> Loop1 wing with high lift devices.	116
5.1	<i>IRON</i> Loop 1 operating conditions	126
5.2	<i>IRON</i> configurations comparison	151
5.3	<i>IRON</i> Loop 2 wind tunnel test. Aircraft configurations and relevant aerodynamic derivative.	162
5.4	<i>IRON</i> Loop 2 operating conditions	166

Nomenclature

Abbreviations

ADAS = Aircraft Design and Analysis Software

CFD = Computational Fluid Dynamics

CG = Centre of Gravity

CS2 = Clean Sky 2

DAF = Design of Aircraft and Flight technologies

IRON = Innovative turbopROp configurationN

JPAD = Java API for Aircraft Design

MAC = Mean Aerodynamic Chord

MDAO = Multidisciplinary Design Analysis and Optimization

NACA = National Advisory Committee for Aeronautics

NASA = National Aeronautics and Space Administration

SME = Small and Medium Enterprises

TLAR = Top Level Aircraft Requirements

UniNa = University of Naples

VLM = Vortex Lattex Method

WTT = Wind Tunnel Test

Symbols

\mathcal{R}	Aspect ratio
C_D	Drag coefficient
C_{D0}	Zero-lift drag coefficient
C_{l_α}	Airfoil lift curve slope
C_l^*	Airfoil end of linearity lift coefficient
C_{L_α}	Lifting surface lift curve slope
$C_{L_{MAX}}$	Lifting surface lift curve slope
L_f	Fuselage length
M	Mach number
Re	Reynolds number
S_w	Wing planform area
S_h	Horizontal tail planform area
V_∞	Wind asymptotic velocity
α_{0l}	Zero-lift angle of attack
α^*	End of linearity angle of attack
α_a	Absolute angle of attack
α_b	Angle of attack from flow and body reference line
α_s	Stall angle of attack
α_w	Wing angle of attack
b	Lifting surface span
δ_e	Angle of elevator deflection

δ_f	Angle of flap deflection
ϵ	Downwash angle
η	Adimensional spanwise coordinate
$\frac{d\epsilon}{d\alpha}$	Downwash gradient

*A mia Madre.
E al mio futuro, che porta il Tuo nome.*

Introduction

1.1 Introduction

This research work focuses on the development and on the application of enhanced methodologies for aerodynamic estimation or aerodynamic characteristics estimation during preliminary and conceptual aircraft design phase, with particular emphasis on innovative regional turboprop. There are several reasons for this choice: first of all, the author fascination with all that concerns aerodynamics and aircraft design in general, strengthened in the prosperous environment of the Design of Aircraft an Flight technologies research group (*DAF* research group), made up by experts of this field. Secondly, the international co-operation with aviation companies allows understanding where the aircraft market is moving. Moreover, the challenging European Framework Programme for Research and Innovation Horizon 2020 [15] for an innovative turboprop aircraft, has driven the research efforts to the above mentioned fields. This work makes use of the *Système International d'Unités* (SI) whenever possible, except for those methods taken from reference that use the British imperial units. Each chapter starts with a bulleted list called *Synopsis*, which gives the reader an idea of the content.

Synopsis

- Aircraft industry and airlines are moving to green and cost-efficient aircraft

- Particular emphasis is posed on turboprop aircraft
- In order to design new aircraft, during the first phases of the process, fast and reliable analyses are needed
- The European programme for Research and Innovation H2020 is collocated in this scenario
- The *IRON* project, for a regional turboprop, within Clean Sky 2 programme, will be examined, particularly focusing on the innovative configuration with rear engine installation
- This aircraft is considered as case study for innovative methodologies application
- The aerodynamic analyses performed on the aircraft of *IRON* project have been carried out both through conventional methodologies and innovative ones
- The thesis layout is presented

1.2 Research scenario

The global aeronautical industry is passing through a phase of expected drastic changes. Nowadays, the huge growth of air transport traffic and the increasing attention to the aircraft environmental footprint, led to considerable interest of specialists in new configuration. In fact, reducing environmental impact is, and will continue to be, a key driver for aviation. According to Flightpath 2050 vision, there is the need in aviation to accelerate efforts to increase resource efficiency and, at the same time, reducing noise and gas emissions. Compared to the capabilities of typical aircraft of 2000, the 2050 technologies and procedures available should allow a 75% reduction in CO₂ emissions per passenger kilometre and a 90% reduction in NO_x emissions, while the perceived noise emission should be reduced by 65%. To achieve such environmental goals by 2050, future step-changes are going to be in aircraft design, airframe configuration, propulsion systems (including electric and hybrid), on-board systems, as well as capabilities or modes of operation, will need to prove their worth

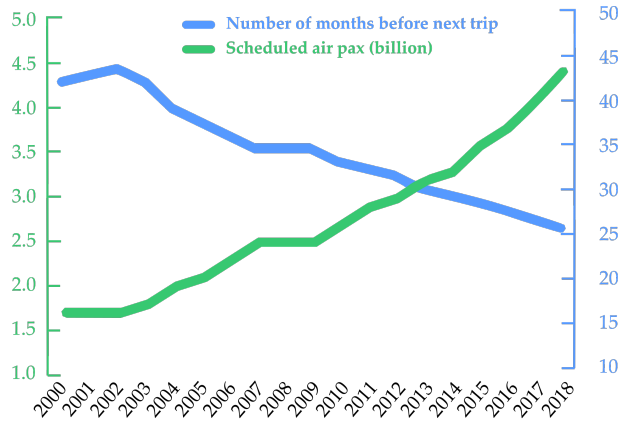


Figure 1.1: Accessibility of air travel [45].

compared with the evolutionary developments, whilst maintaining or improving on the high levels of reliability, safety and usability that customers demand. The aircraft sector is changing not only for even more demanding reduction in environmental impact, but also concerning commercial flight market and volume. The European multinational aerospace corporation, Airbus, in a study named *Airbus forecasts need for over 39,000 new aircraft in the next 20 years*, underlined that the world passenger and freighter aircraft fleet is set to more than double from today's nearly 23,000 to almost 48,000 by 2038 with traffic growing at 4.3% annually. By 2038, of the forecast 47,680 fleet, 39,210 are new and 8,470 remain from today [78]. Air transport is central to world tourism and trade (Fig. 1.1). It has been estimated that tourists have spent about \$850 billion in 2018 for their international travel, and this value has increased of more than 10% over 2017. Years after years, airlines continued to increase the number of city-pair routes globally. In 2019 more than 22,000 city pairs are regularly serviced by airlines. This is an increase of 1,300 over the number of city-pair connections in the previous year [45].

Another issue concerning aeronautical industry is the increasing oil price. Fuel cost is the key concern for airlines because of its value and volatility. Fuel cost actually drives between 40% and 50% of cash operating cost depending on stage length, business model, and aircraft type. Fuel consumption is highly related to the aircraft aerodynamics, structural efficiency, and powerplant technology, which are even more im-

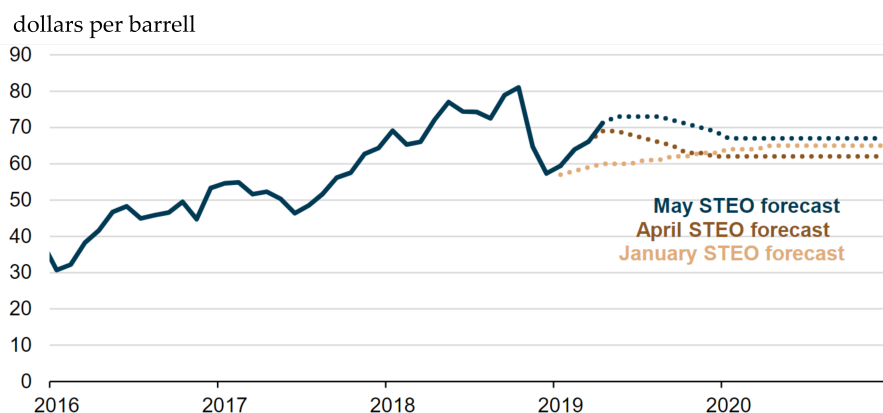


Figure 1.2: Monthly average Brent crude spot price (Jan 2016 - Dec 2020) [4].

proved. This cost pressure is paramount to airlines aircraft choice as it can generate millions of US dollars savings [6]. In its May 2019 edition of the Short-Term Energy Outlook (STEO), The U.S. Energy Information Administration (EIA) revised its price forecast for Brent crude oil upward, reflecting price increases in recent months, more recent data, and changing expectations of global oil markets. Several supply constraints have caused oil markets to be generally tighter and oil prices to be higher so far in 2019 than previous STEO expected [4] (Fig. 1.2). Moreover, from an analyses carried out by Avions de Transport Régional ATR, fuel price is higher in regional airports than in main airports due to higher fuel transportation costs, which translates to a worldwide average extra cost of +34% [6] (Fig. 1.3).

In light of the above, even more countries will be connected by airlines, moving towards cost-effective solutions. This shows the utmost importance for developing local economies and territorial cohesion. By efficiently connecting such a large diversity of communities, with the most limited environmental footprint, turboprops turn out to be an effective solution, enabling and sustaining the economic development of many regions, and thanks to its relationship with fuel price.

The turboprop airliner market has experienced a considerable revival since 2004, as high fuel prices and a need to cut operating costs have resulted in regional carriers acquiring turboprops in significant numbers. The current regional aircraft fleet amounts to around 7200 units (30-120

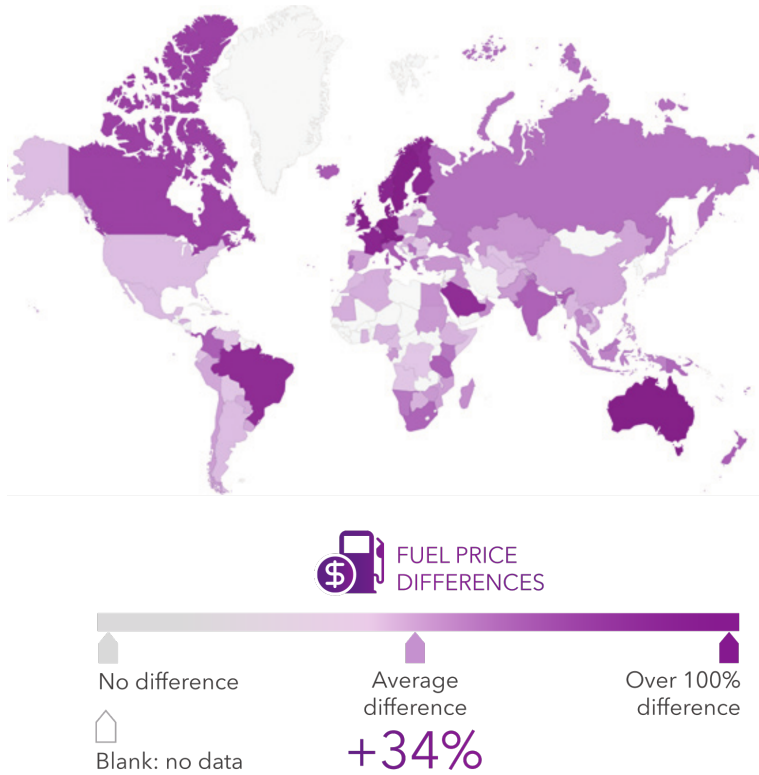


Figure 1.3: Difference in fuel price between main airports and regional ones. [6].

seats), of which 40 % are turboprops. The average age of this fleet is 15 years (19 years for turboprops and 11 years for regional jets. Routes that require a minimum level of aviation services or regionally specific routes (such as to isolated islands, etc.) are supposed to need turboprops, even if they are low in demand. Aircraft with 15 to 19 seats are expected to continue to be operated on those routes with 512 to be delivered. ATR in their forecasts about future turboprop market, advocate that about 30% of turboprop activity in 2037, comes from new routes, leading to 2,770 potential new routes created) [6] (Fig. 1.4). However, while 20 years ago this sector was well represented by manufacturers producing a wide range of commercial turboprops, only few now remain. Currently, the only companies manufacturing regional turboprops are the Canadian manufacturer Bombardier, and the Franco-Italian company (ATR), whose forecast have been reported. To meet the above-mentioned market requirements, challenging and interesting projects are arising worldwide, and in particular in Europe, where effectively operates Horizon2020 Programme. Researcher and company are called to answer to different challenges and, as it is easy to understand, is it useful to be able to perform fast and reliable analyses to develop new aircraft configurations.

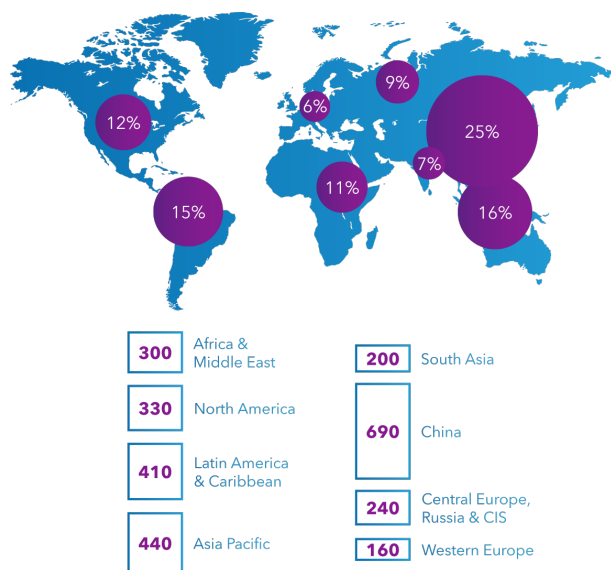


Figure 1.4: Future turboprop routes [6].

1.3 European Framework Programme - Clean Sky 2

This research work is framed within the *IRON* project that complies with the European Union topic *Green and cost-efficient Conceptual Aircraft Design including Innovative Turbo-Propeller Power-plant* as part of the *CS2* program for Horizon 2020.

"Clean Sky is the largest European research programme developing innovative, cutting-edge technology aimed at reducing CO₂, gas emissions and noise levels produced by aircraft. Funded by the EU's Horizon 2020 programme, Clean Sky contributes to strengthening European aero-industry collaboration, global leadership and competitiveness."

Clean Sky is the most significant, ambitious and integrated engagement that has ever existed between the European Commission and Europe's aeronautics industry, and this relationship, formalised under the structure of a Public Private Partnership (PPP), comprises entities with clearly defined roles: *CS2* is a Joint Technology Initiative, a public-private partnership bringing together companies, Universities, public laboratories, innovative *SMEs* and the European Commission. It develops and demonstrates break-through technologies for the civil aircraft market to cut aircraft emissions and noise and secure the future international competitiveness of the European aviation industry. It brings together Europe's aeronautics industrial leaders and public research. The *CS2* programme is jointly funded by the European Commission and the major European aeronautics companies, and involves an EU contribution (financial) from the Horizon 2020 programme budget of €1.755 bn. Associates (Clean Sky 1) and Core Partners (Clean Sky 2) are private or public organisations that have applied and have been selected through an open and transparent competition to become permanent members of the Clean Sky JU. They support the programme financially with in-kind contributions and can receive up to 30% of the programme funding for their projects. Leaders and Associates/Core Partners are commonly referred to as our Members [15].

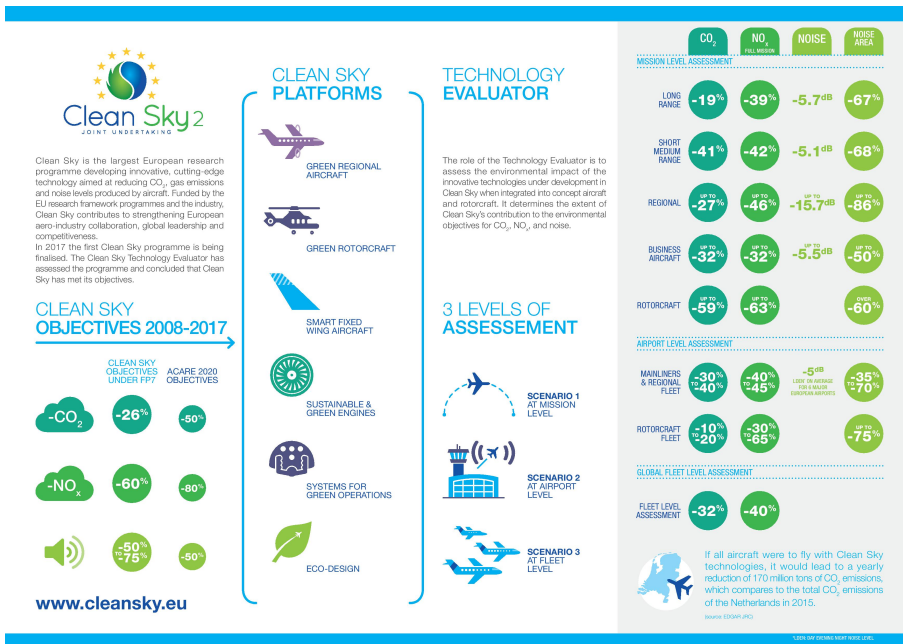


Figure 1.5: Clean sky 2 infographic.

1.4 The *IRON* project

The Innovative turboprop configuration (*IRON*) project complies with the European Union topic Green and cost-efficient Conceptual Aircraft Design including Innovative Turbo-Propeller Power-plant (JTI-CS2-2015-CPW02-REG-01-03) as part of the Clean Sky 2 program for Horizon 2020. The topic leader is Leonardo, while CIRA (Italian Aerospace Research Center) is the coordinator and several core-partners are involved into the project including the University of Study of Naples Federico II. The *IRON* project boasts the following further partner among the Europe:

- GE Aviation System LTD (Dowty, UK),
- GE Global Research (GRC, Germany),
- GE AVIO SRL (AVIO, Italy),
- Centre de Recherche en Aeronautique ASBL (CENAERO, Belgio),

- Stichting Nationaal Lucht – EN Ruimtevaartlaboratorium (NLR, Netherland),
- Office National d'Etudes et de Recherches Aerospatiales (ONERA, Francia),
- Politecnico di Torino (POLITO, Italia),
- Technische Universiteit Delft (TUD, Netherlands)

The topic in object aims at improving the efficiency of regional aircraft in the 90+ pax turboprop segment. This will be applied to two different platforms: a conventional architecture and an innovative one whose main activities are: Life cycle costs; Aerodynamic design, Power-plant design and low noise propeller; Safety valuation; WTT analysis. The first configuration is a wing mounted turboprop, while the second one is intended to be the revolution due to its innovative platform design with rear mounted engine. The rear propeller installation can lead to a cleaner wing with possibilities to achieve laminar flow extension. In addition, the wing without engine nacelle, and free of propeller interference effects will be characterized by a more efficient high-lift system (flap) with a possible increase in aircraft maximum lift coefficient, which will positively affect ground performance. However, the rear engine installation will lead to a wing weight increment (in wing-mounted engine configurations, the engine weight usually contributes to a reduction of bending moment, structural stress and wing weight). Due to its innovation, the rear propeller installation has to be carefully aerodynamically analysed to have a reliable prediction of aircraft tail aerodynamics including propulsive effects. The *IRON* project is focused on the feasibility study of the innovative turboprop regional configuration above mentioned. The research addressed to the analysis and design of this innovative regional platform will be developed through the following three different loops with increasing level of complexity and fidelity as shown in 1.6: (i) Loop 1: based on preliminary Top Level Aircraft Requirements (TLAR) and technological targets. In accordance with the requirements, the adequate type of power-plant is proposed by Core Partners and, then, selected by the topic leader. (ii) Loop 2: an intermediate configuration based on the upcoming outcomes from the previous loop. (iii) Loop 3: The final layout. The aircraft configuration will be assessed through numerical simulations

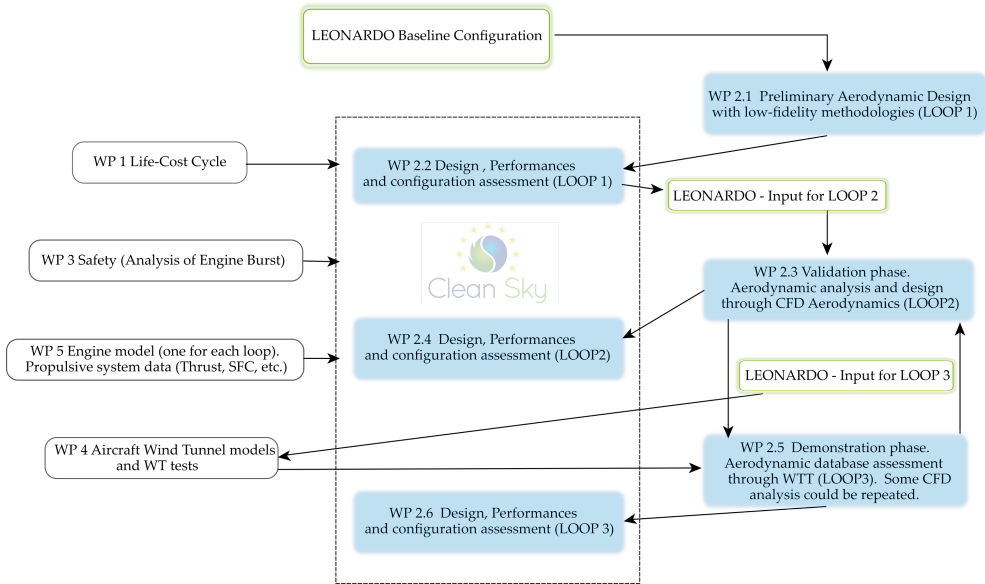


Figure 1.6: *IRON* project Loops.

during the first and second design phase, and experimental validations will be performed during the third loop, so that at the end of the project a Technology Readiness Level (TRL) 4 will be reached. The entry in service of this technological platform is estimated beyond 2035. The aircraft under investigation is an innovative layout with low wing. TLAR, issued by Leonardo company, have been very challenging: a cruise Mach number of 0.62 at 30000 feet, with a moderately maximum lift coefficient and low drag to achieve a cruise aerodynamic efficiency about 18. In particular, a maximum lift coefficient of 2.4 and 3.0 in take-off and landing conditions are respectively required. Moreover, it is expected that the inner wing airfoils have 18% relative thickness to reduce the wing weight and to allow the landing gear to be stored within. A summary of the main TLAR is reported in 1.1 1.2 and 1.3, while in Table 1.4 some of the main dimensions are illustrated.

The baseline was provided by Leonardo in January 2017 and represented in Fig. 1.7, Fig. 1.8 and its technical drawing is in Fig.1.9. The cabin Layout for 130 pax is five-abreast and it is shown in Fig.1.10. This reference aircraft has used for preliminary analyses within WP2.1 and WP2.2, within the Loop 1. The aim of Loop 1 analyses is to fulfil the

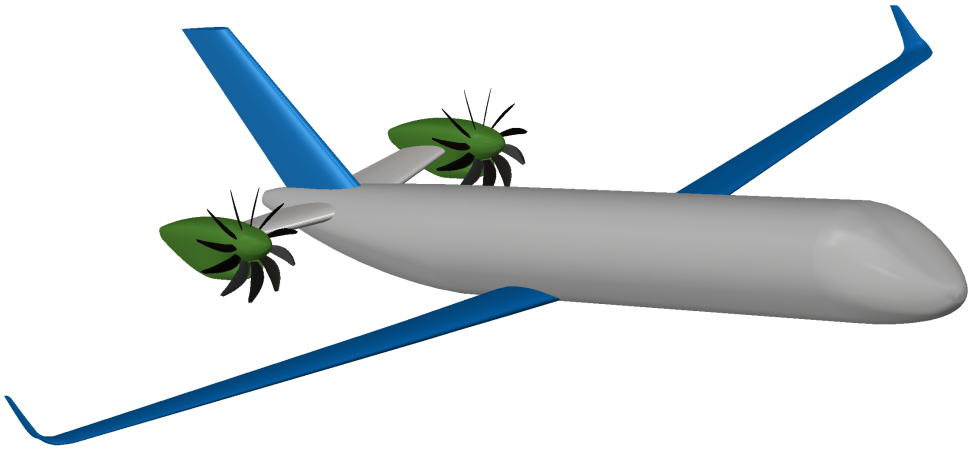


Figure 1.7: *IRON* project, baseline configuration provided by Leonardo Company.

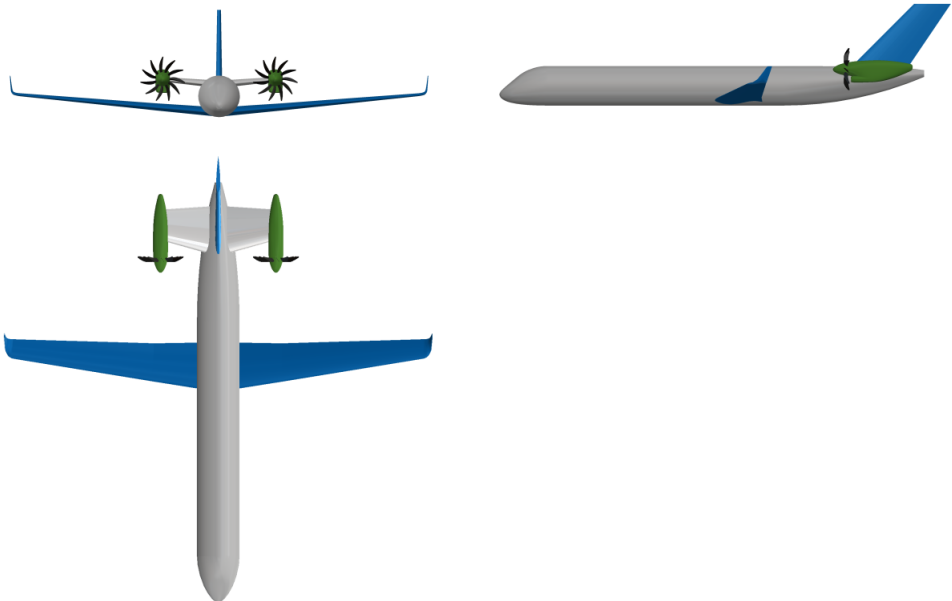


Figure 1.8: *IRON* project, baseline configuration provided by Leonardo Company, three views.

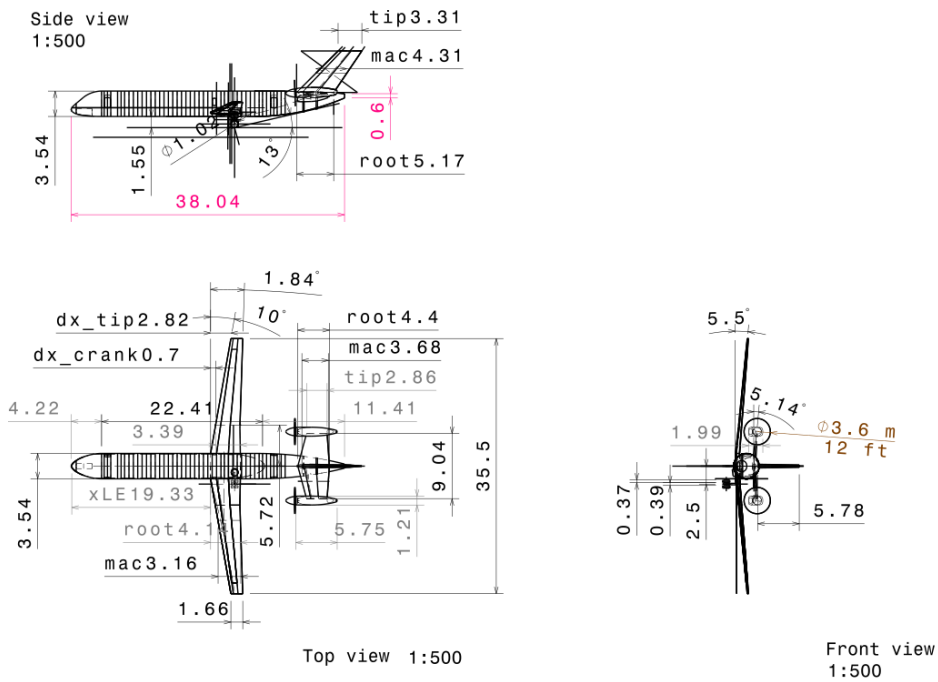


Figure 1.9: *IRON* project, baseline configuration technical drawing.

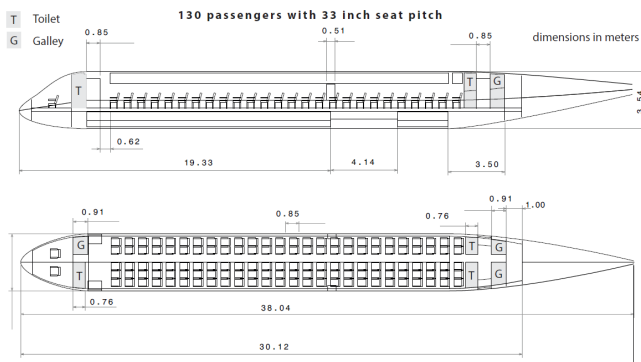


Figure 1.10: *IRON* project, cabin configuration layout.

Design parameters	Values
Passengers capacity	130 at 32" seat pitch
Design range	1600 nm with 130 passengers at 104.5 kg 30' holding at 1500 ft 100 nm alternate at 15000ft 5% fuel reserve
Cruise speed	M = 0.62 at 30 kft and 97% <i>MTOW</i>
Time to climb	<= 13' from 1500 ft to 25 kft
OEI ceiling	>= 16500 ft with 97% <i>MTOW</i> (ISA+10°)
TOFL	<= 1400 m with <i>MTOW</i> (ISA-SL)
LFL	<= 1300 m with <i>MTOW</i> (ISA-SL)

Table 1.1: *IRON* Top Level Aircraft Requirements

Aerodynamic targets	Values
Cruise efficiency	18.0
C_{Lmax} clean	1.6
C_{Lmax} take-off	2.4
C_{Lmax} landing	3.0

Table 1.2: *IRON* aerodynamic target of innovative configuration

Weights assumptions	Values
<i>MTOW</i>	53610 kg
<i>MLW</i>	52000 kg
<i>OEW</i>	33550 kg
Design Payload	13585 kg

Table 1.3: *IRON* Loop 1 weights assumptions.

preliminary assessment of the aircraft configuration and to provide a preliminary design and sizing of all those items that are missing from the input data received by Leonardo, such as the high lift devices, ailerons, elevator and rudder control surfaces. This task has been accomplished with two preliminary design frameworks: *ADAS* (Aircraft Design and Analysis Software) [39], developed at the Industrial Engineering Department of the University of Naples Federico II and *JPAD*, two software based on the classical semi-empirical approaches extensively used in the

Fuselage	Height/width	3.55 m
	Length	38.04 m
Wing	Area	105 m ²
	Aspect ratio	12
	Leading edge sweep angle	10.00°
	Taper ratio	0.40
	Root chord	4.480 m
	Kink non-dimensional station	0.3
Horizontal tail	Area	32.94 m ²
	Aspect ratio	2.5
	Leading edge sweep angle	10.38°
	Taper ratio	0.65
Vertical tail	Area	24.50 m ²
	Aspect ratio	1.36
	Leading edge sweep angle	45°
	Taper ratio	0.64

Table 1.4: *IRON* reference aircraft major geometric characteristics.

preliminary phase of aircraft design. Then the studies have been moved on the design of the wing airfoils in order to match the requirements. The set of airfoils provided by Leonardo in the CAD file has considered not to be suitable for the *IRON* project specifications and requirements, mainly because that set of airfoil does not show an extended laminar flow which is crucial to match the prescribed requirements. The wing planform is made up of three airfoils: root, kink and tip. Root and kink airfoil have the same relative thickness (0.18) while the tip airfoil has a relative thickness of 0.14 according to the geometric constraints provided. The wing incidence angle of +2° has been assigned (with respect to the fuselage reference line) and a linear distribution of the twist angle has been assigned from kink to the tip, the wing tip incidence angle is 0° with respect to the fuselage reference line. The design of the airfoil moves around three points:

- Target A: to match the required cruise efficiency a laminar airfoil is required (laminarity at 40% at least), avoiding any drag wave.
- Target B: in order to reach the prescribed maximum lift coefficients

(1.6), the airfoil must have a good enough maximum clean lift coefficient (1.87).

- Target C: in order to avoid a large decay of both aerodynamics and performance, the off-design conditions must be checked.

The airfoil design, 3D wing lift and drag distributions are verified by means of Computational Fluid Dynamics (CFD) RANS (Reynolds Average Navier Stokes) solver and SST k-omega turbulence model. Then, in order to comply the requirements, high-lift devices have been designed. Three wing sections have been considered for the flap design, choosing a fowler flap. Due to the fact that the maximum lift coefficients required for the take-off and especially for the landing requirements could be hard to be achieved with a single fowler flap design, leading edge high lift devices have been also designed. Because the wing laminar flow is mandatory, and due to the fact that the conventional leading edge high lift devices (i.e. slats) causes transition to turbulent flow immediately after the slat gap, in order to achieve the target efficiency, smart seamless and gapless high lift devices at the wing leading edge (Droop nose) turned out to be mandatory. Once terminated the reference wing analysis, the geometry of the winglet has been defined. Then higher fidelity aerodynamic analyses have been performed on the defined configuration, including fuselage analysis, drag polar estimation, longitudinal and lateral-directional stability and control. The final output of the aerodynamic database assessment is the complete set of trimmed drag polar curves at main flight conditions. To achieve this task, the estimation of the most forward and most aft position of the aircraft centre of gravity is needed. With respect to the centre of gravity excursion the horizontal stabilizer must be adequately sized. The aircraft weights breakdown has been accomplished according to Torenbeek's [25] methodology also considering suggestions coming from Leonardo Company, by means of *JPAD* software. The centre of gravity excursion is very large, from 4% to 52% of the mean aerodynamic chord. This wide centre of gravity shift leads to a large variation in the static stability margin. The large stability margin in the most forward centre of gravity position entails significant trim drag because a centre of gravity position well forward of the neutral point must be counteracted by a large download on the tail, resulting in a lower maximum lift coefficient (flap down). Also, the cruise efficiency will be significantly affected by

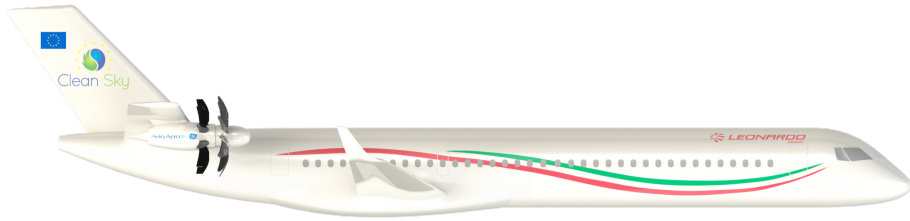


Figure 1.11: Rendering of *IRON* model manufactured to ILA Berlin Air Show 2018.

this large centre of gravity shift. Once the limits of the load and balance diagram have been determined, a complete aircraft stability analysis has been performed. The aircraft stability has been checked in the most aft centre of gravity position (the most critical condition), while the aircraft cruise efficiency (the TLAR target is 18 at $C_{L,cruise} = 0.61$ at FL300) and the take-off and landing $C_{L,max}$ have been evaluated in the most forward centre of gravity position. In this case, the cruise efficiency is about 16.7, well below the required target of 18. The maximum take-off and landing lift coefficients result to be 2.15 and 2.30 respectively. Those results highlight how the baseline configuration design and sizing must be revised to meet the TLAR. The activities performed during the first loop was focused on the preliminary aerodynamic design. Several work has been already published in different international conferences, such as [36], [38] and [37].

Massive dissemination activities have been carried out during these phases of the project. Beside the numerous conferences above cited ([36], [38], [37]), the 1:25 scaled model of the Loop 1 configuration has been exposed in ILA Berlin Air Show 2018 whose rendering is shown in Fig.1.11.

The Loop 2 started from the revision of the Loop 1 criticalities. As the typical CG (Centre of Gravity) range for similar aircraft, from 15% MAC to 33% MAC turned out to be too optimistic, different problems occurred. The performed analyses showed that for this innovative con-

figuration, the centre of gravity excursion is very large, highlighting the inadequate sizing of the horizontal tailplane to trim the aircraft in the whole centre of gravity excursion range. A similar CG excursion behaviour has been highlighted also by previous NASA works dealing with the design of a high-speed regional turboprop/prop-fan starting from the well-known McDonnell-Douglas DC-9 aircraft [41]. To overcome this issue, different aircraft configurations have been considered. Among them also three lifting surfaces has been investigated. This latter has been identified as the most promising solution to best comply with the provided aerodynamic requirements. Each of the analysed configurations is the result of a preliminary MDO (Multi-Disciplinary Optimization) process, in which all the disciplines involved (Weight and Balance, Aerodynamics, Stability and Control) have been analysed with low fidelity approaches. According to the chosen number of design parameters, more than 7000 different aircraft configurations have been generated and analyzed to define a response surface necessary to optimization process. Targets was the cruise drag, and the take-off and landing factors $MTOW/(S_W C_{L_{max}})$, which affects the ground performance. As mentioned, to define the Loop 2 aircraft configuration, three different solutions have been considered:

- Configuration 1: with the minimum limitations on the centre of gravity shift;
- Configuration 2: with heavy limitations to aircraft operational flexibility;
- Configuration 3: with three lifting surfaces and a minimum limitation of the CG excursion range.

All configurations have been designed following the same procedure:

- Multidisciplinary analysis carried out using JPAD software. A large number of configurations have been generated by varying several design parameters (wing position, wing area, wing sweep angle, horizontal tail area, horizontal tail aspect ratio, and so on);
- Results of those analyses have been used to build up response surfaces useful for an optimization process;

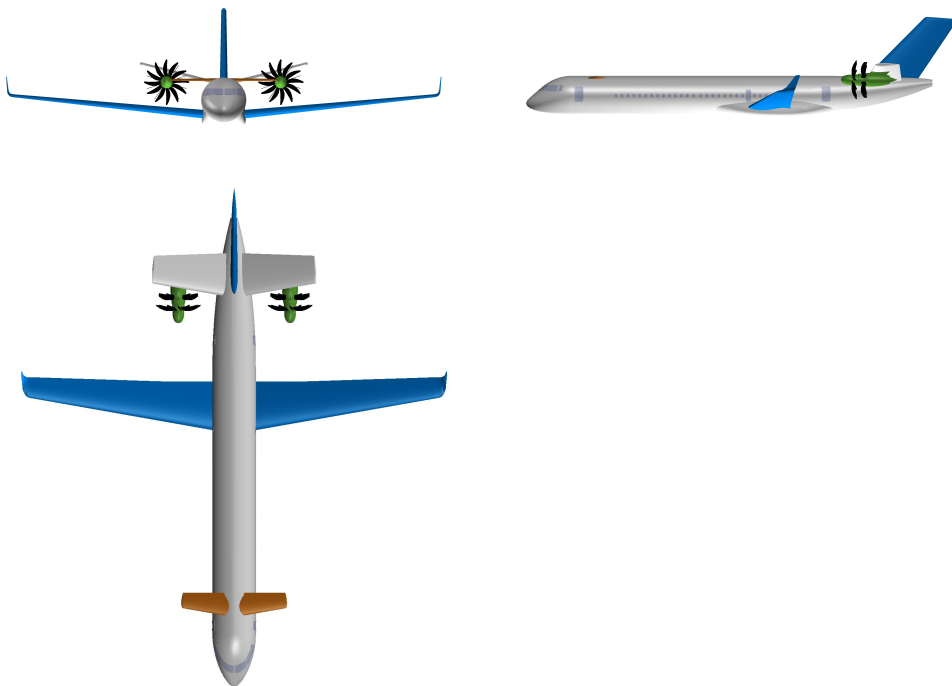


Figure 1.12: *IRON* project, Loop 2 configuration.

- Configuration optimization.

After the MDO process, the three lifting surfaces configuration has proven to be the most promising one in terms of aerodynamics, boarding diagram limitations with a slightly increment of the maximum take-off weight with respect to the Loop 1 baseline. Once the optimum configuration has been selected, all aerodynamic analyses have been carried out. *IRON* Loop 2 aerodynamic database will be assessed by means of high-fidelity tools, to allow aircraft performance and costs evaluation. The optimized aircraft, to be used as input for Loop 2 performance analyses, is shown in Fig. 1.12 and 1.13. All geometrical characteristics have been shown in Tab. 1.5, whereas main weights data and other mission-related assumptions have been reported in Tab. 1.6.

The first phase of second loop design activity was to enhance the aircraft cruise performances, just acting on wing airfoil shape, without reducing to much the high-lift characteristics of the baseline wing section. The geometrical constraints came from structural and wing internal volume

Fuselage	Height/width	3.55 m
	Length	38.04 m
Wing	Area	98.60 m²
	Aspect ratio	12.07
	Leading edge sweep angle	10.00°
	Taper ratio	0.372
	Root chord	4.25 m
Horizontal tail	Area	39.02 m²
	Aspect ratio	4.47
	Leading edge sweep angle	10.38°
	Taper ratio	0.62
Vertical tail	Area	24.50 m ²
	Aspect ratio	1.36
	Leading edge sweep angle	45°
	Taper ratio	0.64
Canard	Area	11.5 m²
	Aspect ratio	5.57
	Leading edge sweep angle	10.00°
	Taper ratio	0.65
	Root chord	1.74 m

Table 1.5: *IRON* Loop 2 aircraft major geometric characteristics. Bold data underline the differences between Loop 2 and baseline configuration.

Weights assumptions	Values
<i>MTOW</i>	55174 kg
<i>MLW</i>	49657 kg
<i>OEW</i>	34167 kg
Design Payload	14040 kg

Table 1.6: *IRON* Loop 2 weights assumptions.

requirements. This has been made defining all the winglet parameters and comparing the results with and without winglet. Several high-fidelity analyses have been performed to assess the aerodynamic and stability, as explained more in detail in the Chapter 5. The aerodynamic assessment of the aircraft longitudinal characteristics has highlighted some criticalities

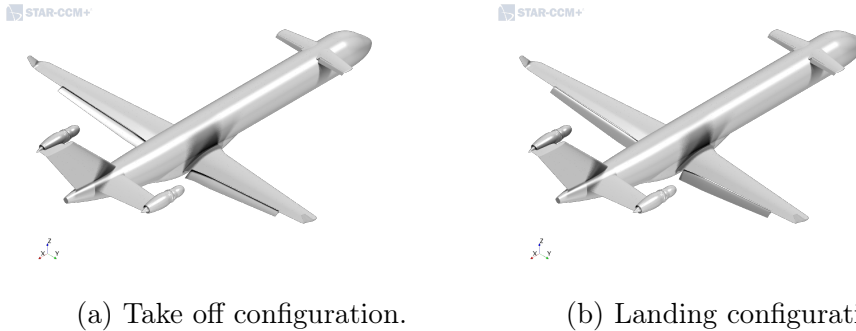


Figure 1.13: Complete Aircraft high-lift configurations in take off and landing condition

dealing with the interference effects of a three-lifting surface aircraft at full flap conditions [16], [17]. Several CFD-RANS simulations have been performed on the wing-body and wing-body plus canard configuration to assess the effects of the canard wake at full flap condition ($\delta_f = 35^\circ$ and $\delta_f = 25^\circ$) (Fig. 1.13). These analyses have highlighted that the canard, when its flaps are deployed, introduces a strong downwash on the main wing leading to a lift loss in the inner wing sections. On the other hand, the canard tip vortex introduces an upwash on the outer wing sections leading to a premature stall at the wing tip region. To mitigate this effect, a design study has been performed by changing the wing twist distribution in order to compensate both the lack and the excess of lift in the inner and outer wing region respectively. The wing twist has been changed accordingly to the estimation of the deficit in wing local angle of attack. This latter has been derived by comparing the wing lift distribution of the canard on and canard off configurations. Thanks to the wing twist optimization, it has been possible to increase the stall angle of about 5° gaining a delta in $C_{L_{max}}$ of about 0.4. At full flap condition, the canard wake has also a detrimental effect on the aircraft longitudinal stability. At low Angle of Attack (AoA), from 0° up to 6° , the canard wake moves from the lower to the upper side of the horizontal tail. In this range of AoA the aircraft stability is reduced. This interference effect was expected due to the reduced vertical stagger between the tail plane and the canard; however, it was supposed to be not so critical (considering the preliminary results carried out with low/medium fidelity tools like semi-

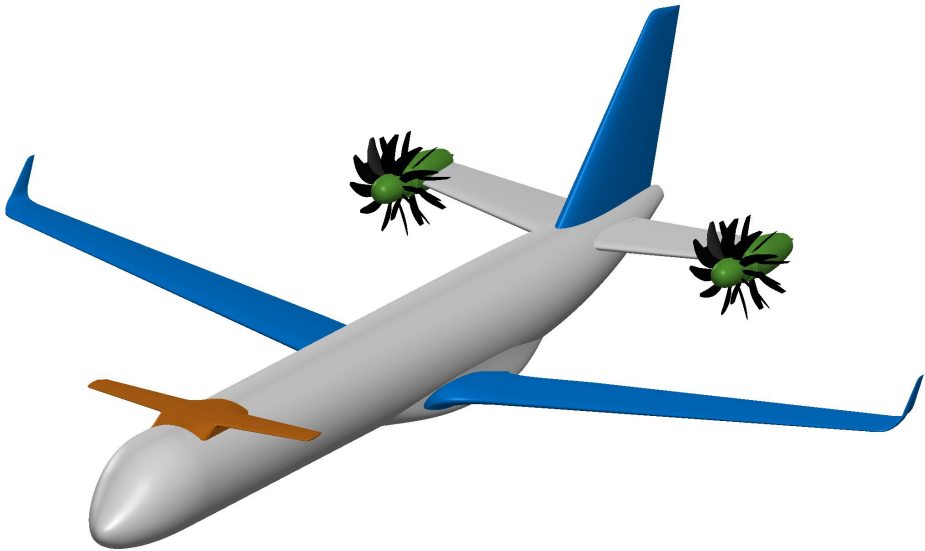


Figure 1.14: *IRON* Loop 3 configuration.

empirical approaches, panel code approach and vortex lattice methods). This issue has been mitigated in the Loop 3 configuration by shifting up the canard surface of about 30cm, by adding a fairing to reduce the interference effects of the canard-fuselage junction, and by reducing the canard flap deflection from $\delta_f = 25^\circ$ to $\delta_f = 15^\circ$. Moreover, canard root incidence angle has been set to $+2^\circ$ to allow canard to stall before the wing. Loop 3 configuration is shown in Fig. 1.14

1.5 Thesis objective and layout

The scenario outlined in this chapter underlines the motivations behind this research work. Aircraft market is in constant change and the focus on the regional turboprop transport is due to economic reasons clarified in previous sections. These, coupled with the substantial interest to noise and emissions issues, are a main topic of some European calls within Horizon 2020 framework, in which this work has developed.

The aim of this study is to offer innovative methodologies and framework that allow to perform preliminary analyses useful in the design process of

modern and future aircraft focusing on the innovative regional turboprop configuration within the *IRON* project. The work has been organized following not the real order in which the task have been achieved but following a logical thread made to provide the best experience for the reader. This is made also due to the fact that a cross-work between aircraft design and computer science need various work cycles in order to meets the expected results. This work is structured as follow:

Chapter 2 presents the computer framework built up for preliminary design and analysis optimization. The software has been designed and developed during the put in writing of this work, strictly coupling software engineering and aeronautical competencies. In the first section, the more common aircraft design and optimization tools from literature are presented. Then the focus is moved on the software structure emphasizing the organization of all that concerns aerodynamics in general. All the methodologies for aerodynamic parameters calculation are introduced in the following chapter (Chap. 3). Main results obtained using *JPAD* software, compared to literature ones, are contained in the last section, dedicated to software validation. All the innovative methodologies presented in the following chapter are integrated within *JPAD* to be easily used during the first phases of the design of an aircraft.

Chapter 3 discusses all the aerodynamic methodologies implemented in the software and explain the main innovation that this work is intended of bringing. In this part of the thesis all the innovative methodologies are introduced focusing on procedures and on the accuracy of results.

Chapter 4 deals with the validation of the above mentioned methodologies. CFD analyses have been carried out in order to figure out, in some cases, the behaviour and to validate the results. By the end of the Loop 2 and Loop 3 of the *IRON* project, wind tunnel tests have been performed and this permitted to experimental validate the introduced methodologies.

Chapter 5 presents the aerodynamic dataset of the entire *IRON* project obtained throw the conventional and innovative methodologies presented in the previous chapter. At the end, the last chapter presents the conclusion and introduces related future research topic. The main objective of this thesis work is to provide an improvement within the aircraft design concerning high lift prediction. The purpose is to overcome the current state of art in terms of low fidelity methodologies taking into account,

in the lift coefficient evaluation, different aspect ignored by traditional methodology. The results of this methodology are the maximum lift coefficient and the stall angle both in clean configuration and with high lift devices. To comply with the above-mentioned expectations, different applications have been carried out. The improved methodology turns out to be highly accurate with an error lower than 5% in all the considered case study both for the maximum lift coefficient and for the stall angle of attack.

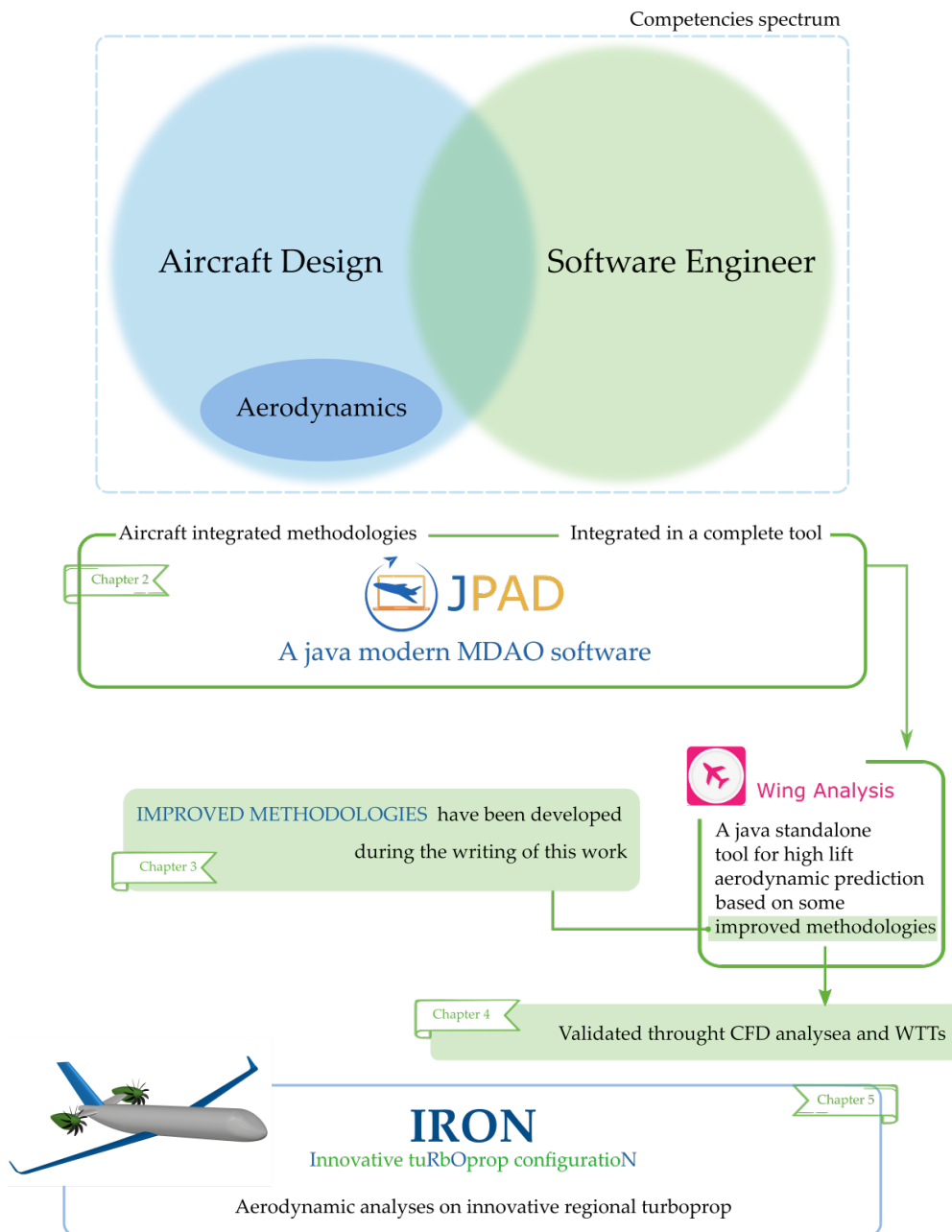


Figure 1.15: Test flow chart and work organization.

A java framework for aircraft design and optimization

2.1 Introduction

During preliminary design phases, for initial steps, the analysis to be performed need to be very fast, and with a certain grade of accuracy. During the conceptual and the preliminary phases, in fact, the goal is to search for the design that best fulfils the requirements. In this scenario has been developed a new java toolchain able to analyse and optimize different configuration of conventional and innovative aircraft. To successfully build a framework aim at effectively performing different analyses, deep link among aircraft design and software engineering had become a challenging task. This software environment is named *JPAD* (Java toolchain of Programs for Aircraft Design) and it has been completely realized at the Department of Industrial Engineering at University of Naples “Federico II” by *DAF* research group. *JPAD* is a java-based framework, with a user-friendly GUI, conceived as a fast and efficient tool useful as support in the preliminary design phases of an aircraft, It is modular and easily extendible; is based on advanced features of Java (Java 8+ and JavaFX [62]) and is designed using object-oriented and functional criteria;. The software platform is made to perform fast multi-disciplinary analyses of an established aircraft configuration and searching for an optimized configuration in a domain whose boundaries are defined by the user. The principal focus of *JPAD* is the overall aircraft model, conceived as a set of interconnected and parametrized components: wing, horizontal and vertical tail, fuselage, nacelles, and the propulsion system. The library

has been developed with the purpose of simplifying the composition of the input file for the user and doing fast analyses with a satisfying grade of accuracy. By using a multi-disciplinary framework, it is possible to perform a complete analysis on a complete aircraft or on a component. It allows to generate different aircraft, or different configurations of the same model, combining different components [90].

Synopsis

- There are a lot of framework and methodologies for aircraft preliminary design in literature
- *JPAD* architecture
- Particular emphasis is posed on all aerodynamic and stability modules of the framework
- A case study is presented in order to validate the software

2.2 Software for aircraft MDAO

Nowadays the preliminary design phase of an aircraft is becoming very challenging due to ever more demanding requirements. The goal of first design stages is to search for the configuration that best fit all requirements, among the results of a great number of multi-disciplinary analyses, as fast as possible, and with a certain grade of accuracy. The continuous improvement of computer calculation capabilities over years has allowed the growth of a large family of software dedicated to aircraft preliminary design activities concerning also multi-disciplinary analyses, and optimizations. A key feature that most of this software provide, is the possibility to parametrically define both aircraft components and complete aircraft configuration leading to a very fast and intuitive definition process of a generic aircraft model. With software and computer hardware currently available in aerospace industry, the design process has become very effective and employs, a very sophisticated and highly optimized chain of calculation tools. A modern preliminary aircraft design tool should be characterized by a certain level of accuracy and reliability (although using fast and simple semi-empirical procedures), the capability

to perform multidisciplinary analyses and optimizations, and reasonably short computational times for a complete analysis process. Because of the relevance of aircraft performance, noise and emissions levels, maintenance and operative costs in the commercial success of a transport aircraft, a modern software framework must be developed aiming at a multidisciplinary approach. Another important feature lies in the user-friendliness of the software allowing users to interact with the framework in an easy, fast, and efficient way. To ensure longevity and to enrich future exploitation capabilities, the possibility to include in the software multiple fidelity analysis methodologies or to easily implement new semi-empirical models, is of primary importance. One remarkable example is given by the possibility to easily generate and export the aircraft configuration *CAD* model in one or more standard formats and to execute high-fidelity analyses with external tools (i.e. Computational Fluid Dynamics *CFD* or Finite Element Method *FEM* solvers). Major aerospace companies have developed their own codes to estimate aero-structural characteristics and aircraft stability in the conceptual/preliminary design phase, as well as universities which have developed various codes for educational and research purposes. Major aircraft design software is listed below:

- **PACELAB**[42]: This framework is written in C#, developed by the German company Pace, part of the Italian TXT Group. The preliminary design platform Pacelab Suite helps design and systems engineers at aircraft, ship, rail and motor vehicle OEMs and first-tier suppliers to reliably assess future product characteristics and performance and to explore more design alternatives. This systems architecture supports investigations at the aircraft level with a fully-fledged preliminary aircraft design environment. Delivering instant feedback on the global impact, costs and benefits of architectural alternatives. It is made up of several interconnected modules. This framework distribution consist of two different kind of commercial licenses: academic and industrial one.
- **SUAVE**[9]: This is an open source software, written in Python, developed by the Stanford University. It is a conceptual level aircraft design environment built with the ability to analyse and optimize both conventional and unconventional designs. This capability is achieved in part by allowing analysis information for aircraft to be

drawn from multiple sources. Many other software tools for aircraft conceptual design rely on fixed empirical correlations and other handbook approximation. SUAVE instead provides a framework that can be used to design aircraft featuring advanced technologies by augmenting relevant correlations with physics-based methods.

- **CEASIOM**[27]: The CEASIOM application is a Conceptual Aircraft design tool. It was developed within the frame of the SimSAC (Simulating Aircraft Stability And Control Characteristics for Use in Conceptual Design) Specific Targeted Research Project (STREP) approved for funding by the European Commission 6th Framework Programme on Research, Technological Development and Demonstration. The SimSAC project aims at significantly enhancing CEASIOM functionality by introducing software that initially focuses on rapid low fidelity analysis, and as appropriate, resort to higher fidelity numerical simulations. Moreover, CEASIOM involve stability and control driven sizing and optimization earlier in the design cycle than is standard practice today. CEASIOM integrates into the application the main design disciplines, aerodynamics, structures, flight dynamics and flight performance. The CEASIOM software is offered to everyone as freeware. User must agree the End User License Agreement before downloading.
- **AAA (Advanced Aircraft Analysis)**[8]: AAA is a comprehensive aircraft design program that gives users full authority over the entire preliminary design process. It has been developed by DAR Corporation and it allows to calculate from weight and performance sizing to aerodynamics and stability and control analysis. The high fidelity, physics-based methods of AAA, combined with its time-tested semi-empirical methods, have improved the ability for aerospace engineers to analyse more unconventional aircraft designs and to stay at the forefront of our ever-evolving industry. The software is sold with a CD-ROM and particular discounts are available for educational and multiple licenses.
- **RDS^{win}**[21]: This framework has been developed by Conceptual Research Corporation of Raymer, D., P. It allows to manage aircraft design from first conceptual layout through functional analysis,

leading to performance, range, weight, cost results, and optimization. The tool is able to manage both conventional configuration and unconventional ones and it is sold under commercial licence for PRO version.

- **FLIGHT**[60]: First developed in 2006 by leading aeronautical authority Filippone, A., FLIGHT specialises in the prediction and modelling of fixed-wing aircraft performance. This is a multi-disciplinary software for the analysis of the performance of airborne vehicles and sub-systems to accurately map aircraft operation under all flight conditions, allowing for numerous logistical variations. A great benefit of this software is the ability to calculate the impact of noise, both within and around an airport. A trial version is available online and the software is sold under license.
- **ADAS**[39]: A Software for the conceptual/preliminary design of transport aircraft (Transport Jet, regional TBP, business jet) and light aircraft written in VISUAL BASIC. The software has been developed by Prof. Nicolosi, F., and Eng. Paduano, G. at University of Naples Federico II. This tool allows to perform pre-design analyses and design analyses for weight aerodynamics, stability and control and performance. This tool is distributed for free to students.

Since 2013 the DAF group has been involved in the development on a complex open-source Java library named *JPAD* [90], built as a modular framework, gathering all the lessons learned in the past few decades of tool development for aircraft design coupling the scientific know-how and the Software Engineering skills gained. As expert users of the above-mentioned software, authors have focused *JPAD* development taking into account main advantages and disadvantages of these latter. The main features of *JPAD* are the following:

- Software for the preliminary design of transport aircraft (conventional, hybrid-electric and innovative).
- Integrated environment able to assist the designer in all phases of his/her work, from the definition of the mission requirements to the multi-disciplinary analysis of the aircraft and its optimization.

- Multi-fidelity analysis approach applied since the initial phases of a project, capable to reduce the overall time required for the design phases.
- Easy to use thanks to a modern graphical user interface (GUI) 2.1.
- Advanced CAD generation functions for the automatic construction of complex aircraft models, ready to be imported by the main commercial high-fidelity CAE tools. In addition to the possibility of generating the aircraft model, it is also possible to generate the following isolated subparts: wing-fuselage junction, winglets, control surfaces and high-lift devices, propellers, turbofan engines (with attached housing, pylons and nacelles).

The strong know-how of the team, reached within the aircraft design field and as expert users of the above-mentioned software, has driven the *JPAD* development to the resolution of real design problems, overcoming the state of art of software current available. In particular, this vision has driven the development of *JPAD* as a modular framework, and it is characterized by innovative methodologies for preliminary design, contrary to most of the competitors that use semi-empirical methodologies strictly connected with the user experience. In fact, in recent years, the DAF group has gained knowledge and experience in developing, testing and validating several approaches and methodologies concerning aircraft design field of application. For instance, an improved approach regarding the vertical tail plane design and sizing was accomplished by means of numerical and experimental analyses [18] [31] [32]. This methodology was also applied to size the vertical tail plane of a new twin-engine commuter aircraft [34], then was validated through wind tunnel tests [35]. Past research activities have, also, focused on aerodynamic derivatives estimation on light and General Aviation aircraft [29]. Another methodology, regarding the design of the fuselage and the prediction of its aerodynamic characteristics, was developed through CFD-RANS calculations performed on several fuselage geometries suited for regional transport aircraft [33]. The research group have developed a deep experience as far as aircraft design [19] [50] [30] is concerned also for innovative technologies [63], such as for design and aerodynamic analysis of airfoil and high lift devices [20] and performance estimation of light aircraft with morphing

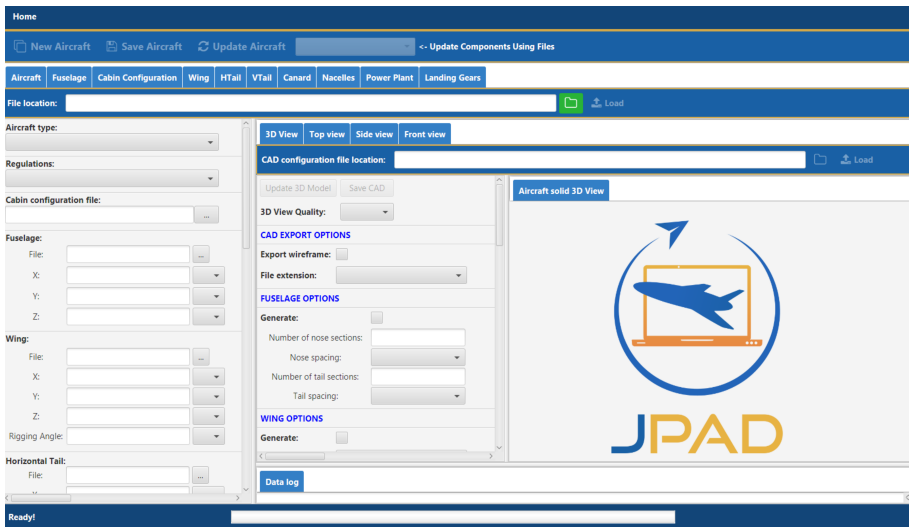


Figure 2.1: JPAD *Graphical User Interface*.

devices [64]. Most of these knowledges have been included in the *JPAD* library using dedicated external databases [90]. As mentioned in the bullets list, *JPAD/JPADCAD* is one of the several available geometry modellers conceived for conceptual aircraft design [91]. It is certainly one of the few freely available. *JPADCAD* stands out for being an open source software, in its basic functionalities at least, capable of exporting high fidelity CAD geometries. Its advanced functionalities include detailed movable surfaces in various standard formats, with the possibility of being used as an external library in third party applications and also fairing solids, although as draft shapes, connecting lifting surfaces to the fuselage. Nacelles, pylons and engines can also be handled by *JPADCAD*. Two possible solutions are available: To import a pre-designed baseline engine, stretch its shape, and put in position as appropriate; or to automatically generate the nacelle geometry starting from its wireframe representation. One feature still unimplemented in *JPAD/JPADCAD*, to be added in future releases, is the possibility to model internal structures with different levels of fidelity.

2.3 The software structure

Starting from the need of a comprehensive tool able to perform design and optimization analyses, the *JPAD* library has been conceived to be used in an industrial and research environment across conceptual and preliminary design phases. In these phases a lot of different configurations should be analysed, so the software has been developed to provide results in a short period of time and with a certain grade of accuracy. In order to perform fast analyses, there is a need of relying on semi-empirical methods. A comprehensive study of the methods available in literature has been firstly carried out to test the accuracy of the results. These methodologies have been implemented in the framework coupled with others made in-house after years of research, some of which by author itself. The result is a complete *MDAO* software which allow to perform analyses with different methodologies, more or less common or even innovative, based on user needs.

JPAD is completely written in Java. This programming language is a general-purpose, concurrent, class based and object-oriented. One design goal of the Java language is the portability, which means that programs written for the Java platform must run similarly on any combination of hardware and operating system with adequate runtime support. The choice of this programming language has been driven by several considerations, including the existence of open source libraries, especially for I/O tasks and for complex mathematical operations. Currently Java is the most used programming language according to TIOBE [13], as shown in Fig. 2.2. The TIOBE Programming Community index is an indicator of the popularity of programming languages. The index is updated once a month. The ratings are based on the number of skilled engineers worldwide, courses and third-party vendors. It is important to note that the TIOBE index is not about the best programming language or the language in which most lines of code have been written, but the index can be used to check whether your programming skills are still up to date or to make a strategic decision about what programming language should be adopted when starting to build a new software system.

To enhance the user-friendliness of the library, *JPAD* has been provided with a Graphical User Interface (GUI). The main goal of the GUI is to guide the user throughout all the *JPAD* functionalities starting from

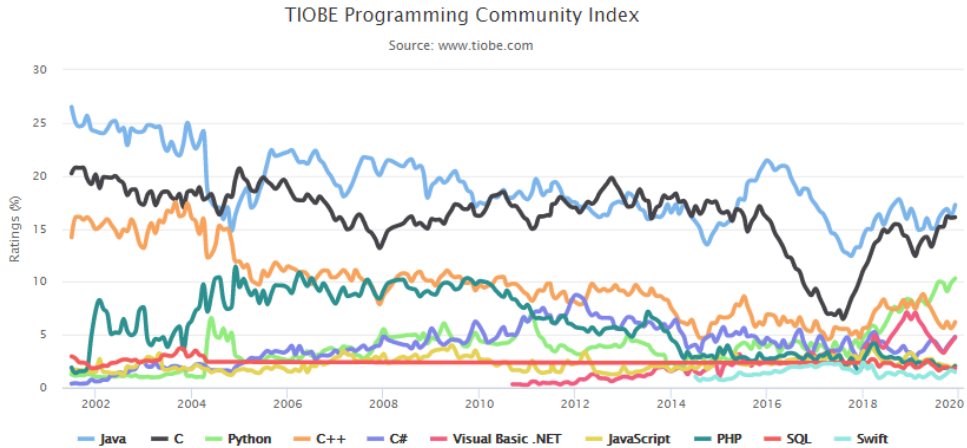


Figure 2.2: *Programming Language popularity trade ranked by TIOBE tiobe .*

the aircraft model generation up to the visualization and the management of the analyses results.

To achieve an understandable input file organization, a considerable study has been done. The result is an input structure composed by different interconnected XML files aiming to provide the maximum level of flexibility to the user both in the generation of an aircraft model, both in the execution of one or more analyses. In Fig. 2.3 the entire structure of the software is schematized. It is possible to clearly note that there are two main blocks: input and core. The input block is defined by two main parts: aircraft and analyses definitions. The aircraft input file defines a parametric aircraft model using a main file (Aircraft.xml) which collects all the components positions and the related xml file name (i.e. fuselage.xml, vtail.xml, and so on) whit all geometrical data. This structure allows to generate different aircraft, or different configurations of the same model, by simply combining different components in this way is easy to perform comparisons between these latter. The analyses input file defines all necessary data for each analysis present inside the Core module.

One of the most important feature of *JPAD* is that it is capable of automatically generate and export the aircraft CAD model in several for-

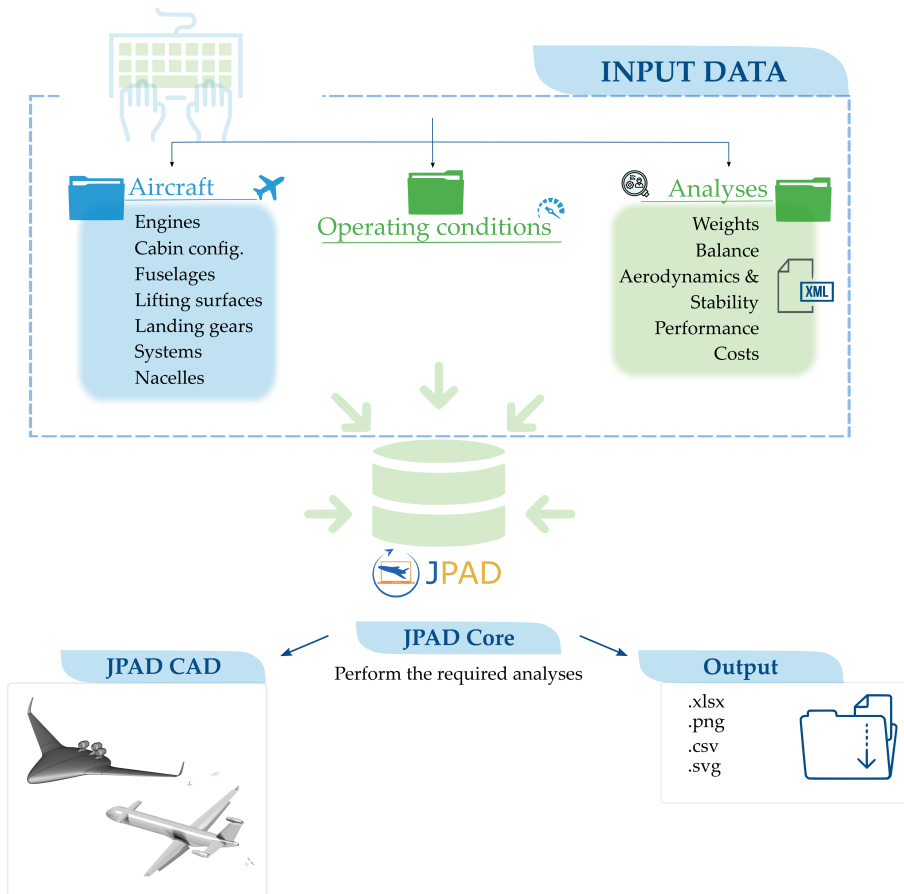


Figure 2.3: JPAD *input data infographic*.

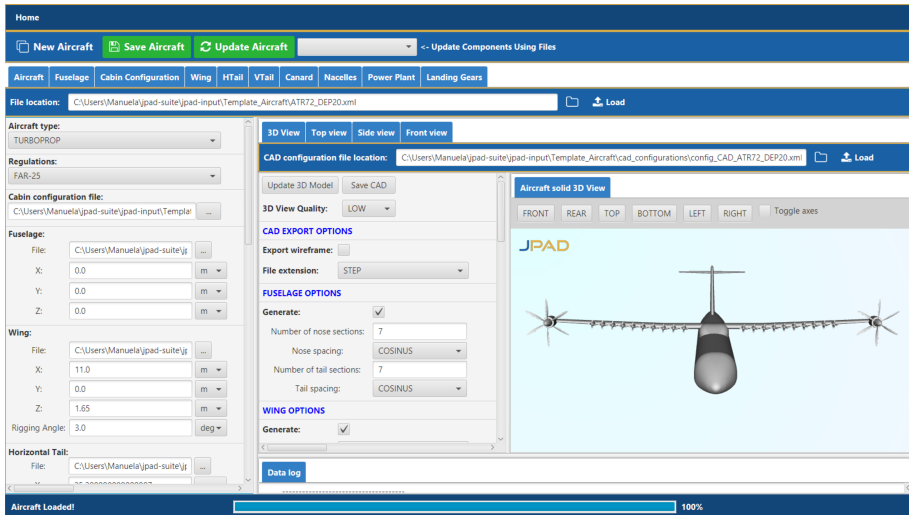


Figure 2.4: JPAD *Graphical User Interface, CAD generator.*

mats (i.e. STEP, BRep, etc.) (Fig. 2.4). This can be easily imported in external tools like CAD, CFD or FEM suites. The CAD model is conceived to allow also the automatic creation of complex elements such as wing tips and fairings. The possibility to generate a CAD model gives to the user an immediate feedback about the data provided to the application and allows for an accurate estimation of the wet surface of each component. CAD models are created in *JPAD* using the Open CASCADE library [79], an open source software development kit, written in C++ and released by Open Cascade SAS. The software is able to manage also complex geometries for non conventional aircraft as shown in Fig. 2.5.

The main block of *JPAD* is the Core which manages all the available analyses illustrated in Fig. 2.6. This contains several independent modules, that deals with following application fields. As illustrated, each of those can be further divided in several sub-modules related to a specific discipline calculation.

Weights

The weight module estimates the aircraft weight breakdown starting from a first guess maximum take-off weight and some mission profile specifica-

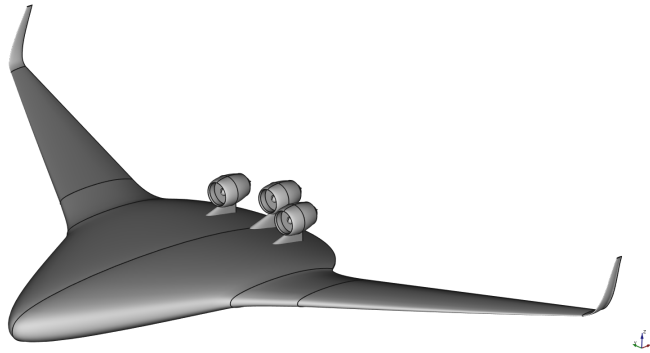


Figure 2.5: Blended wing body CAD, generated by JPAD.

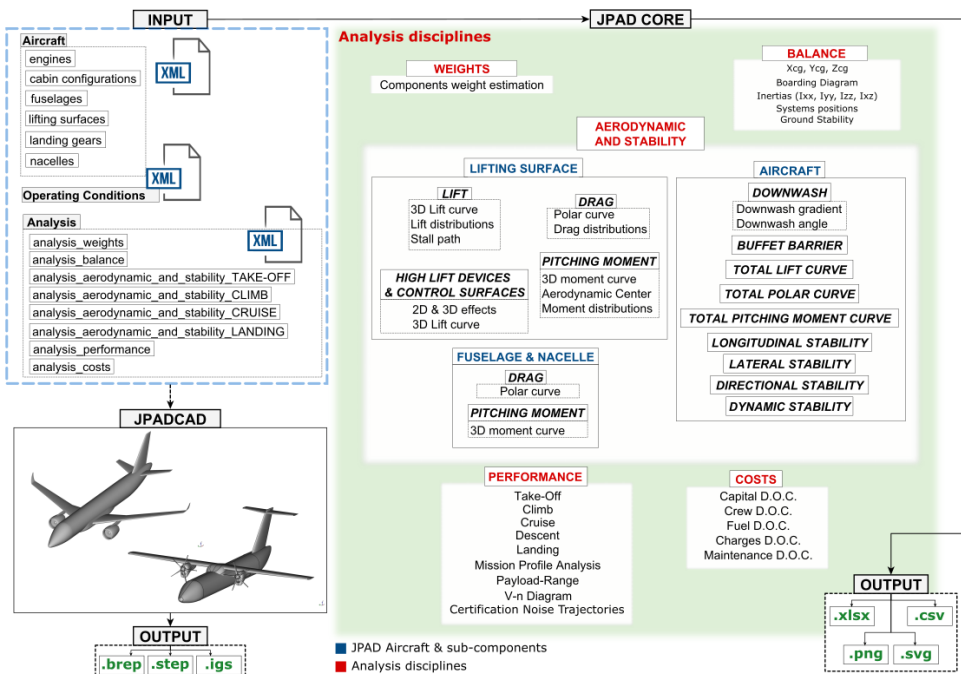


Figure 2.6: JPAD structure infographic.

tions. It evaluates each aircraft component mass using a mix of several semi-empirical equations [80] [56] [22] [44] [7] [86] [85]. The module is designed to allow users to choose for each component the calculation method or an averaged weight estimation using all the available methodologies. In addition, the user is provided with a calibration module which allows to manage each component estimated mass value. The weight analysis GUI is illustrated in Fig. 2.7. The user is allowed to choose whether to use a specific calculation method or a mean value of all component-related methods. The last strategy usually provides better results and can also take into account for different effects (e.g. mass relief effects of wing-mounted engines, fuselage mass increment due to podded landing gears, etc.) coming from different literature formulas. In addition to this, the analysis manager is also provided with the possibility to manually calibrate each component weight according to its experience. These, by means of a dedicated set calibration factors which can also be used in a parametric study to simulate technological trends. The weight estimation starts with a user-defined first guess $MTOW$ which is used to assess first guess values for MEW , $MZFW$ and MLW respectively assumed as 50%, 75% and 90% of the $MTOW$. Then payload and crew masses are calculated from the related cabin configuration input data assuming a user-defined mass for the generic passenger and a constant value of 76.51 kg for the generic crew member mass. Starting from the design passengers number, also the operating items mass is estimated checking if the user-defined reference mission range is higher or lower than 2000 nautical miles. At this point a reference value for each component mass is estimated as a fraction of the $MTOW$ according to the statistical percentages reported in Table 2.1. These values will be used to estimate each component calculation method percentage relative error.

Component	Mass percentage (w.r.t. <i>MTOW</i>)
Fuselage	10.00%
Wing	10.60%
Horizontal tail	1.15%
Vertical tail	1.15%
Canard (if present)	1.00%
Power plant	8.30%
Nacelles	1.90%
Landing gears	4.1%
Overall systems	13.60%

Table 2.1: Component reference mass percentages with respect to the *MTOW*.

Balance

In this part of the software, several characteristics are estimated, such as the centre of gravity position related to each weight condition and the balance diagram. The module allows also to manage each aircraft system and equipment group positions to better estimate the centre of gravity excursion. User can assign each group position or let the module to estimate them assuming typical positions as provided in [80].

Aerodynamics and Stability

The aerodynamic part estimates all the aerodynamic characteristics concerning lift, drag and moments coefficients at different operating conditions both for the complete aircraft and each component (wing, tails, fuselage and nacelles). Moreover, the stability module gives useful data about longitudinal and lateral-directional static stability of the whole aircraft considering non-linearity effects as well (i.e. pendular stability, non-linear downwash gradient, etc.). This module will be described more in detail in Section 2.4

Performance

This module evaluates the most important aircraft performance producing several useful reports and charts such as the Payload-Range diagram,

a detailed mission profile analysis report, the cruise flight envelope, climb and ground performance simulations as well as the Specific Air Range (SAR) chart. The calculation of the take-off and landing distances have been implemented using a simulation-based approach. This expects to solve an appropriate set of ordinary differential equations (ODE), which describes the aircraft equations of motion during all the take-off and landing phases. The developed module has proven to be very reliable and versatile as it performs the calculation of the required performance with almost no computational effort and with a good accuracy, providing a less than the 5% difference with respect to the statistical trend and a difference from the flight manual or public brochure data around 10%. Further information about this module are in [89].

Costs

Here is estimate the Direct Operating Costs (D.O.C.) breakdown. This concerns flight operations and consider different items:

- **Capital costs:** depreciation, interest, and insurance
- **Fuel cost**
- **Charges:** landing, navigation, ground handling, noise, emissions
- **Crew costs:** flight and cabin
- **Direct maintenance:** airframe and engine

To estimate these cost items, the methodologies defined by AEA [59] for capital, fuel, a part of charges (landing, navigation and ground-handling) and crew costs has been implemented while the ATA [58] method has been used for direct maintenance costs. Noise charges are calculated by using the formulation recommended by the Transport Aircraft Noise Classification Group (TNAC) within the European Civil Aviation Conference (ECAC) [57][26]. The emissions charges are estimated using formulation prescribed by ICAO in annex 16 volume 2 [46]. A detailed explanation of this module is provided in [24]. This module is described more in detail in [87].

To enhance the framework flexibility, the framework has been conceived to allow both a complete analysis Loop involving all disciplines,

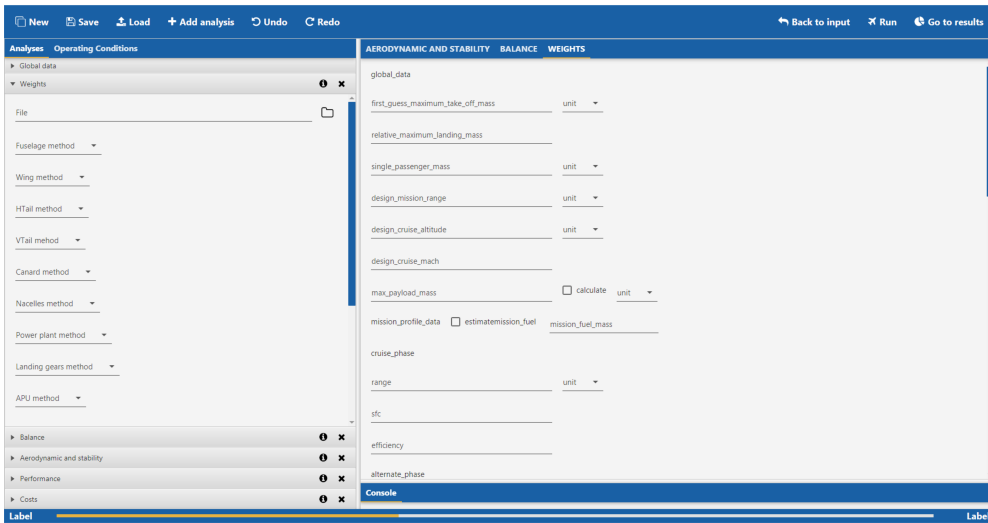


Figure 2.7: JPAD *input manager perspective for weights analysis*.

both standalone analyses using one or more calculation modules. In case the user wants to carry out a complete analysis cycle, the *JPAD* framework uses a combination of its analysis modules as shown in Fig. 2.8

JPAD allows to obtain different kind of output: analyses report in Excel format, charts in .png and .svg format and charts points in .csv format. Using Excel file, the comparison between two or more aircraft (or simply between slightly different configurations of the same aircraft) is easier and more efficient. Using specific native Java classes (such as `java.lang.Runtime` and `java.lang.Process`), this programming language al-

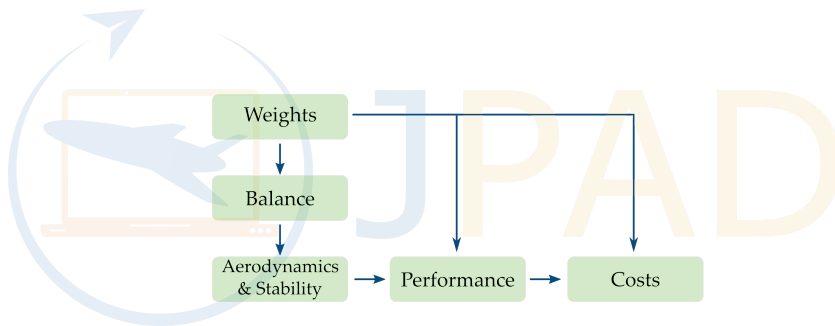


Figure 2.8: JPAD *core modules dependencies*.

allows *JPAD* to interconnect directly to external tools that can be launched in batch mode. At this time, the *JPAD* library is provided with launchers for the following external software: AVL(a program for aerodynamic and flight dynamics analysis)[52], Digital Datcom (a static stability and dynamic-derivative characteristics calculator)[28], STAR-CCM+ (a CFD analysis software) [5] and JSBSim2 (a multi-platform, general purpose object-oriented Flight Dynamics Model (FDM) written in C++) [47]. *JPAD* is also able to manage CPACS data format thanks to the collaboration with the German aerospace research institute DLR, within the European H2020 project named AGILE [67].

2.4 Aerodynamic and stability module

The aerodynamic and stability module of *JPAD*, and its related classes, have a complex structure due to the deep interconnection between the variables involved. In this section the software structure is explained not focusing in very detailing way on classes and methods but highlighting the link between parameters and the logic flow. A complete flow chart is in Fig.2.10. Each light blue box represents a java class which interacts with others. First of all, the aircraft data and operating condition have been read in the test class and have been given to aircraft class to build it. In the figure this is shown with xml files on the top. Particular attention is given to airfoil data due to the fact that input data have to be modified taking into account the operating conditions (TAKE OFF, LANDING, CRUISE or CLIMB). All data are stored whiting the code to be used in the analyses. Further details of airfoil management and related methodologies are in 3.2.1. Known airfoil aerodynamic parameter, the class `LiftingSurface` calculates discrete characteristics among 50 points along the semispan to prepare the surface to the analyses. Here the lifting surfaces are ready for the analysis. At this stage, known all input parameters and related data, as shown in Fig. 2.9, the main class calls the analysis manager to perform all the required analyse, using methods of the related manager class (such as weight manager, balance manager and etc.) All the aerodynamic analyses are managed by the class `ACAerodynamicAndStabilityManager`, one for each condition, which are associated to the aircraft. This class has input data about Mach and

Reynolds number and calculates the aerodynamic parameters of each component first, such as lift coefficient curve and polar curve, and the downwash angles. Know all components parameter, the class calculates the total aircraft ones. Through a longitudinal static stability analysis, it is possible to evaluate the trimmed lift and drag curves that are input data for the performance module as shown in Fig. 2.10

2.5 Result validation

In this section a test case is presented in order to validate the software: the twin-engine, medium-range jet *A220-300* in order to highlight the sweep effect on the aerodynamics.

2.5.1 Case study: Airbus A220-300

The Airbus A220-300, is a family of narrow-body, twin-engine, medium-range jet airliners (Fig. 2.11). The airliner was designed and originally marketed by Bombardier Aerospace, as the Bombardier CS300. It now marketed by Airbus as A220-300 and built by joint venture Airbus Canada Limited Partnership. It features 38.7m of overall length, a wingspan of 35.1m, and a total height of 11.5m. It can accommodate from 130 (in a 2-class configuration) to 160 passengers (single-class layout) with two-by-three seating. This aircraft offers one of the highest overhead bin volumes per passenger and one of the widest aisle [65]. Being a clean sheet design, the A220-300 features the latest generation flight deck, fly-by-wire, and a large use of composites along with aluminum-lithium alloys, which help managing target operating weights.

A data summary concerning main geometric characteristics and the interior arrangements, maximum weights and capacities have been reported in Tab. 2.2 and Tab. 2.3.

The aircraft has been analysed through a complete analysis flow using *JPAD* software. The first step of this case study concerns the generation of the aircraft parametric model used as baseline for the multi-disciplinary analysis process. The cabin layout has been modelled taking as reference the seat map presented in [2], while data concerning airfoils have been taken from [23] considering the SC(2)-0714 as root and kink stations airfoil

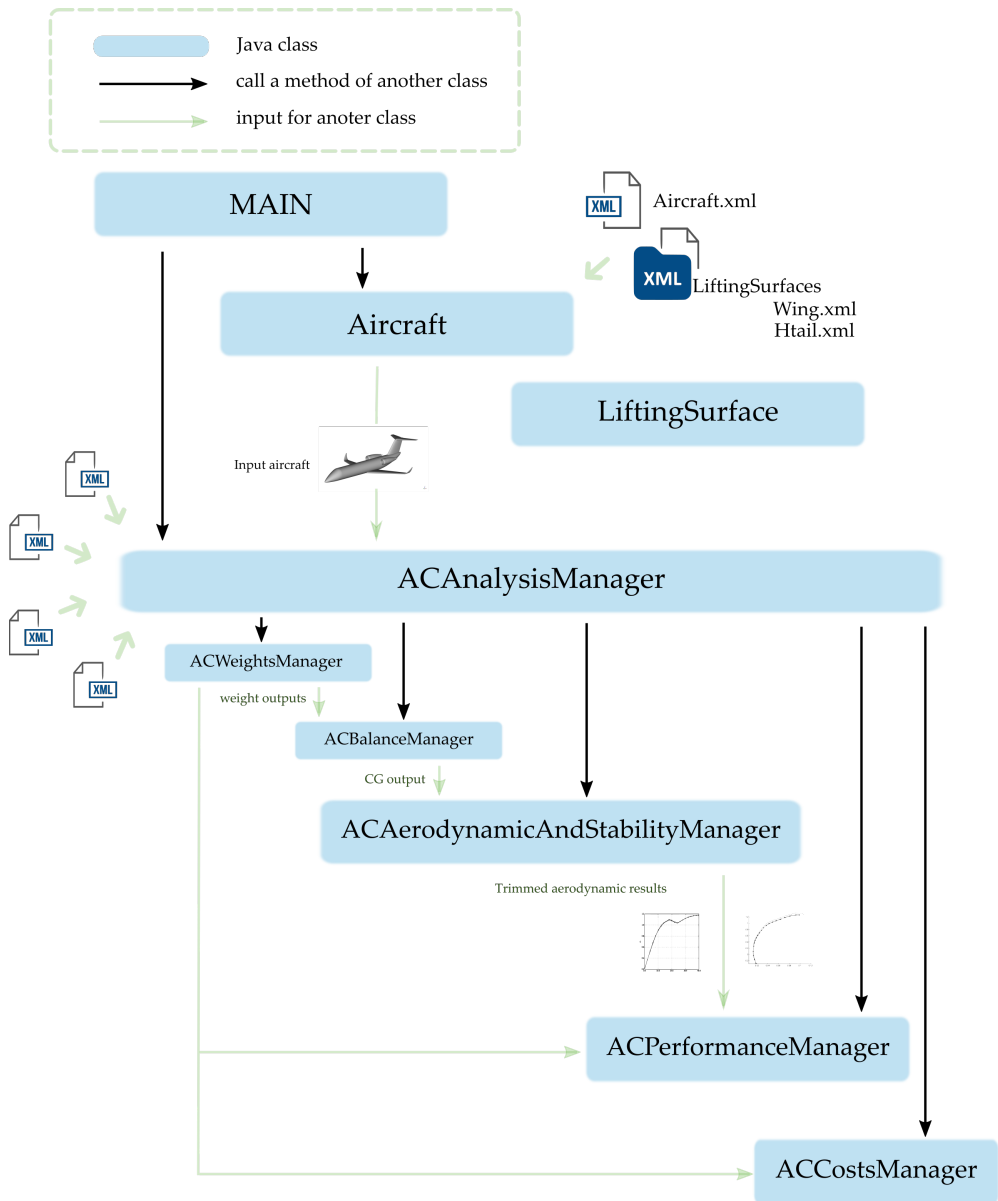


Figure 2.9: JPAD core modules structure and dependencies.

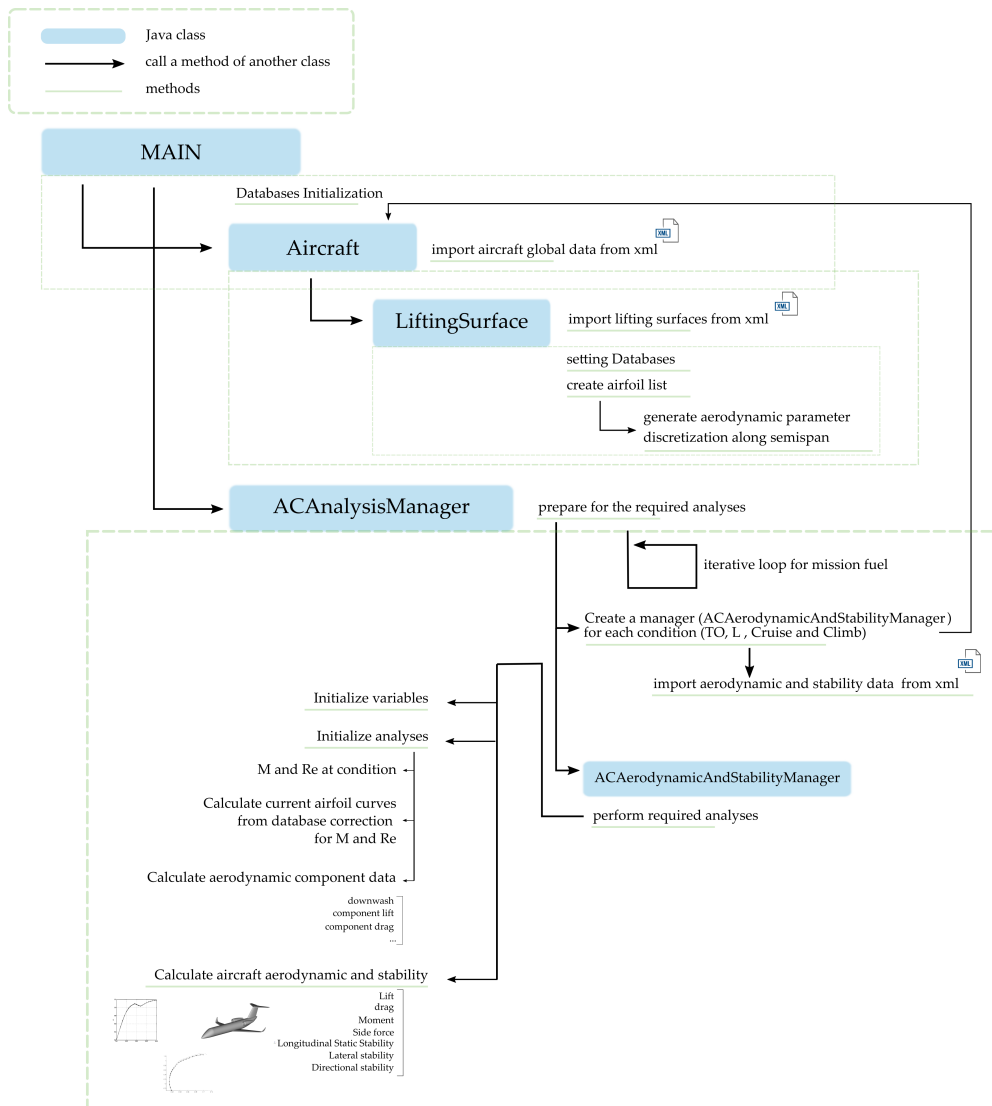


Figure 2.10: JPAD aerodynamic and stability module flow chart.



Figure 2.11: *A220 family (former Bombardier CSeries) 3-views.*

and the SC(2)-0710 as tip airfoil. Airfoil representation is in figure 2.12 and 2.13, while data are in Tab. 2.4.

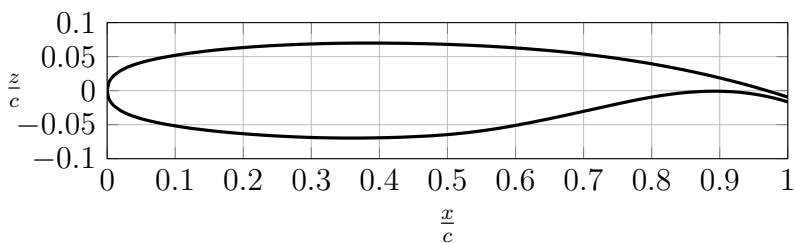


Figure 2.12: A220-300 root and kink airfoil SC(2)-0714 considered for analyses in *JPAD*, data from [23].

Overall length	38.71 m
Overall height	11.5 m
Wingspan	35.1 m
Wing area	112.3 m ²
Fuselage diameter	3.7 m
Cockpit crew	2 pilots
Cabin crew	3 (minimum)
Passengers	130 (2-class) - 160 (full economy)
Seat configuration	2-3 (full economy)
Seat pitch	81.3 cm (full economy)
Seat width	47-48 cm (full economy)
Cargo volume	31.6 m ³
Cabin width	3.28 m
Cabin height	2.13 m

Table 2.2: A220-300 main geometrical data and interior arrangements [65] [2] [66].

MTOW	67585 kg
MLW	58740 kg
MZFW	55792 kg
OEW	37081 kg
Max Payload	18711 kg
Max Fuel mass	17726 kg

Table 2.3: A220-300 main weights data [2].

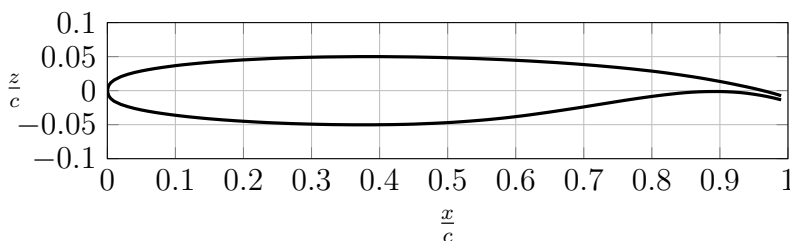


Figure 2.13: A220-300 tip airfoil SC(2)-0710 considered for analyses in *JPAD*, data from [23].

	SC(2)-0714 root-kink	SC(2)-0710 tip
α_{ol} (deg)	-4.00	-4.00
α^* (deg)	7.27	7.27
α_s (deg)	18.0	18.0
X_{ac}	0.256	0.254
C_{l_α} (deg ⁻¹)	7.17	7.17
C_{l_0}	0.500	0.500
C_l^*	1.30	1.30
$C_{l_{max}}$	2.25	2.23
$C_{d_{min}}$	0.00470	0.00470
C_{l_i}	0.65	0.65
$C_{m_{ac}}$	-0.138	-0.124

Table 2.4: A220-300 airfoil input data from [23]

The resulting aircraft model is shown in Figure 2.14 and Fig 2.15 where the 3-views, together with the related CAD model, have been collected. *JPAD* software is able to immediately generate aircraft 3-views and components to allow user to verify the input data. In addition, Figure 2.16 shows the representation of root airfoil in *JPAD* GUI, while relates lift coefficient data are in Fig 2.17. Finally, Figure 2.18 provides a visual comparison between the aircraft wing from flight manual [2] and the *JPAD* output including its movables. Once the aircraft model has been created, the second step of this case study is related to the configuration of each analysis input file needed to perform a complete multi-disciplinary analysis process involving all disciplines reported in Figure 2.6. The aerodynamic analyses have been at three different operating conditions: Cruise, Climb, Take off and Landing, summarized in Tab. 2.5 and Tab. 2.6 while control surface geometrical data are in 2.7.

The first discipline investigated by the *JPAD* multi-disciplinary analysis process concerns the weights. Table 2.8 reports main weights analysis output data compared with A220-300 weights coming from Table 2.3 (when available) and taken from [72].

Each component weight has been used as input for the balance analysis aiming to calculate the centre of gravity excursion of the parametric model under investigation. Fig. 2.19 shows the calculated boarding dia-

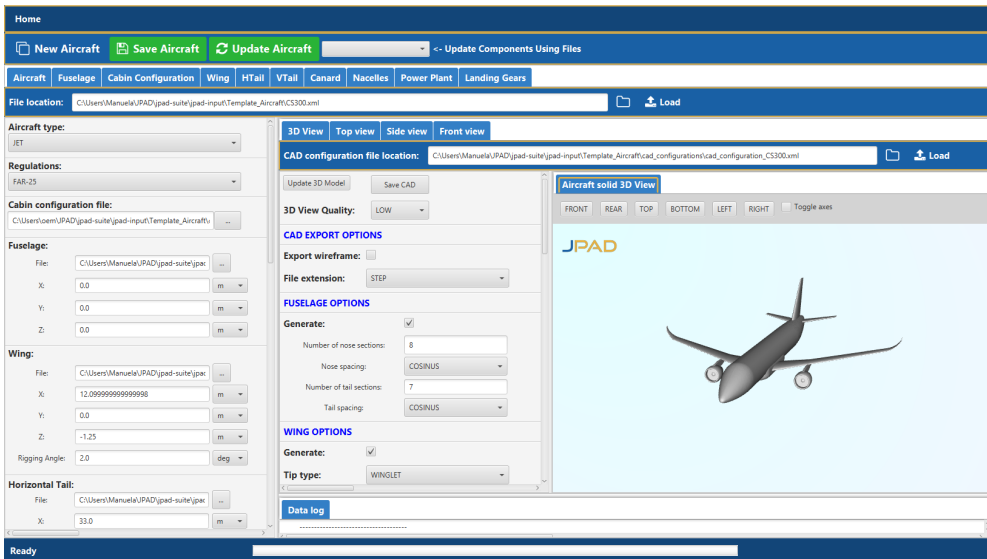


Figure 2.14: A220-300 CAD model representation in JPAD GUI.

Condition	Altitude (ft)	Mach number
Cruise	37000	0.78
Climb	37000 (top of climb)	0.4
Take Off	0	0.2
Landing	0	0.172

Table 2.5: A220-300 operating conditions.

Input data	Take-off	Climb	Cruise	Landing
Flaps deflection	15 deg	0 deg	0 deg	35 deg
Slats deflection	10 deg	0 deg	0 deg	25 deg
Horizontal tail incidence angle	-4 deg	0 deg	0 deg	-4 deg

Table 2.6: A220-300, control surface setting in different conditions.

gram. From the center of gravity positions envelope, in fact, the balance manager builds the boarding diagram from which the maximum forward, the maximum afterward and the operative center of gravity position are estimated.

Considering both cases related to the maximum afterwards and the

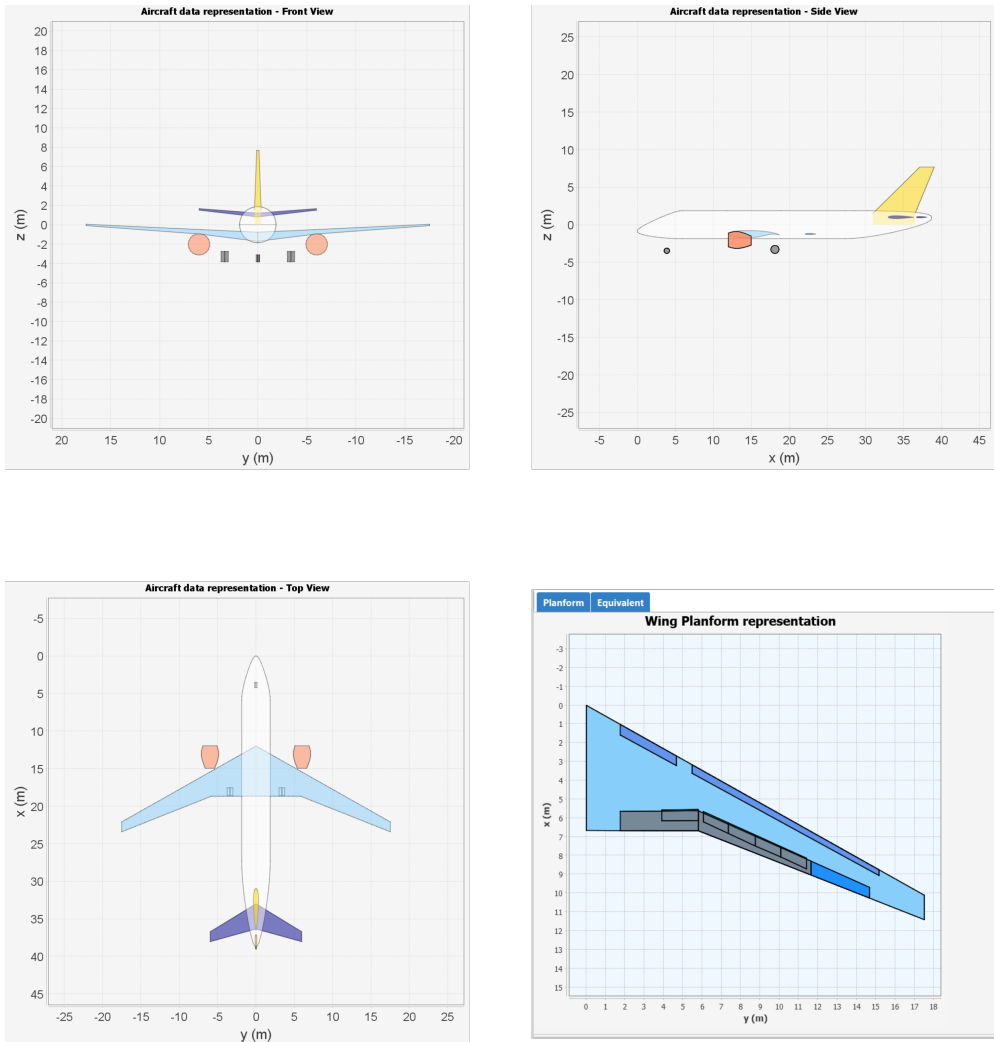


Figure 2.15: *A220-300 3-view and wing representation made by JPAD.*

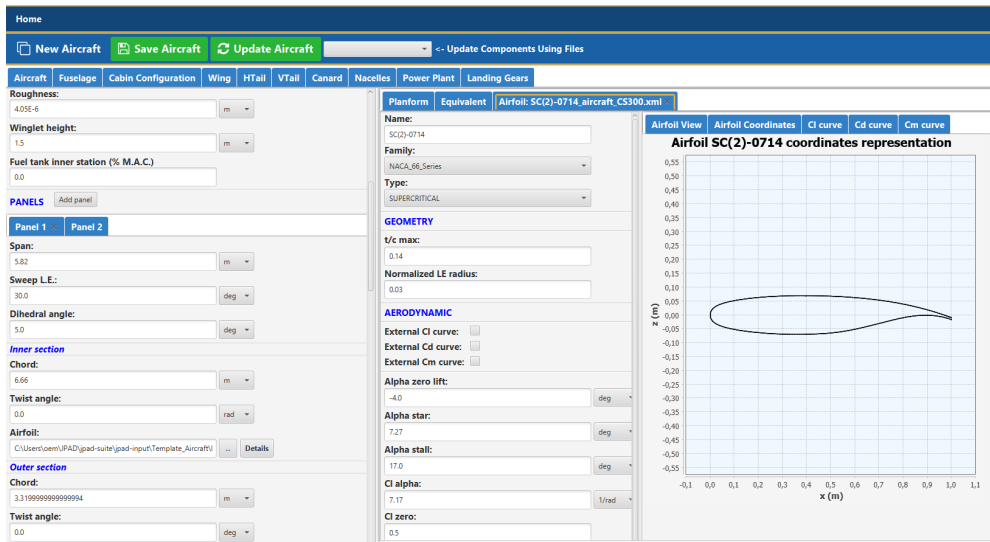


Figure 2.16: JPAD airfoil input data GUI. A220-300 root airfoil.

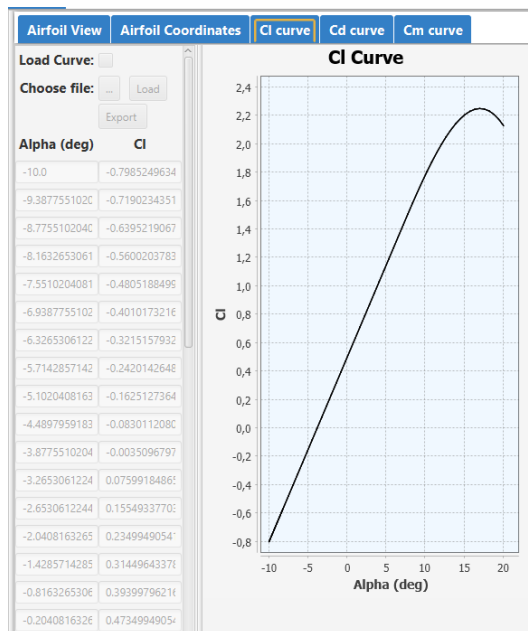


Figure 2.17: JPAD airfoil input data GUI. A220-300 root airfoil, lift coefficient curve $M=0.2$, $Re=1e6$.

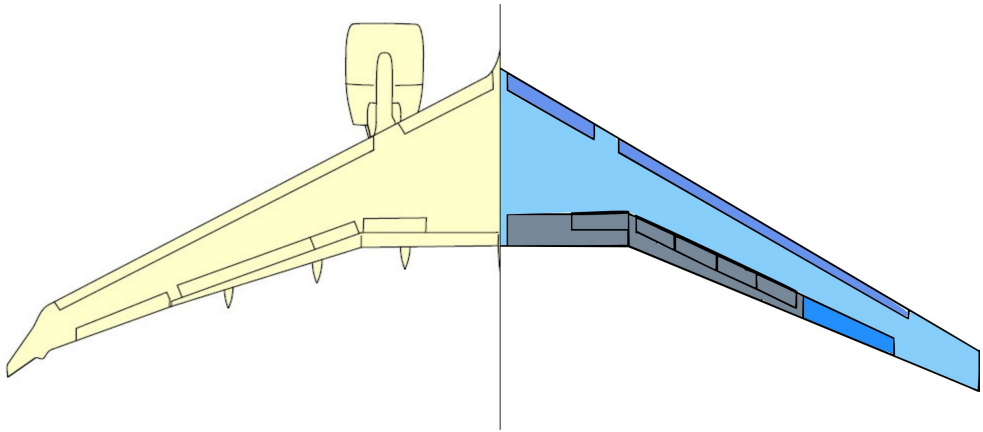


Figure 2.18: Comparison between the A220-300 wing [2] and the JPAD wing.

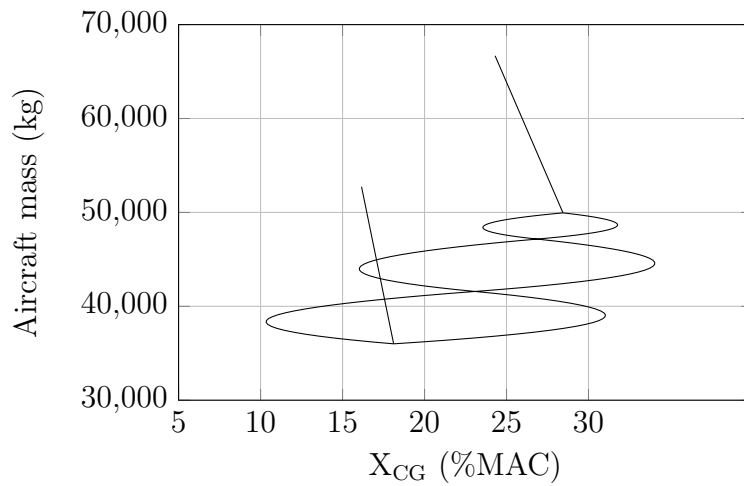


Figure 2.19: Boarding diagram of the A220-300 parametric model - JPAD. Max forward and max afterwards limits are in line with the centre of gravity envelope chart of the A220-300 reported in [1].

Control surface	η_{in}	η_{out}	outer chord ratio
Fowler flap	0.1	0.331	0.32
Fowler flap	0.331	0.6648	0.32
Slat	0.1	0.26	0.13
Slat	0.313	0.866	0.18

Table 2.7: A220-300, control surface geometry.

Output data	JPAD	A220-330	Difference (%)
MTOW	66676 kg	67585 kg	-1.34%
MLW	56675 kg	58740 kg	-3.51%
Max fuel mass	16784 kg	17726 kg	-5.3%
MZFW	54715 kg	55792 kg	-1.93%
Max payload	18711 kg	18711 kg	0%
Design payload	13964 kg	-	-
OEW	36004 kg	37081	-2.90%
Crew mass	459 kg	-	-
Operating items mass	2021 kg	-	-
MEW	33524 kg	-	-
Structural mass	18789 kg	-	-

Table 2.8: Main output data concerning the *JPAD* weights analysis of the A220-300 parametric model and from [72].

operative centre of gravity positions, a complete aerodynamic and stability analysis has been performed to calculate trimmed lift curves and trimmed drag polar curves needed by the performance manager of *JPAD* to carry out the overall performance assessment. Performance outputs, obtained from aerodynamic assessment described in detail in this work and presented in [89], will be briefly shown and in order to make a comparison with publicly available data concerning the A220-300 to show the level of accuracy reached by *JPAD* for a typical transport aircraft model.

Concerning aerodynamic analyses, first of all, components analyses have been performed with methodologies described in Chap. 3. In particular the application of the improved method for lift estimation, in which development the author has been involved, shows good results in terms of 3D lift coefficient both for clean configuration and flapped one as shown in Chap. 4. Lift coefficient curves for the isolated wing are shown in Fig. 2.20 and Tab. 2.9. In order to validate these results, wing aerodynamic analysis has been performed both with *JPAD* software and with an in-house panel method software for the aerodynamic analysis, based on the linearized equation of steady, compressible flow theory, at the same operating conditions. Results are shown in Fig. 2.21. To obtain these curves, airfoil data have been considered as input, and they are modified by preprocessor analysis (Sec. 3.5) to take into account high lift devices deflections. In Fig. 2.22, cC_l obtained with improved method is shown for take off and landing at $\alpha_w = 2^\circ$, while nacelle is shown in Fig. 2.23 and fuselage pitching moment is shown in Fig. 2.24. All operating conditions for the following results are referred to data in Tab. 2.5.

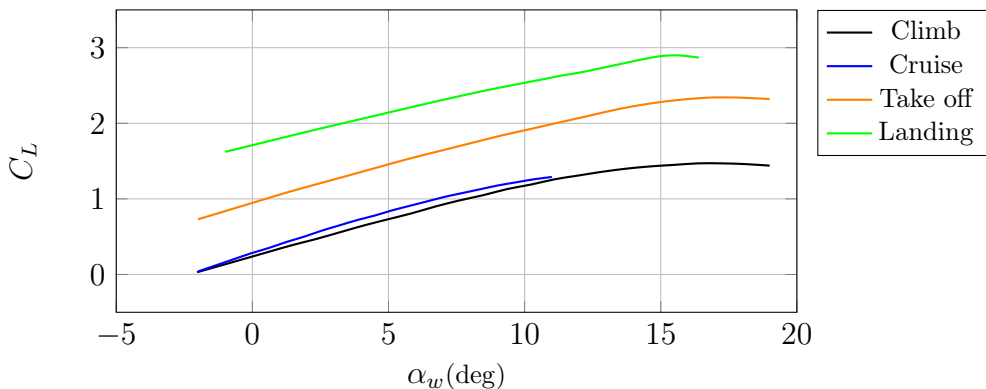


Figure 2.20: A220-300 aerodynamic assessment with *JPAD* software. Wing lift coefficient curves calculated with improved method in different operating conditions summarized in Tab. 2.5 and Tab. 2.6.

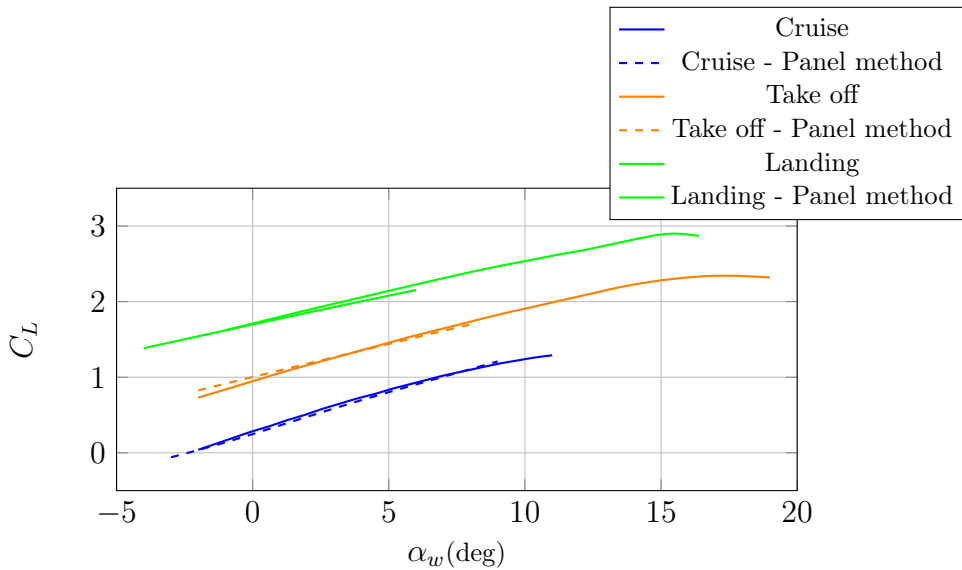


Figure 2.21: A220-300 Wing lift coefficient curves comparison calculated with improved method and with OpenVSP.

Condition	C_{L_0}	$C_{L_{MAX}}$	α_{0L}
Cruise	0.28	-	-2.42°
Climb	0.24	1.47	-2.38°
Take Off	0.91	2.34	-8.66°
Landing	1.71	2.89	-19.2°

Table 2.9: A220-300 operating conditions.

After all aerodynamic analyses on each component have been carried out, the analysis moves on complete aircraft. First of all the angle of attach of each component is calculated and for horizontal tail it is in terms of downwash angle shown in Fig. 2.25. In this picture two different approaches have been reported: the classical approach from literature from [84] and the improved one, described in Sec. 3.2.2. Then, from balance equation, the pitching moment with respect to the centre of gravity of the whole aircraft is calculated for each component, each operating condition and each centre of gravity position. Fig. 2.26, 2.27, 2.28, 2.29. Known the pitching moment coefficient of component it has been possible

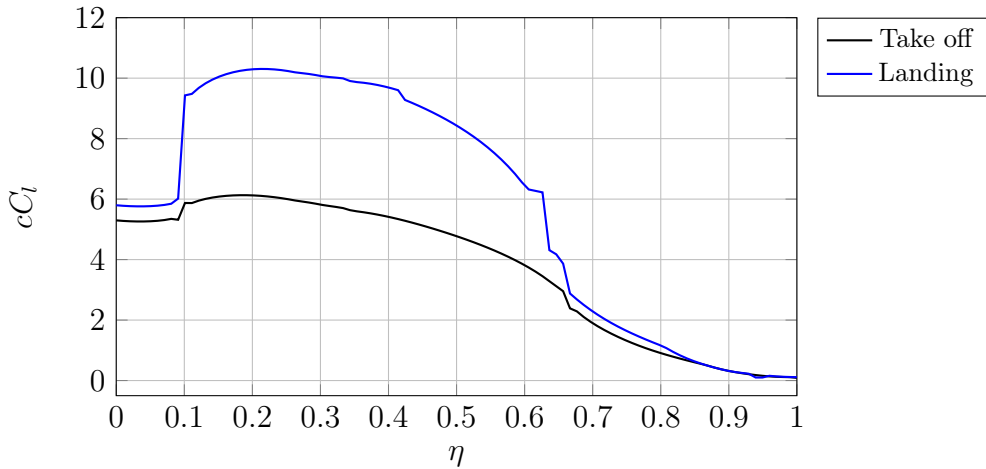


Figure 2.22: A220-300 aerodynamic assessment with *JPAD* software. cC_l distribution along semispan calculated with improved method explained in Chap. 3, in configuration with high lift devices deflected, in different operating conditions summarized in Tab.2.5 and Tab. 2.6, at $\alpha_w = 2^\circ$.

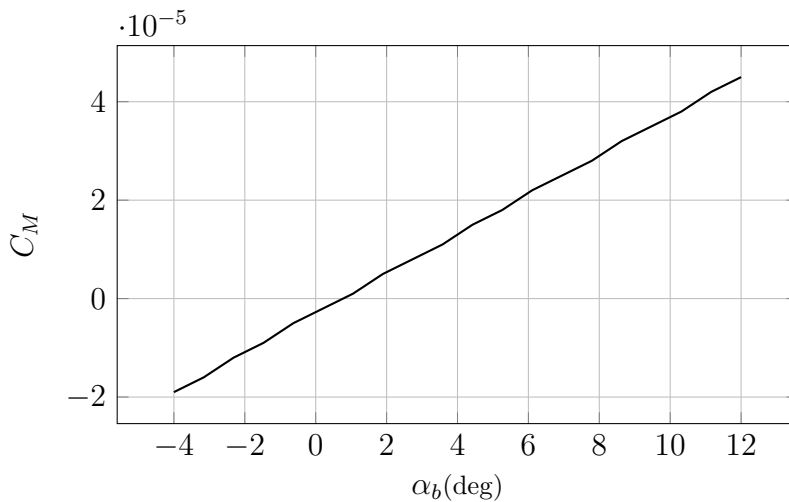


Figure 2.23: A220-300 aerodynamic assessment with *JPAD* software. Nacelle pitching moment, for each nacelle, landing condition.

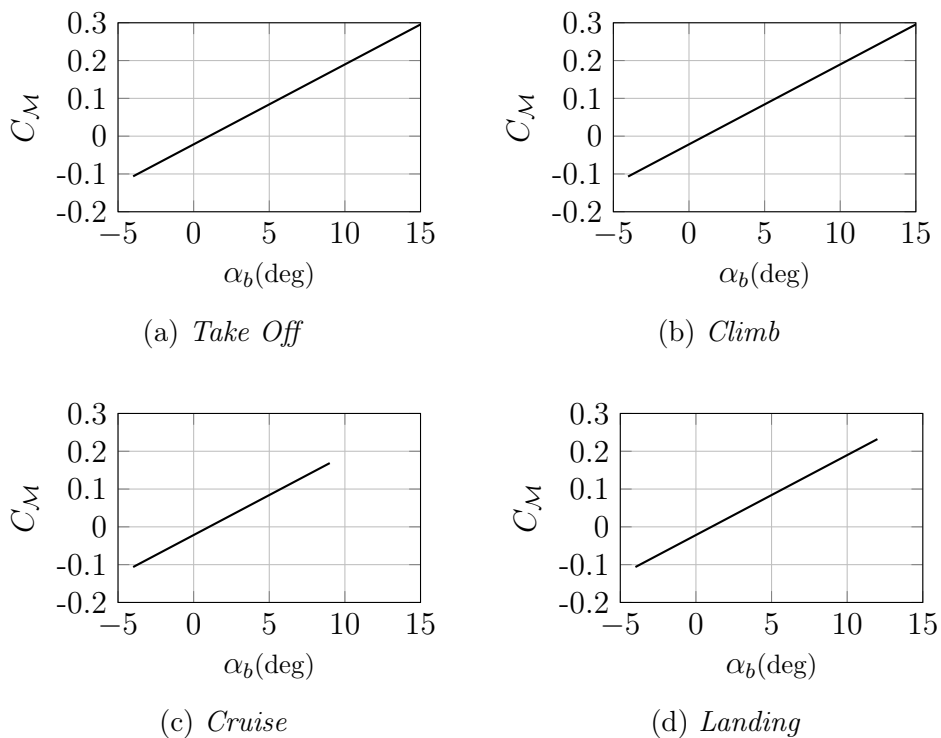


Figure 2.24: A220-300 aerodynamic assessment with *JPAD* software. Fuselage pitching moment in different operating conditions.

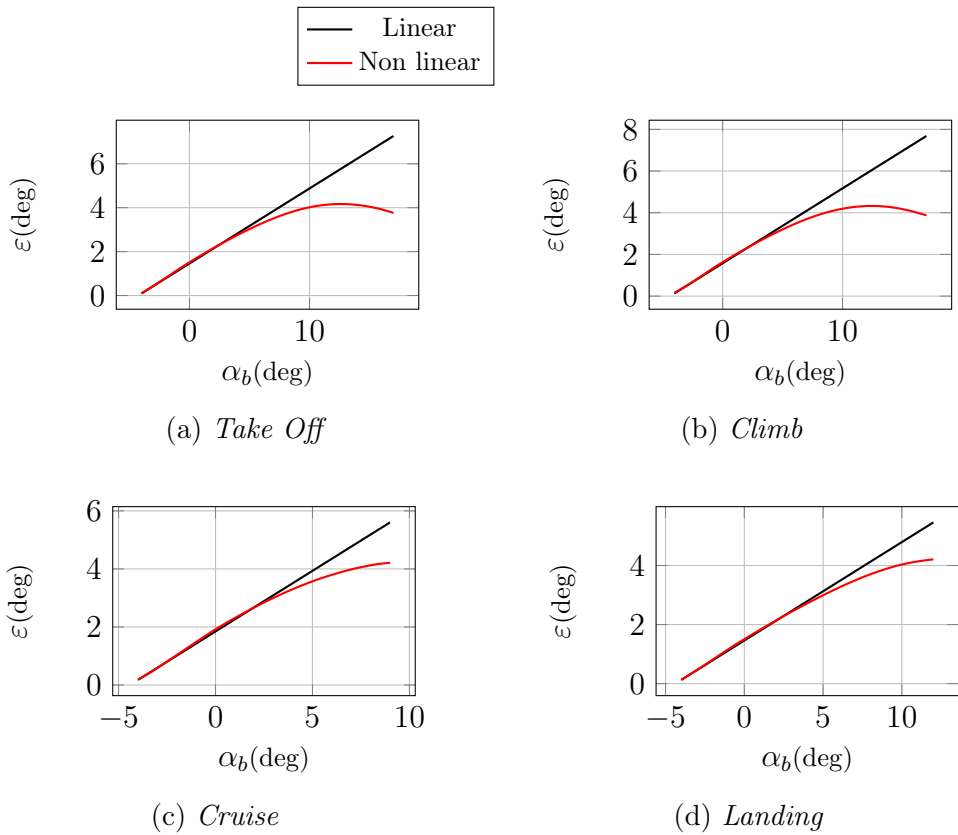


Figure 2.25: A220-300 aerodynamic assessment with *JPAD* software. Downwash angle in various operating conditions.

to evaluate the aircraft pitching moment for different angles of elevator deflection. This result is shown in Fig. 2.30 for landing condition. From equilibrium equation described in Sec. 3.2.4, it has been possible to evaluate the equilibrium lift coefficient of horizontal tail, (Fig. from 2.31 to 2.34) and the total equilibrium lift and drag coefficient. Main results of lateral-directional stability are in Fig. 2.35 and Fig. 2.36. Finally the trimmed lift, drag and efficiency curves for each condition are in Fig. 2.38, 2.39 and 2.40. There latter are the input data for performance analyses. In Fig. 2.41 is shown *CAD* output produced by *JPAD*

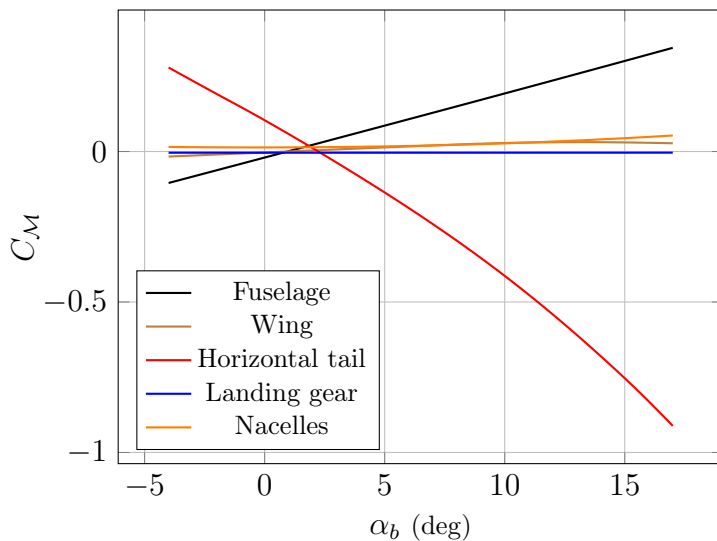


Figure 2.26: A220-300 aerodynamic assessment with *JPAD* software. Total moment coefficient breakdown at take off condition, $X_{cg} = 34\%$ MAC.

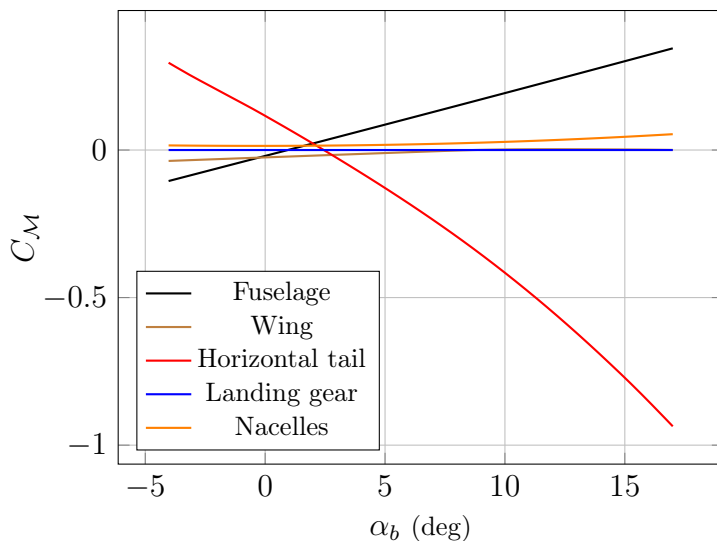


Figure 2.27: A220-300 aerodynamic assessment with *JPAD* software. Total moment coefficient breakdown at climb condition, $X_{cg} = 34\%$ MAC.

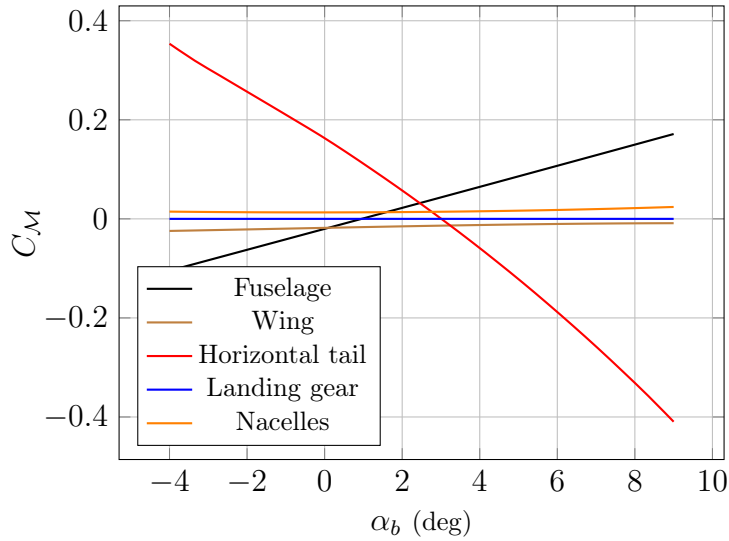


Figure 2.28: A220-300 aerodynamic assessment with *JPAD* software. Total moment coefficient breakdown at cruise condition, $X_{cg} = 34\%$ MAC.

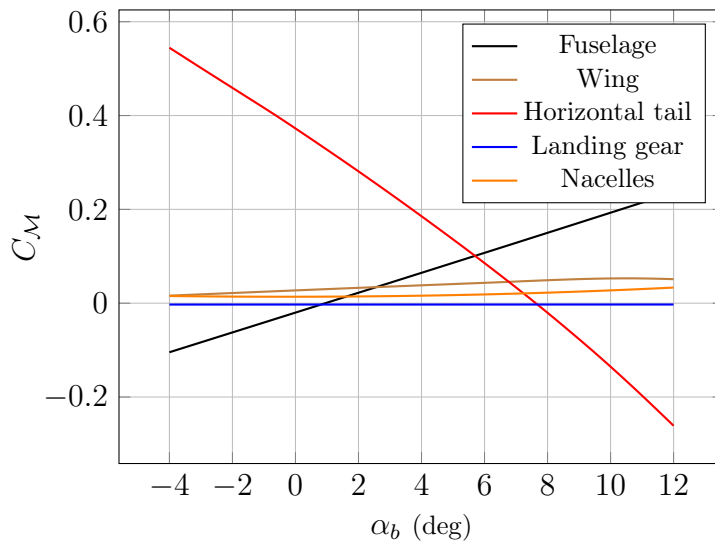


Figure 2.29: A220-300 aerodynamic assessment with *JPAD* software. Total moment coefficient breakdown at landing condition, $X_{cg} = 34\%$ MAC.

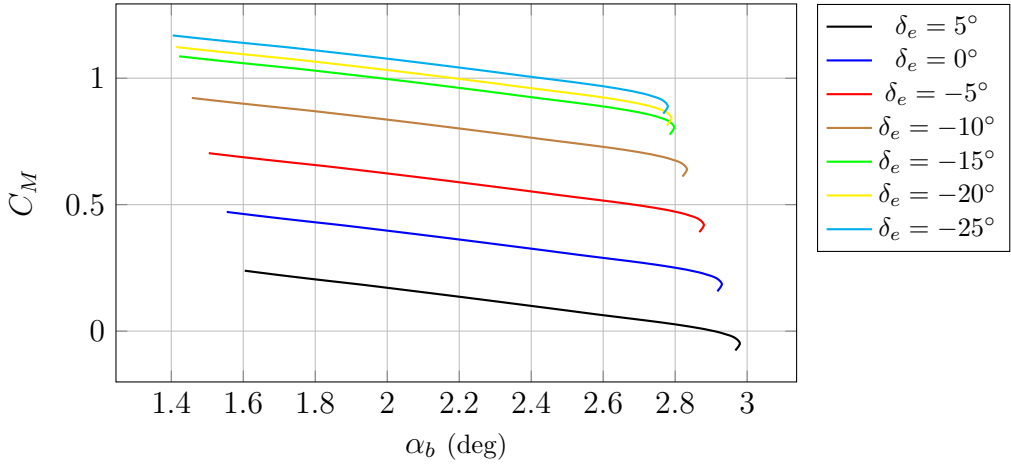


Figure 2.30: A220-300 aerodynamic assessment with *JPAD* software. Moment coefficient for different angles of elevator deflection, landing condition, $X_{cg} = 34\%$ MAC.

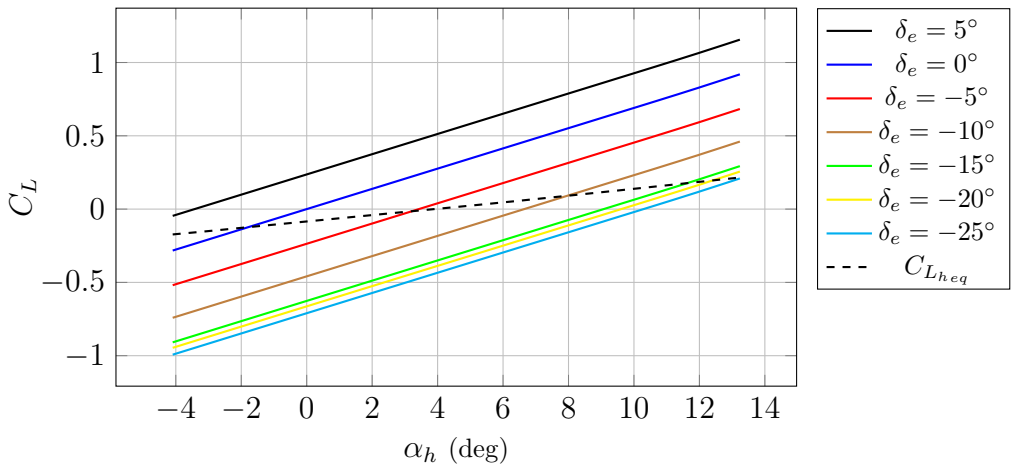


Figure 2.31: A220-300 aerodynamic assessment with *JPAD* software. Horizontal tail lift coefficient for different angles of elevator deflection and equilibrium lift coefficient curve, take off condition, $X_{cg} = 24.3\%$ MAC.

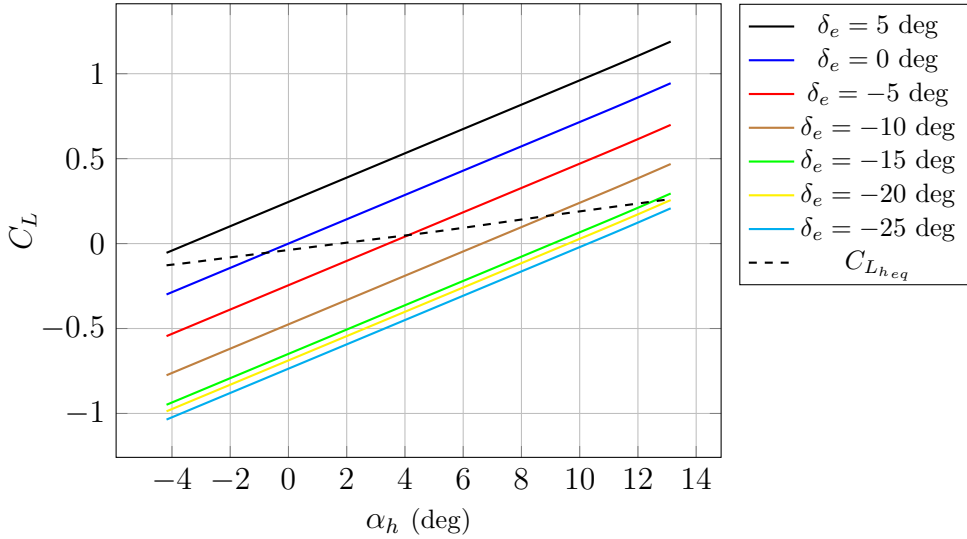


Figure 2.32: A220-300 aerodynamic assessment with *JPAD* software. Horizontal tail lift coefficient for different angles of elevator deflection and equilibrium lift coefficient curve, climb condition, $X_{cg} = 24.3\%$ MAC.

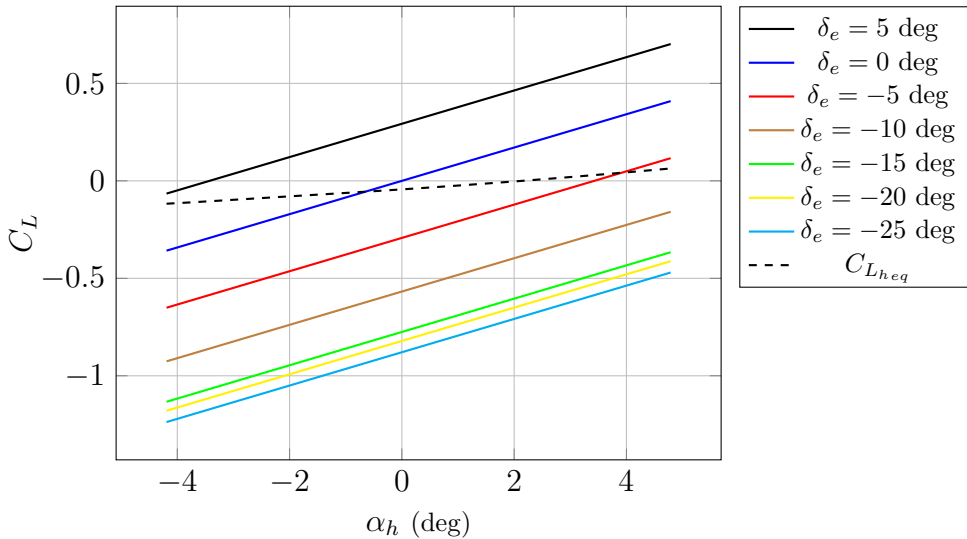


Figure 2.33: A220-300 aerodynamic assessment with *JPAD* software. Horizontal tail lift coefficient for different angles of elevator deflection and equilibrium lift coefficient curve, cruise condition, $X_{cg} = 24.3\%$ MAC.

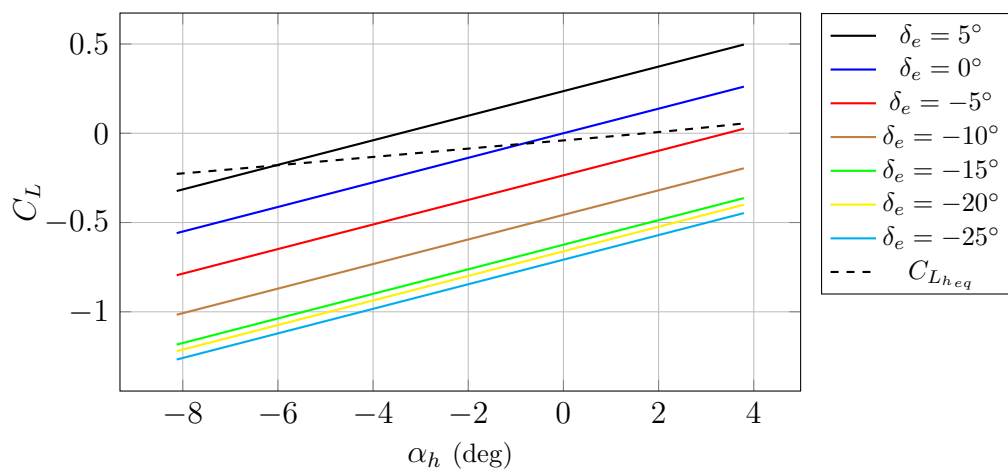


Figure 2.34: A220-300 aerodynamic assessment with *JPAD* software. Horizontal tail lift coefficient for different angles of elevator deflection and equilibrium lift coefficient curve, landing condition, $X_{cg} = 24.3\%$ MAC.

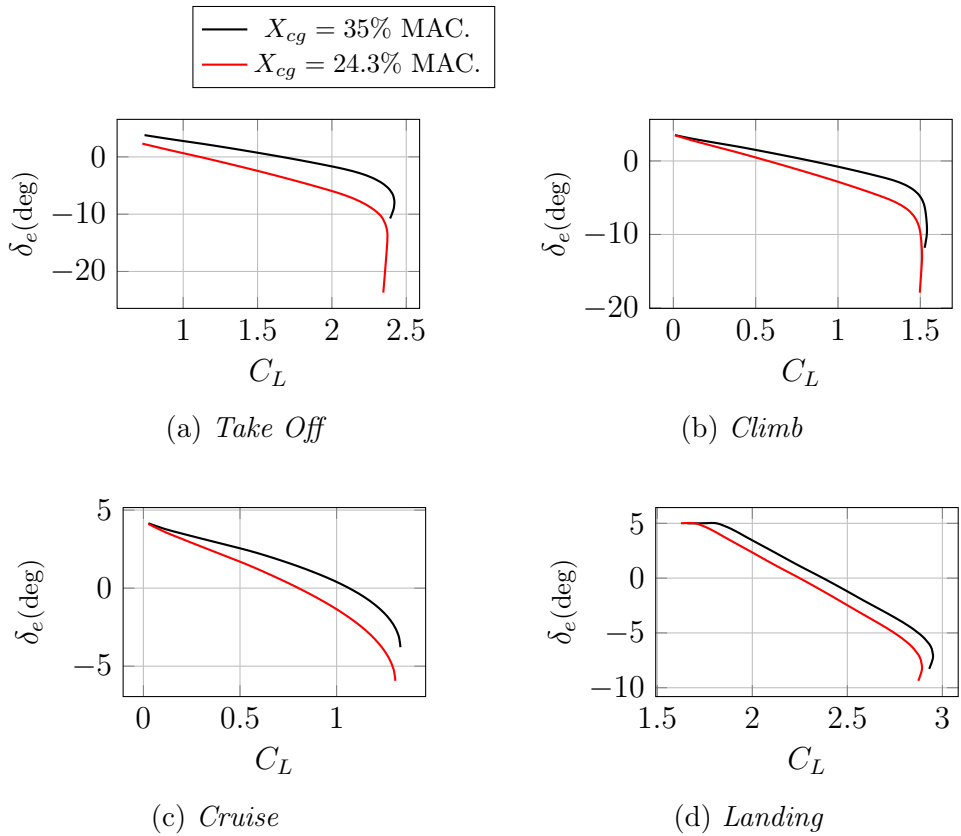


Figure 2.35: A220-300 aerodynamic assessment with *JPAD* software. Angle of elevator equilibrium deflection in various conditions.

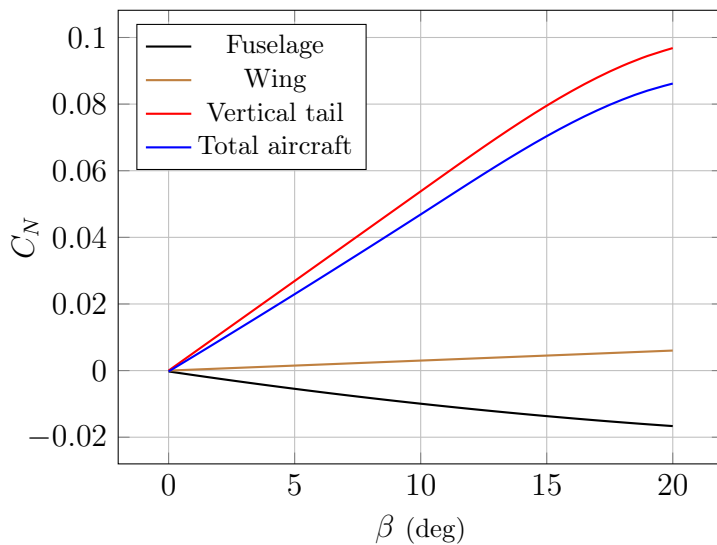


Figure 2.36: A220-300 aerodynamic assessment with *JPAD* software. Total yawing coefficient breakdown at landing condition.

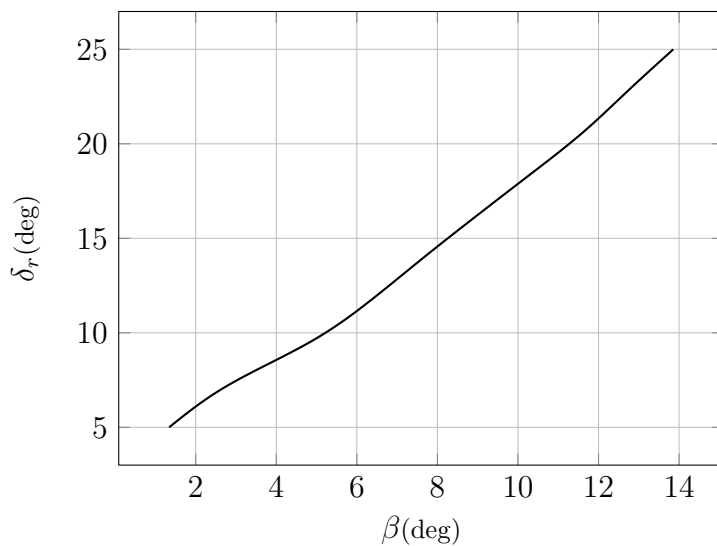


Figure 2.37: A220-300 aerodynamic assessment with *JPAD* software. Rudder deflection required for equilibrium vs angle of sideslip. Landing condition.

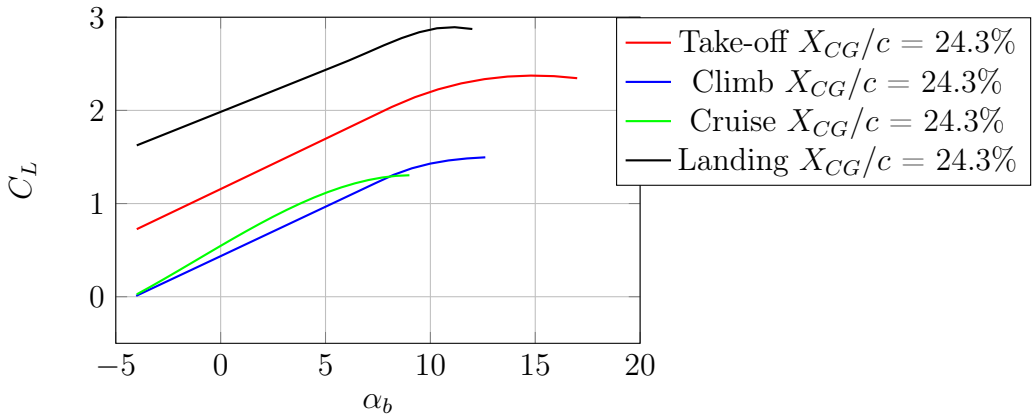


Figure 2.38: A220-300 aerodynamic assessment with *JPAD* software. Aerodynamic efficiency in equilibrium conditions vs lift coefficient in different operative conditions summarized in Tab.2.5.

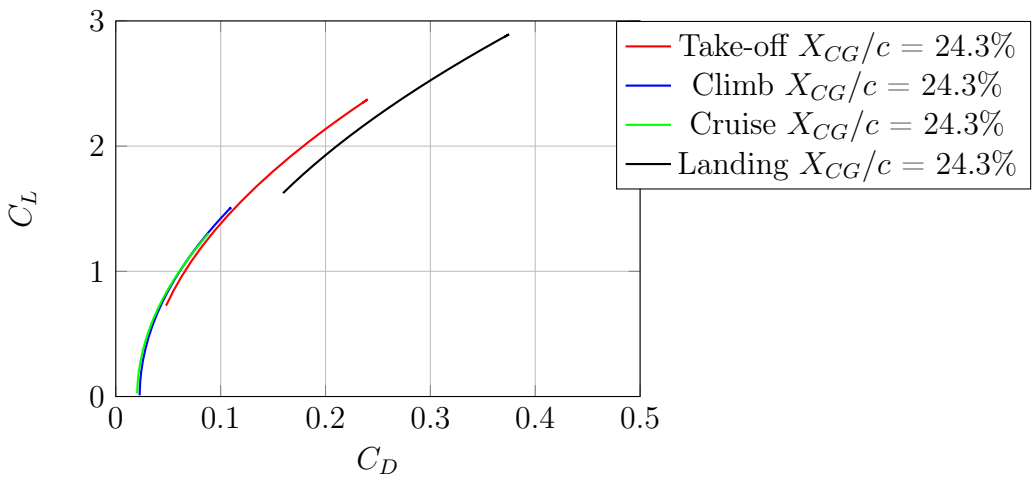


Figure 2.39: A220-300 aerodynamic assessment with *JPAD* software. Total equilibrium polar curves calculated with improved method in different operative conditions summarized in Tab.2.5.

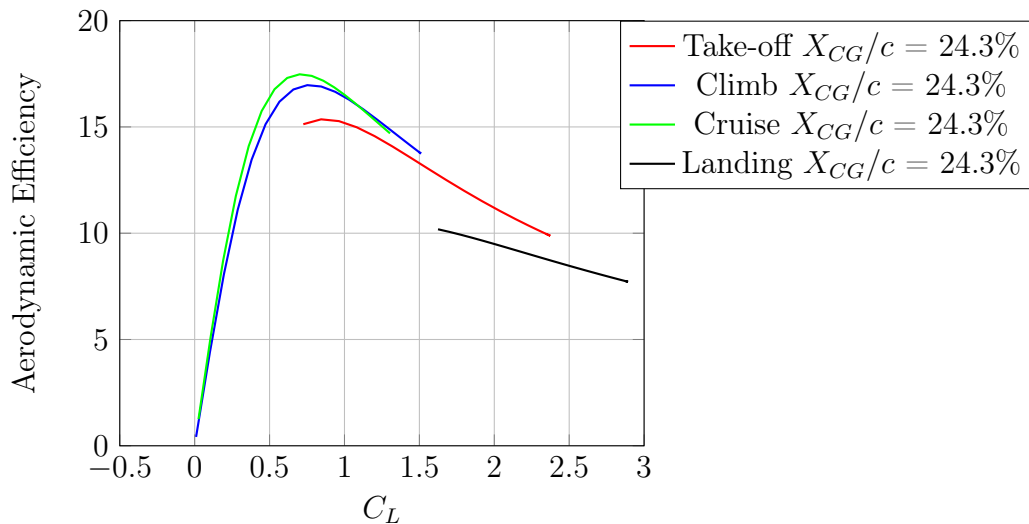


Figure 2.40: A220-300 aerodynamic assessment with *JPAD* software. Total equilibrium efficiency curves calculated with improved method in different operative conditions summarized in Tab.2.5.



Figure 2.41: A220-300 CAD model automatically produced by *JPAD*.

Aerodynamic methodologies for aircraft preliminary design

3.1 Introduction

Nowadays the preliminary design phase of an aircraft has become very challenging due to ever more demanding requirements. The goal of first design stages is to search for the configuration that best fit all requirements, among the results of a great number of multi-disciplinary analyses, as fast as possible, and with a certain grade of accuracy. One of the first disciplines to analyse is the aerodynamics. There are a lot of methodologies for the estimation of aerodynamic characteristics of an aircraft and its components in literature collected in books such as [75] [74] and [25]. A compendium of the above-mentioned is in [80]. These methodologies, useful in the first stages of design process, should be able to give fast and reliable results and are often integrated within *MDAO* tools. Nevertheless, these methodologies have frequently a limited range of applicability for conventional aircraft. However, future aircraft will be significantly different from the current ones. To support the development of such novel configurations, new design methodologies are required that go beyond statistical and analytical methods. To that extent, also design support tools are developed to be able to sustain the improvement of current aircraft design, as well as to support the investigation of novel aircraft configurations.

Synopsis

- First of all, traditional aerodynamic methodologies, included within *JPAD*, are briefly introduced
- Improved methodologies are presented more in detail, as far as lift, drag and downwash is concerned
- An extension of the above mentioned improved methodologies taking into account the presence of high lift devices is presented

3.2 Aerodynamic conventional methodologies

It is well known that a lot of conventional aircraft methodologies are based on semi-empirical analyses. Empirical evidences are the outcome of an experiment and hence the empirical result is a unified confirmation. In light of the above, semi-empirical methods uses part of experimental results to calculations. However, due to their dependence from experiments, these methodologies are strictly related to some boundaries of the models. In the following section the conventional methodologies implemented in *JPAD* are described.

3.2.1 Airfoil database

An aircraft may have several lifting surfaces, fixed with respect to the fuselage, that are the main component responsible for the lift generation. Regardless of the type of lifting surface, its aerodynamic characteristics will be strongly affected by the shape of the wing section in $X-Z$ plane, called airfoil. The airfoil has indeed a great relevance in aircraft aerodynamic. It, in fact, affects the cruise speed, take-off and landing distances, stall speed, handling qualities (especially near the stall), and overall aerodynamic efficiency during all phases of flight. However, the applicability of mere section data to the prediction of the aerodynamic characteristics of wings is limited by the simplifying assumptions made in the development of wing theory. It is assumed, for instance, that each section acts independently of its neighbouring sections except for the induced downwash. Strict compliance with this assumption would require two-dimensional flow, that is, no variation of section, chord, or lift along the span. In light of the above, for an accurate aerodynamic methodology is crucial to

properly manage the airfoil characteristics to obtain 3D data. In *JPAD* (Chapter 2), there are three way to provide airfoil data as input: by means of airfoil name, airfoil values or airfoil curves, shown in Fig. 3.1. Then, in order to perform aerodynamic analyses, two kind of data are needed: the airfoil aerodynamic curves (lift, drag and pitching moment) and the aerodynamic values useful to build the above mentioned curves (in terms of $C_{l_{max}}$, C_l^* , α^* , α_{max} and so on). Providing airfoil curves is useful in case of high-fidelity data availability. However, especially in preliminary design, could be useful to choose an airfoil from an internal database and all the value are extract automatically. The database allows to manage airfoil from the following families [3]:

- NACA 4-digit
- NACA 5-digit
- NACA 6 series
- Supercritical

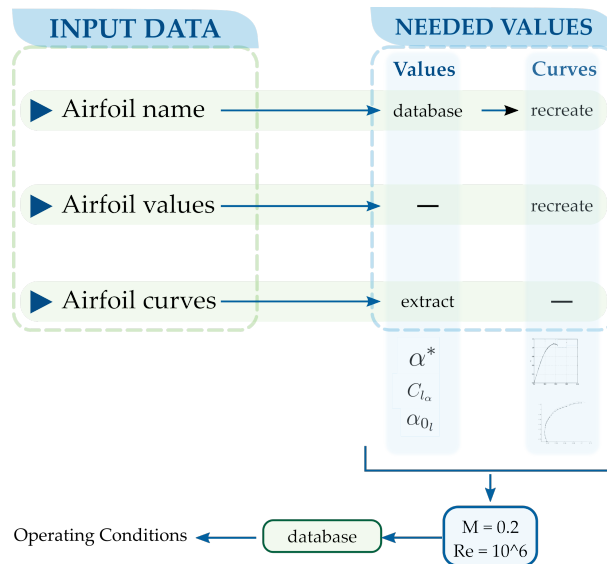


Figure 3.1: Infographics for *JPAD* airfoil data input.

Through the database is it possible to obtain all the necessary values useful to reconstruct the curves of lift, drag and pitching moment in

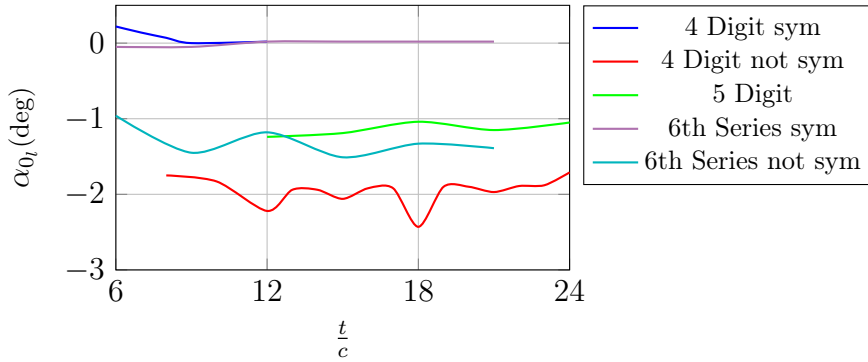


Figure 3.2: α_{0l} of airfoil families varying on thickness ratio.[3]

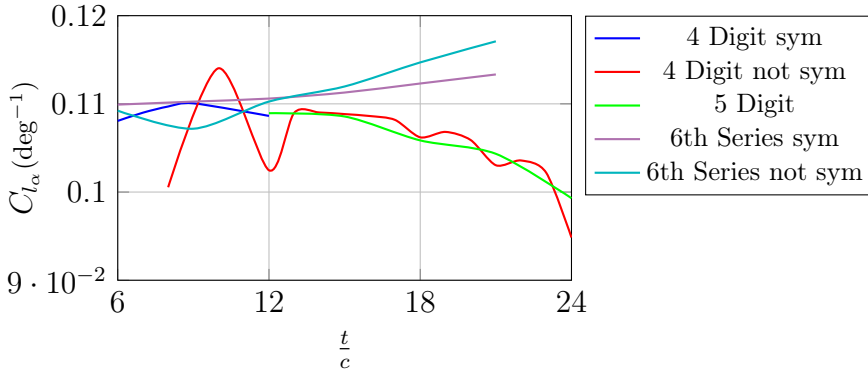


Figure 3.3: C_{l_α} of airfoil families varying on thickness ratio.[3]

function of thickness ratio and curvature for each airfoil family. The database has been built digitizing data from [3] and re-elaborating them with the support of MATLAB in order to build the database in .hdf format. Some of the most relevant values contained in the database are shown in figures from 3.2 to 3.8. A comparison between lift coefficient curve from *xfoil* and reconstructed from database values of NACA 64-215 at $Re = 3e6$ and incompressible flow is shown in Fig. 3.9. As it is possible to appreciate from the figure, the lift coefficient curve obtained from database reconstruction and the curve from *xfoil* are really close and the percentage error is always less than 10%

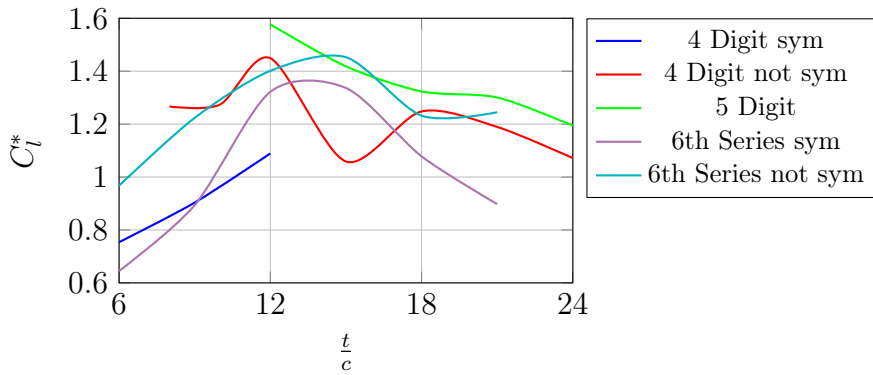


Figure 3.4: C_l^* of airfoil families varying on thickness ratio.[3]

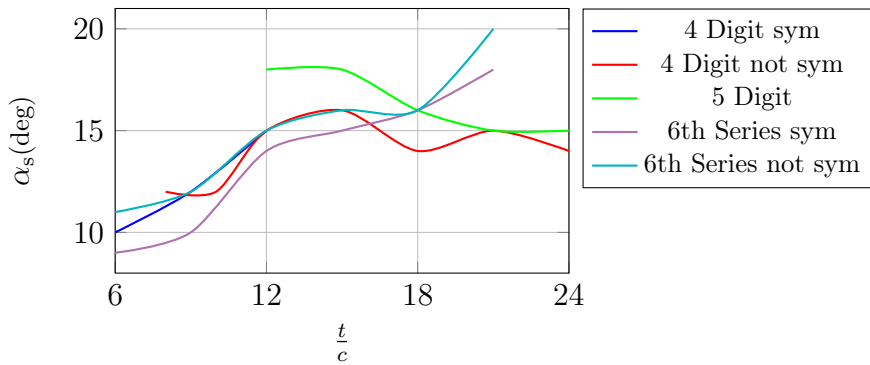


Figure 3.5: α_s of airfoil families varying on thickness ratio.[3]

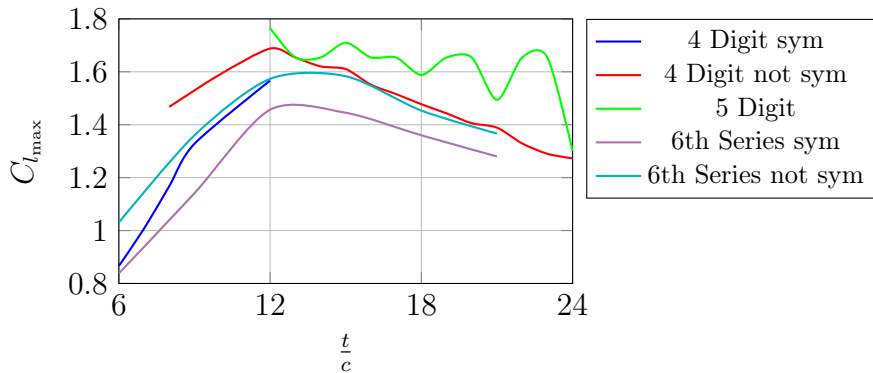


Figure 3.6: $C_{l_{max}}$ of airfoil families varying on thickness ratio.[3]

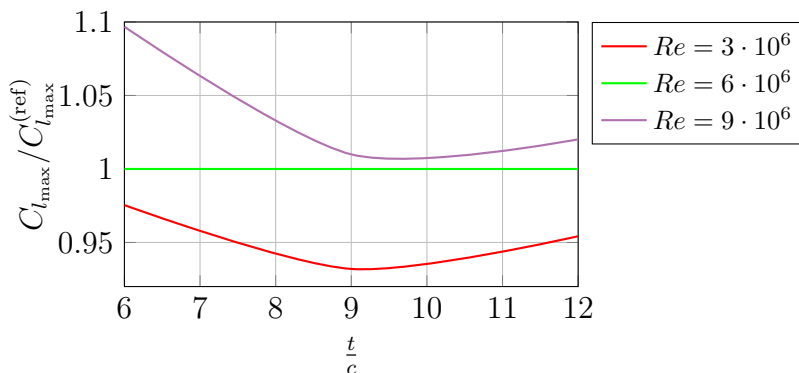


Figure 3.7: $C_{l_{\max}}/C_{l_{\max}}^{(\text{ref})}$ varying on thickness ratio and parameterized for Reynolds number.[3]

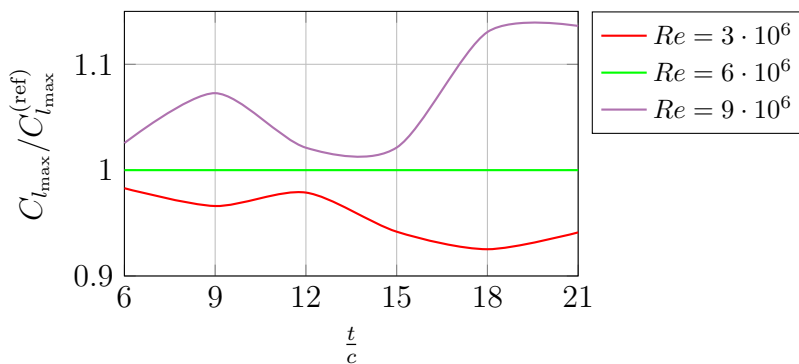


Figure 3.8: $C_{l_{\max}}/C_{l_{\max}}^{(\text{ref})}$ varying on thickness ratio and parameterized for Reynolds number.[3]

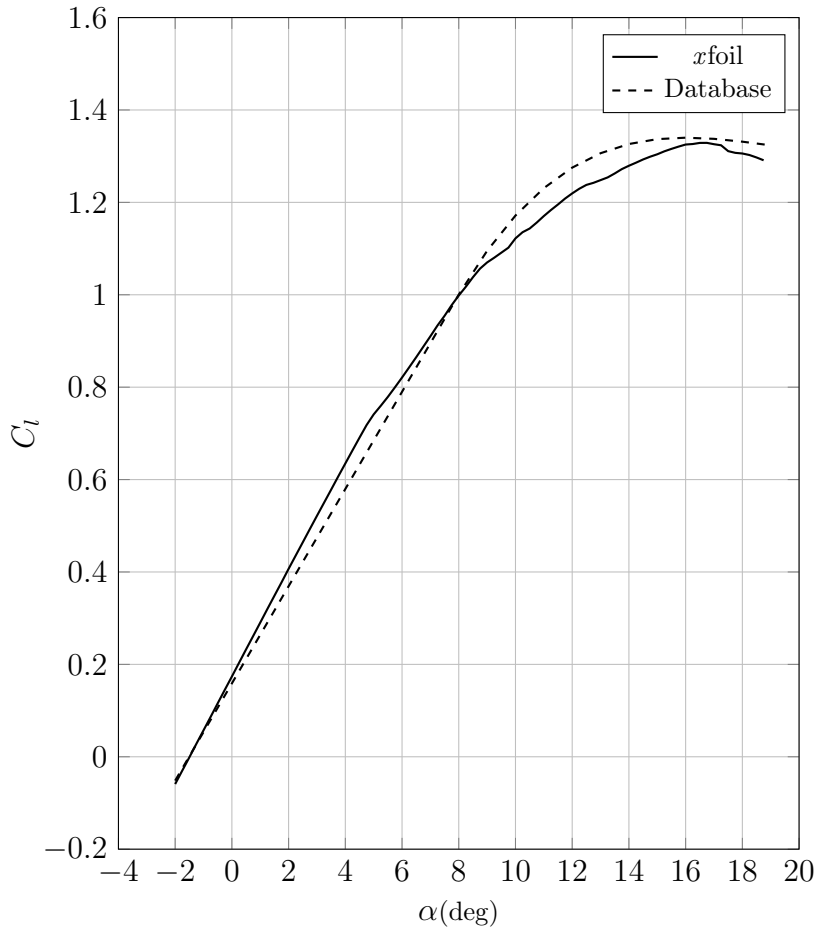


Figure 3.9: Lift coefficient curve for NACA 64-215, $Re = 3e6$, incompressible flow. Comparison between *xfoil* result and reconstruction from database values.

3.2.2 Downwash evaluation for two lifting surfaces

In order to evaluate the characteristics of longitudinal stability of an aircraft it is necessary to assess the flow direction aft of the lifting surfaces. The contribution of horizontal tail surface to the aircraft equilibrium and stability, in fact, strongly depends on the flow direction. The purpose of this section is to introduce the downwash gradient evaluation due to the wing, and eventually canard vortex system, considering a dependence of the downwash angle from the absolute angle of attack. The following thesis is applicable also for a three lifting surface aircraft, so it would be more correct to refer to the changing in flow direction due to the more forward lifting surface to the rear ones. However, in order to make the dissertation simpler, from here the author will refer to the wing as the more forward lifting surface and to the horizontal tail as the backward one.

Due to the finite extension of a generic lifting surface, the wing system, that consists of the bound vortex, located at the wing quarter chord and a vortex sheet which rolling up, at the wing tip, it is considered as two trailing vortices as shown in Fig. 3.10. As matter of fact, the reaction of the air as a fluid to the shape of the wing creates upwash on the front part of the wing and downwash on the rear part. 3.11 [14] [82]. The main effect of this vortex system is to deflect the airflow behind the wing downward relative to the direction of free-stream flow. This angle of deviation is known as *Downwash Angle* (ϵ).

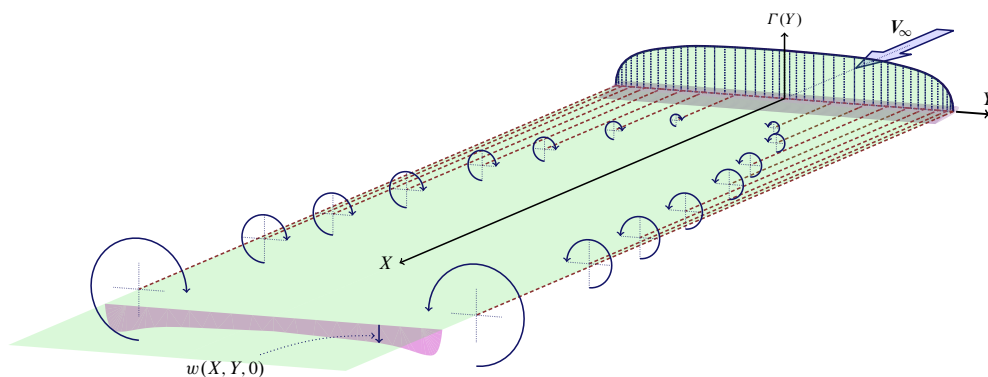


Figure 3.10: The wing vortex sheet.

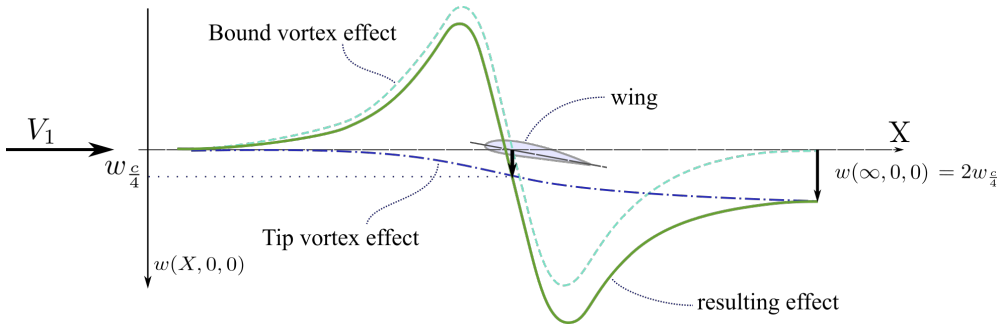


Figure 3.11: Upwash and Downwash in a finite lifting surface.

As consequence of the downwash behind the wing, the local angle of attack on the horizontal tail is reduced by ϵ . In order to evaluate the flow direction behind the wing, another important parameter is the change in downwash angle with angle of attack, that is the *Downwash Gradient* ($\frac{d\epsilon}{d\alpha}$).

This parameter depends principally on the location of the horizontal tail with respect to the wing and the vortex plane. The downwash angle can be expressed in terms of its gradient as in Eq. 3.1.

$$\epsilon = \frac{d\epsilon}{d\alpha_w}(\alpha_w - \alpha_{0_w}) \quad (3.1)$$

Referring to [84] the equation used in order to evaluate the downwash gradient is the Eq 3.2.

$$\frac{d\epsilon}{d\alpha} = \frac{K_{\epsilon\Lambda}}{K_{\epsilon\Lambda=0}} \left(\frac{r}{r^2 + m^2} \frac{0.4876}{\sqrt{r^2 + 0.6319 + m^2}} + \left[1 + \left(\frac{r^2}{r^2 + 0.7915 + 5.0734m^2} \right)^{0.3113} \right] \left\{ 1 - \sqrt{\frac{m^2}{1 + m^2}} \right\} \right) \frac{C_{L\alpha_w}}{\pi \mathcal{R}} \quad (3.2)$$

Where $r \frac{b}{2}$ is the distance between the aerodynamic centre of wing and the aerodynamic centre of the horizontal tail, while the parameter $m \frac{b}{2}$, properly, is the distance between the horizontal tail and the vortex shed plane, as shown in Fig. 3.12

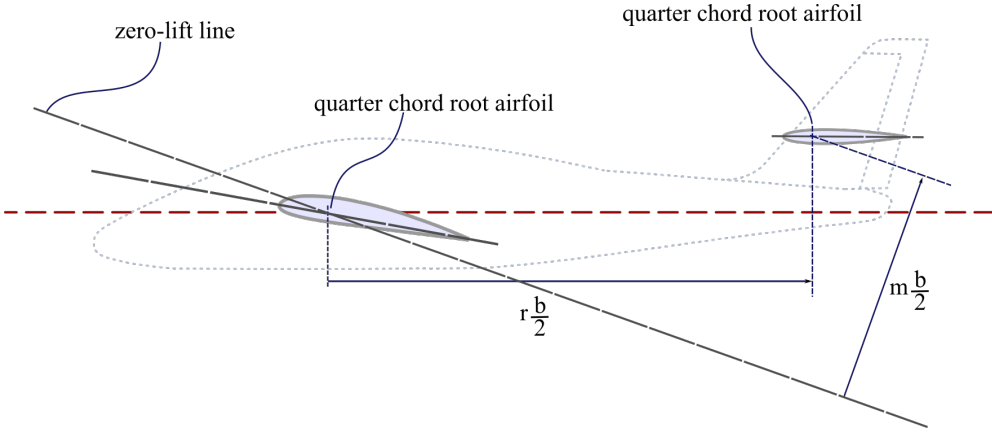


Figure 3.12: Dimensions for determination of Downwash Gradient, considering constant distances.

The two K_ϵ terms in the eq 3.2 accounting for the wing sweep angle effect are defined as follow (where Λ is expressed in radians):

$$K_{\epsilon\Lambda} = \frac{0.1124 + 0.1265\Lambda + 0.1766\Lambda^2}{r^2} + \frac{0.1024}{r} + 2 \quad (3.3)$$

$$K_{\epsilon\Lambda=0} = \frac{0.1124}{r^2} + \frac{0.1024}{r} + 2 \quad (3.4)$$

According to [84], the parameters $r\frac{b}{2}$, $m\frac{b}{2}$ and the slope of the C_L vs α curve in eq 3.2 are considered constant. However, in order to improve the accuracy of the method, these quantities could be considered variable with the angle of attack. In fact, being $r\frac{b}{2}$ the distance between the aerodynamic centre of wing and the aerodynamic centre of the horizontal tail and $m\frac{b}{2}$ the distance between the horizontal tail and the vortex shed plane, these quantities vary with the angle of attack. So, even if to a first approximation this value could be considered constant in alpha, more accurately it is possible to evaluate this dependence considering the reference variable for the calculation of the distances.

Evaluation of non-linear downwash angle

In order to evaluate the downwash angle variable with angle of attack, the reference line of wing should not be considered as a fixed direction,

but it is the vortex shed plane and, consequently, its direction varies with the angle of attack. The location of this plane depends on the value of downwash, but this location is itself necessary to evaluate the downwash. So it is necessary an iterative process in which the position of the vortex reference line at α is calculated from the value of downwash gradient at previous step.

In this process the reference angle of attack is the absolute angle α_a , that is the angle between the flow direction and the zero lift line of the wing. This choice is necessary because for $\alpha_a = 0$ it is possible to assume the downwash zero, but the downwash gradient is not null. In this way it is possible to assume the downwash value in the first step of the iteration and to continue for each step with the previous value as first attempt. In view of stability, however, the reference angle of attack is the α_b . As it is possible to see in the Fig. 3.13, these two angles are related by the relation: $\alpha_a = \alpha_b - i_w + \alpha_{0L}$ in fact, considering the fuselage line as reference, the angle between the root chord and this reference is the wing angle of incidence i_w , while the angle between the root chord and the wing zero lift line is the wing absolute angle of attack α_{0L} .

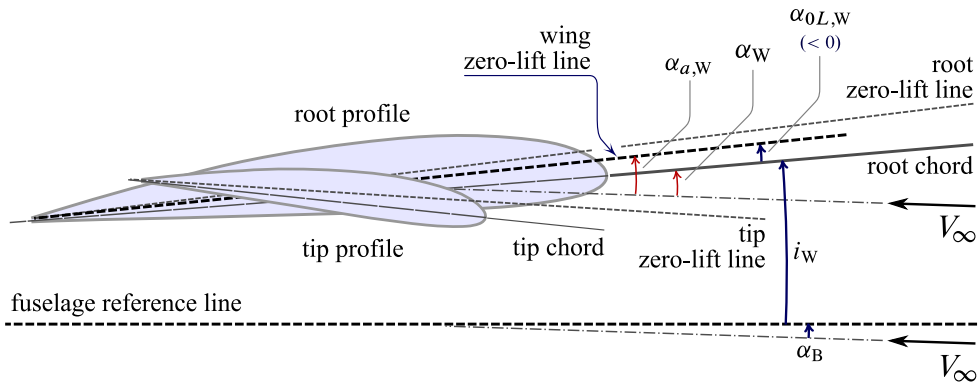


Figure 3.13: Definition of wing angles.

The distances considered in the equation are variable and they are measured from the vortex shed plane. These distances have been calculated referring to the geometrical construction proposed by [40].

First of all, it is necessary to evaluate the geometrical distances m_0 and x_0 , then it is possible to evaluate step-by-step the other distances which,

fixed geometry, only depend with alpha.

Starting from a value of $\alpha_a = 0^\circ$ and proceeding with an increase of angle of attack equal to $\Delta\alpha$, the distances are the following (see fig. 3.14).

- $x_0 \rightarrow$ distance between the aerodynamic centre of the wing and the aerodynamic centre of the horizontal tail calculated along the x axis.
- $m_0 \rightarrow$ distance between the aerodynamic centre of the horizontal tail and the horizontal line passing through the trailing edge of the airfoil root of the wing.
- $d \rightarrow$ distance between the trailing edge of the wing and the aerodynamic centre of the horizontal tail. Considering the triangle \hat{BCD} it is possible evaluate the hypotenuse as follows:

$$d = \sqrt{CD^2 + BD^2} \quad (3.5)$$

where CD is the distance m_0 defined before and it is possible to evaluate the distance BD geometrically:

$$BD = x_0 - \frac{3}{4}c_r \cos(i_w) \quad (3.6)$$

- $\psi \rightarrow$ This is the angle between the distance d and the horizontal reference line.

$$\psi = \arctan\left(\frac{m_0}{BD}\right) \quad (3.7)$$

Starting from these geometrical values it is possible to evaluate the distances m and r for each angle of attack.

- $m|_i = d \sin(\psi + i_w - \alpha_{0L} - i\Delta\alpha + \epsilon)$
- $x|_i = d \cos(\psi + i_w - \alpha_{0L} - i\Delta\alpha + \epsilon) + \frac{3}{4}c_r \cos(-\alpha_{0L} - i\Delta\alpha + \epsilon)$

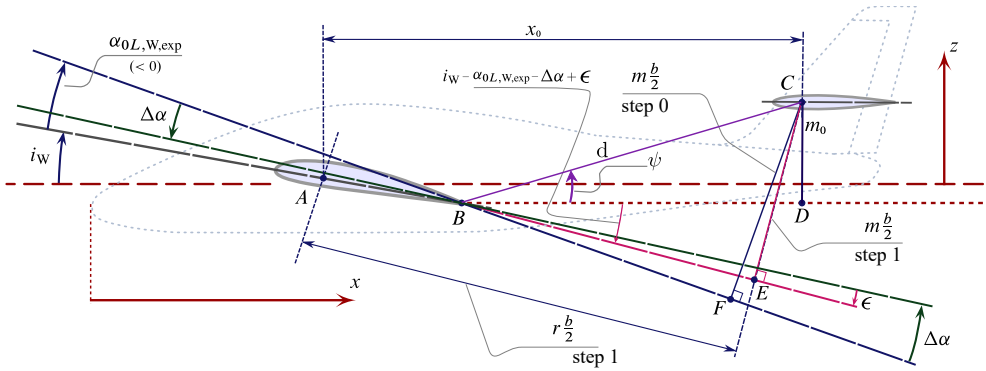


Figure 3.14: Arm definitions for downwash gradient evaluation.

1. First of all, this method creates an array of absolute angle of attack starting from $\alpha_a = 0^\circ$ to $\alpha_a = 20^\circ$ with a step of 0.25° .
2. For the first step the state is the following:
 - $\alpha_a = 0^\circ$
 - $\alpha_B = \alpha_{0L} - i_w$
 - $\frac{d\epsilon}{d\alpha}$ is the constant value
 - $m = d \sin(\phi + i_w - \alpha_{0L})$
 - $r = d \cos(\phi + i_w - \alpha_{0L}) + 0.75c_r \cos(-\alpha_{0L})$
 - $\epsilon = 0$
3. Starting from the second step the process is iterative. Starting from $\alpha_a = 0^\circ$ the absolute angle of attack increase of $\Delta\alpha$. So for the generic i -step we have:
 - $\alpha_a|_i = i\Delta\alpha$
 - $\epsilon_{temp} = \epsilon_{i-1} + \frac{d\epsilon}{d\alpha}|_{i-1} * \Delta\alpha|_i$
 - $m_{\frac{b}{2}}|_{temp}$ is calculated considering the temporary value of downwash angle.
 - $r_{\frac{b}{2}}|_{temp}$ is calculated considering the temporary value of downwash angle.

4. Known these value, it is possible to evaluate the downwash gradient and evaluate again these distances as follow:

- $\frac{d\epsilon}{d\alpha}|_{temp}$ is calculated using the formula and the temporary value of distance.
- $\epsilon_i = \epsilon_{i-1} + \frac{d\epsilon}{d\alpha}|_{temp} * \Delta\alpha|_i$
- $m\frac{b}{2}|_i$ is calculated considering the new value of downwash angle.
- $r\frac{b}{2}|_i$ is calculated considering the new value of downwash angle.
- $\frac{d\epsilon}{d\alpha}|_i$ is updated.
- $\alpha_B = \alpha_{0L} - i_w + \alpha_a$

3.2.3 Downwash evaluation for three lifting surfaces

The most common aircraft configuration with three lifting surfaces is with canard, wing and horizontal tail. A canard is a little lifting surface placed ahead of the main wing: it is used as an aerodynamic device in some aircraft, in substitution or in addition to the classic aft-tail. Depending on its use, it is possible to distinguish between two types of canard: lifting-canard and control-canard. The choice of adopting a lifting-canard on an aircraft could be linked to several reasons, such as:

- generation of an upload instead of a download, as in a conventional aft-tail configuration.
- improvement of wing stall behaviour, as well as avoidance of both tip stall and deep stall.

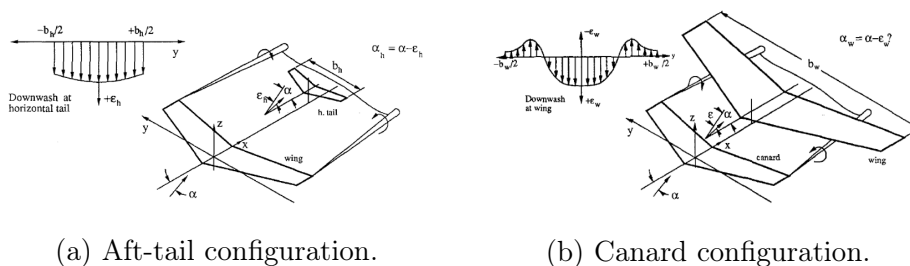
Regarding a control-canard, instead, it could be used for:

- placing the pitch control surface in a region of undisturbed flow, where its control response is generally sure and predictable.
- destabilizing some combat aircraft in order to make them more manoeuvrable.

However, apart from the advantages cited above, canard design has also disadvantages. They are fundamentally related to its destabilizing effect and to the downwash generated on the main wing and on the horizontal tail that could be detrimental in some flight conditions. In light of the above, it results necessary to develop better and more robust methodologies able to predict not only the amount of downwash generated by a canard surface, but also how it affects the wing spanwise loading and eventually the wing stall path. They could be obtained thanks to the technology innovation and an ever growing computing power that gives the possibility to involve high-fidelity tools even during the first phases of the design.

For an aft-tail configuration, the accurate prediction of the downwash gradient is very important for stability issues. In this case, it could be enough to calculate the downwash derivative in the symmetry plane at the longitudinal and vertical location of the tail, being its spanwise variation relatively small and so negligible. In a canard configuration the forward wing has a span smaller than the aft wing, and the spanwise variation of the downwash gradient on the main wing is quite significant; moreover, in this circumstance, not only must the downwash behind the canard be analysed, but also the upwash that occurs outside the tips of the canard has to be taken into account: it, in fact, could tend to stall the outer portions of the wing, limiting to some extent the maximum lift obtainable. Figure 3.15 shows these two different situations compared. However, downwash distribution really affects the aft lifting surface load, and for this reason it must be accurately predicted, especially in some critical situations in which could have dangerous effects (i.e in high-lift conditions with extended flaps).

As far as the downwash of wing on horizontal tail, the term used to account for this interference is usually the average value at the location of the tail. However, to be more accurate, there would be calculated the variation of this influence along the span, especially if the two lifting surfaces dimensions are comparable. There are many studies ([82] [28] [70]) that predicts the influence of the wing on the tail by first estimating the downwash gradient in the plane of symmetry at the longitudinal and vertical location of the tail, and then correcting for the spanwise variation across the tail; however, these references emphasize the case where an aft tail has a much smaller span than the main wing and do not present methods



(a) Aft-tail configuration.

(b) Canard configuration.

Figure 3.15: Comparison between downwash distributions in both aft-tail and canard configuration.

to account for the typical nonlinear variation of the downwash gradient across the wing span that lies behind a canard surface. Rasmussen in [73] studies the effect of a canard surface on the total lift of an un-swept wing in subsonic flow. In this work has been determined the wash on the wing replacing the canard with a single horseshoe vortex and using Glauert equation, and then, by applying certain aerodynamic reciprocity relations achieved through the concept of the reverse flow relations, derives the total change in lift distribution and thus the total change in lift on the main wing. The theory is valid under certain assumptions (symmetrical unswept wings, elliptic lift distribution, wing that lie directly in the wake of the canard) and is extremely difficult to use if not for simple configurations. Several years after, Levy, in [51], provides design charts obtained using the *VLM* which give both the downwash gradient in the plane of symmetry and a correction factors to account for the non-linear variation of downwash gradient induced by a canard across the span of the main wing. The planform is discretized in several panels and each one is modelled with a horseshoe vortex of unknown value. Once the vorticity distribution is known, the vortex induced velocity, and therefore the local downwash angle and thus the downwash derivative, can be calculated. Since the solution for a single case is completed in a very short time, it is possible to investigate a wide variety of planform geometries. The charts, in fact, are parametrized on a series of canard-wing relative positions and geometric parameters (\mathcal{R} , sweep and taper ratio). Currently in *JPAD* is it possible to insert the midspan location downwash gradient for wing and the variation along the semispan on the horizontal tail due to the presence of canard.

3.2.4 Longitudinal static stability

The longitudinal static stability is the stability of an aircraft in the longitudinal, or pitching, plane under steady-flight conditions. The pitch plane is the $X - Z$ plane of aircraft. The linear velocities are along the X-axis and along the Z-axis. Angular velocity is about the Y-axis, known as pitching (positive if nose up). An aircraft is considered statically stable if, from a trimmed state, a disturbance in the angle of attack results in a pitching moment which tends to restore the aircraft to its original state of equilibrium [85]. Since aerodynamic stability is a well-known subject [14, 85, 22, 74], only few words will be spent here. As concern three-lifting surfaces, a feasibility study three possible high-speed turbo-prop/propfan configurations conducted by NASA and McDonnell Douglas jointly in the early eighties [41], has been assumed as a reference starting point. In order to evaluate the characteristics of longitudinal stability of an aircraft it is necessary to express all the forces and the moments acting on it and evaluate the resultant pitching moment about the centre of gravity. The lift and drag are, by definition, always perpendicular and parallel to V_∞ . It is, therefore, inconvenient to use these forces to obtain moments because their moment arms relative to the centre of gravity vary with angle of attack. For this reason, all forces are resolved into normal, N, and chord-wise, C, forces whose axes remain fixed with the aircraft and whose arms are, therefore, constant [56]. According to what said, the aircraft can, in general, be trimmed, that is, put into an equilibrium state where the combined lift of the wing and the tail balances the weight while the moment about the centre of gravity is zero. It is necessary that this equilibrium point corresponds to positive lift. As regards the stability it is necessary that the response of the aircraft to a disturbance in angle of attack the response of the aircraft is to a disturbance in angle of attack will consist in a reaction naturally lowering the disturbance itself. Thus, if flying in equilibrium at one angle of attack and a disturbance increases the angle of attack, the moment produced at this angle of attack must act to reduce it, that is, tend back toward the original equilibrium state. Conversely, if a disturbance decreases the angle of attack, the moment at the new, lower, angle of attack must serve to increase that angle. This means that the rate of change of the moment about the centre of gravity must be negative for static stability: an increase in α should reduce $C_{M_{cg}}$ and

a decrease in α should increase $C_{M_{cg}}$ [80]. The higher is the slope of the curve, the greater is the restoring moment. Thus the slope of the curve is called *Static Margin*. Static margin is a concept used to characterize the static longitudinal stability and controllability of aircraft. In aircraft analysis, static margin is defined as the distance between the centre of gravity and the neutral point of the aircraft, expressed as a percentage of the mean aerodynamic chord of the wing. In order to have static stability, thus, is necessary that the neutral point is behind the centre of gravity. All the forces and moment acting in the $x-z$ plane are shown in Fig. 3.16 and explained in Tab 3.1. The canard drag force has been neglected in this context in Eq. 3.8. For the main lifting surface, identified by the wing, the forces in the equation are the normal and the chord-wise, while for the others lifting surfaces the differences between these two and lift and drag is neglected. The distances are considered to have a positive momentum according to the convention.

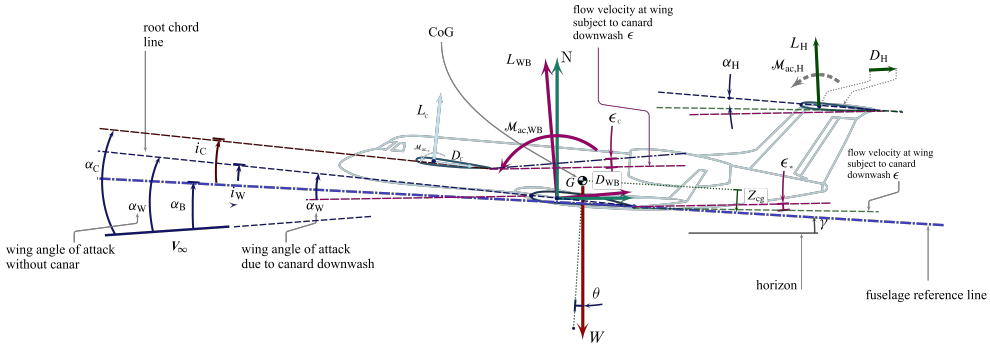


Figure 3.16: Forces and moment acting on an aircraft with three lifting surfaces for longitudinal static stability.

$$M_{CG} = L_c \times (\bar{x}_{cg} - \bar{x}_{ac_c}) + M_{ac_c} + N_{wb} \times (\bar{x}_{cg} - \bar{x}_{ac_{wb}}) + C_{wb} \times (\bar{z}_{cg} - \bar{z}_{ac_{wb}}) + M_{ac_{wb}} + L_h \times (\bar{x}_{cg} - \bar{x}_{ac_h}) + D_h \times (\bar{z}_{gc} - \bar{z}_{ac_h}) \quad (3.8)$$

$$C_{M_{CG}} = C_{L_c} \times (\bar{x}_{cg} - \bar{x}_{ac_c}) + C_{M_{ac_c}} + C_{N_{wb}} \times (\bar{x}_{cg} - \bar{x}_{ac_{wb}}) + C_{C_{wb}} \times (\bar{z}_{cg} - \bar{z}_{ac_{wb}}) + C_{M_{ac_{wb}}} + C_{L_h} \bar{V}_H \eta_T + C_{D_h} \frac{S_h}{S_w} \frac{\bar{z}_h}{\bar{c}_w} \eta_T \quad (3.9)$$

Symbol	Explanation
L_c	Canard lift force
D_c	Canard drag force
M_{ac_c}	Canard pitching moment (with respect to its AC)
L_{wb}	Wing-body lift force
D_{wb}	Wing-body drag force
$M_{ac_{wb}}$	Wing-body pitching moment
L_h	Horizontal tail lift force
D_h	Horizontal tail drag force
M_{ac_h}	Horizontal tail pitching moment (with respect to its AC)
\bar{x}_{ac_c}	Canard aerodynamic centre (as a fraction of MAC)
$\bar{x}_{ac_{wb}}$	Wing-body aerodynamic centre (as a fraction of MAC)
\bar{x}_{ac_h}	Horizontal tail aerodynamic centre (as a fraction of MAC)

Table 3.1: Lift and pitching moment contributions in x - z plane

The term $\eta_H = \frac{q_{\infty T}}{q_{\infty}}$ is called the tail efficiency factor, or dynamic pressure ratio, and it takes into account the influence of the wing on the free-stream velocity striking the tail. This term accounts for the possibility that the horizontal tail will be aerodynamically working with reduced dynamic pressure due to the downwash generated by the lifting wing, particularly at higher angles of attack of the wing [80]. This term assumes values between 0.85 and 1, related to the relative position between horizontal tail and wing. The value 1 is assumed when the horizontal tail has the major distance from the wing. The term $\bar{V}_H = \frac{S_h}{S_w} \frac{(\bar{x}_{cg} - \bar{x}_{ac_h})}{\bar{c}_w}$ is the volumetric ratio and it is an important design parameter because it defines the effectiveness of horizontal tail. It is important to note that the horizontal component of the aerodynamic force introduces a contribute in stability equation as shown in Fig. 3.17. The arm of this force is z_a .

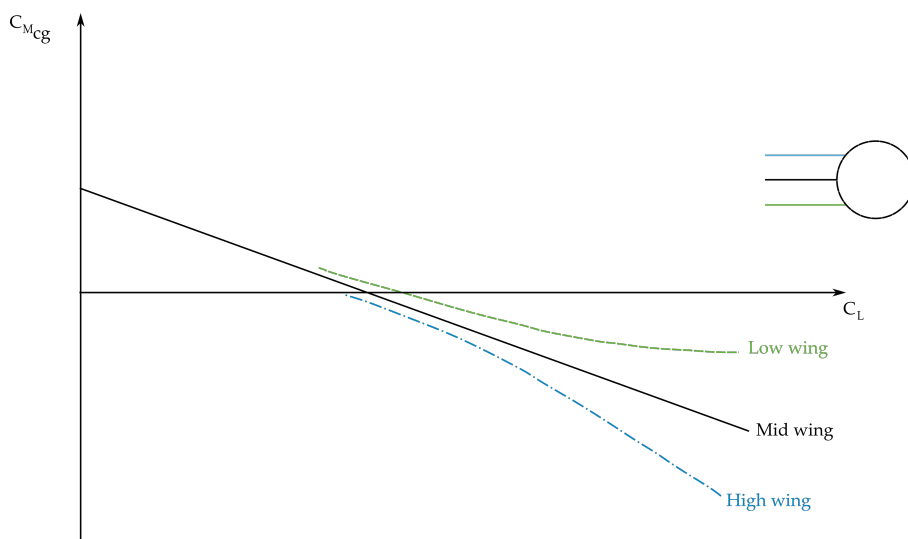


Figure 3.17: Qualitative effect of vertical location of c.g. on pitching moment.

If the c.g. position is under the wing aerodynamic centre, z_a will be negative and the term will be stabilizing, whereas if the c.g. is over the wing aerodynamic centre, the term will produce an unstable contribution. This term is usually very small with respect to the first term except at high values of the lift coefficient. [14]

In order to calculate the stability, the C_{MCG} in Eq.3.9 is equal to zero and the horizontal tail lift coefficient is calculated. In light of the above, evaluating the equilibrium condition, means to calculate what is the elevator angle deflection in order to trim the aircraft and assess if it is allowable considering structural boundaries. To evaluate this contribute it is necessary to consider the deflection of the horizontal tail control surface. This can feature a fixed or adjustable structure on which any movable control surfaces are hinged, or it can itself be a fully movable surface (Fig. 3.18).

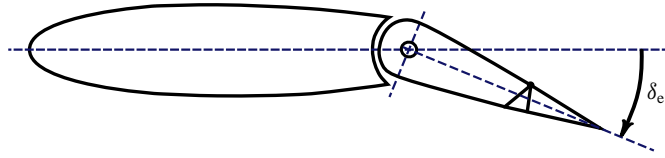


Figure 3.18: Characteristic angles of the horizontal tail.

The variation of zero lift angle is not constant with the angle of deflection. So, it is necessary to evaluate the tau factor which is defined as follows:

$$\tau_e = \frac{d\alpha_{0l}}{d\delta_e} \tag{3.10}$$

Introducing this parameter, the lift coefficient of the horizontal tail can be rated as follows:

$$C_{L_H} = C_{L_0} + C_{L_{\alpha_H}} \alpha_H + C_{L_{\alpha_H}} \tau_e \delta_e \tag{3.11}$$

Considering a symmetrical horizontal tail, the term C_{L_0} is zero, so it is possible to express the lift coefficient in the following form:

$$C_{L_H} = C_{L_{\alpha_H}} (\alpha_H + \tau_e \delta_e) \tag{3.12}$$

In general, the value of τ is constant up to about 15 deg; after this value, due to the flow separation, the effectiveness of elevator decrease and consequently the product $\tau_e \delta_e$ that appears in the equation of lift coefficient (Fig. 3.19).

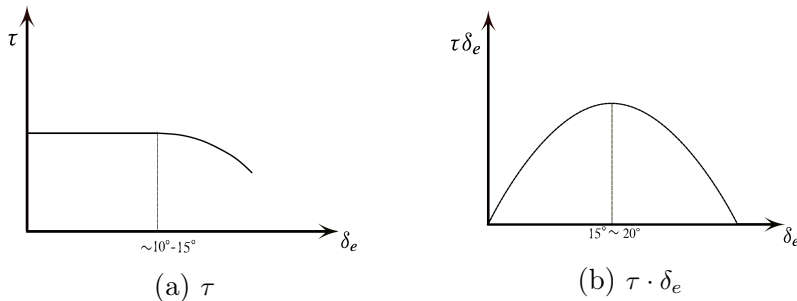
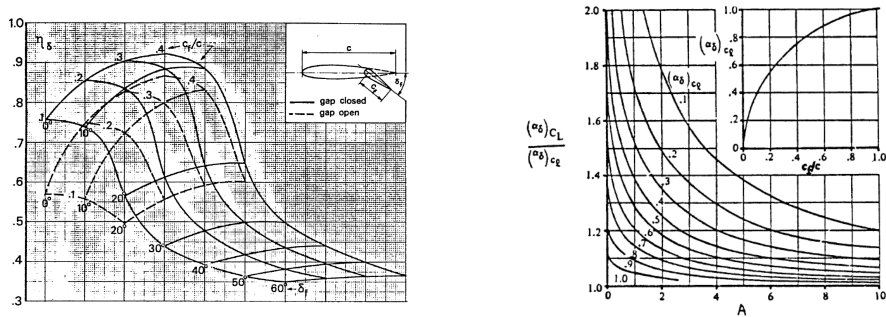


Figure 3.19: Qualitative behaviour of elevator efficiency index vs elevator deflection.

The evaluation of tau is made by means of external database, from [25], Fig. 3.20.

$$\tau = \alpha_{\delta} \eta_{\delta} = \frac{\alpha_{\delta c_L}}{\alpha_{\delta c_l}} \alpha_{\delta c_l} \eta_{\delta} \quad (3.13)$$



(a) 2D efficiency correction for elevator. (b) $\frac{d\alpha_{0L}}{d\delta_e}$ 2D and 3D correction.

Figure 3.20: Efficiency correction factor for plain flap.

The construction of the C_L vs α curve is made as follows for each value of elevator deflection.

1. It is necessary to know the value of $C_{L\alpha}$ and α_{0L} for clean configuration
2. The $\alpha_{0L\delta_e}$ is obtained starting from the τ value

$$\alpha_{0L\delta_e} = \alpha_{0L_{clean}} - (\tau \delta_e) \quad (3.14)$$

3. In order to evaluate the variation in $C_{L\alpha}$ due to elevator deflection, references to [85] have been made. In particular, this text provides the following equation which approximates the results of the exact theory fairly accurately and is in qualitative agreement with experimental data.

$$C_{l\alpha(\text{flap down})} = C_{l\alpha} \left[\frac{c'}{c} \left(1 - \frac{c_f}{c'} \sin^2 \delta_f \right) \right] \quad (3.15)$$

This equation is then corrected for the three-dimensional wing as follows.

$$C_{L\alpha(\text{flap down})} = C_{L\alpha} \left\{ 1 + \frac{\Delta C_{L0}}{\Delta C_{l0}} \left[\left(\frac{c'}{c} \left(1 - \frac{c_f}{c'} \sin^2 \delta_f \right) - 1 \right) \right] \right\} \quad (3.16)$$

4. The new value of C_{L0} is obtained from the following equation

$$C_{L0} = -C_{L\alpha\delta_e} \alpha_{0L\delta_e} \quad (3.17)$$

5. An empirical method for predicting airfoil maximum lift increments for plain and slotted flaps is presented in [80]. The maximum lift increment provided to an airfoil by the deflection of a trailing edge flap is given by the (3.18).

$$\Delta C_{l_{\max}} = k_1 k_2 k_3 (\Delta C_{l_{\max}})_{\text{base}} \quad (3.18)$$

Here $(\Delta C_{l_{\max}})_{\text{base}}$ is the section maximum lift increment for 25 percent-chord flaps at the reference flap-deflection angle. The quantity k_1 is a factor accounting for flap-chord-to-airfoil-chord ratios, $\frac{c_f}{c}$, other than 0.25. The quantity k_2 is a factor accounting for flap deflections other than the reference value. Finally, k_3 is a factor accounting for flap motion as a function of flap deflection.

As far as the ΔC_{D_0} is concerned, the evaluation of this parameter for horizontal tail is usually made by means of parametrized curves from [93] for plain flap. By means of a validation campaign it results that this method overestimates the ΔC_{D_0} , so from CFD analyses on *IRON* aircraft (Chap.5), an interpolating function has been obtained to estimate the variation, reported in Eq. 3.19 and in Fig. 3.21

$$\Delta C_{D_0} = 0.0000156\delta_e^2 + 0.000002\delta_e; \quad (3.19)$$

Following in the Tab.3.2 are summarized all the aerodynamic and stability module output in the software *JPAD*, explained in Chapter 2

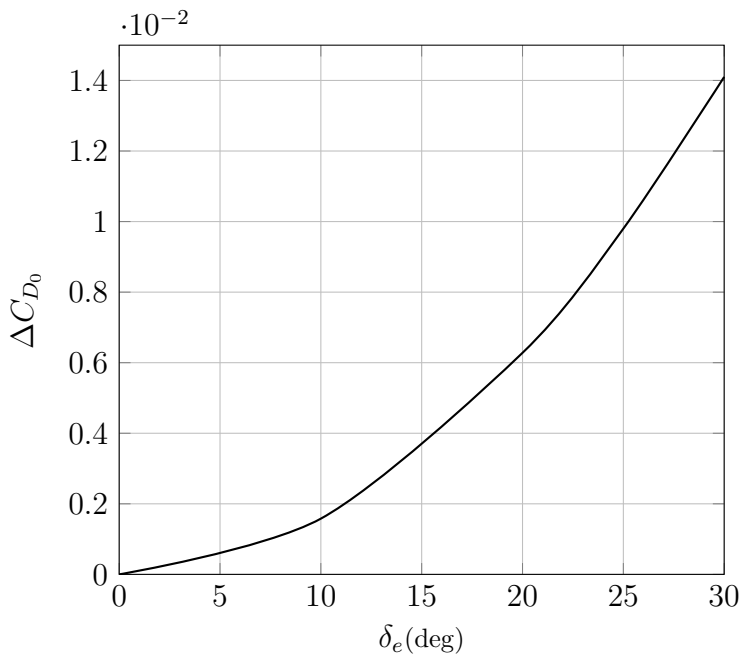


Figure 3.21: Interpolating function of ΔC_{D_0} built by CFD-RANS analyses on *IRON* aircraft performed by software Star-CCM+.

Symbol	Explanation
$C_{L_{tot}}$	Total lift coefficient varying on δ_e
$C_{D_{tot}}$	Total drag coefficient varying on δ_e
$C_{M_{tot}}$	Total moment coefficient varying on δ_e
$C_{L_{heq}}$	Horizontal tail equilibrium lift coefficient
$C_{L_{TOTeq}}$	Total equilibrium lift coefficient
$C_{D_{TOTeq}}$	Total equilibrium drag coefficient
$\delta_{e_{eq}}$	Elevator equilibrium angle of deflection
MSS	Static stability margin
X_N	Neutral point

Table 3.2: Output of longitudinal static stability module in *JPAD*.

Research of optimum i_h value

In the longitudinal static stability module, *JPAD* calculates the optimum angle of incidence that allows to trim the aircraft at the maximum number of angles of attack for each of the required conditions. In the input file an angle of incidence for every surface is given and, in correspondence of that angle, trimmed lift and polar curves are calculated. Due to structural limitations, it is possible that, considering the given horizontal tail angle of incidence, the trim at very high or very low angles of attack is not allowable. For this reason, the final lift coefficient and drag coefficient curves, useful for performance module, are possibly cut in correspondence of the structural limitation. In light of the above, for each flight condition, the ideal angle of incidence is calculated as follow: for a number of angle of incidence trimmed curves are calculated and the one that allow to trim the major number of angles of attack corresponds to the optimum value of the angle of incidence (Fig. 3.22).

3.2.5 Lateral and Directional stability

Stability about the aircraft longitudinal axis, which extends from the nose of the aircraft to its tail, is called lateral stability. Positive lateral stability helps to stabilize the lateral when one wing gets lower than the wing on the opposite side of the aircraft. There are four main design factors that make an aircraft laterally stable: dihedral, sweepback, keel effect,

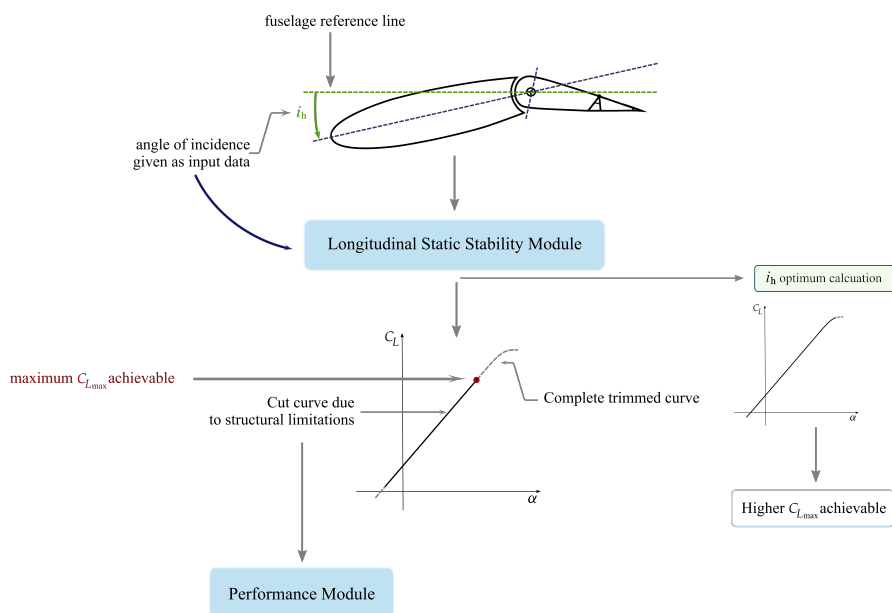


Figure 3.22: FlowChart of optimum angle of incidence of horizontal tail calculation.

and weight distribution. It is far from this work purpose to explain in detail the equations of lateral and directional stability. The calculation formulas implemented in *JPAD* and used in this text are mostly based on the well-known USAF DATCOM [28] and [55]. These equations assume the validity of the superposition principle and express all quantities referred to the aircraft as a sum of several contributions. Each aerodynamic coefficient is computed first evaluating the contribution due to each part taken singularly; then the extra contribution due to aerodynamic interferences are estimated; finally, all contributions are summed up. As far as the index of rudder effectiveness, τ_r , is concerned, the evaluation of this parameter could be made by means of parametrized curves ([25]) for plain flap. By means of a validation campaign it results that this method overestimates the τ_r , so from CFD analyses on *IRON* aircraft (Chap.5), an interpolating function has been obtained to estimate this value, reported in Fig. 3.21

Following in the Tab.3.3 are summarized all the aerodynamic and stability module output in the software *JPAD*, explained in Chapter 2

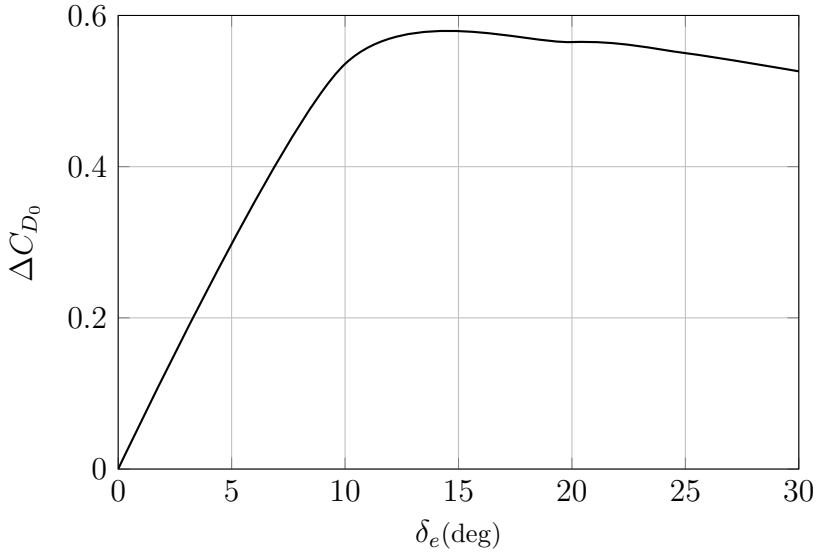


Figure 3.23: Interpolating function of τ_r built by CF analyses on *IRON* aircraft.

Symbol	Explanation
C_Y	Steady-state lateral force coefficient
$C_{\mathcal{L}}$	Steady-state rolling moment coefficient
$C_{\mathcal{N}}$	Steady-state yawing moment coefficient
C_{Y_p}	Unsteady-state lateral force coefficient
$C_{\mathcal{L}_p}$	Unsteady-state rolling moment coefficient
$C_{\mathcal{N}_p}$	Unsteady-state yawing moment coefficient

Table 3.3: Output of lateral stability module in *JPAD*.

3.2.6 VMU

An aircraft in the take-off configuration at the maximum angle of attack allowed by the geometry is shown in 3.24

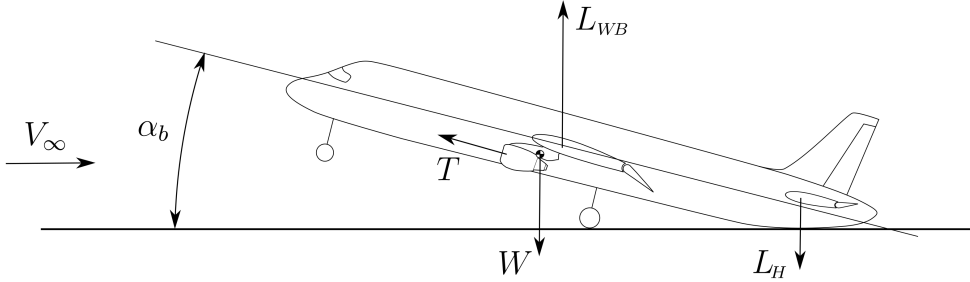


Figure 3.24: Takeoff configuration for the assessment of VMU

where:

$$\alpha_W = \alpha_b + i_W$$

$$\alpha_H = \alpha_b - \varepsilon + i_H$$

The V_{MU} is the speed at which the aircraft takes off in this configuration, i.e. the speed that makes the algebraic sum of lift (wing-body lift and horizontal tail lift) and thrust upwards component equals to the weight of the aircraft.

In formulas:

$$L_{TOT} = L_{WB} + L_H + T \sin \alpha_b = W \quad (3.20)$$

$$L_{TOT} = C_{L_{WB}} \frac{1}{2} \rho V_\infty^2 S_W + C_{L_H} \frac{1}{2} \rho V_\infty^2 \eta S_H + T \sin \alpha_b = W \quad (3.21)$$

from which it is obtained:

$$V_{MU} = \sqrt{\frac{W - T \sin \alpha_b}{C_{L_{WB}} \frac{1}{2} \rho S_W + C_{L_H} \frac{1}{2} \rho \eta S_H}} \quad (3.22)$$

where $C_{L_{WB}}$ and C_{L_H} are influenced by the ground effect. In particular it results in a new wing-body lift coefficient curve and new downwash angle. This effect generally become measurable at a height above the ground of one wing-span and increase in magnitude as the height above the ground decreases. Both theoretical and experimental investigations indicate that ground proximity produces an increase in the lift-curve slope, a decrease

in drag, and a reduction of nose-up pitching moment for most aircraft planforms in the clean configuration. However, high-lift configurations deviate from this trend in that the ground effect tends to reduce the lift-curve slope [28]. The majority of the theoretical approaches analysing ground effects employ an image-vortex theory to represent the ground plane. The salient aspects of this theory are discussed below. Away from the ground plane, the downwash of the two trailing vortices contributes to the wing drag due to lift by rotating the force vector rearward. However, near the ground plane, the trailing vortices have an upwash component that reduces the downward rotation of the flow direction caused by the wing trailing vortices, thus decreasing the wing drag due to lift. The ground effects on lift are determined somewhat by the planform of the configuration. For low-aspect-ratio delta configurations, the general trend is a constant increase in C_L due to ground effect, as shown in figure 3.25. However, transport-type configurations show quite a different trend, as presented in figure 3.26.

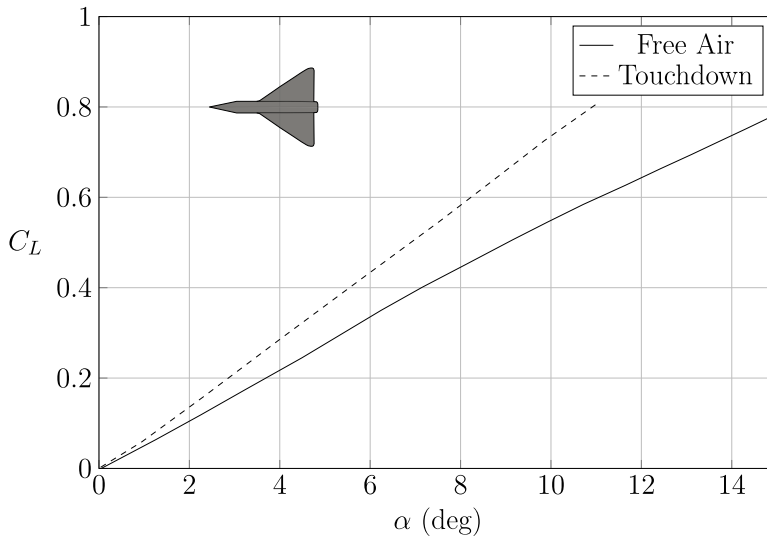


Figure 3.25: Ground effect on 55° delta configuration

For most aircraft, calculating the change in lift due to ground effects consists of evaluating two components:

- the change in wing-body lift;

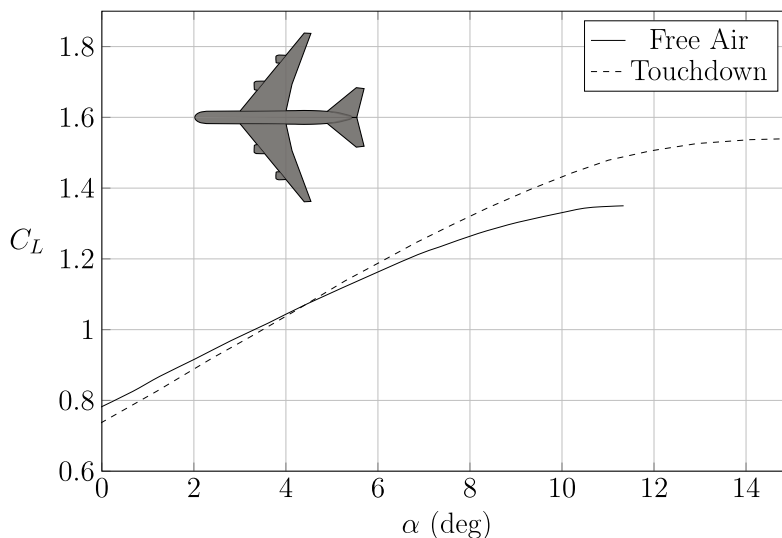


Figure 3.26: Ground effect on a jet transport configuration

- the change in tail-body lift due to the effects of downwash.

The change in tail-body lift due to the presence of the ground is generally small in comparison to the downwash effects and is neglected in the Datcom methods. According to the methods presented in [28] wing-body and tail-body lift curves in ground effect are based on their corresponding free-air lift curves by shifting the free-air lift curves at every C_L by the corresponding increment in angle of attack due to ground effect at constant lift coefficients. In the reference [28] two methodologies are presented. The method implemented in *JPAD* estimates the ground effects on lift in the linear-lift range for a subsonic transport configuration. It includes the effects of taper ratio, sweep-back, dihedral, and flap deflection, while neglecting the effects of wing thickness since they are generally small. The wing-flap effects are valid only for split and slotted flaps as they are accounted for by empirical curves.

3.3 Improved methodology for Lift estimation

One of the main issues of classical vortex methods, such as the one presented in this work developed in a NASA research centre and published in a NASA technical note [12], is their reliability only in the linear range of lift curve and the fact that these methods neglect the real airfoil lift coefficient slope, considering it equal to 2π (rad^{-1}) from Glauert theory. The developed method modifies the load distribution obtained using the Blackwell approach, taking into account the real airfoil curves and extend the results until stall. The methodology follows the logical steps shown in Fig.3.29 and Fig. 3.30. The method is divided in two parts: a pre-analysis in which the airfoil input curves are modified taking into account the 3D effects, and the processor whose output is the 3D lift coefficient.

3.3.1 Pre-analysis

This phase is the one called PRE-PROCESSOR in Fig. 3.30 and described at the left of Fig. 3.29. In this part of the method the airfoil input curves are modified in order to take into account the 3D effects. In fact, the blue curves in Fig. 3.29 become the green ones. According to literature [12], in fact, due to 3D effects such as cross-flow, the airfoil work at a lower lift coefficient slope. This reduction is calculated for each section comparing the initial C_{l_α} of Nasa-Blackwell method (2π (rad^{-1})) and the resulting ones. In particular these latter are obtained calculating the lift coefficient distribution along semispan through Nasa-Blackwell method and gathering the lift coefficient slope for each section. Known this value a new lift coefficient curve has built for each section, applying the reduction obtained in lift coefficient slope from the vortex method to the real airfoil curves, and rotating the curve. That is the starting point for the following analysis, called NASA BLACKWELL solver in Fig. 3.30.

3.3.2 Analysis

First, the wing semispan is divided into n (defined by j index) sections (typically 50). Each of these n points corresponds to an intermediate

airfoil with its own lift characteristics. The calculation procedure is summarized as follows, and this procedure is repeated for each lifting surface angle of attack. The flow described in Fig. 3.30 is for each angle of attack. The used nomenclature is shown in Fig.3.27.

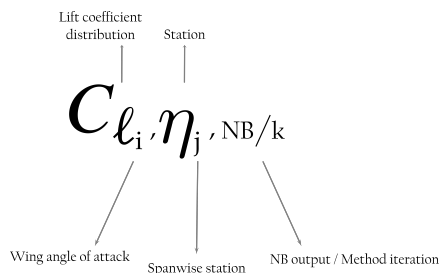


Figure 3.27: Notation for improved methodology for lift coefficient estimation.

1. The inviscid lift distribution is evaluated using the above mentioned Nasa-Blackwell method, by calculating the local C_l at n points along the semispan (number 1 in Fig. 3.30).
2. For all sections, knowing the local lift coefficient ($C_{l_i, \eta_j, NB}$), it is possible to enter in the corresponding airfoil chart, the one linear, with 3D modification, obtaining the local angle of attack at which the airfoil is working. This angle of attack is the summation of the lifting surface angle of attack, the angle of incidence, the local twist and the induced angle of attack (number 2 in Fig. 3.30).

$$\alpha_j = \alpha_{LS} + \epsilon_j + \alpha_{ind_j} \quad (3.23)$$

3. Using this angle of attack, it is possible to enter in the real lift curve of the airfoils obtaining a new local C_l , which takes into account the real slope and viscous effects.
4. A new lift distribution along the semispan, which considers the 2D non-linearity, is obtained (number 3 in Fig. 3.30).
5. his new lift coefficient distribution causes a new distribution of induced angle of attack, which produces, in turn, a new C_l distribution. So, an iterative process is needed. Known the lift coefficient distribution, the γ distribution is calculated, being:

$$\gamma(\eta) = \frac{cC_l(\eta)}{2b} \quad (3.24)$$

and the induced angle of attack distribution from Prandtl theory [53]. In order to calculate this, a coordinate transformation is made from the linear one (η) to angular one (θ) (Fig.3.28):

$$\eta = -\cos \theta \quad (3.25)$$

$$\alpha_i(\theta) = \sum_{n=1}^{\infty} \frac{n}{2} B_n \frac{\sin(n\theta)}{\sin \theta} \quad (3.26)$$

6. Known the new induced angle of attack distribution it is possible to calculate the new angle of attack and lift coefficient distributions, from Eq.3.23 and the airfoil curves. The wing C_L is obtained integrating the final lift distribution once the convergence is reached.

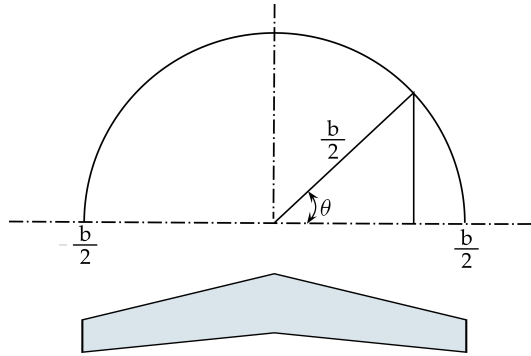


Figure 3.28: Coordinate transformation used in the reduction of the lifting line equation.

3.4 Drag estimation

For a generic isolated lifting surface in clean configuration, the drag polar can be express as follows, where some terms are variable with the angle of attack:

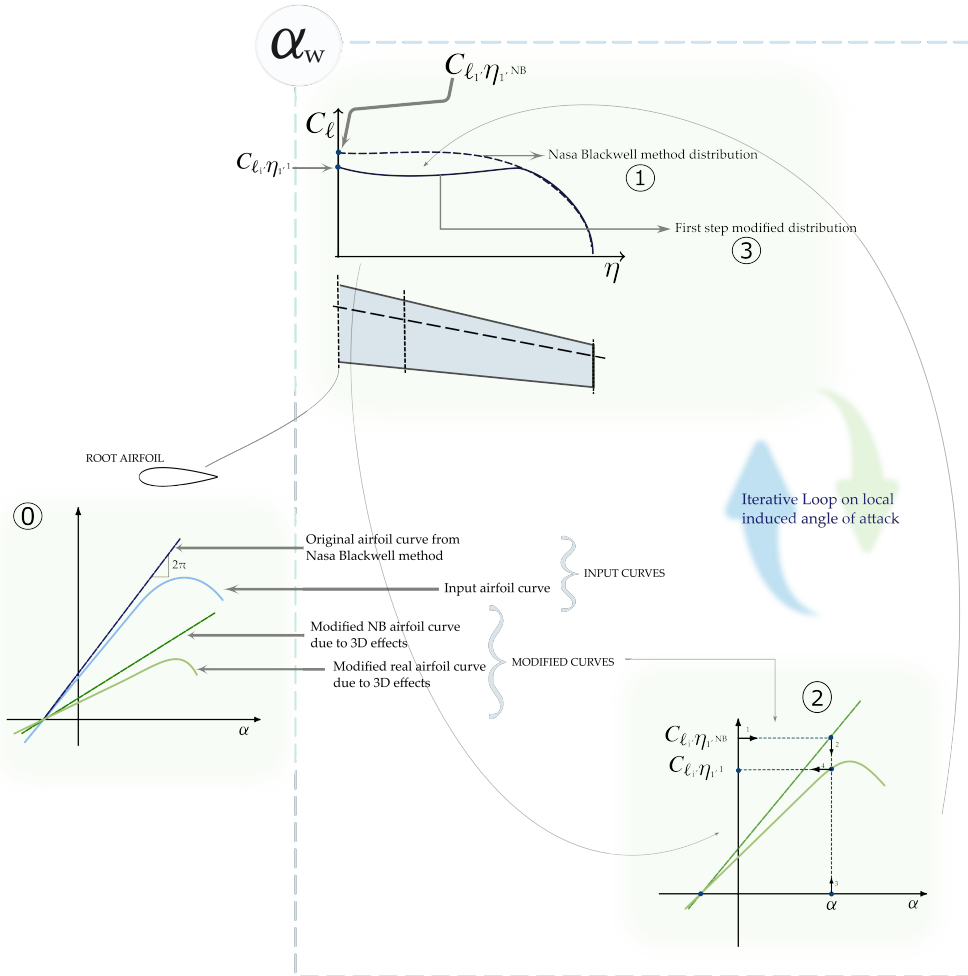


Figure 3.29: Infographic for improved methodology for lift coefficient estimation.

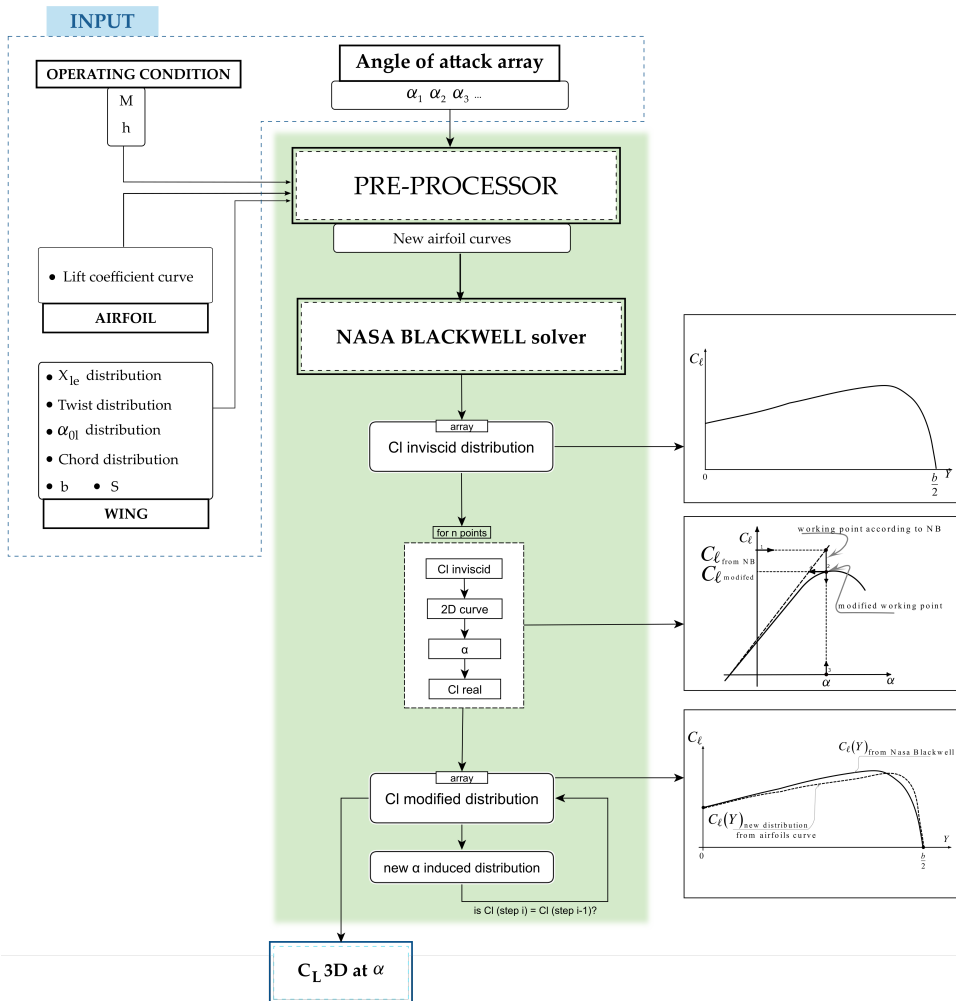


Figure 3.30: Flow chart of improved methodology for lift coefficient estimation.

$$C_{D_{LS}} = C_{D_{parasite}}(\alpha) + C_{D_{gap}} + C_{D_{induced}}(\alpha) + C_{D_{wave}}(\alpha) \quad (3.27)$$

The term $C_{D_{0parasite}}(\alpha)$ is calculated starting from airfoil drag polar and integrating the drag coefficient distribution along semispan. In *JPAD* the term $C_{D_{0gap}}$ is from [25] and $C_{D_{0wave}}(\alpha)$ is taken from [43] and the critical Mach number is calculated using method suggested by Kroo, reported in [76]. Concerning the vortex drag, or induced drag, it has calculated from Prandtl theory [53]. The induced drag is the drag that results from the generation of a trailing vortex system downstream of a lifting surface of finite aspect ratio and it is expressed in Eq. 3.28. For a given planform shape, δ is a constant that is normally small in comparison to unity. It therefore represents, for a given wing, the fractional increase in the induced drag over the optimum elliptic case. The numerical determination of δ will now be outlined for the simplified lifting line model.

$$C_{D_i} = \frac{C_L^2}{\pi AR} (1 + \delta^2) \quad (3.28)$$

Is it possible to evaluate the δ factor, using a coordinates transformation from linear ones to angular ones (Eq. 3.25) using the Fourier coefficient for wing load γ .

$$\gamma(\theta) = \sum_{n=1}^{\infty} B_n \sin(n\theta) \quad (3.29)$$

$$B_{n_i} = \int_{-\pi}^{\pi} \gamma(\theta) \sin(n\theta) d\theta \quad (3.30)$$

And then it is possible to evaluate δ

$$\delta^2 = \sum_{n=2}^{\infty} \frac{nB_n^2}{B_1^2} \quad (3.31)$$

3.5 Improved methodology for high lift devices

In this section is reported the developed methodology for wing with high lift devices. To consider the presence of these devices, the method works

using the flapped airfoil aerodynamic characteristics where appropriate. The purpose is to take into account the presence on the lifting surface of high lift devices, such as flaps and/or slats. This method needs a small number of input data as shown in Fig. 3.32. The method works replacing the clean wing parameters with the flapped ones, obtaining an adapted wing planform geometry to which the modified vortex-lattice method, presented in Sec. 3.3 is applied. The wing with high lift devices deployed is adapted from the clean wing by substituting the following parameters:

- Chord distribution
- α_{0i} distribution
- X_{le} distribution
- $C_{l_{max}}$ distribution

These values are calculated considering for each station the 2D variation due to the presence of the high lift device. These modified arrays are the new input values for the method, most of which can be calculated using a semiempirical approach, such as the one suggested by [85], or by means of high fidelity *CFD* analyses to have more reliable results. The guideline that is followed is to analyze separately the effects of trailing-edge and the leading-edge devices. The local changes in aerodynamic characteristics of airfoils are evaluated in order to calculate the global effects on the entire wing. As far as the $C_{l_{max}}$ distribution is concerned, the distribution is modified considering the 3D effects due to the high lift devices. The method works modifying the maximum lift coefficient distribution with flaps and slats, considering the mutual interaction between the sections with high lift devices and the clean adjacent sections. As shown in Fig. 3.31

In fact, the presence of high lift devices modifies also the aerodynamic characteristics of clean airfoil close to them. For each station, a function that returns the ΔC_l due to high lift devices, along the semispan, is evaluated. This function depends on two contributes: the local section spanwise, as consequence of the distance from the devices and on the angle of attack. It is obtained through the vortex-lattice method, evaluating the load distribution at different angles of attack and represents the mutual effect of high-lift device deployment on the wing. The main steps of the method are the following:

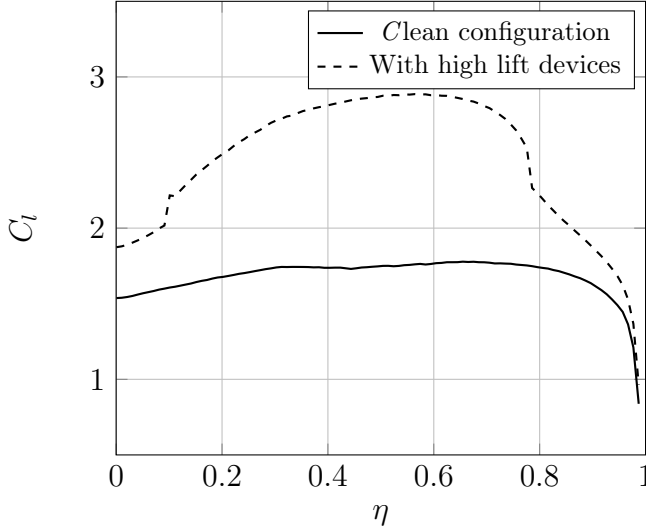


Figure 3.31: C_l distribution comparison for $\alpha_w = 4^\circ$ with and without high lift devices performed by a *CFD* analysis for a wing with $S=105 \text{ m}^2$, $\mathcal{R}=12$, and with two fowler flaps deflected of 15° . Complete data and analyses results are reported in Chap. 5.

1. For each angle of attack, two C_l distributions are evaluated, i.e. the clean one C_l^{clean} with a standard vortex method, and the modified one C_l^{hl} due to the presence of high lift devices using the adapted wing geometry described above.
2. For each station j along the semispan, the amount

$$\Delta C_l|_j = f(\eta, \alpha_w(\alpha|_j)) = C_l^{\text{hl}}|_j - C_l^{\text{clean}}|_j \quad (3.32)$$

is evaluated by subtracting the two distributions. The local difference ΔC_l is a function of how much the local airfoil is far from the high lift device as well as the angle of attack $\alpha_w(\alpha|_j)$. The latter is the wing angle of attack that determines the local $\alpha|_j$ distribution and $\Delta C_l|_j$.

3. For each station, the effective angle of attack is calculated thanks to the evaluation of the induced angle of attack distribution.
4. For each station, at the local stall angle of attack, it is now possible to know the related wing angle of attack $\alpha_w(\alpha|_j)$ and calculate the

$C_{l_{MAX}}^h$ as follows:

$$C_{l_{MAX}}^h|_j = C_{l_{MAX}}^{clean}|_j + \Delta C_{l_{MAX}}|_j(\eta, \alpha_W(\alpha|_j)) \quad (3.33)$$

where the term $\Delta C_{l_{MAX}}|_j$ represents the $\Delta C_l|_j$ in Eq. 3.32 evaluated at local airfoil stall angle of attack α_s

Applying this method it is possible to obtain a new $C_{l_{MAX}}$ distribution that turns out to be smoother than the unmodified 2D distribution. In Fig. 3.32 a flow chart of the improved methodology. As in the clean configuration case, the method starts with a PRE-PROCESSOR in which the airfoil curves are modified and, only for configuration with high lift devices, during the preprocessor 2D values such as chord distribution and zero lift angle, are modified. The NASA BLACKWELL solver works very similarly to the one in clean configuration, with an iterative process using the modified 2D values.

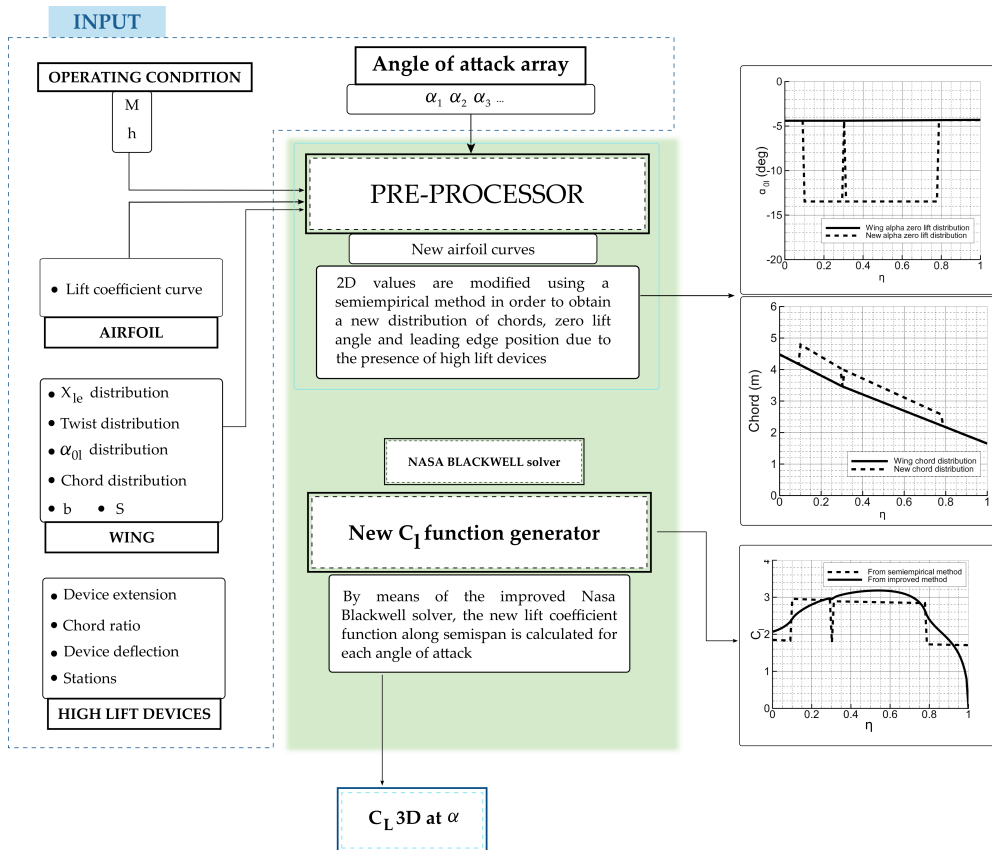


Figure 3.32: Flow chart of improved methodology for lift coefficient estimation with high lift devices.

Methodologies validation

In this Chapter some case study are presented in order to validate the improved methodology for lift estimation explained in Chap. 3.3 and in Chap. 3.5 both for a wing in clean configuration and with high lift devices deflected. Three cases study are following presented:

- **Case a:** A swept wing ($\Lambda_{le} = 37.2^\circ$) in clean configuration - *WTT* comparison
- **Case b:** A swept wing ($\Lambda_{le} = 37.2^\circ$) in configuration with high lift devices deflected (Double slotted $\delta_f = 48.85^\circ$) - *WTT* comparison
- **Case c:** A wing ($\Lambda_{le} = 10^\circ$) with high lift devices deflected (Fowler $\delta_f = 15^\circ$) - *CFD* comparison

Case a

To have reliable values to compare with, a case study with wind tunnel tests result has chosen from literature [49]. This wing configuration has been choose to verify the method even on a wing with a considerable sweep. The wing planform is shown in Fig. 4.1 while main geometrical data are in Tab. 4.1. The airfoil section is NACA 64₁-212.

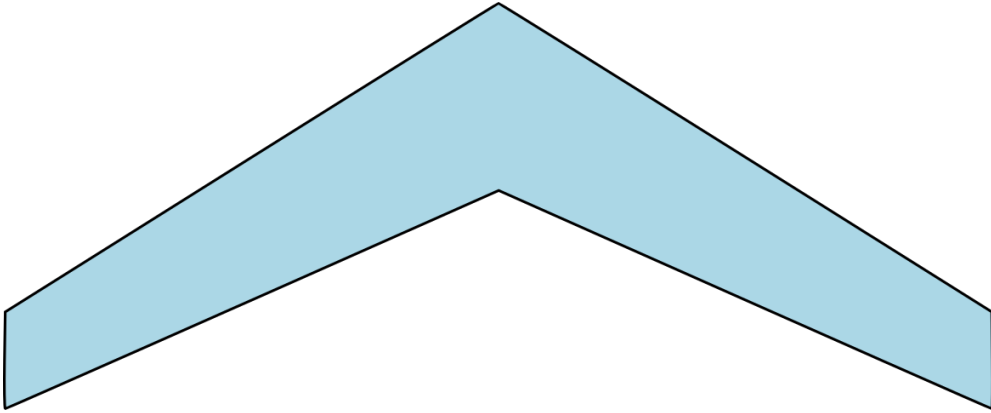


Figure 4.1: *Wing planform in clean configuration, whose data are in 4.4.*

Wing Data	Value
Root chord	1.42 m
Tip chord	0.71 m
Sweep leading edge	37.2°
Area	6.83 m ²
Span	6.40 m

Table 4.1: Main wing geometrical characteristics from [49]

Operating condition	Value
Mach number	0.13
Reynolds number	6.8e5

Table 4.2: Main wing geometrical characteristics from [49]

Given the airfoil and geometry characteristics, the wing has been analysed with the improved method and thorough a classical vortex method from literature [12] coupling with stall path method from [80] in order to compare these two approaches. As it is possible to appreciate from Fig.4.2 and Tab. 4.3, the improved method led to a percentage error less than 2% as far as the lift curve slope an maximum lift coefficient is concerned and less than 3% as regards the stall angle of attack.

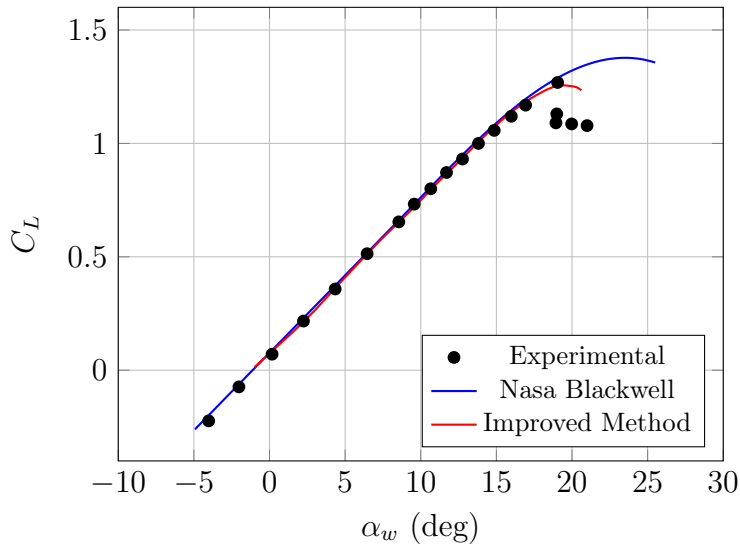


Figure 4.2: 3D lift coefficient curve comparison

Value	Experimental data	Improved method	Error (%)
C_{L_α} (deg^{-1})	0.0703	0.0715	1.69%
$C_{L_{max}}$	1.28	1.26	1.56%
α_s (deg)	18.9°	19.4°	2.43%

Table 4.3: Results comparison from Improved method and experimental data in clean configuration, from [49]

Case b

The same wing as the previous section has analysed in configuration with high lift devices deflected. These are two double slotted flaps deflected of $\delta_f = 48.84^\circ$, as shown in Tab. 4.4. Wing planform is shown in Fig. 4.3.

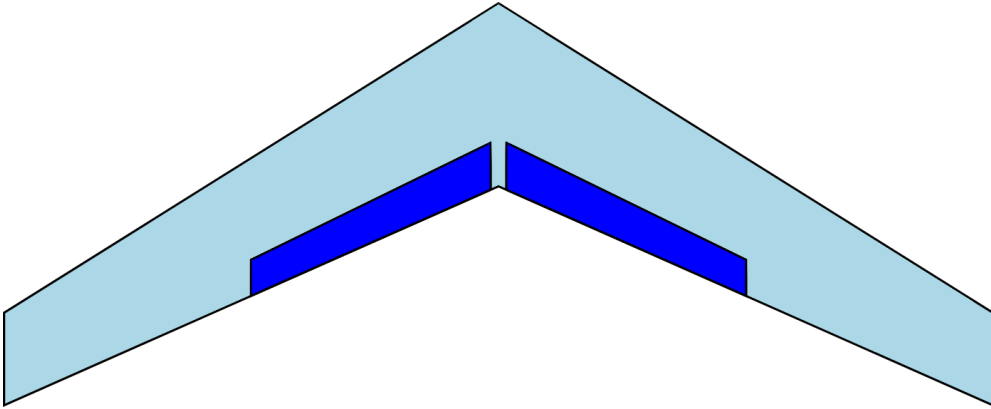


Figure 4.3: *Wing planform modelling with high lift devices, whose data are in 4.4.*

High lift device data	Value
Type	Double Slotted
Flap chord ratio	0.25
Flap deflection	48.85°
Inner station (η)	0.0018
Outer station (η)	0.5

Table 4.4: Main wing high lift devices data from [49].

First of all, discretized data for chord and zero-lift angle of attack have been modified due to the presence of high lift devices deflected. In Fig. 4.4 the chord comparison between the real wing planform and the modified one for the effect of flap is represented. As it is possible to appreciate, there is an increment in chord in the section with high lift device. Then the lift coefficient distribution along the semispan has been calculated for $\alpha_w = 18.7^\circ$ in clean configuration (and compared with experimental data) and in configuration with high lift devices, in Fig. 4.5. 3D results are shown in Fig. 4.6 and Tab. 4.5 where it is possible to appreciate that the percentage error is less than 5% for each value.

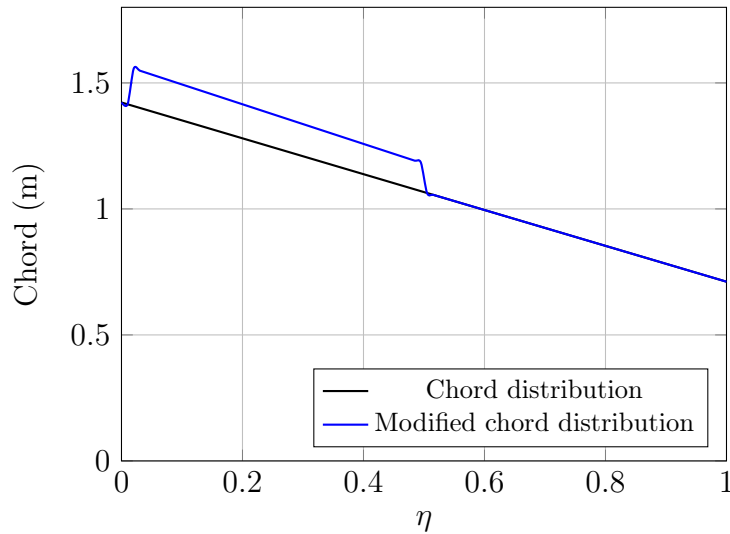


Figure 4.4: Chord distribution comparison between the real and the one with high lift devices deflected of $\delta_f = 48.85^\circ$, wing from [49].

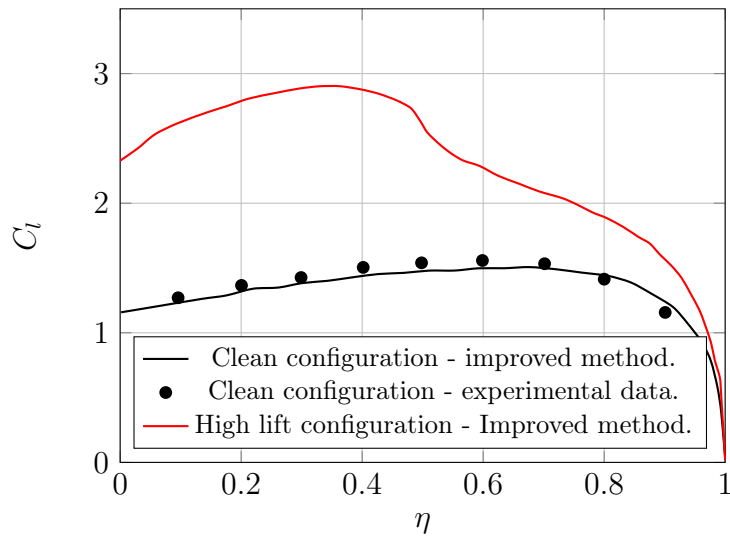


Figure 4.5: C_l distribution in clean configuration from Nasa-Blackwell method [12] and from experimental data from [49], and in configuration with high lift devices deflected of $\delta_f = 48.85^\circ$ calculated with improved method at angle of attack of 18.7° .

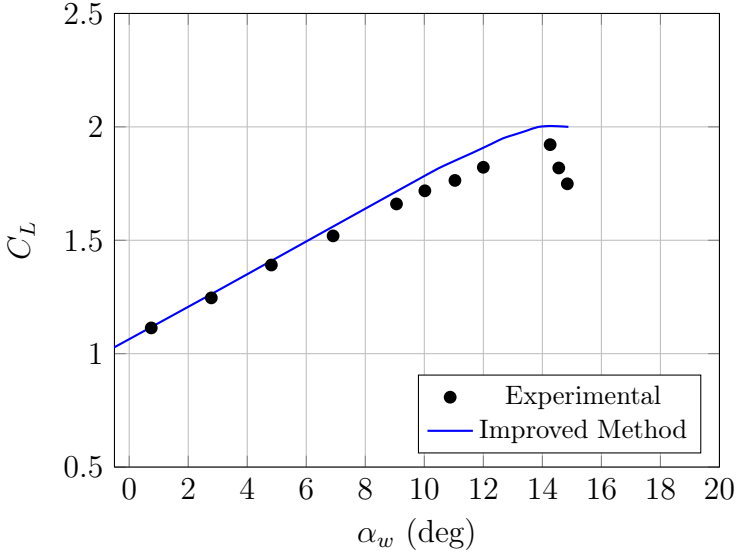


Figure 4.6: 3D lift coefficient curve comparison with high lift devices deflected $\delta_f = 48.84^\circ$. Experimental data from [49]

Value	Experimental data	Improved method	Error (%)
C_{L_α} (deg^{-1})	0.0712	0.0720	1.17%
$C_{L_{max}}$	1.92	2.01	4.68%
α_s (deg)	14.26°	14.31°	0.35%

Table 4.5: Results comparison from Improved method and experimental data in configuration with high lift devices deflected ($\delta_f = 48.84^\circ$), experimental data from [49]

Case c

This case study concerns the wing of *IRON* Loop 1, described more in detail in Sec. 1.4 and in Chap 5. Wing planform and main data are in Fig. 4.7 and Tab. 4.7 and Tab. 4.6. This configuration is considered with two fowler flap deflected of $\delta_f = 15^\circ$ as in take off configuration. First of all, the modified distribution in terms of chord distribution and zero lift angle of attack have been calculated and here shown in Fig. 4.8 and 4.9. Then in order to verify the lift coefficient distribution along semispan, the ones obtained with modified method are compared to the *CFD* results. As it is possible to appreciate from Fig. 4.10 to 4.10, the results obtained with improved method are really close to the ones with an higher fidelity method, especially for higher angles of attack. The percentage error has been calculated considering the mean of errors calculated for each station along semispan between the values from improved method and the ones from *CFD*. This result is shown in Tab. 4.8. 3d lift curves are shown in Fig. 4.13.

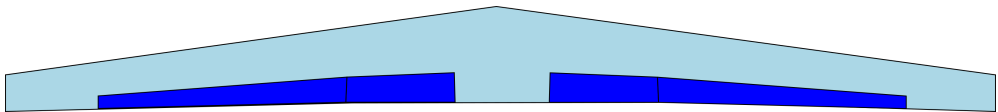


Figure 4.7: *IRON* Loop 1 configuration wing planform with high lift devices.

High lift device data	Value
Type	Fowler
Number of flaps	2
Inner chord ratio	0.29
Outer chord ratio	0.32
Flap deflection	15° , 15°
Inner stations (η)	0.1 , 0.3
Outer station (η)	0.3 , 0.78

Table 4.6: Main wing flap data of *IRON* Loop 1 data.

Wing Data	Value
Root chord	4.48 m
Tip chord	1.79 m
Sweep leading edge	10°
Span	35.49 m

Table 4.7: Main wing geometrical characteristics of *IRON* Loop 1 data.

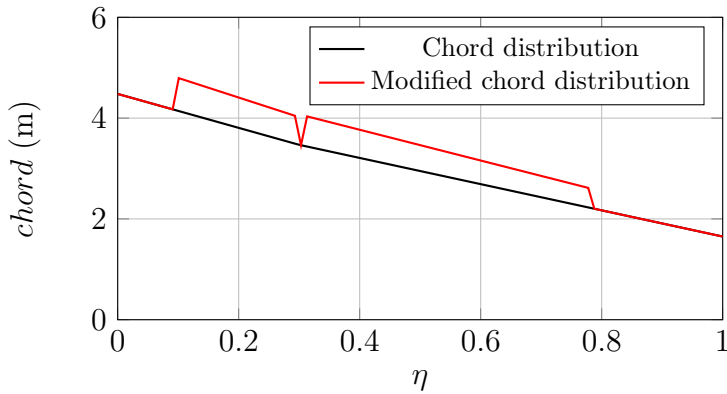


Figure 4.8: *IRON* Loop 1 chord distribution comparison. Real configuration compared with the one due to the high lift devices deflection.

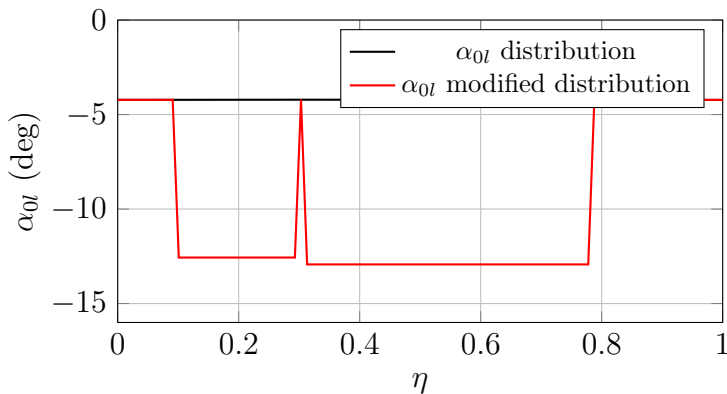


Figure 4.9: *IRON* Loop 1 zero lift angle distribution comparison. Real configuration compared with the one due to the high lift devices deflection.

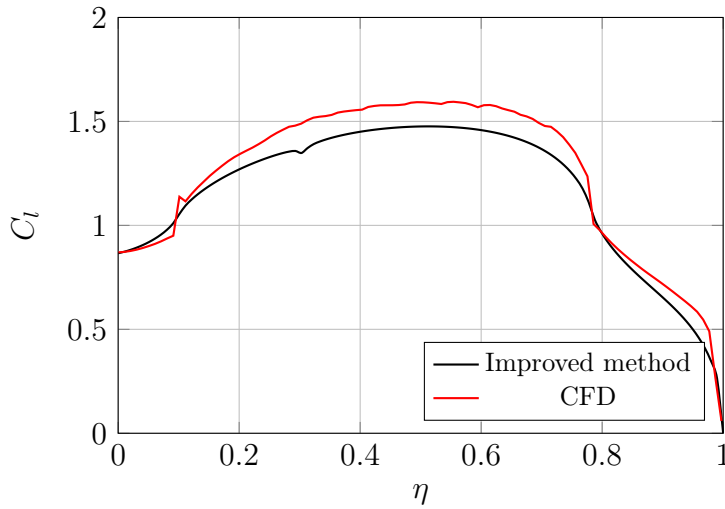


Figure 4.10: *IRON* Loop 1 configuration. Lift coefficient distribution for configuration with two fowler flaps deflected of $\delta_f = 15^\circ$. Comparison between improved method and *CFD*. $\alpha = 2^\circ$.

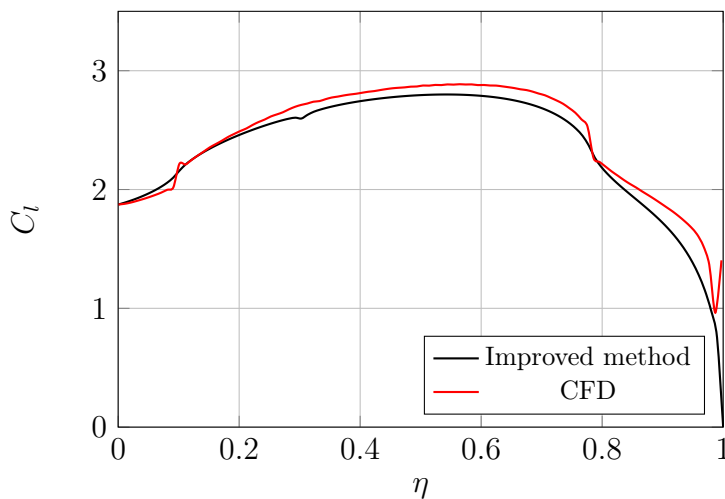


Figure 4.11: *IRON* Loop 1 configuration. Lift coefficient distribution for configuration with two fowler flaps deflected of $\delta_f = 15^\circ$. Comparison between improved method and *CFD*. $\alpha = 14^\circ$.

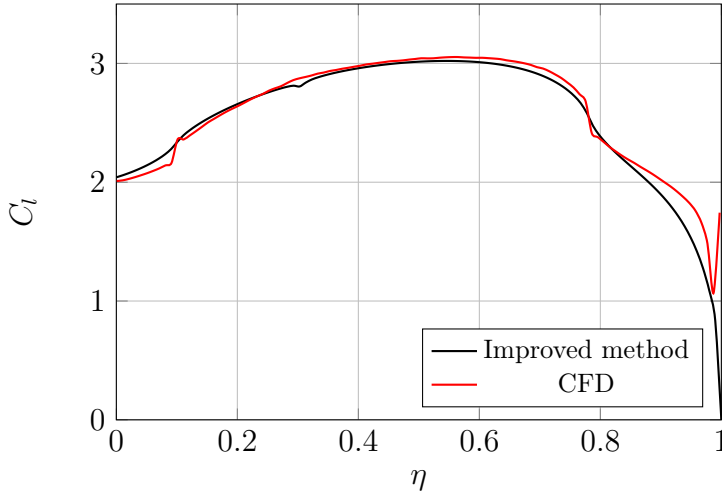


Figure 4.12: *IRON* Loop 1 configuration. Lift coefficient distribution for configuration with two fowler flaps deflected of $\delta_f = 15^\circ$. Comparison between improved method and *CFD*. $\alpha = 16^\circ$.

Angle of attack	Mean error along semispan (%)
$\alpha = 2^\circ$	6.7%
$\alpha = 14^\circ$	3.91%
$\alpha = 16^\circ$	1.99%

Table 4.8: Results comparison between wing span lift coefficient calculated with improved method and with *CFD* analyses, for *IRON* Loop1 wing with high lift devices.

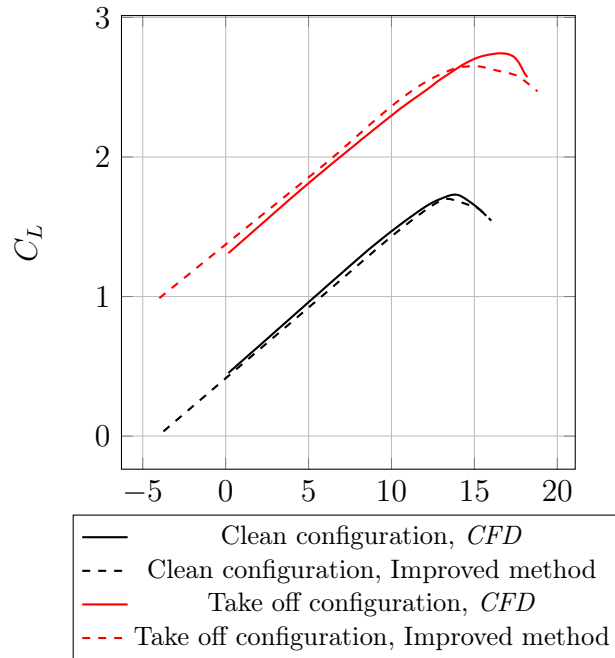


Figure 4.13: *IRON* Loop1 configuration. 3D lift coefficient curve comparison in clean configuration and with high lift devices deflected in take off, $\delta_f = 15^\circ$.

**Aerodynamic analysis of innovative regional
turboprop**

5.1 Introduction

In this chapter the analyses loops performed for the *IRON* project are reported in detail, focusing on the aerodynamic results. As introduced in Chap. 1, the *IRON* project is focused on the feasibility study of an innovative turboprop regional configuration. The research addressed to the analysis and design of this innovative regional platform will be developed through three different Loops with increasing level of complexity and fidelity. The Loop 1 started in July 2016 from the baseline configuration provided by Leonardo Company and ended in January 2017. The aircraft under investigation is an innovative layout with low wing. Engines are rear installed on the horizontal tail tips. The Loop 2 started in the second half of 2017 and ended in 2018. At the beginning of second Loop, a careful weight and balance breakdown, revealed a very large centre of gravity excursion, compelling to review the aircraft configuration, a Multi-Disciplinary Analysis and Optimization (*MDAO*) has been performed, selecting a three lifting surfaces layout as the best solution. A configuration comparison is shown in Fig. 5.1. Criticalities resultant from high fidelity analyses performed during the second Loop bring to the Loop 3, or better defined as Loop2 revised configuration, with canard and wing high lift devices refinements.

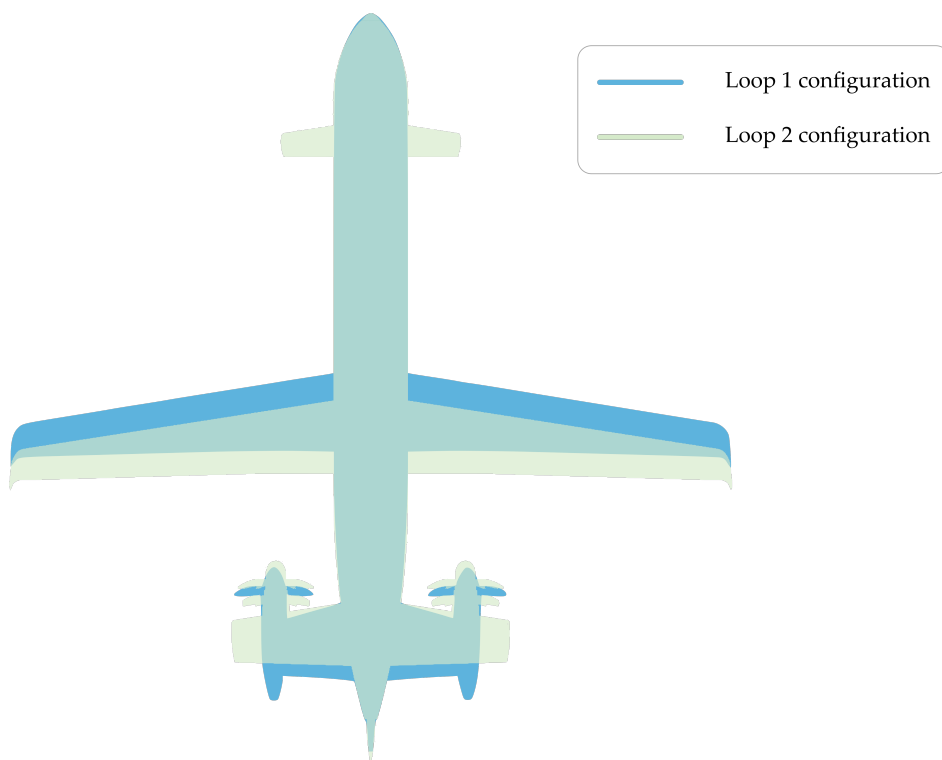


Figure 5.1: *IRON* Loop 1 and Loop 2 configuration comparison.

Synopsis

- First of all, the analyses performed during the Loop 1 are presented
- An overview on the three lifting surface configuration is illustrated
- The analyses on Loop 2 are introduced

5.2 IRON LOOP1 analyses

Starting from Leonardo *TLAR* and related assumptions, reported in Chap. 1 in Tab.1.1, Tab. 1.2 and Tab. 1.3, analyses on Loop 1 configuration have been performed. The aerodynamic analysis, and thus the structure of this section, has been broken down in the following topics:

- Airfoil and high lift devices design have been designed. This task was challenging because of the high aerodynamic efficiency required having an airfoil with 18% of thickness. Natural laminar flow was mandatory to comply with *TLAR*. Moreover, the airfoil should provide acceptable aerodynamic characteristics also in fully turbulent flow. Once the wing airfoil has been defined an efficient fowler flap has been designed. To improve the landing maximum lift coefficient, the effects of a droop nose has been also evaluated. To assess the wing maximum lift capabilities, a 3D isolated wing *CFD* analyses have been performed.
- Winglets have been specifically designed to reduce the induced drag improving mainly the climb performance.
- Fuselage aerodynamic characteristics have been estimated through several methods, including *CFD-RANS* analyses.
- Low fidelity aerodynamic analyses have been performed in order to calculate drag polar and to assess the longitudinal, lateral and directional stability.
- A detailed weight and balance analyses has been performed to assess the design and sizing of the baseline configuration. This task has highlighted some criticalities of such a configuration dealing with the centre of gravity excursion which resulted to be very wide (from 4% to 52% of the mean aerodynamic chord). Due to this issue, a review of the aircraft configuration and sizing has been done.
- According to the weight and balance estimation, at the beginning of the Loop 2, the baseline configuration has been revised (regarding wing position, horizontal tail area, and so on.) to ensure stability and control for each considered centre of gravity excursion. Three solutions have been investigated, considering also a three lifting surfaces configuration.

Some of the above mentioned aspects are debated in this work. For other information is it possible to refer to [36].

Airfoil design

The wing airfoil design has driven by three major conditions as illustrated in Fig. 5.2. To match the cruise efficiency, a laminar airfoil was required, avoiding any drag increase deriving from strong shock waves. To reach the prescribed wing maximum lift coefficient, airfoils themselves must have a moderately high maximum lift coefficient. Finally, in order to avoid a large decay of the aerodynamic performance, the off-design conditions must be checked. Moreover, aircraft requirements fixed the wingspan thickness: root and kink sections must have a relative thickness of 18% and the tip relative thickness is 14%. The airfoil design has been accomplished by means of the inverse design routine of *MSES* software [61], by modifying the pressure coefficient distribution until the desired aerodynamic characteristics have been reached. The inverse design started from the *NACA 66(3)-418* reference airfoil and was focused on the kink airfoil.

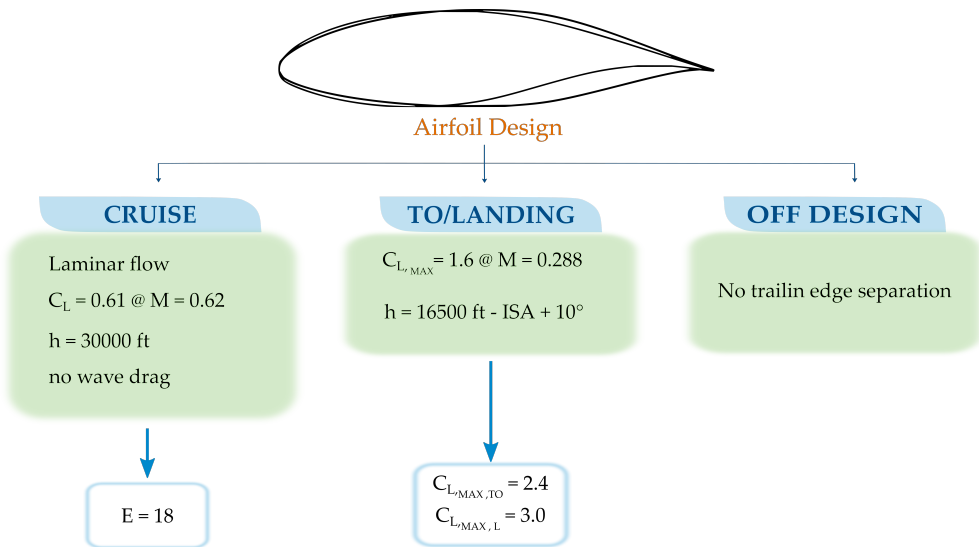


Figure 5.2: Airfoil target from *TLAR*, useful for its design.

The design of the new set of airfoils has been accomplished through the following steps:

1. Estimate of the design lift coefficients from the wing span loading evaluation

2. Design of two airfoils (root/kink and tip) by means of the inverse design routine of *MSES* software
3. Optimisation of the most promising airfoil set by means of optimisation tool

For the optimization design loop, the starting point for this new airfoil design is the kink airfoil obtained in the second phase and corrections to better comply with the maximum achievable lift coefficient and off design conditions have been provided. The following consideration have been made to drive the new design:

- Avoid the trailing edge separation in off design conditions
- Keep fixed the maximum thickness
- Increase the maximum lift coefficient in fully turbulent conditions
- Loose about 10-15% of laminar flow extensions
- Have a minimum drag coefficient around 40/45 drag counts for a range of C_l

The designed airfoil, called FS Kink airfoil, is compared to the reference airfoil in Fig. 5.3.

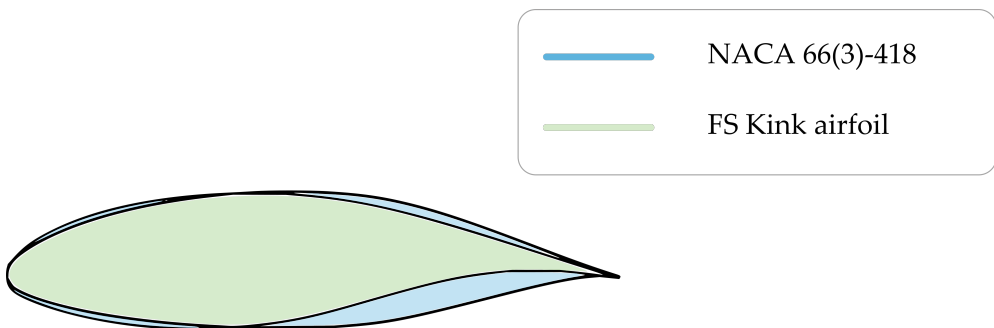


Figure 5.3: Kink airfoil: comparison with the reference *NACA* laminar airfoil.

The laminar drag bucket is spread over a wide range of lift coefficient showing its minimum (40 drag counts) at the cruise lift coefficient of about

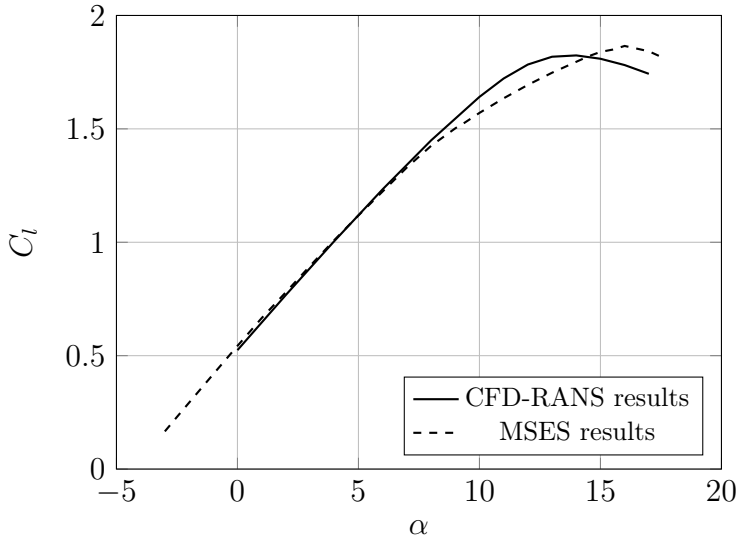


Figure 5.4: Kink airfoil: Lift coefficient comparison of CFD vs. MSES results, stall conditions $M=0.28$ $Re=13.6e6$.

0.6-0.7. Thanks to this characteristic, the wing tip airfoil can be derived from the kink section. In particular, the kink airfoil thickness has been adequately scaled and its camber has been reduced to centre the minimum drag at the required lift coefficient. A minimum drag coefficient of about 40 drag counts (which is 20/25 drag counts lower than a non-laminar airfoil having the same thickness) is the minimum value to reach the wing parasite drag that comply with the prescribed aircraft cruise efficiency. The high lift characteristics in clean configuration have been also assessed by means of high-fidelity tools such as a RANS (Reynolds Average Navier Stokes) solver. The comparison between the MSES prediction and the RANS results are shown in Fig. 5.4, Fig. 5.5 and Fig. 5.6.

Main aerodynamic results

This section deals with the preliminary estimation of the complete aircraft aerodynamic results without propulsive effects. The final wing airfoil in the previous section have been considered to perform the calculations. The analyses have been carried out in four different operating conditions, shown in Tab. 5.1. In all the conditions three different centre of gravity

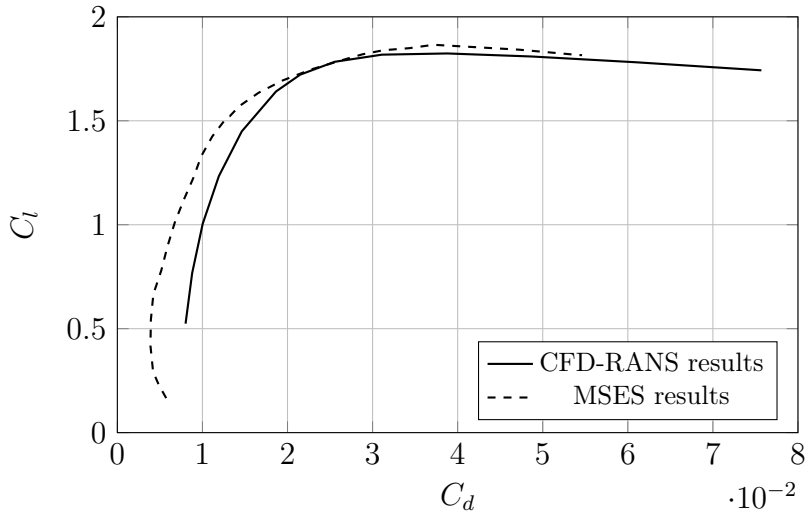


Figure 5.5: Kink airfoil: Polar comparison of Star-CCM+ CFD vs. MSES results, stall conditions $M=0.28$ $Re=13.6e6$.

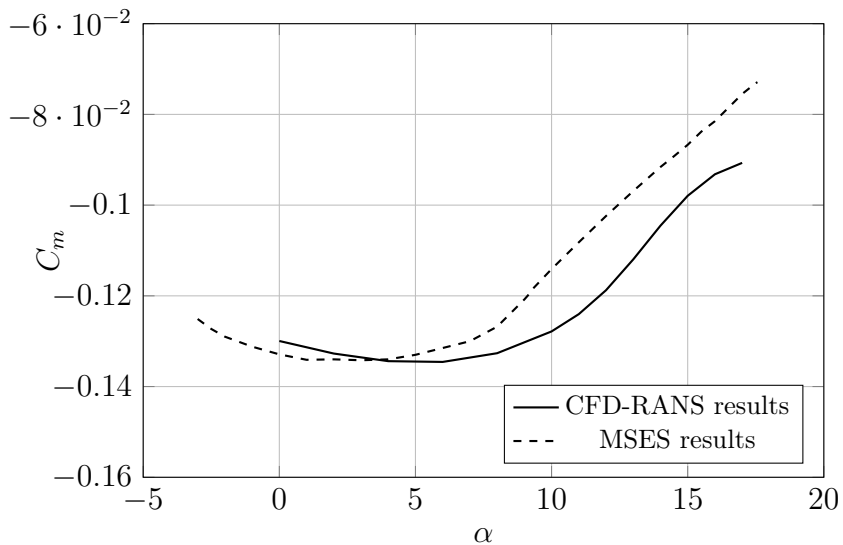


Figure 5.6: Kink airfoil: Moment coefficient comparison of Star-CCM+ CFD vs. MSES results, stall conditions $M=0.28$ $Re=13.6e6$.

locations have been considered. From further higher fidelity analyses the CG excursion turned out to be higher than the initially assumed.

Condition	Altitude (ft)	Mach number	Reynolds number
Cruise	30000	0.62	18e6
Stall Clean	16500 (ISA + 10°)	0.288	12.7e6
Take Off	0	0.171	12.7e6
Landing	0	0.171	12.7e6

Table 5.1: *IRON* Loop 1 operating conditions

In this phase the analyses have been carried out through semi-empirical methodologies. The lifting surface lift coefficient has been calculated using the Nasa-Blackwell method [12] coupled with stall path method [80]. Knowing the lift coefficient distribution and the airfoil $C_{m_{ac}}$ it has been possible to calculate the centre of pressure location along the span shown in Fig. 5.7 through the Eq. 5.1, and the 3D C_{M_0} . The validation of this data is obtained through Fig. 5.8 where all forces and arms are shown. The other contributes for downwash, high lift devices are calculated as described in Chap. 3. From Fig. 5.9 to Fig. 5.15 main component results are shown.

$$\frac{x_{cp}}{c} = \frac{x_{ac}}{c} - \frac{C_{m_{ac}}}{c_l} \quad (5.1)$$

The aircraft drag polar is sum of several contributions calculated as follows:

- **WING:** integration of airfoils drag coefficient (coming from MSES aerodynamic calculations) along the wing span to estimate the parasite contribution.
- **FUSELAGE:** CFD Navier-Stokes calculation has been used as function of fuselage angle of attack.
- **HORIZONTAL TAIL:** this contribution has been computed in the same manner of wing (integration of airfoil parasite drag along tail span); the drag dependent from horizontal tail lift has also been considered according parabolic formulation with an Oswald factor equal to $e_h = 0.9$.

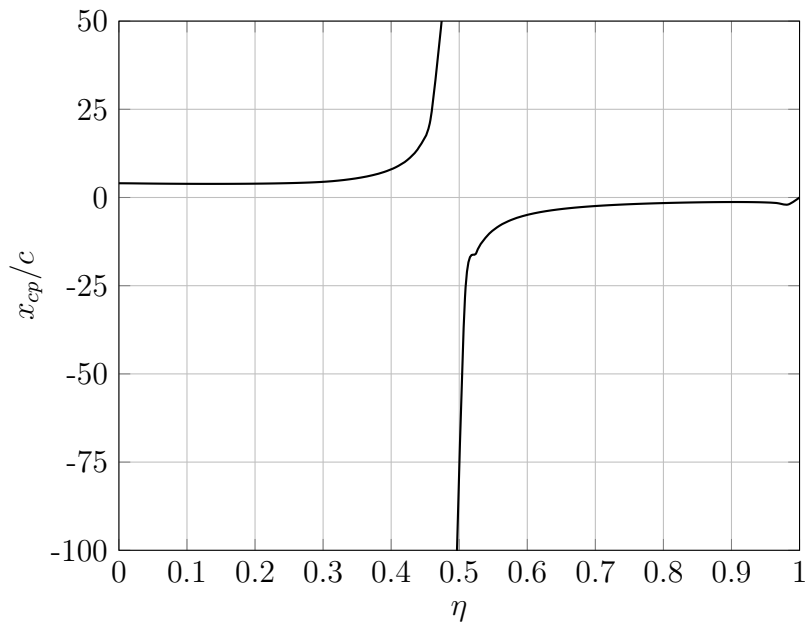


Figure 5.7: *IRON* Loop 1 aerodynamic assessment. Wing centre of pressure location along semi span calculated for zero lift angle of attack. Climb condition: $M = 0.288$, $Re = 1.3e7$.

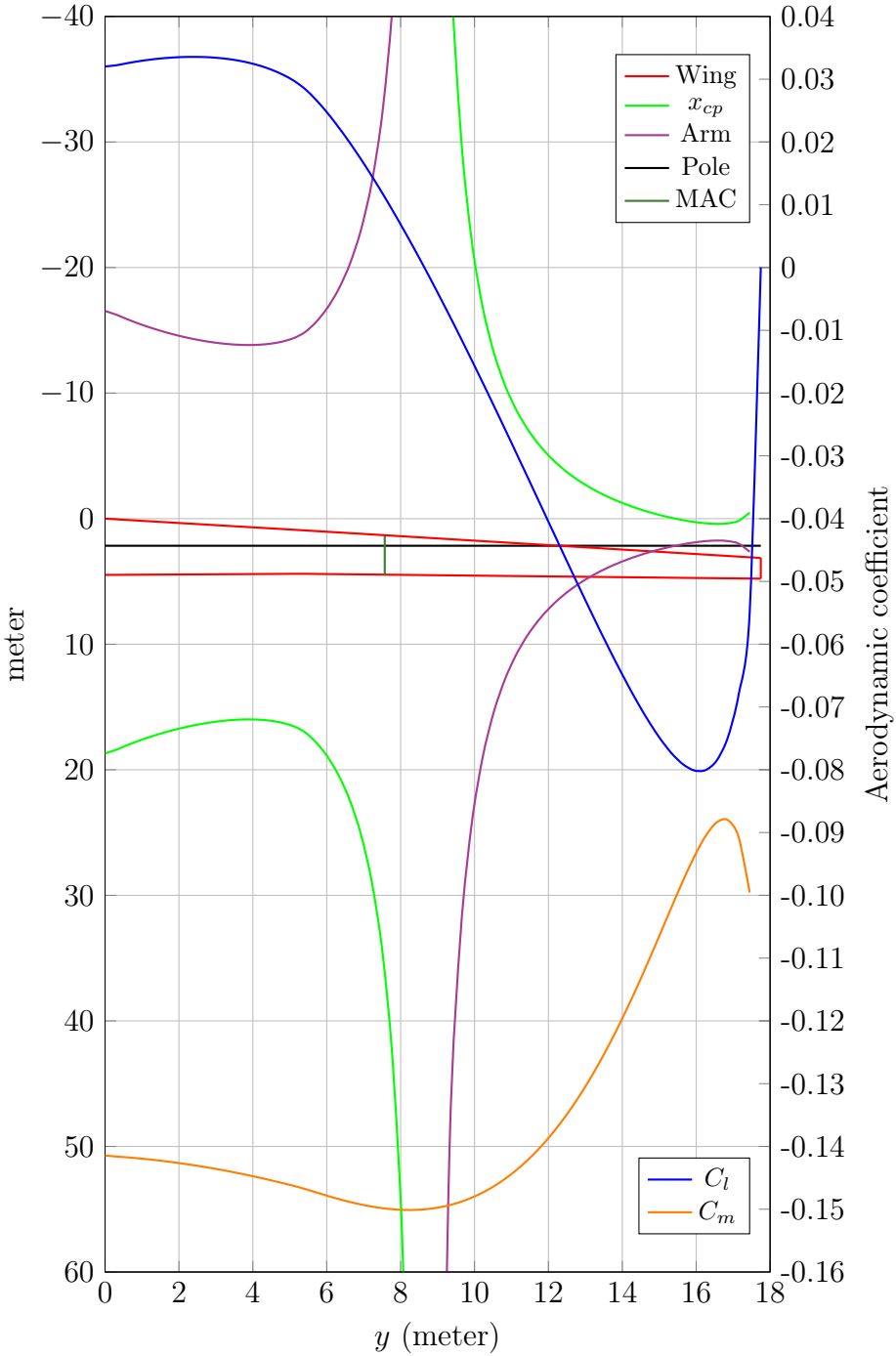


Figure 5.8: *IRON* Loop 1 aerodynamic assessment. Wing construction used to verify the calculated C_{M_0} . Climb condition: $M = 0.288$, $Re = 1.3e7$.

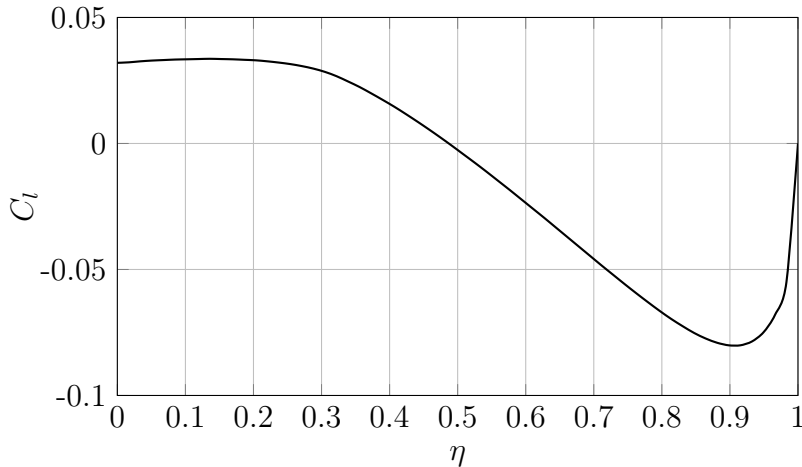


Figure 5.9: *IRON* Loop 1 aerodynamic assessment. Wing lift coefficient distribution calculated with Nasa-Blackwell method and for zero lift angle of attack. Climb condition: $M = 0.288$, $Re = 1.3e7$.

- **OTHER COMPONENTS:** Vertical tail, nacelles, wing-fuselage interference, horizontal-nacelles interference, excrescences and miscellaneous items have been taken into account as a constant parasite drag source [22].

Longitudinal static stability assessment

In order to evaluate the characteristics of longitudinal stability of an aircraft is necessary to express all the forces and the moments acting on it and evaluate the resultant pitching moment with respect to the centre of gravity of the whole aircraft as described in Chap. 3. The wing pitching moment coefficient has been computed by the integration of the airfoil pitching moment coefficient along the wing span, according the above mentioned Nasa-Blackwell procedure. In take-off and landing conditions, the values of wing pitching moment coefficient have been calculated from the clean values and adding the increment due to the high lift devices from semi-empirical methodologies [25]. To evaluate the pitching moment of the fuselage a has been used a method that has been developed at the Dept. of Industrial Engineering, University of Study of Naples

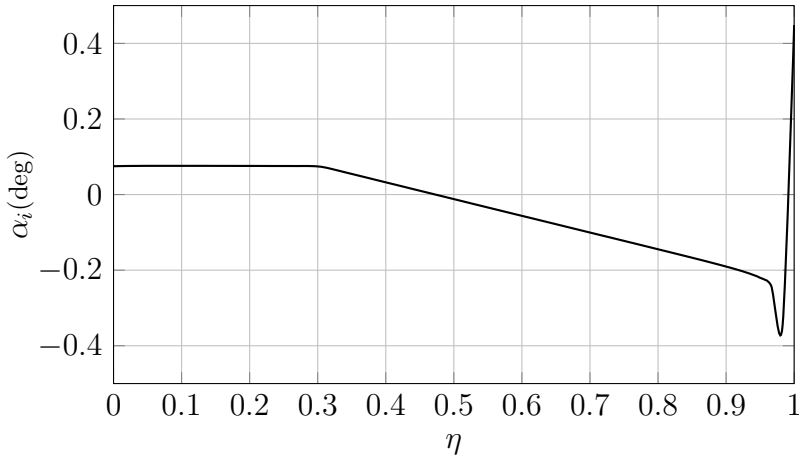


Figure 5.10: *IRON* Loop 1 aerodynamic assessment. Wing induced angle distribution calculated for zero lift angle of attack. Climb condition: $M = 0.288$, $Re = 1.3e7$.

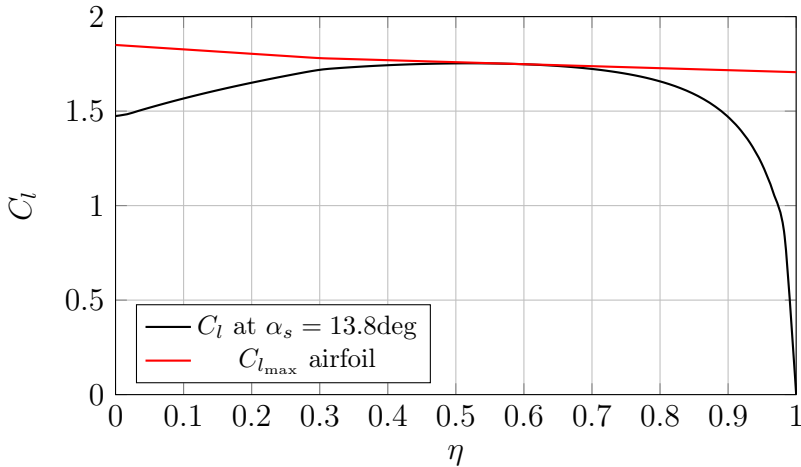


Figure 5.11: *IRON* Loop 1 aerodynamic assessment. Wing stall path method. Lift coefficient distribution calculated with Nasa-Blackwell method corresponding to the angle of attack for which the first station reaches the local airfoil maximum lift coefficient. Climb condition: $M = 0.288$, $Re = 1.3e7$.

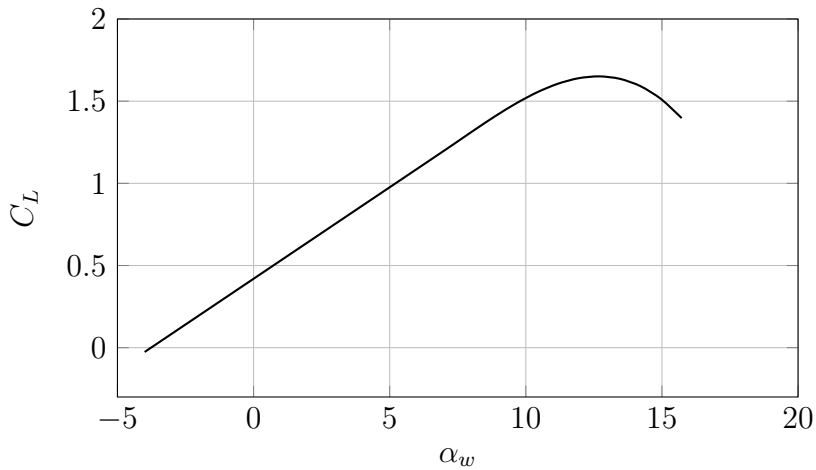


Figure 5.12: *IRON* Loop 1 aerodynamic assessment. Wing 3D lift coefficient calculated with Nasa-Blackwell method coupled with stall path method. Climb condition: $M = 0.288$, $Re = 1.3e7$.

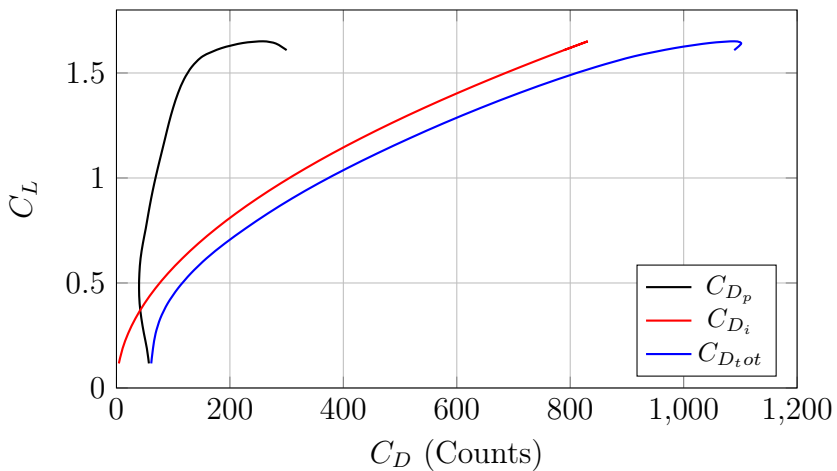


Figure 5.13: *IRON* Loop 1 aerodynamic assessment. Wing 3D polar breakdown. Climb condition: $M = 0.288$, $Re = 1.3e7$.

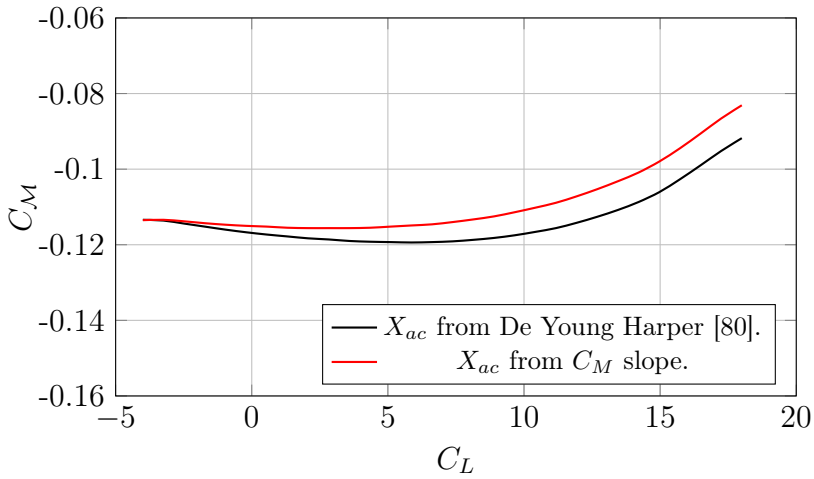


Figure 5.14: *IRON* Loop 1 aerodynamic assessment. Wing 3D moment coefficient curve. Climb condition: $M = 0.288$, $Re = 1.3e7$.

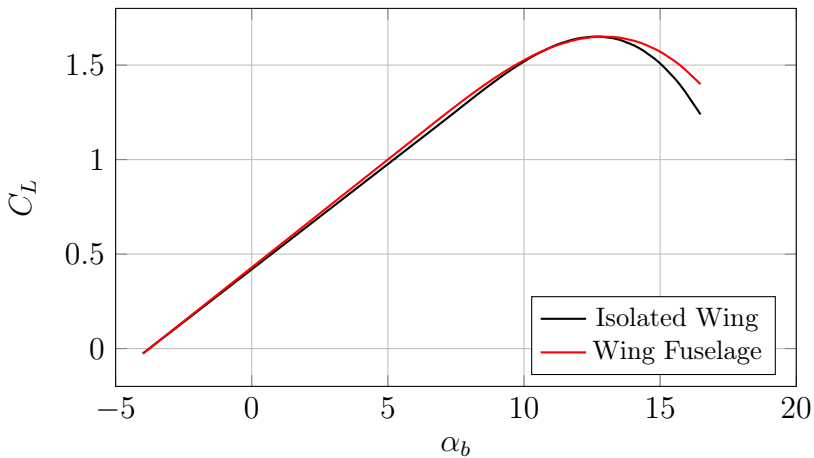


Figure 5.15: *IRON* Loop 1 aerodynamic assessment. Fuselage effect on 3D wing lift coefficient curve. Climb condition: $M = 0.288$, $Re = 1.3e7$.

Federico II, by numerical aerodynamic analyses performed with *STAR-CCM+* [33]. Main results of the Loop 1 are shown from Fig. 5.16 to Fig. 5.42

5.3 Three surfaces configuration

The final output of the aerodynamic database assessment is the complete set of trimmed drag polar curves at main flight conditions. To achieve this task, the estimation of the most forward and most aft position of the aircraft centre of gravity is needed. The first Leonardo assumption for centre of gravity excursion was from 15% to 33% of the mean aerodynamic chord. An in-depth weight and balance analysis carried out by Leonardo Company at the end of the first project loop, taking also into account for on-board systems weights and positions, highlighted a larger centre of gravity excursion, with respect to first assumption, passing to a 4-52% of the mean aerodynamic chord as illustrated in Fig. 5.44. This mainly due to the rear-mounted engines configuration and systems positions. This resulted in three critical issues summarized in Fig. 5.43:

- The aircraft was not stable with the most afterwards centre of gravity position (52% of the mean aerodynamic chord).
- The trimmed C_{LMAX} in landing configuration was lower than the prescribed value of 3.0.
- The revision of the neutral point position (27% of the mean aerodynamic chord) together with the new centre of gravity excursion provided a large region where the aircraft cannot be operative.

The operative envelope illustrated in Fig. 5.45 highlighted a drastic reduction of the minimum payload at which the aircraft can be used requiring different systems positions or a stabilizing mass in the forward part of the fuselage to solve the issue.

This larger centre of gravity excursion highlighted that the baseline aircraft configuration must be revised to meet the aerodynamic targets by the end of Loop1. During this phase, the UniNa DAF research group of the University of Naples Federico II played a fundamental role by carrying out intense research activities aimed at identifying the best design

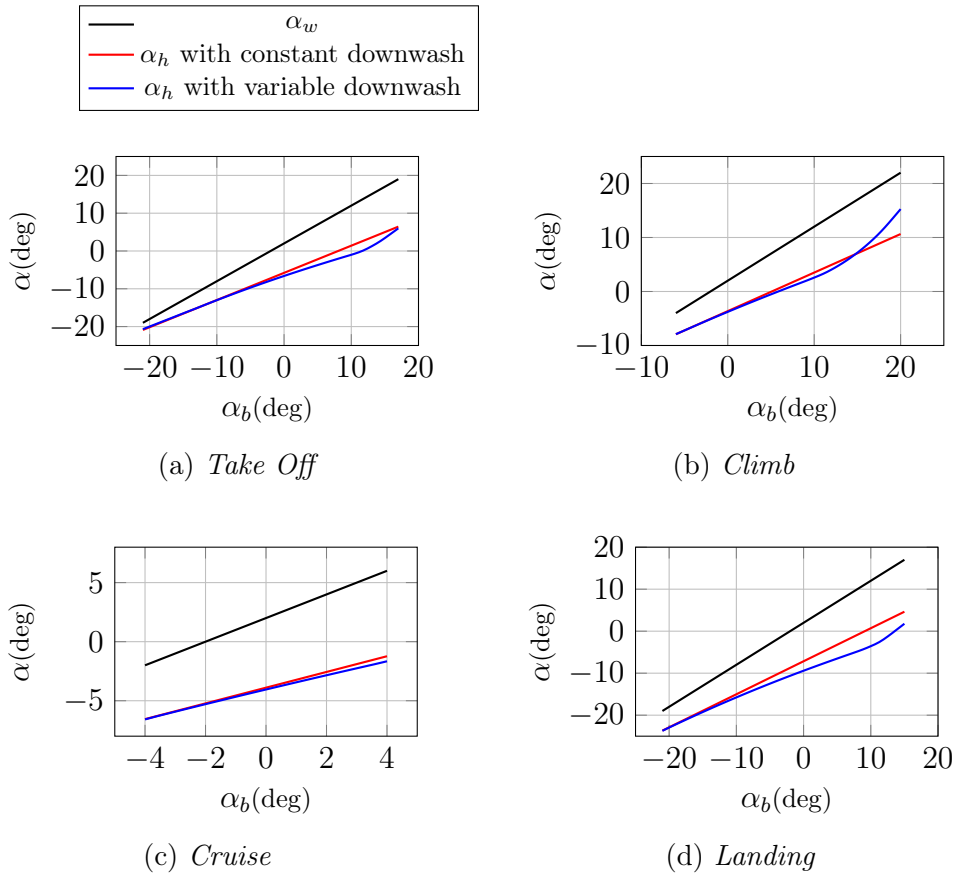


Figure 5.16: *IRON* Loop 1 aerodynamic assessment. Local angle of attack variation due to component angle of incidence and local downwash calculated with Slingerland method [84], in four different operating condition summarized in Tab. 5.1.

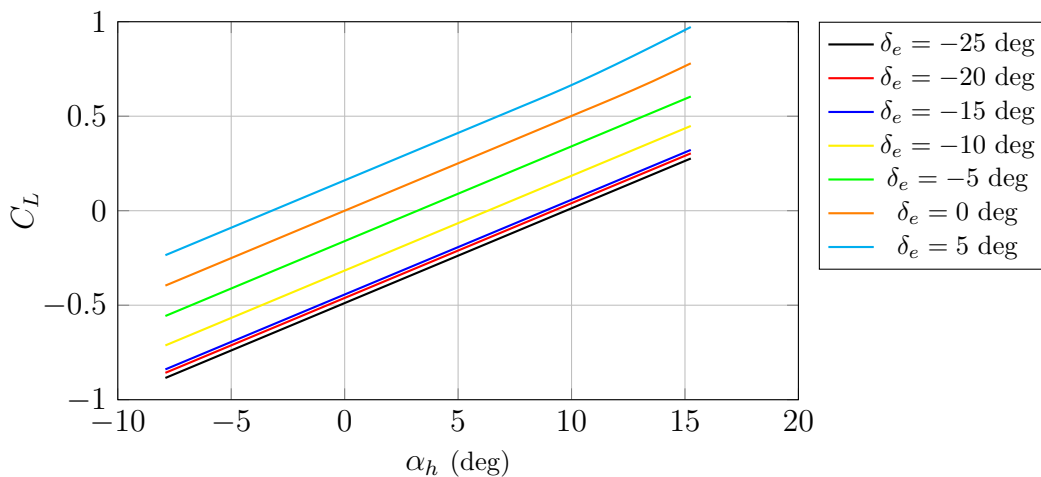


Figure 5.17: *IRON* Loop 1 aerodynamic assessment. Horizontal tail 3D lift coefficient for different angles of elevator deflection. Climb condition : $M = 0.288$, $Re = 1.3e7$.

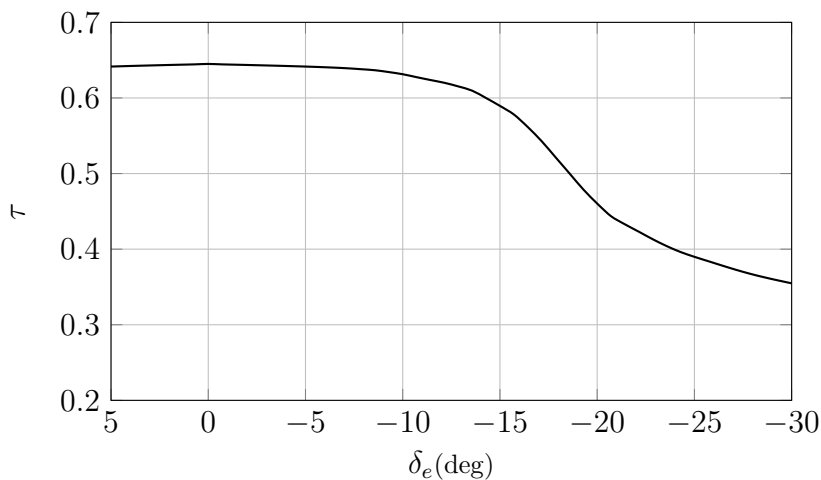


Figure 5.18: *IRON* Loop 1 aerodynamic assessment. Elevator effectiveness. Climb condition : $M = 0.288$, $Re = 1.3e7$.

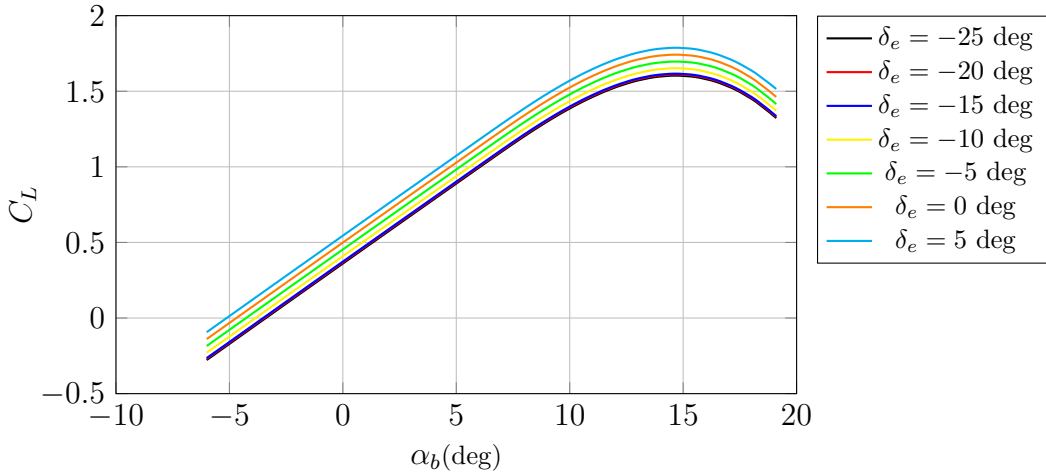


Figure 5.19: *IRON* Loop 1 aerodynamic assessment. Total lift coefficient for different angles of elevator deflection. Climb condition : $M = 0.288$, $Re = 1.3e7$.

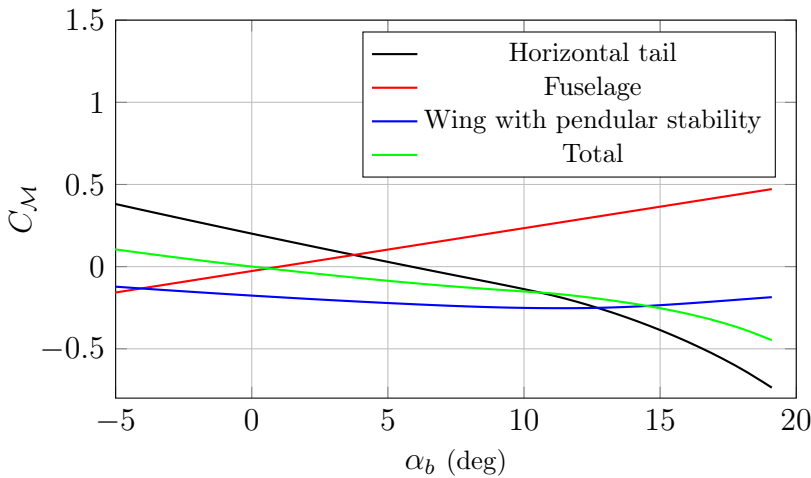


Figure 5.20: *IRON* Loop 1 aerodynamic assessment. Total moment coefficient breakdown with respect to the centre of gravity $CG = 15\%$ of MAC. Climb condition : $M = 0.288$, $Re = 1.3e7$.

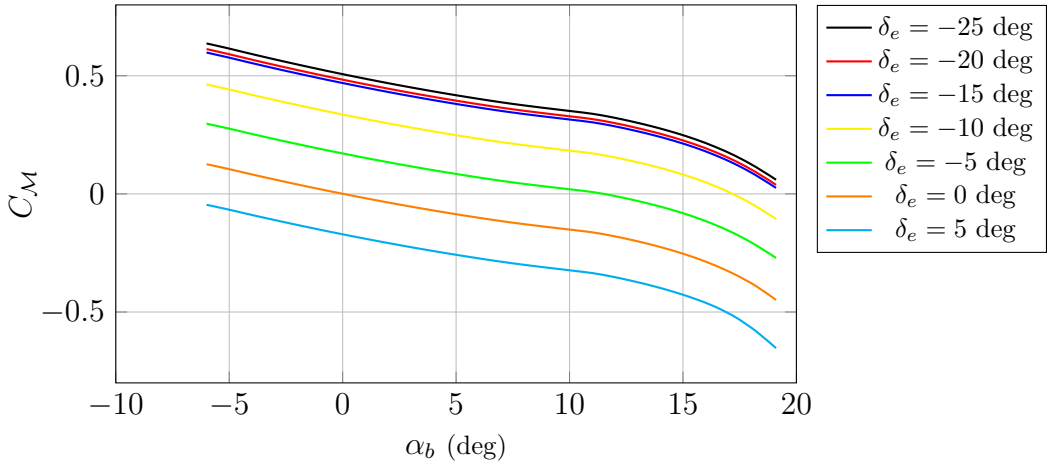


Figure 5.21: *IRON* Loop 1 aerodynamic assessment. Total moment coefficient with respect to the centre of gravity $CG = 15\%$ of MAC, for different angles of elevator deflection. Climb condition : $M = 0.288$, $Re = 1.3e7$.

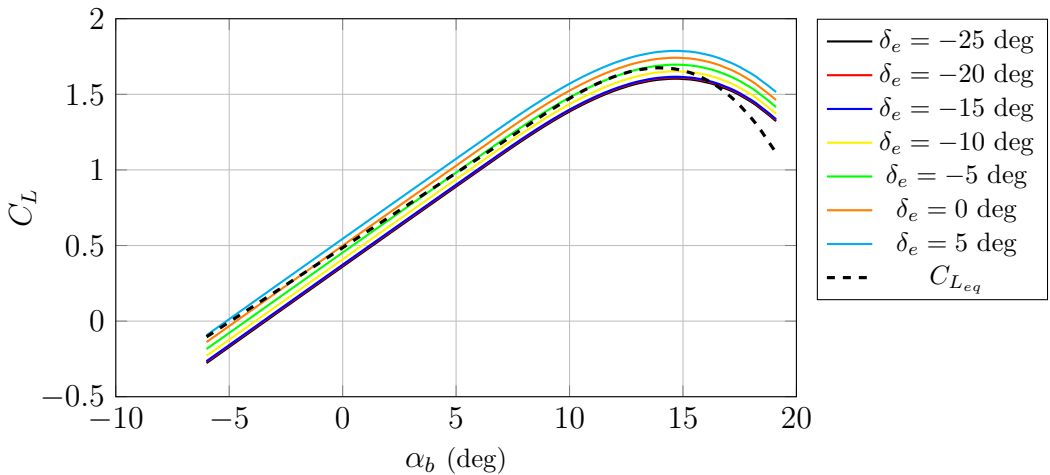


Figure 5.22: *IRON* Loop 1 aerodynamic assessment. Total equilibrium lift coefficient calculated for $CG = 15\%$ MAC. Climb condition : $M = 0.288$, $Re = 1.3e7$.

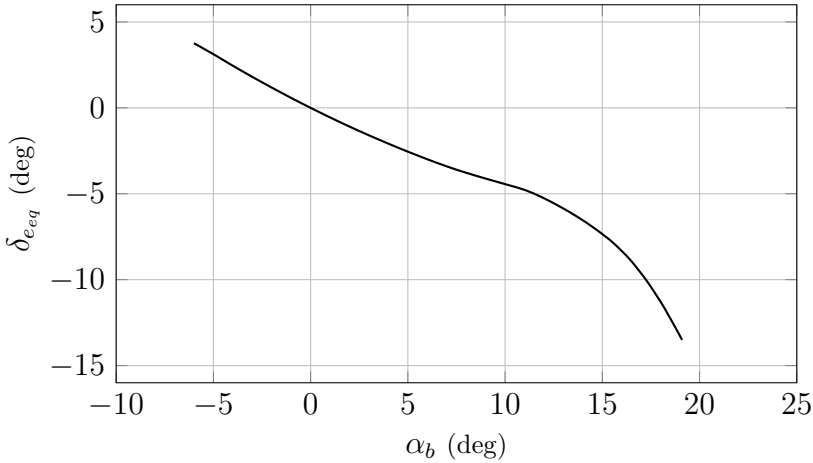


Figure 5.23: *IRON* Loop 1 aerodynamic assessment. Angle of equilibrium of elevator deflection calculated for CG = 15% MAC. Climb condition : M = 0.288, Re = 1.3e7.

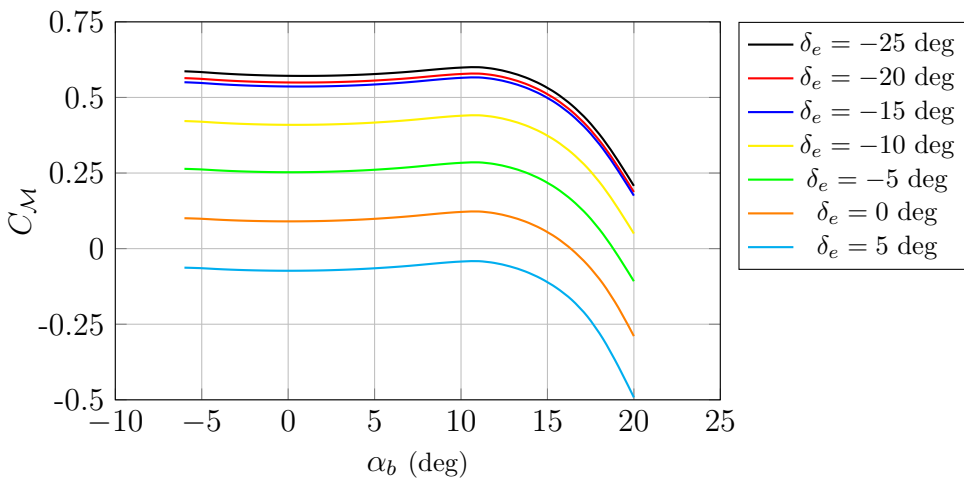


Figure 5.24: *IRON* Loop 1 aerodynamic assessment. Total moment coefficient with respect to the centre of gravity CG = 33% MAC , for different angles of elevator deflection . Climb condition : M = 0.288, Re = 1.3e7.

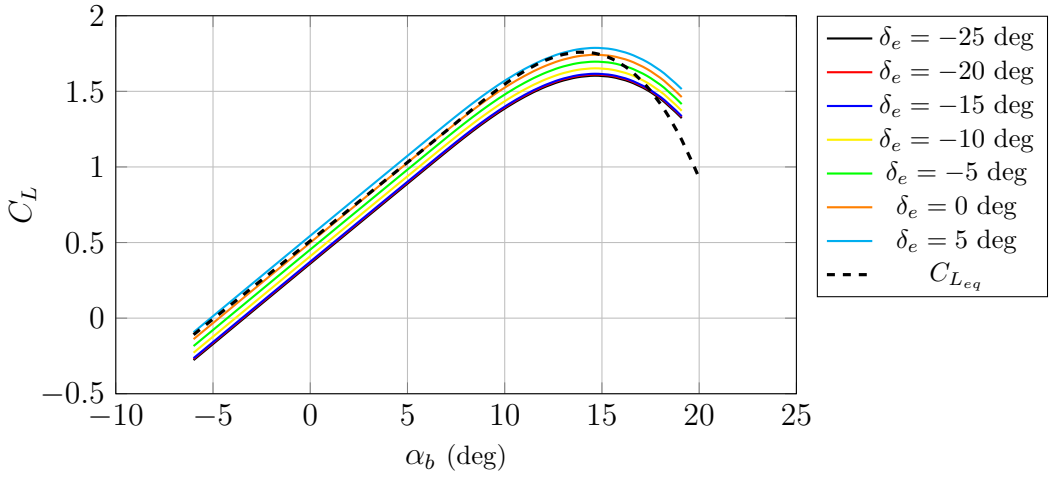


Figure 5.25: *IRON* Loop 1 aerodynamic assessment. Total equilibrium lift coefficient calculated for $CG = 33\%$ MAC. Climb condition : $M = 0.288$, $Re = 1.3e7$.

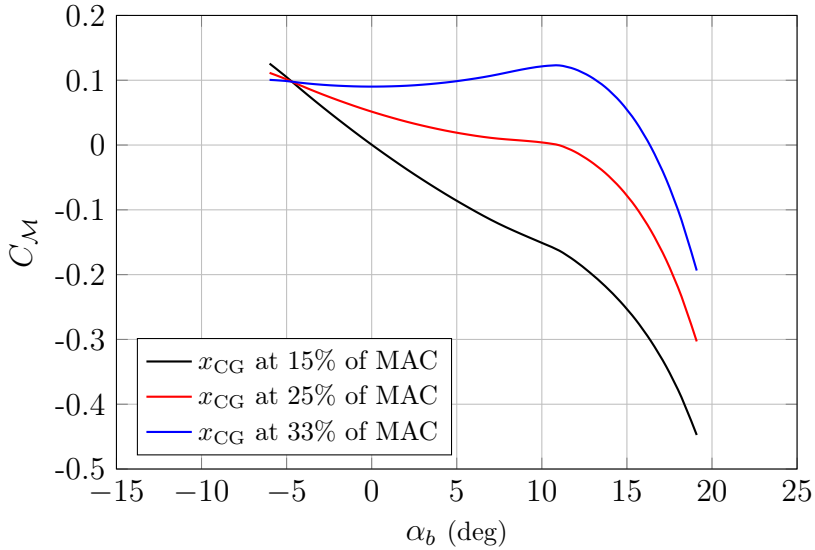


Figure 5.26: *IRON* Loop 1 aerodynamic assessment. Total moment coefficient with respect to the centre of gravity. Climb condition : $M = 0.288$, $Re = 1.3e7$.

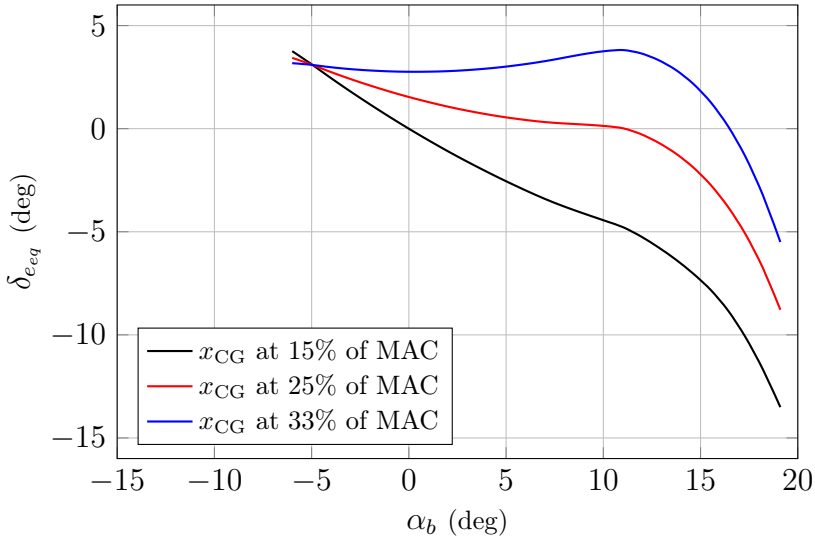


Figure 5.27: *IRON* Loop 1 aerodynamic assessment. Angle of equilibrium of elevator deflection calculated with respect to the centre of gravity. Climb condition : $M = 0.288$, $Re = 1.3e7$.

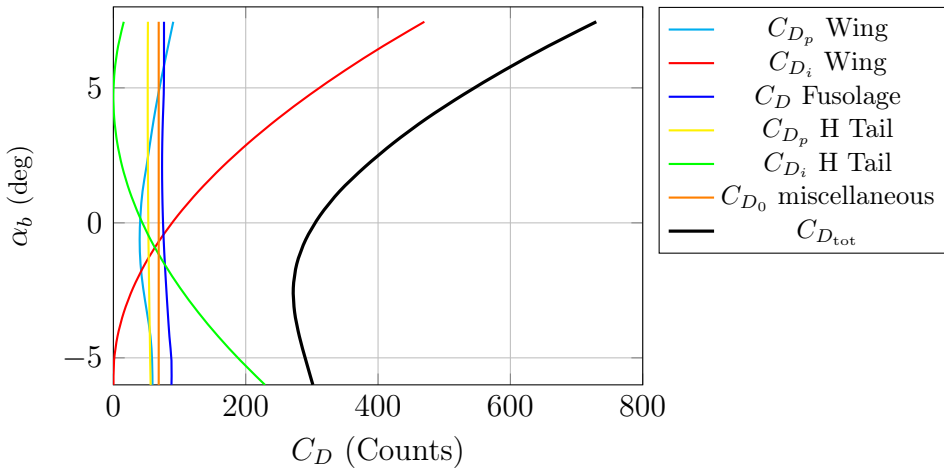


Figure 5.28: *IRON* Loop 1 aerodynamic assessment. Aircraft polar breakdown. Climb condition : $M = 0.288$, $Re = 1.3e7$.

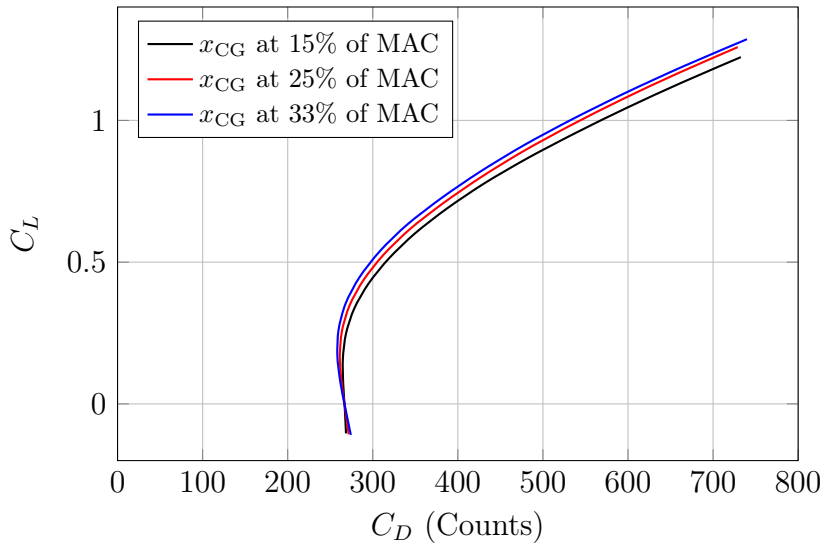


Figure 5.29: *IRON* Loop 1 aerodynamic assessment. Equilibrium polar curve calculated at different centre of gravity location. Climb condition : $M = 0.288$, $Re = 1.3e7$.

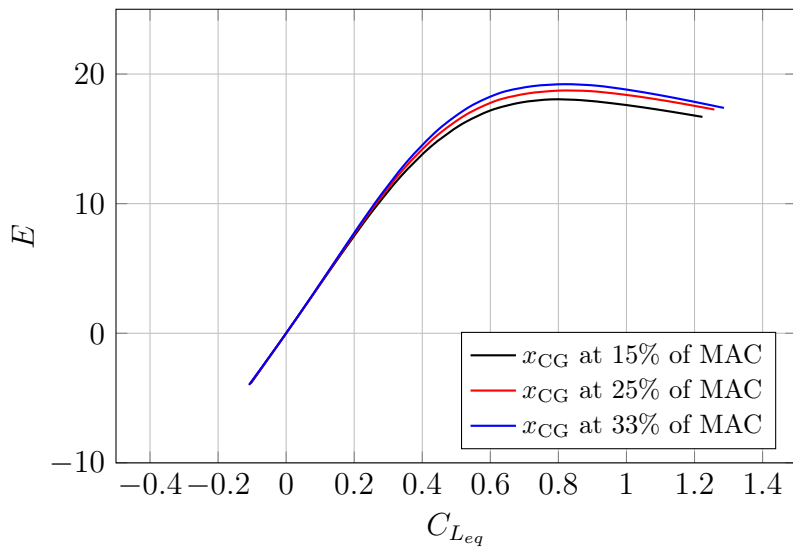


Figure 5.30: *IRON* Loop 1 aerodynamic assessment. Efficiency curve calculated at different centre of gravity location. Climb condition : $M = 0.288$, $Re = 1.3e7$.

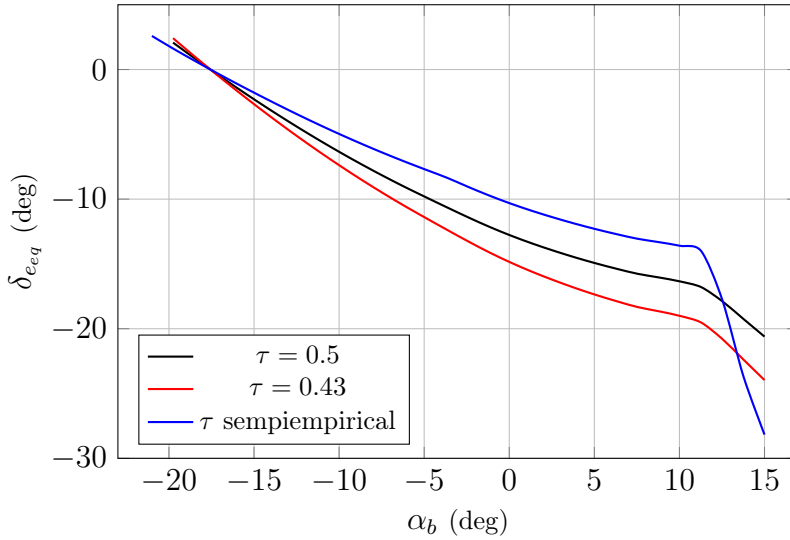


Figure 5.31: *IRON* Loop 1 aerodynamic assessment. Angle of equilibrium of elevator deflection calculated with respect to the centre of gravity CG=15% MAC. Landing condition : M = 0.154, Re = 1.1e7.

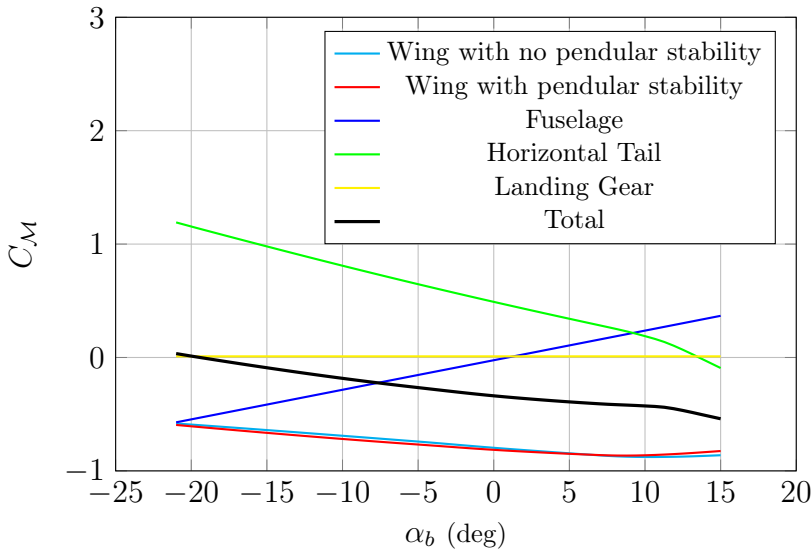


Figure 5.32: *IRON* Loop 1 aerodynamic assessment. Total moment coefficient breakdown with respect to the centre of gravity CG = 15%MAC. Landing condition : M = 0.154, Re = 1.1e7.

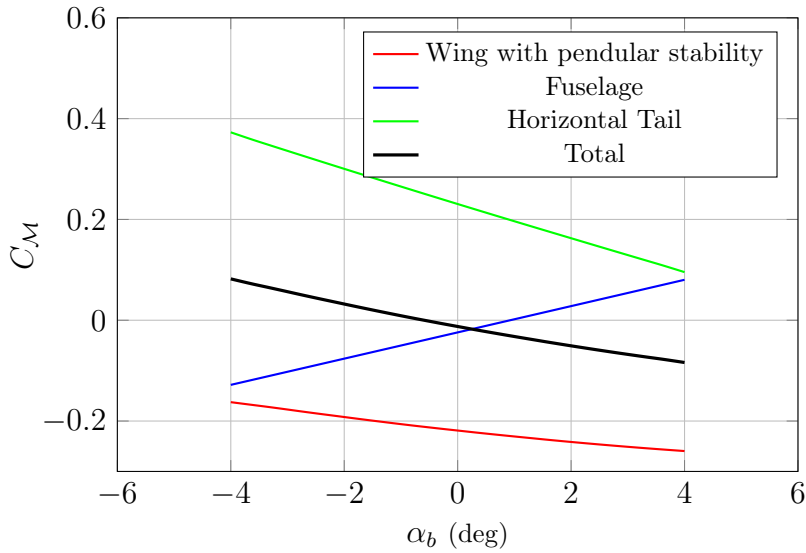


Figure 5.33: *IRON* Loop 1 aerodynamic assessment. Total moment coefficient breakdown with respect to the centre of gravity $CG = 15\%MAC$. Cruise condition : $M = 0.62$, $Re = 1.1e7$.

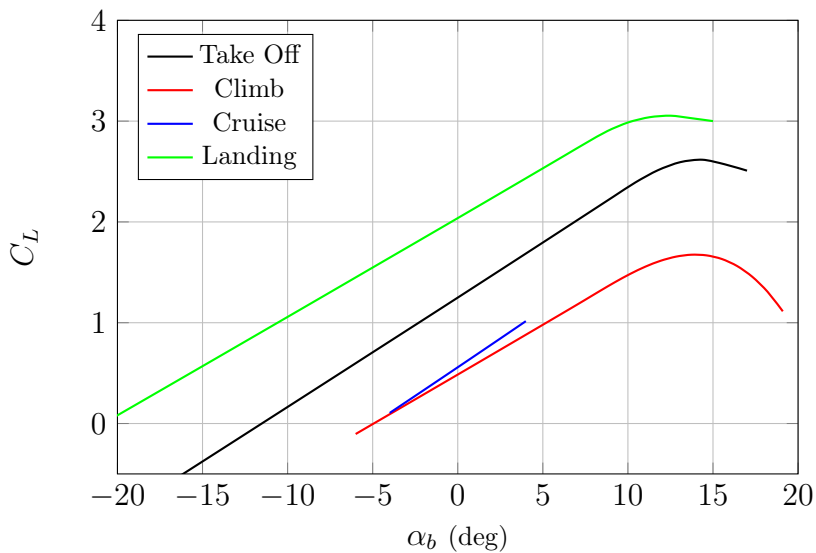


Figure 5.34: *IRON* Loop 1 aerodynamic assessment. Equilibrium lift coefficient curve in different condition calculated for $CG = 15\% MAC$. Operating conditions are summarized in Tab. 5.1.

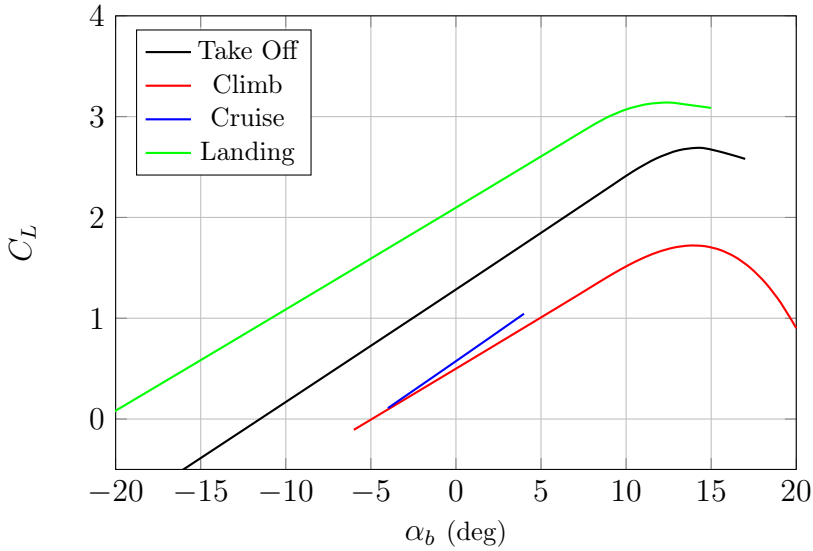


Figure 5.35: *IRON* Loop 1 aerodynamic assessment. Equilibrium lift coefficient curve in different condition calculated for $CG = 25\%$ MAC. Operating conditions are summarized in Tab. 5.1.

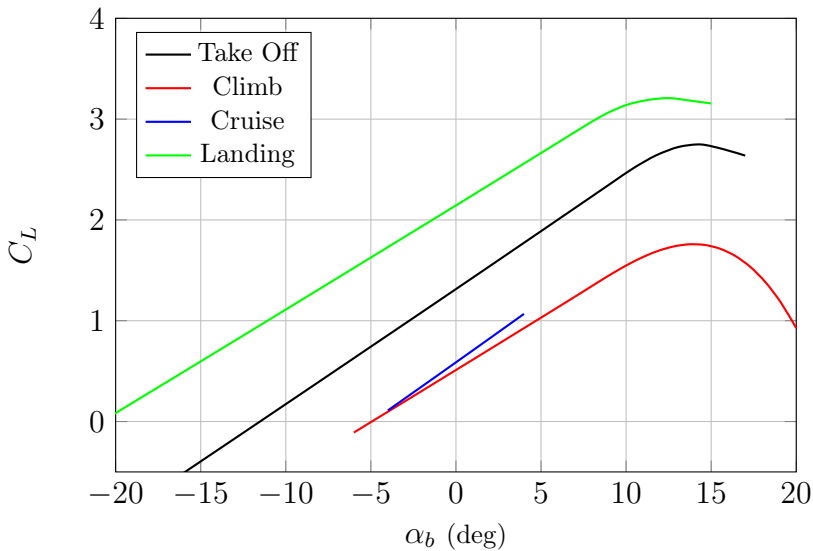


Figure 5.36: *IRON* Loop 1 aerodynamic assessment. Equilibrium lift coefficient curve in different condition calculated for $CG = 33\%$ MAC. Operating conditions are summarized in Tab. 5.1.

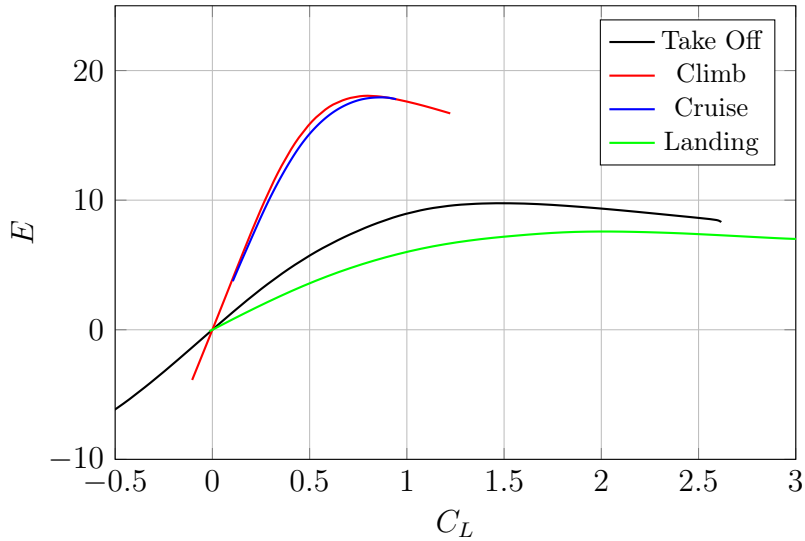


Figure 5.37: *IRON* Loop 1 aerodynamic assessment. Efficiency curve in different condition calculated for $CG = 15\%$ MAC. Operating conditions are summarized in Tab. 5.1.

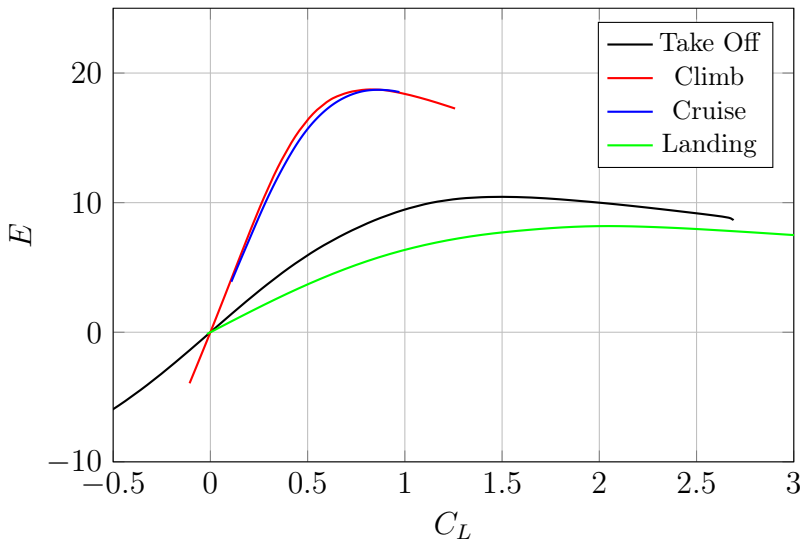


Figure 5.38: *IRON* Loop 1 aerodynamic assessment. Efficiency curve in different condition calculated for $CG = 25\%$ MAC. Operating conditions are summarized in Tab. 5.1.

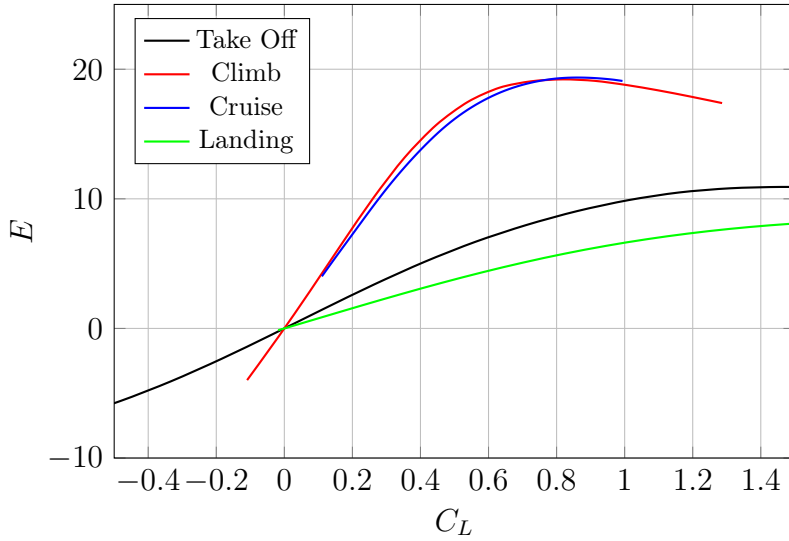


Figure 5.39: *IRON* Loop 1 aerodynamic assessment. Efficiency curve in different condition calculated for CG = 33% MAC. Operating conditions are summarized in Tab. 5.1.

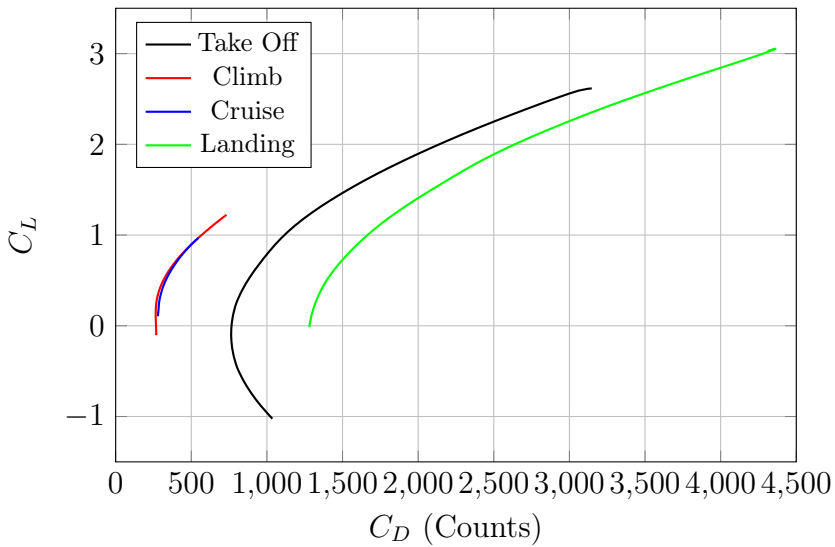


Figure 5.40: *IRON* Loop 1 aerodynamic assessment. Polar curve in different condition calculated for CG = 15% MAC. Operating conditions are summarized in Tab. 5.1.

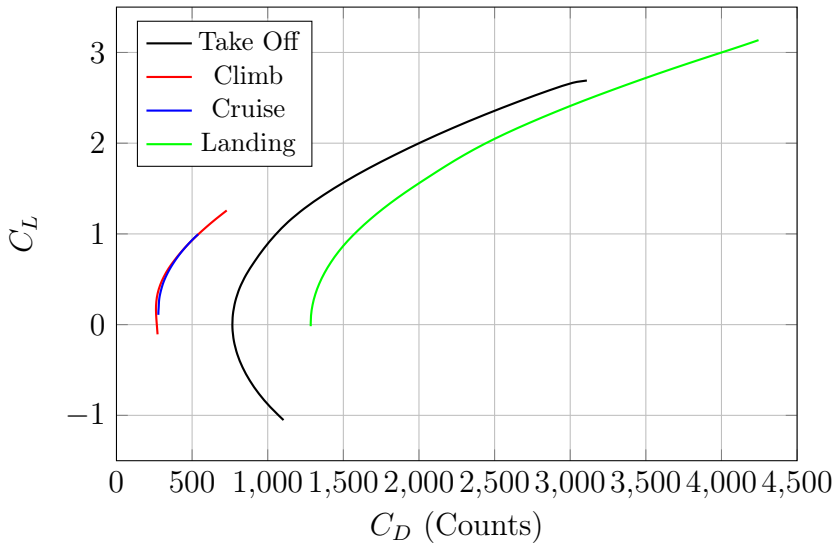


Figure 5.41: *IRON* Loop 1 aerodynamic assessment. Polar curve in different condition calculated for $CG = 25\%$ MAC. Operating conditions are summarized in Tab. 5.1.

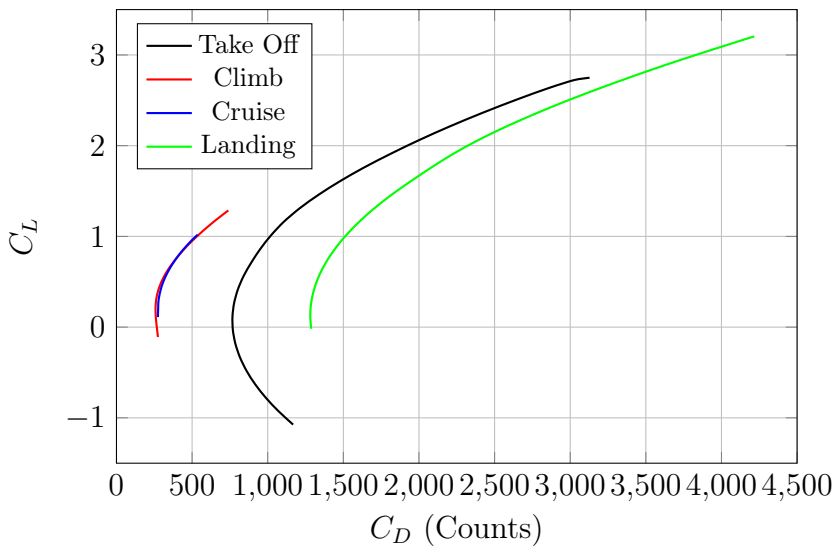


Figure 5.42: *IRON* Loop 1 aerodynamic assessment. Polar curve in different condition calculated for $CG = 33\%$ MAC. Operating conditions are summarized in Tab. 5.1.

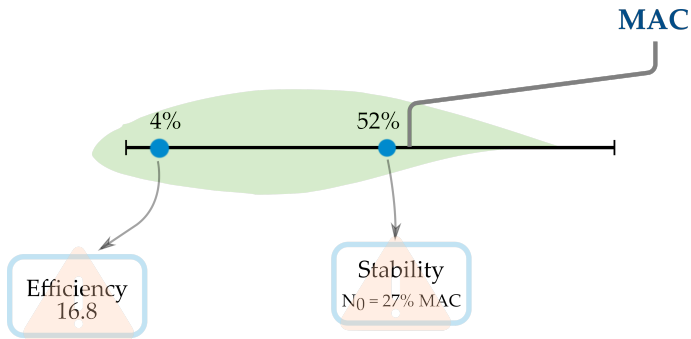


Figure 5.43: *IRON* Loop 1 centre of gravity excursion problems.

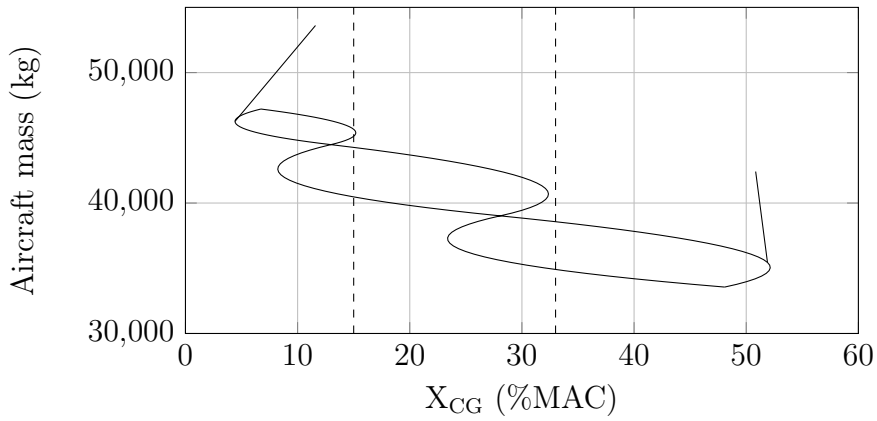


Figure 5.44: *IRON* boarding diagram - Loop 1 ending.

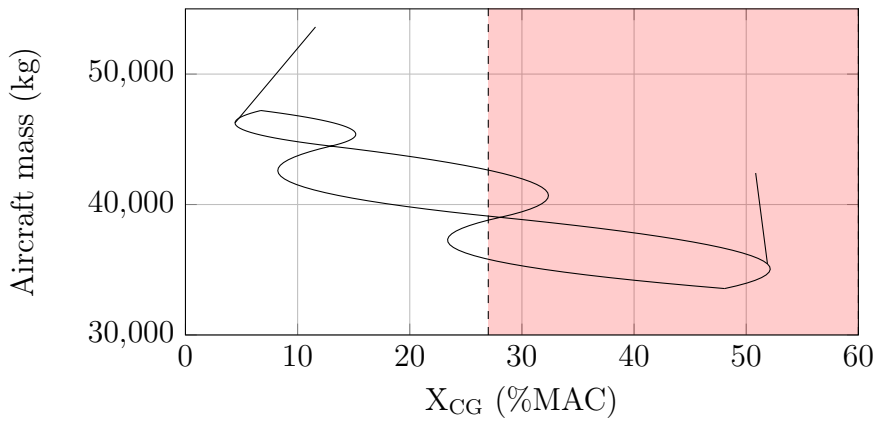


Figure 5.45: *IRON* boarding diagram limitations - Loop 1 ending.

solution for the innovative configuration. The starting point of these design activities has been an in-depth literature review of all possible design solutions. The main reference research work has been the one developed by NASA together with McDonnell Douglas Corporation in 1981 [41]. In this work, three possible high-speed turboprop/propfan configurations appeared to be feasible to compete with the reference aircraft platform assumed as the DC-9 Super 80.

1. Upper-wing mounted propfan.
2. T-Tail configuration with aft fuselage mounted propfan.
3. Horizontal tail mounted propfan.

The selection of those was made after a first qualitative comparison between many different possible layouts, followed by a multi-disciplinary quantitative analysis of the following three selected configurations. Results of preliminary research did prove that the initial *IRON* configuration of the first loop was indeed a good solution, however some adjustments were necessary. Following the path of the NASA work, three possible solutions were proposed to solve the first loop issues. To comply with the requirements, three different aircraft configurations, shown in Fig. 5.46, are here discussed:

1. **Configuration 1:** Preserve the original configuration and shift back the wing while increasing the horizontal tail area and its aspect ratio - with the minimum limitations on the centre of gravity shift.
2. **Configuration 2:** Limiting the increase on the horizontal tail - with major limitations on the centre of gravity shift.
3. **Configuration 3:** Change the configuration to a three-lifting surface layout - with three lifting surfaces and a minimum limitation of the centre of gravity shift.

All configurations have been designed following the same procedure: i) semi-empirical methodologies, implemented in *JPAD*, have been used to analyse a large number of configurations generated by varying several design parameters (wing position, wing area, wing sweep angle, horizontal tail area, horizontal tail aspect ratio, and so on); ii) results of

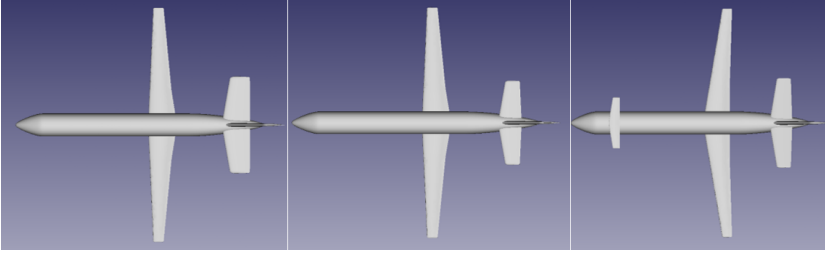


Figure 5.46: *IRON* configurations comparison before Loop 2 - Top views

those analyses have been used to build up response surfaces useful for an optimization process; iii) configuration optimization. The optimization process has been accomplished by means of the *MOEA* Framework which is a free and open source Java library for developing and experimenting with multi-objective evolutionary algorithms (*MOEAs*), and other general-purpose computational intelligence. Here the ϵ -*NSGA-II* and *OMOPSO* algorithms are used. ϵ -*NSGA-II* is an extension of *NSGA-II* that uses an ϵ -dominance archive and randomized restart to enhance search and find a diverse set of Pareto solutions. Full details of this algorithm are given in [48]. *OMOPSO* is a multi-objective particle swarm optimization algorithm that includes an ϵ -dominance archive to discover a diverse set of Pareto optimal solutions. *OMOPSO* was originally introduced in [81]. According to the chosen number of design parameters, more than 7000 different combinations (each combination represents an aircraft) have been generated and analysed to define the response surface on which perform the optimization process. The Pareto front, in this optimization problem is a multidimensional frontier, according to the chosen design parameters. Targets of the optimization process have been the cruise parameter $\frac{W}{E}$, the take-off and landing factors $\frac{W}{S_W * C_{L_{MAX}}}$. To ensure the aircraft stability, a static margin of 5% has been assigned as constraint. Fig. 5.48 shows an example of two objectives Pareto front for the optimization of the Configuration 1., considering the two parameters $\frac{W}{S_W * C_{L_{MAX}}}|_{land}$ and $\frac{W}{E}|_{cruise}$. All the major results are summarized in Tab. 5.2. To ensure the required stability, Configuration 1 is characterized by a very large horizontal tail area ($S_H = 56m^2$) about 51% of the wing area. This provides an increment of both the maximum take-off weight and induced drag which lead to the lowest cruise efficiency among the

	Loop 1	Config. 1	Config. 2	Config. 3
W_{TO} (kg)	54410	54976	54105	54849
Cruise efficiency	16.7	17.3	17.7	18.4
$C_{L_{MAX}} _{clean}$	1.53	1.70	1.70	1.91
$C_{L_{MAX}} _{TO}$	2.15	2.63	2.63	2.90
$C_{L_{MAX}} _{lan.}$	2.30	3.19	3.09	3.40
S_w (m ²)	105	103	105	98.6
Cruise Mach	0.61	0.63	0.64	0.66

Table 5.2: *IRON* configurations comparison.

three solutions. To avoid a large horizontal tail area, a limitation on the centre of gravity range has been imposed leading to the Configuration 2. This aircraft must operate within the imposed c.g. variation (11% to 40% MAC). This allows to reach a higher cruise efficiency with respect to the first configuration ($E = 17.7$), a lower maximum take-off weight and a slightly reduction of maximum lift coefficient in landing. The first two configurations do not meet the required cruise aerodynamic efficiency. Configuration 3 provides a three lifting surfaces layout. In this case the wing area is reduced, and its position is back shifted. This latter leads to a c.g. range that lies forward the mean aerodynamic chord leading edge. For this aircraft, in cruise condition, it is possible to trim the aircraft with a reduced download on the horizontal tail, allowing a lower trim drag. This provides a higher cruise efficiency (18.4 with respect to 17.7 of the Configuration 2). Moreover, the maximum achievable lift coefficients are increased thanks to the canard surface.

Temporary speaking, the definition of the three-lifting surfaces model (Configuration 3) came later during the preliminary design activities of the second design loop of the *IRON* project. In the meanwhile, Configuration 2 was used as reference model to better understand possible operative advantages coming from the use of such an innovative turbo-prop configuration. The conference paper presented at the 2018 AIAA Aviation Technology, Integration, and Operations Conference [38], provides a detailed review of the analyses carried out on the Configuration 2 aircraft model. Fig. 5.47 shows the comparison between the aerodynamic efficiency at several flight conditions for all the three considered configurations at max aft c.g. position. As it can be appreciated, the solution

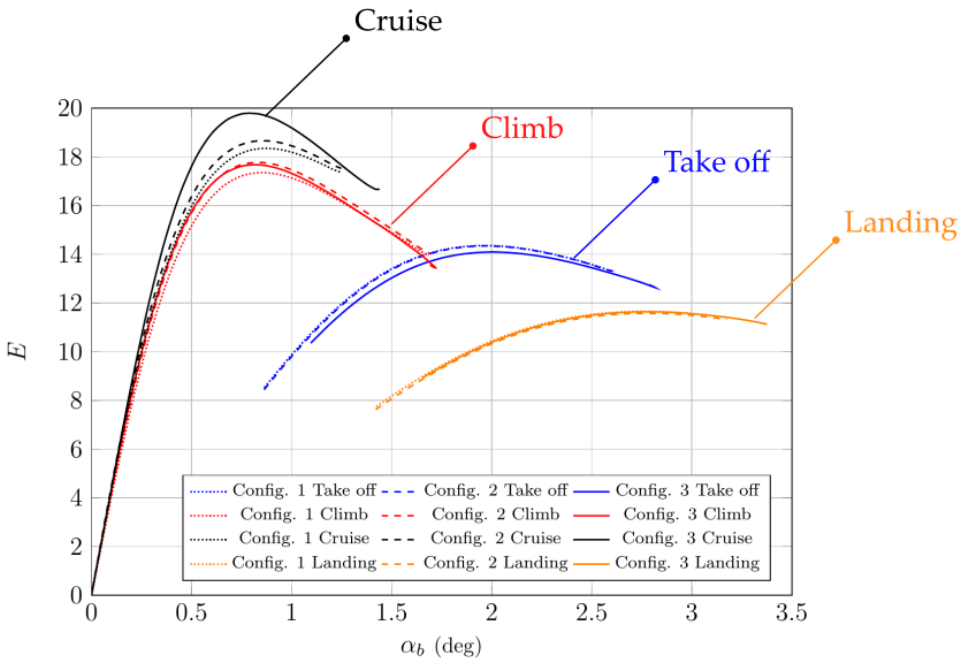


Figure 5.47: *IRON* efficiency curves comparison for the three different configuration.

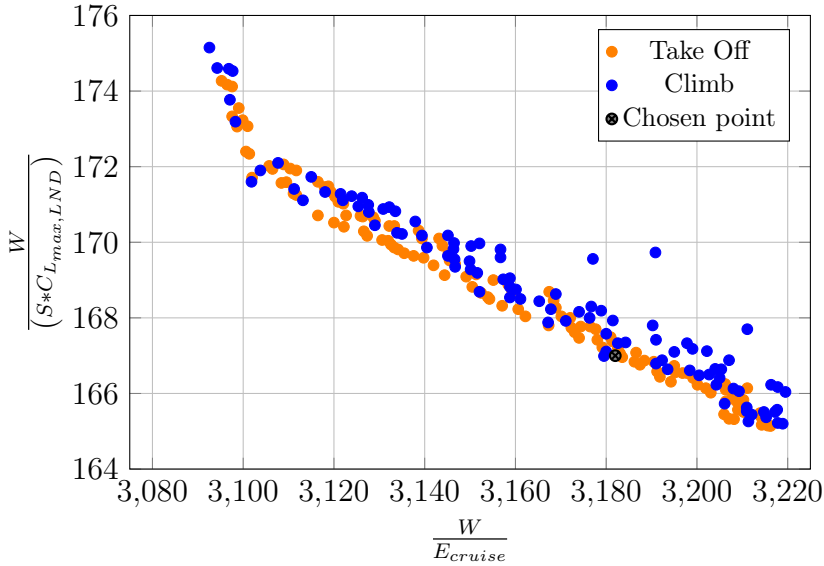


Figure 5.48: Example of Pareto front for the optimization of Configuration 1 - *IRON* Loop 2.

with the canard is the one that gives the maximum cruise efficiency being the only one configuration above the required value of 18 at $C_L = 0.61$. These considerations, together with preliminary results coming from the comparison of the three Loop 2 configurations (see Tab. 5.2), led to the selection of the three-lifting surfaces as the reference aircraft to be used for loop 2 in-depth analyses.

5.4 IRON LOOP2 aerodynamic assessment

After the MDO process, the three lifting surfaces configuration has proven to be the most promising one in terms of aerodynamics, boarding diagram limitations with a slightly increment of the maximum take-off weight with respect to the Loop 1 baseline. Main data are summarized in Tab.1.5. The aerodynamic design activities have been focused on the following topics:

- Wing airfoil design and optimization

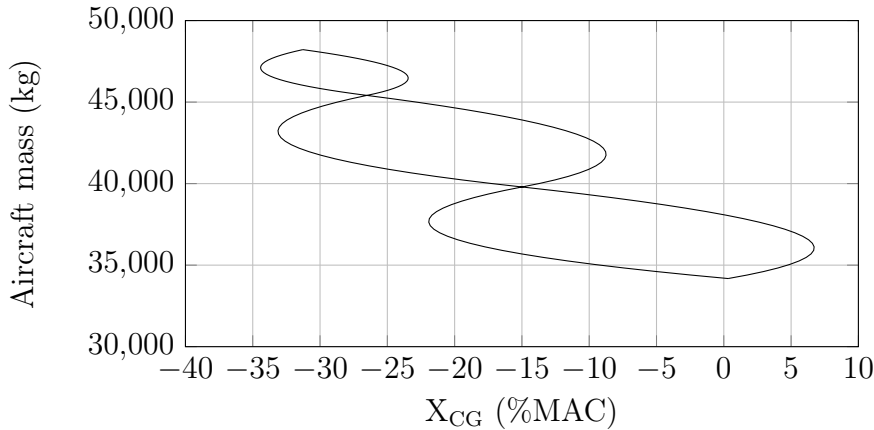


Figure 5.49: *IRON* boarding diagram - Loop 2 configuration.

- Winglet design and analysis
- High lift devices design and analysis
- Complete aircraft maximum lift coefficient analysis in different conditions
- Wing-Body laminar flow effects prediction
- Longitudinal stability and control analysis
- Complete aircraft trimmed drag polar curves in different conditions

Starting from the optimum design variables coming from the optimization, all geometrical parameters of this configuration have been fixed. These have been used to assess a class II weight estimation from [85] and Leonardo assumptions. Then, starting from the Operating Empty Weight centre of gravity position and according to the supposed cabin layout, the boarding diagram, shown in Fig. 5.49, has been estimated.

Concerning the aerodynamics, all lifting surfaces characteristics have been derived by integrating the 2D airfoil data coming from Loop 1 design. Fuselage aerodynamics has been evaluated by means dedicated *CFD* analyses (from Loop 1 activities). Aircraft trimmed drag polar curves have been calculated assuming that the longitudinal equilibrium is granted

only by the horizontal tail plane, while the canard (provided with its own high lift device) is used to augment the aircraft maximum lift capabilities, especially in take-off and landing configurations. The baseline airfoil, developed in Loop 1, has been used as reference to enhance the aircraft cruise performances, just acting on wing airfoil shape, without reducing to much the high-lift characteristics of the baseline wing section. In order to reach the design goals an optimization process has made using multiple objective genetic algorithm (GA-ME, Genetic Algorithm for Multi-Element airfoil design [92]). By changing the aircraft configuration with respect to the one assigned for the first loop of design, second loop aerodynamic design activities have involved the re-design and optimization not only of the above mentioned the wing airfoils, but also of the wing natural laminar flow assessment and the re-design of the high-lift devices, also including a slot flap on the canard surface.

5.4.1 Nacelle positioning

The longitudinal static stability of the new IRON configuration is one of the main aspects which must be deepened to assure the feasibility of the three-lifting surfaces model. The evaluation of aircraft aerodynamics during the preliminary design of Loop 1 aircraft configuration has been assessed by low-fidelity tools, based on coupling two-dimensional airfoil data with semi-empirical methods as suggested by [85] [22]. During Loop 2, medium and high-fidelity analyses have been carried out coupled with wind tunnel test performed in University of study of Naples Federico II to check the results of lower fidelity methods. Several issues about aircraft stability due to canard wake and engine nacelle position have been observed. As concern longitudinal stability, the effect of the engine nacelles mounted under the horizontal tail is detrimental, as analysed in [88]. Low-fidelity calculations were not showing these effects and only after several *CFD* analyses it has been decided to investigate other possible positions for the engine on the horizontal tailplane. Wind tunnel tests performed on the scaled model, confirmed the reduction of lift capabilities of the horizontal tailplane due to the nacelle interference showing a reduction in the stability derivative of about 20%, as shown in Fig. 5.50.

To reduce the aerodynamic interference of the engine installation on the tail, a parametric study on nacelle position has been carried out.

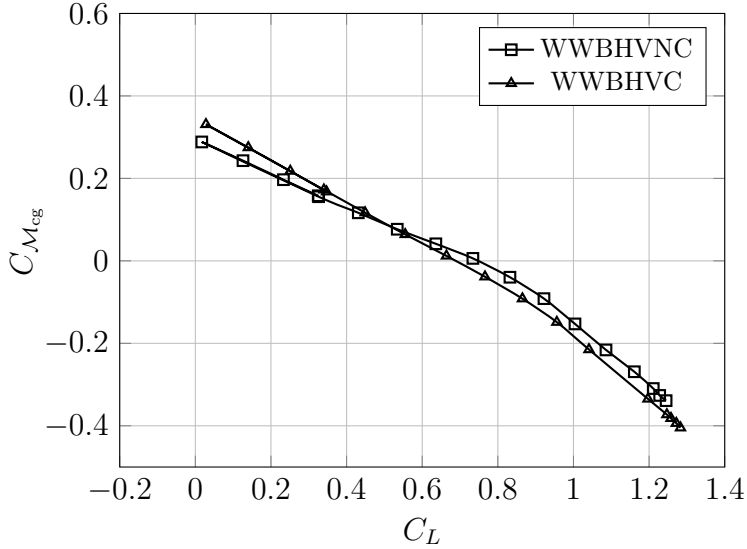


Figure 5.50: *IRON* Loop2, Wind tunnel test results. Nacelle effect on longitudinal stability, $Re=315000$

New configurations have been obtained by varying the pylon length (to distance the engine from the plane) and the spanwise position in Fig. 5.51. In the last case, the engine has been positioned at tip of the tail. The configurations have been analysed through *CFD* analyses, but to reduce the computational cost of the simulations, the tailplanes with engine have been investigated in isolated configuration. Among them, the most promising configurations in terms of longitudinal stability, are those of Fig. 5.51c and Fig. 5.51d. These two have been included in the complete aircraft *CFD* simulation. These latter show that the only stable configuration has the engine nacelle at the tip of horizontal tailplane. This configuration (Fig. 5.51d) is the one chosen for the Loop 2 revised one, shown in Fig. 5.52, where differences with the former configuration are highlighted: the nacelle have been placed at horizontal tail tip and the dihedral angle of this lifting surface has changed.

However, it is necessary say that the more detrimental effect on stability is caused by the canard wake on the tail. The Loop 2 nacelle positioning, make unstable a neutrally stable configuration, as shown in Fig. 5.53

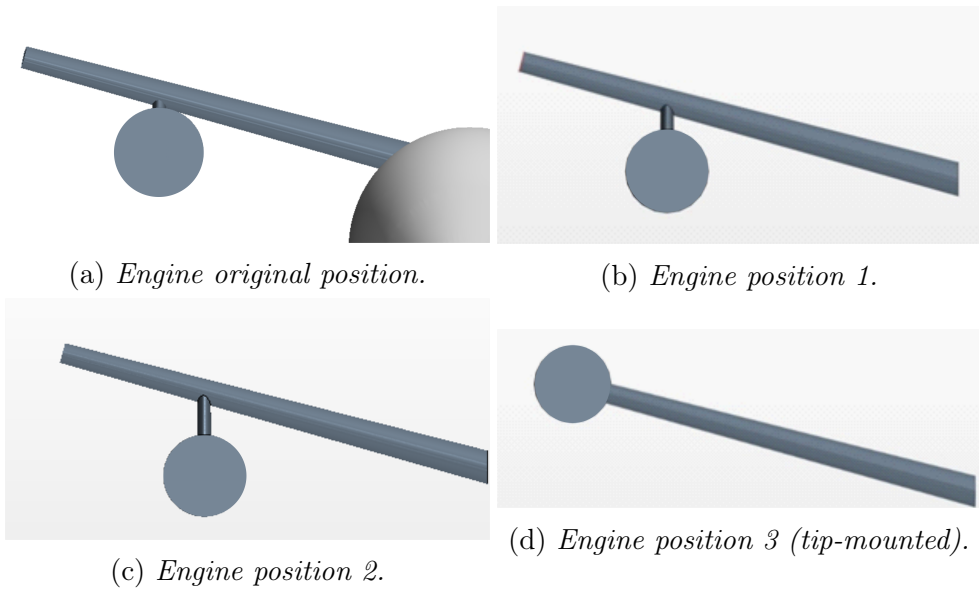


Figure 5.51: *IRON* Loop2, alternative engine positions.

5.4.2 Longitudinal static stability assessment

Once the configuration has been defined, the *DAF* research group had in charge the aerodynamic assessment of the proposed concept, in particular of the longitudinal stability of the three-lifting surface aircraft for both high-lift and clean conditions. Different operating conditions have been investigated, at different centre of gravity position. The analyses are addressed to check if the horizontal tail plane is properly sized to grant a minimum Static Stability Margin of about 5% at both climb and cruise flight speeds. Two different approaches have been used to carry out the aerodynamic assessment of the aircraft: a three-dimensional panel code method and *CFD-RANS* solver. Panel code methodology is very useful to estimate in fast and reliable enough way downwash gradients of a three lifting surfaces configuration, allowing a better design of wings behind a canard, while the *RANS* approach has been useful to validate panel code results, with respect to high-fidelity numerical simulations, and to perform a fine analysis of the maximum lift capabilities. The downwash behind a lifting surface and methods to account for effects on an aft lifting surfaces, lying behind the first one, are presented in several references.

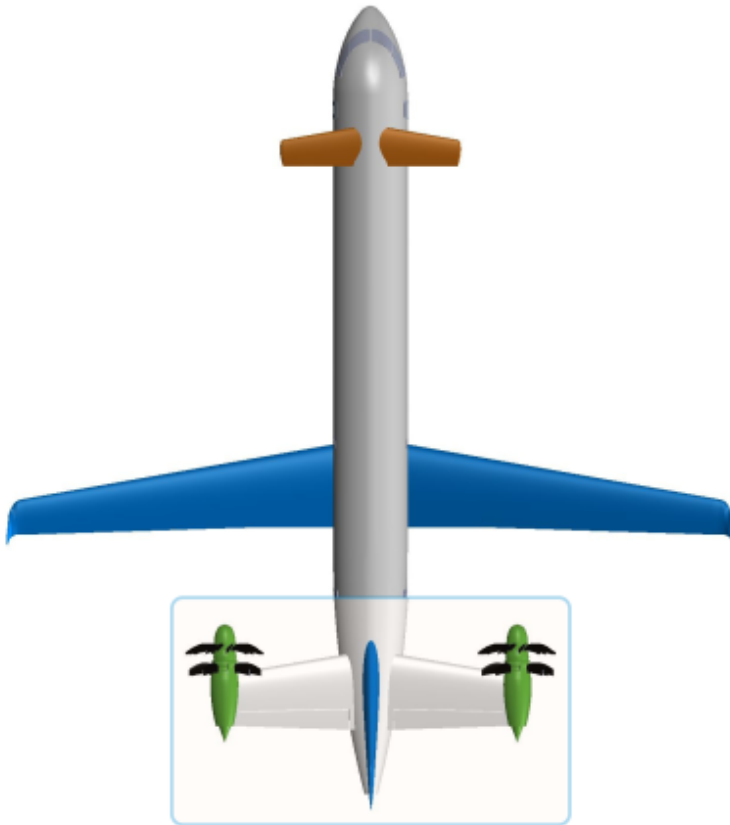


Figure 5.52: *IRON* Loop2 revised configuration.

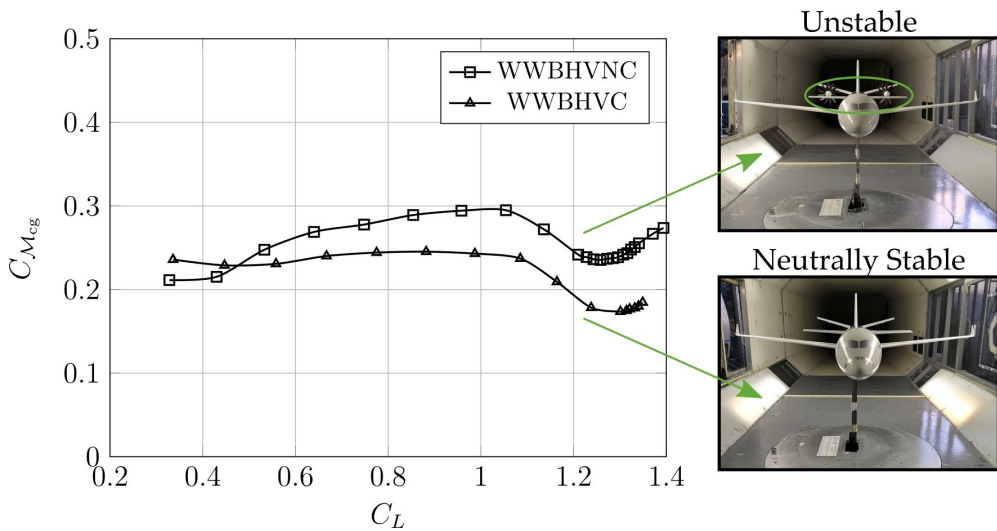


Figure 5.53: *IRON Loop2*, Wind tunnel test results. Nacelle effect on longitudinal stability with canard, $Re = 315000$.

These methods include linear approaches (such as Silverstein [82], [83]) and non-linear ones ([84]). However, these references emphasize the case where an aft tail has a much smaller span than the main wing. The influence of the wing on the tail is calculated by first estimating the downwash gradient in the plane of symmetry at the longitudinal and vertical location of the tail, and then correcting for the spanwise variation across the tail. However, the data in literature are limited to a span ratio, $\frac{b_h}{b_w} = 0.4$, and where the downwash gradient spanwise variation is relatively small, leading to a unique value for downwash derivative on a conventional tail plane. In case of a canard configuration, where the forward wing has a smaller span than the aft wing, previous methods do not properly work and the spanwise variation of downwash gradient becomes quite significant. A first attempt to provide a method evaluating downwash for canard configuration is proposed by Philips [69] [68]. He evaluated downwash in the plane of symmetry for an elliptical loaded wing and then calculated the integral downwash gradient effect. This method approximated a generic wing as an elliptical one and does not account for real wing geometrical parameters. Moreover, Philips' method did not account for wing span loading distribution, avoiding any design indication for lifting sur-

faces twist angle distribution. To overcome limitations of the previous methodologies, in the *IRON* project Loop 2, a three-dimensional panel code method has been used at preliminary stage to well understand downwash behaviour and improve wing lift capabilities by modifying the wing twist distribution. Once the lifting surfaces geometries have been well assessed, *CFD-RANS* analyses have been performed: firstly, the panel code aerodynamic analysis have been compared with a *CFD-RANS* calculation, then the maximum achievable lift coefficient has been computed for the Wing-Body (WWB), the Wing-Body-Canard (WWBC) and Wing-Body-Horizontal tail-Canard (WWBHC). The aerodynamic assessment of the aircraft longitudinal characteristics has highlighted some criticalities dealing with the interference effects of a three-lifting surface aircraft at full flap conditions [77]. Several *CFD-RANS* simulations have been performed on the wing-body and wing-body plus canard configuration to assess the effects of the canard wake at full flap condition ($\delta_{f_w} = 35^\circ$ and $\delta_{f_c} = 25^\circ$). These analyses have highlighted that the canard, when its flaps are deployed, introduces a strong downwash on the main wing leading to a lift loss in the inner wing sections as shown by the wing lift distribution illustrated in Fig.5.54. On the other hand, the canard tip vortex introduces an upwash on the outer wing sections leading to a premature stall at the wing tip region, these effects are highlighted by the wing loading distribution shown in Fig. 5.55.

Further aerodynamic and stability analyses have been performed in wind tunnel. Tests have been conducted on several aircraft configurations exploiting the modularity of the model. The main test campaign objective is to estimate the aerodynamic effects of canard on wing and tail plane. The neutral point is shifted from 50% of the mac to the 39% of the MAC (see Tab. 5.3). The value in Tab. 5.3 needs to be analysed more in detail. It is important to highlight, in fact, that the SSM for WWBVHN configuration, that seems to be stable, is referred to a centre of gravity location of the Loop2, i.e with the canard itself. This means that the canard has been necessary in order to shift afterwards the centre of gravity position, by shifting component, ad to reach the required values for $C_{L_{MAX}}$ and efficiency. This means that, as mentioned before, the configuration without canard is not stable, and positive SSM in Tab. 5.3 are in any case referred to the CG position with canard.

As concerns the configuration with canard, the reduction of longitu-

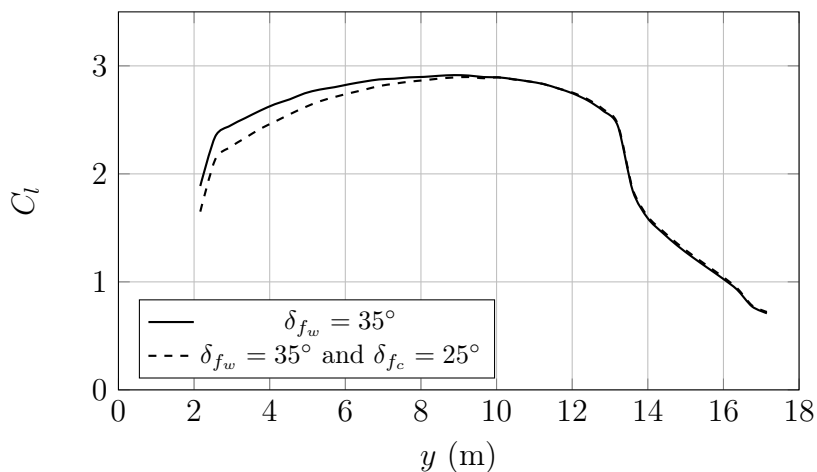


Figure 5.54: *IRON* Loop 2 aerodynamic assessment. Wing lift characteristics: comparison between wing lift distribution of canard on and canard off at $AoA = 0^\circ$. *CFD-RANS* analysis, $\delta_{f_w} = 35^\circ$ and $\delta_{f_c} = 25^\circ$.

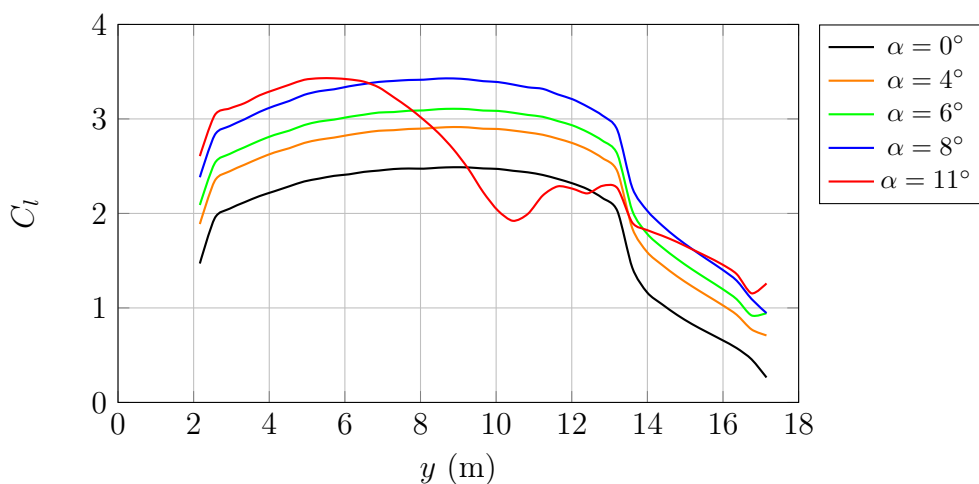


Figure 5.55: *IRON* Loop 2 aerodynamic assessment, WWB configuration. Wing lift distribution till the stall occurrence, *CFD-RANS* analysis, $\delta_{f_w} = 35^\circ$.

Configuration	Parameter	Value	SSM (positive if stable)
WB	$C_{L\alpha}$	0.0800	
WWB	$C_{L\alpha}$	0.0870	
WWBVH	$C_{M_{C_L}}$	-0.502	50%
WWBVHN	$C_{M_{C_L}}$	-0.393	39%
WWBVHNC	$C_{M_{C_L}}$	0.065	-6.5%

Table 5.3: *IRON* Loop 2 wind tunnel test. Aircraft configurations and relevant aerodynamic derivative.

dinal stability is dramatic. As matter of fact, the configuration becomes unstable as shown in Fig. 5.56. More in detail, the stability derivative value assumes a positive value which means the neutral point is shifted ahead of the MAC (6.5%).

In light of the above, the wind tunnel tests have been highlighted the longitudinal instability of the aircraft configuration. Nacelle positioning and canard are the main causes. At full flap condition, the canard wake has also a detrimental effect on the aircraft longitudinal stability. At low angles of attack, from 0° up to 6° , the canard wake moves from the lower to the upper side of the horizontal tail with a consequence reduction in stability. This interference effect was expected due to the reduced vertical stagger between the tail plane and the canard; however, it was supposed to be not so critical (considering the preliminary results carried out with low/medium fidelity tools like semi-empirical approaches, panel code approach and vortex lattice methods).

At the end of Loop 2, different components have to be re-designed in order to overcome the above mentioned issues. To mitigate the loss of load along wing semispan, a design study has been performed by varying the wing twist distribution in order to compensate both the lack and the excess of lift in the inner and outer wing region respectively. The wing twist has been changed accordingly to the estimation of the deficit in wing local angle of attack. This latter has been derived by comparing the wing lift distribution of the canard on and canard off configurations. The beneficial effects of this design study are highlighted in Fig. 5.57, where the lift curves of the wing-body plus canard configuration with the initial and the optimized twist distributions are illustrated. Thanks to the wing twist optimization, it has been possible to increase the stall angle

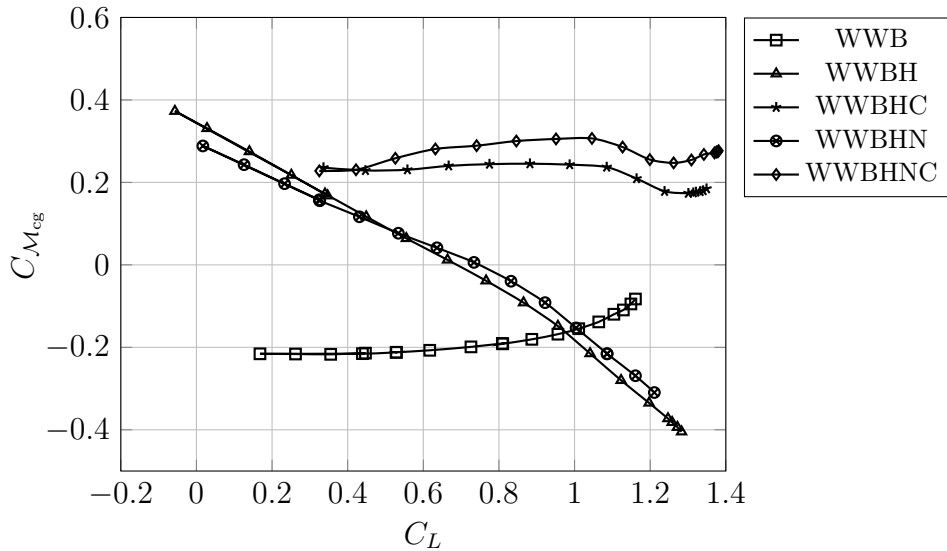


Figure 5.56: *IRON* Loop 2 configuration, wind tunnel tests. Moment coefficient curve for different configurations, $Re=315000$

of about 5° gaining a delta in $C_{L_{MAX}}$ of about 0.4. It leads to an equilibrium maximum lift coefficient of $C_{L_{MAX}} = 3.23$, shown in Fig. 5.58. The analysis including also the horizontal tail-plane has highlighted a longitudinal stability reduction at low angle of attack when the canard flap is deployed. This latter has compelled to shift up the canard by introducing a canard/fuselage fairing and to reduce the canard flap deflected for landing condition only. As far as the issue concerning the canard wake on horizontal tail at low angles of attack, that has been mitigated by shifting up the canard surface of about 0.3m along the vertical axis, by adding a fairing to reduce the interference effects of the canard-fuselage junction. The flap angle reduction has slightly affected the maximum achievable lift coefficient but has helped to mitigate the stability issue at low angles of attack. These considerations led to a new *IRON* configuration, known as Loop 2 revised.

To increase the cruise aerodynamic efficiency, an additional technology, in the form of riblets, has been considered to reduce the aircraft drag [71] [54] [10] [11]. As explained in [71], riblets are small surface protrusions aligned with the direction of flow, which confer an anisotropic

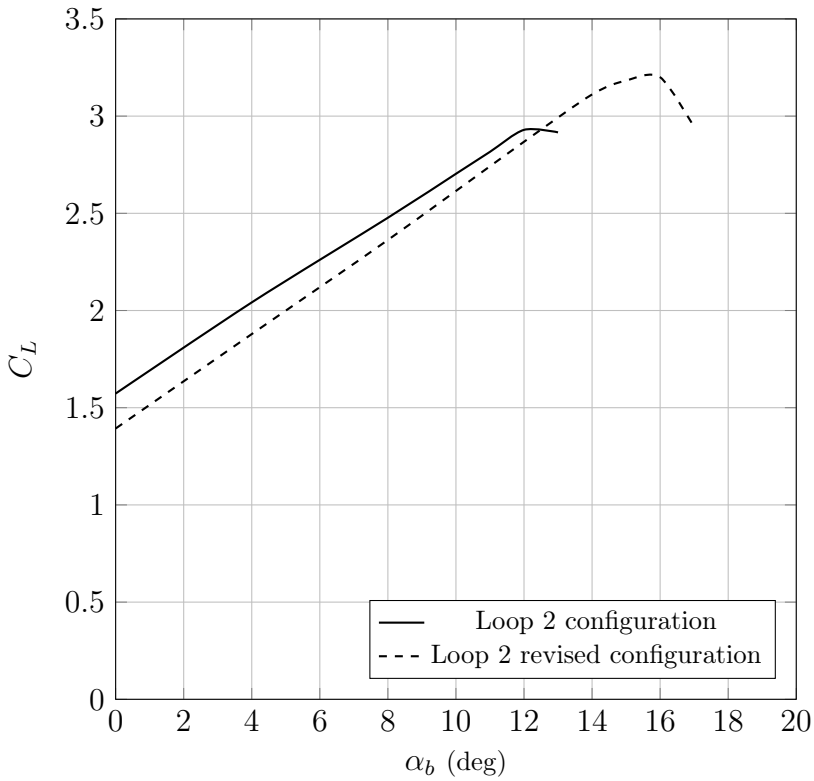


Figure 5.57: *IRON* Loop 2 aerodynamic assessment. Wing-body-canard configuration, lift coefficient characteristics comparison between Loop 2 configuration and Loop 2 revised configuration with different wing twist. Landing condition, $\delta_{f_w} = 35^\circ$, $\delta_c = 25^\circ$.

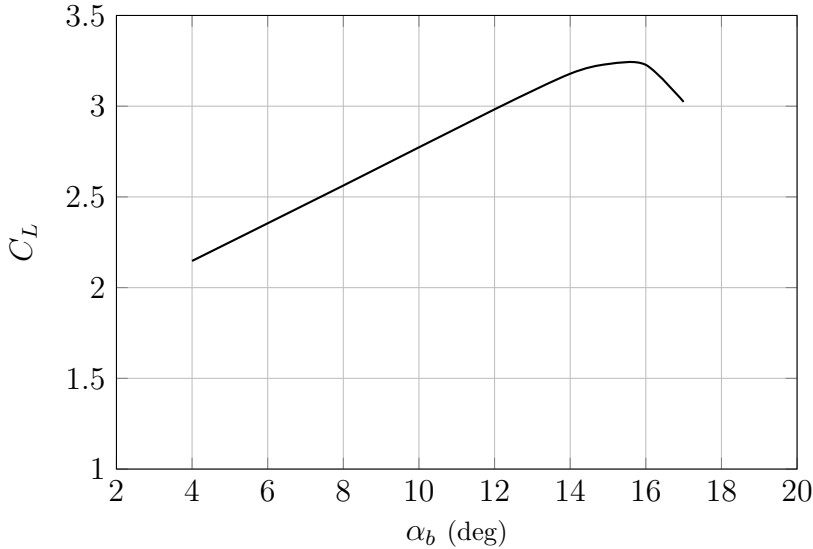


Figure 5.58: *IRON* Loop 2 revised aerodynamic assessment. Total equilibrium lift coefficient in landing condition, $\delta_{f_w} = 35^\circ$, $\delta_c = 25^\circ$ with $i_h = -5^\circ$.

roughness to a surface. They are one of the few techniques that have been successfully applied to the reduction of the skin friction in turbulent boundary layers, both in the laboratory and in full aerodynamic configurations. The main aerodynamic effect provided by riblets is a reduction of the skin friction drag, which is substantially constant with the angle of attack, resulting in an increment of the aerodynamic efficiency in all centre of gravity conditions. In order to obtain the complete aircraft equilibrium curves on the Loop 2 revised configuration, high fidelity analyses on components have been performed and the aerodynamic output have been used as input in *JPAD* to calculate the longitudinal static stability. Main results are shown in 5.60 and 5.59, calculated for the operative condition of $X_{cg} = -22\%$, chosen as reference. The centre of gravity position effect is shown in Fig. 5.61. Trimmed polar and lift curves have been used as input for performance analyses. As can be seen, the large centre of gravity excursion provided by this aircraft configuration leads to a consistent reduction of the aerodynamic efficiency during the cruise phase. In fact, due to the fuel consumption, the aircraft weight reduces

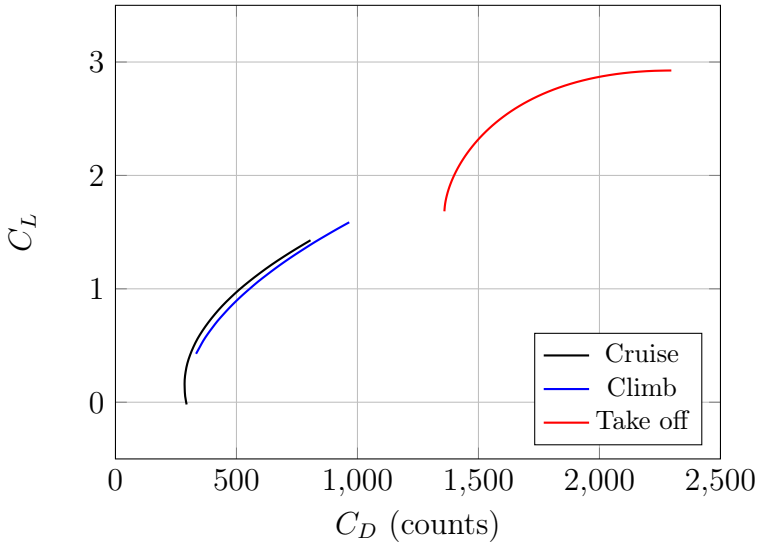


Figure 5.59: *IRON* Loop 2 revised configuration, polar curve in various operating conditions, $X_{cg} = -22\%$ MAC. Component curves calculated with *CFD* in fully turbulent condition and riblets off.

during the cruise making the centre of gravity position shift forward. It has to be highlighted that, in case of riblets installation, the required cruise aerodynamic efficiency of 18.0 is substantially matched while, in case of no riblets installation, the aerodynamic efficiency can decrease up to 17.20. An averaged effect of riblets can be estimated in a +3.5% increment in aerodynamic efficiency for each operative cruise centre of gravity positions.

Condition	Mach number	Reynolds number
Cruise	0.64	18.2e6
Climb	0.33	14.7e6
Take Off	0.18	13.0e6
Landing	0.15	11.0e6

Table 5.4: *IRON* Loop 2 operating conditions.

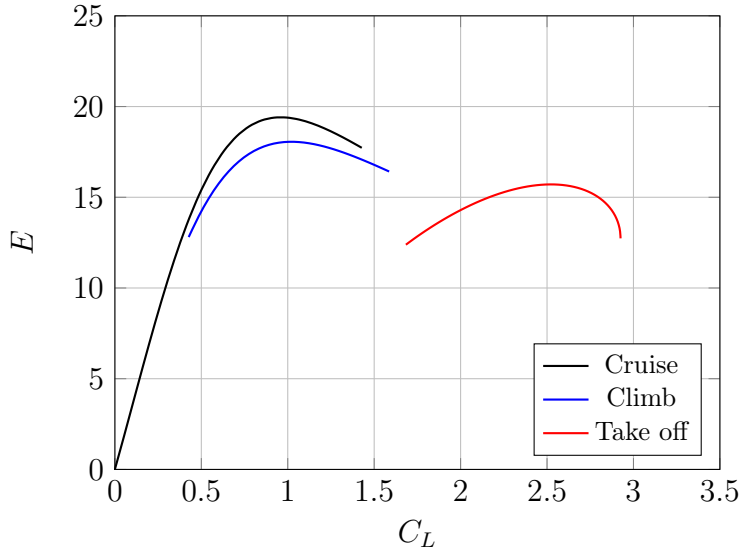


Figure 5.60: *IRON* Loop 2 revised configuration, efficiency in various operating conditions, $X_{cg} = -22\%$ MAC. Component curves calculated with *CFD* in fully turbulent condition and riblets off.

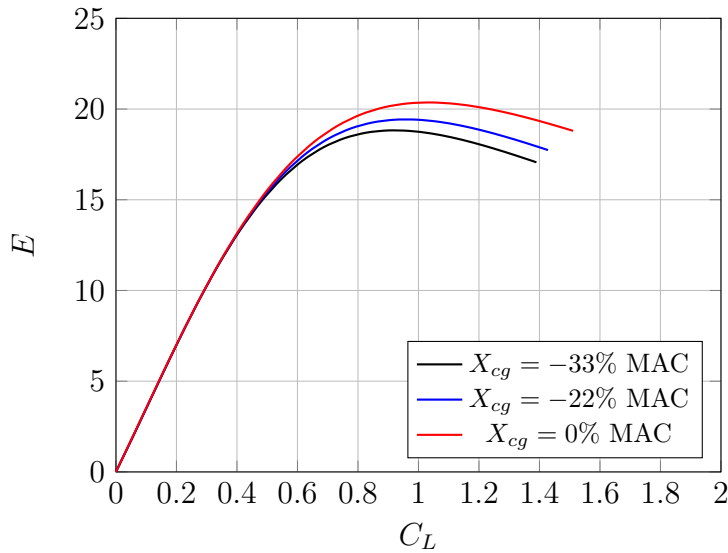


Figure 5.61: *IRON* Loop 2 revised configuration, comparison efficiency in cruise, components curve calculated in fully turbulent condition, riblet off. Comparison at different centre of gravity position.

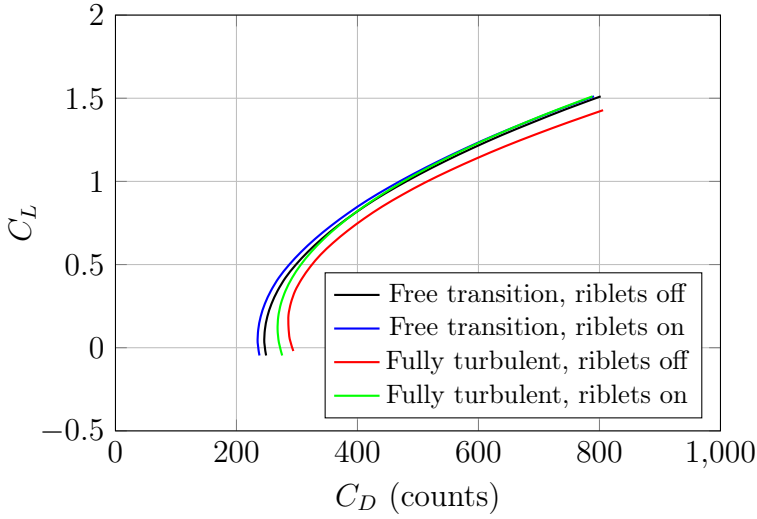


Figure 5.62: *IRON* Loop 2 revised configuration, comparison polar curve in cruise, $X_{cg} = -22\%$ MAC, using 3D component curves calculated for different conditions with high-fidelity methods.

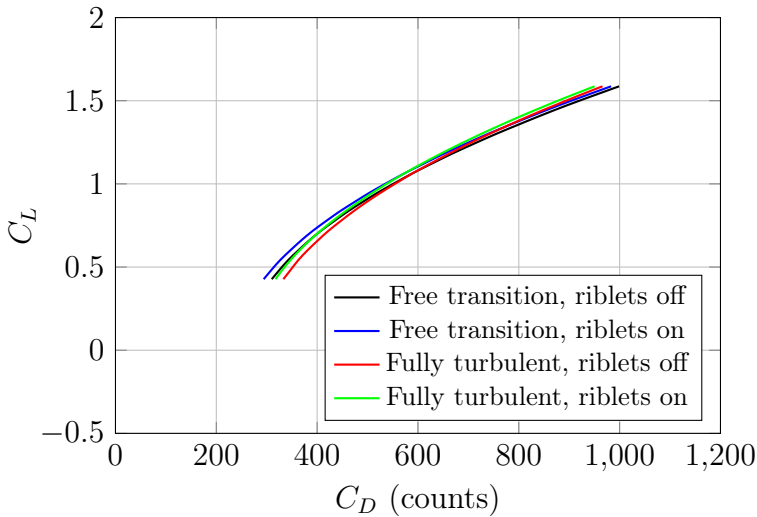


Figure 5.63: *IRON* Loop 2 revised configuration, comparison polar curve in climb, $X_{cg} = -22\%$ MAC, using 3D component curves calculated for different conditions with high-fidelity methods.

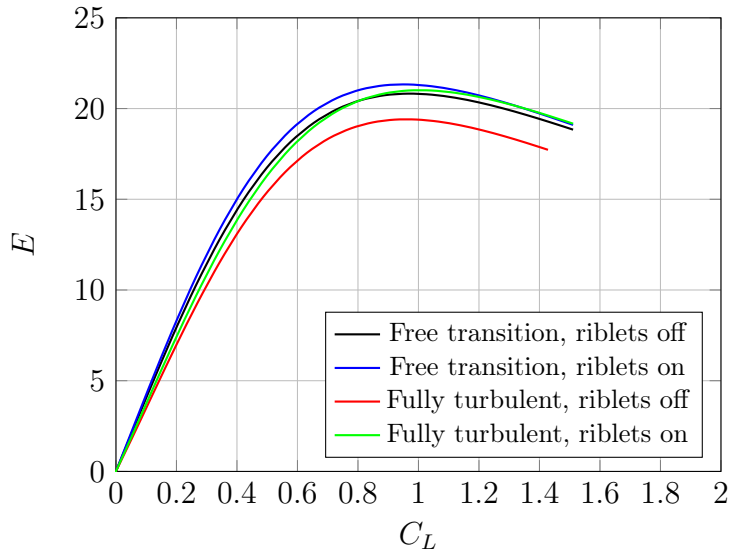


Figure 5.64: *IRON* Loop 2 revised configuration, comparison efficiency in cruise, $X_{cg} = -22\%$ MAC, using 3D component curves calculated for different conditions with high-fidelity methods.

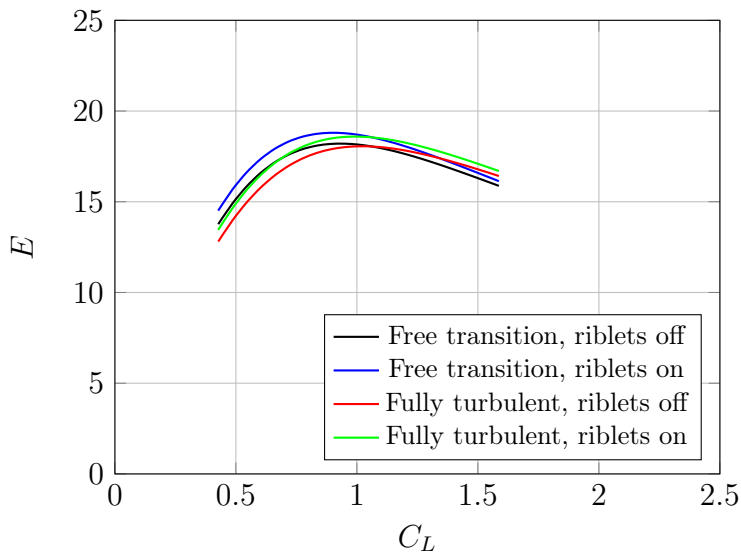


Figure 5.65: *IRON* Loop 2 revised configuration, comparison efficiency in climb, $X_{cg} = -22\%$ MAC, using 3D component curves calculated for different conditions with high-fidelity methods.

Conclusions

This work offers a comprehensive approach to all concerns the aerodynamics during the preliminary phases of aircraft design, presenting an advanced *MDAO* software in which classical and innovative methodologies are implemented and focusing mainly on the development of improved methodologies for aircraft parameters estimation in whose development the author has been involved. The aim of this study is to answer the research question "How is it possible to enhance the current state of art of aerodynamic parameters estimation within the aircraft design, coupling aeronautical and software competencies, focusing mainly on an innovative configuration for regional turboprop?". The main results achieved in this work are summarized following:

- An improved methodology for aerodynamic prediction shows an error lower than 2% in term of $C_{L_{MAX}}$ and lower than 5%
- An advanced MDAO software has been developed in which also the improved methodologies are implemented
- This software has been used for aerodynamic and stability analysed of *IRON* project in terms of innovative configuration

More in detail, this study is collocated within the design of an innovative regional turboprop in the European Union topic JTI-CS2-2015-CPW02-REG-01-03 fully outlined in the Chapter 1. To fully answer this question, the second chapter of this thesis starts presenting the multi-disciplinary analysis and optimization software for aircraft preliminary

design applications named *JPAD* in whose development the author has been deeply involved. The author has developed the aerodynamic structure and methodologies implemented within the software and has been involved in the development and test phases of some improved methodologies presented more in detail in Chapter 3 and Chapter 4 and enclosed in *JPAD*. Even though main features of these methodologies are explained in Chapter 3, a complete analysis concerning aerodynamics is presented at the end of Chapter 2 as case study for software validation, where the Airbus A220-300 is analysed. Starting from components aerodynamic analysis, trimmed curves has been calculated in four different condition (Cruise, Climb, Take-off and Landing) and the results are the input for further performance evaluation. Results show a cruise maximum efficiency of 17.48 and $C_{L_{MAX}}|_{to} = 2.37$ and $C_{L_{MAX}}|_{to} = 2.89$, coherent with similar aircraft data and with declared flight data. The analyses have been carried out through the innovative methodologies explained in detail in the following chapter. As shown in Chap 4, for a similar wing (sweep leading edge of 30°) the error in $C_{L_{MAX}}$ is lower than 2% while the error in estimating the stall angle of attack is lower than 3% in clean configuration. This methodology allows also to take into account high lift devices, having an error in $C_{L_{MAX}}$ lower than 5%. The Chapter 5 shows all outcomes related to the preliminary design activities carried out by the author, together with the DAF research group of the Department of Industrial Engineering of the University of Naples Federico II, during the first two loops of the European Clean Sky 2 project named *IRON*. As a result of aerodynamic analyses on Loop 1 first and Loop 2 then, the three lifting surfaces high-capacity turboprop configuration has appeared to be a very promising solution for regional applications, reaching the Clean Sky 2 target block fuel reduction of -25% (with respect to the current state of the art of the regional jets segment, represented by the Airbus A220-300), but the canard has detrimental impact on longitudinal static stability, as shown in Sec. 5.4. Thanks to the encouraging results as regards the aerodynamic improved methodology in terms of reliability of results, further research work can involve the author to investigate more about drag prediction of the improved methodology and to reduce computational cost, that is currently of about 300 seconds for a complete aircraft analysis in four different condition. To answer to the initial research question, coupling the development of improved method-

ologies with Software Engineering, it is possible to enhance the current state of art of aerodynamic prediction of aircraft design, particularly for innovative configurations where conventional methodologies are often not suitable, in terms of reliability of results and range of applicability. An added value provided by the author of this thesis has been the development, together with the DAF group, of the multi-disciplinary analysis and optimization software *JPAD* that has swiftly become an efficient support for aircraft design.

Bibliography

- [1] Aircraft recovery publication. Technical Report BD500-3AB48-10400-00 issue 55, Bombardier Aerospace Commercial Aircraft, 2018.
- [2] Airport planning publication. Technical Report BD500-3AB48-32000-00 issue 13, Airbus Canada Limited Partnership, 2019.
- [3] I. H. Abbott and A. E. von Doenhoff. *Theory of Airfoil Sections*. Dover, 1959.
- [4] U.S. Energy Information Administration. Short-term energy outlook (steo), November 2019.
- [5] Siemens AG. Star-ccm+. URL: <https://mdx.plm.automation.siemens.com/star-ccm-plus>.
- [6] ATR Aircraft. Turboprop market forecast 2018-2037. URL: <http://www.atraircraft.com/turboprop-market-forecast.html>.
- [7] Kundu A.K. *Aircraft design*. Cambridge University Press, 2010. doi:<https://doi.org/10.1017/CB09780511844652>.
- [8] DARCorporation. AAA Advanced Aircraft Analysis. URL: <https://www.darcorp.com/advanced-aircraft-analysis-software/>.
- [9] Various Authors. Suave: An aerospace vehicle environment for designing future aircraft. URL: <http://suave.stanford.edu/>.

- [10] Mele B. and Tognaccini R. *Numerical Simulation of Riblets on Airfoils and Wings*. doi:10.2514/6.2012-861.
- [11] Mele B., Tognaccini R., and Catalano P. Performance assessment of a transonic wing-body configuration with riblets installed. *Journal of Aircraft*, 53(1):129–140, 2016. doi:10.2514/1.C033220.
- [12] J. A. Jr Blackwell. A finite-step method for calculation of theoretical load distributions for arbitrary lifting-surface arrangements at subsonic speeds, 1969.
- [13] 2019 TIOBE Software BV. Tiobe index. URL: <https://www.tiobe.com/tiobe-index/>.
- [14] Perkins C.D. and Hage R. *Airplane Performance Stability and Control*. John Wiley and Sons Inc., 1949.
- [15] European Commision. Clean sky 2 joint undertaking development plan. URL: <https://www.cleansky.eu/sites/default/files/inline-files/51.%20CS2DP%20December%202017.pdf>.
- [16] P. Nicolosi F. Ciliberti D. Corcione, S. Della Vecchia and C. Cusati. Design and aerodynamic analysis of a regional turboprop innovative configuration. *AIAA Aviation*.
- [17] V. Nicolosi F. Cusati C. Ciliberti D. Corcione, S. Trifari, C. Cusati, and P. Della Vecchia. Feasibility study of innovative regional turbo-prop: an overview of the european project iron. *EASN conference*. doi:<https://doi.org/10.1051/mateconf/201930403014>.
- [18] Ciliberti D., Della Vecchia P., Nicolosi F., and De Marco A. Aircraft directional stability and vertical tail design: A review of semi-empirical methods. *Progress in Aerospace Sciences*, 95:140–172, 2017. doi:<http://dx.doi.org/10.1016/j.paerosci.2017.11.001>.
- [19] Coiro D. and Nicolosi F. Design of low-speed aircraft by numerical and experimental techniques developed at dpa. *Aircraft Design Journal*, 4(1):1–18, 2001. doi:[https://doi.org/10.1016/S1369-8869\(00\)00020-3](https://doi.org/10.1016/S1369-8869(00)00020-3).

- [20] Coiro D., Nicolosi F., and Grasso F. Design and testing of multi-element airfoil for short-takeoff-and-landing ultralight aircraft. *Journal of Aircraft*, 46(5):1795–1807, 2009. doi:<https://doi.org/10.2514/1.43429>.
- [21] Raymer D. Rds-win aircraft design software. URL: <http://www.aircraftdesign.com/rds.shtml>.
- [22] Raymer D. *Aircraft Design: A Conceptual Approach*. AIAA, 2012.
- [23] Schiktanz D. and Scholz D. Survey of experimental data of selected supercritical airfoils. Technical report, Aero – Aircraft Design and Systems Group Department of Automotive and Aeronautical Engineering, Hamburg University of Applied Sciences, 2011.
- [24] Cusati V. Trifari V. Ruocco M. Nicolosi F. De Marco, A. and P. Della Vecchia. A java toolchain of programs for aircraft design. *Aerospace Europe 6th CEAS Conference*, 2017.
- [25] Torenbeek E. *Synthesis of subsonic airplane design: an introduction to the preliminary design of subsonic general aviation and transport aircraft, with emphasis on layout, aerodynamic design, propulsion and performance*. Springer Netherlands, 1982. doi: 10.1007/978-94-017-3202-4.
- [26] European Civil Aviation Conference (ECAC). Recommendation ecac/27-4, nox emission classification scheme.
- [27] CFS Engineering. Ceasiom. URL: <https://www.ceasiom.com/wp/>.
- [28] D.E. Hoak et al. The usaf stability and control digital datcom, 1978.
- [29] Nicolosi F., De Marco A., Della Vecchia P., and Sabetta V. Roll performance assessment of a light aircraft: flight simulations and flight tests. *Aerospace Science and Technology*, 76:471–483, 2018. doi:<https://doi.org/10.1016/j.ast.2018.01.041>.
- [30] Nicolosi F., Ciliberti D., Della Vecchia P., and Corcione S. Wind tunnel testing of a generic regional turboprop aircraft modular model and development of improved design guidelines. In *AIAA Aviation*

- and Aeronautics Forum and Exposition*. American Institute of Aeronautics and Astronautics, 2018. doi:<https://doi.org/10.2514/6.2018-2855>.
- [31] Nicolosi F., Della Vecchia P., and Ciliberti D. Aerodynamic interference issues in aircraft directional control. *Journal of Aerospace Engineering*, 28(1), 2015. doi:[https://doi.org/10.1061/\(ASCE\)AS.1943-5525.0000379](https://doi.org/10.1061/(ASCE)AS.1943-5525.0000379).
- [32] Nicolosi F., Della Vecchia P., Ciliberti D., and Cusati V. Development of new preliminary design methodologies for regional turboprop aircraft by means of cfd analyses. In *29th Congress of the International Council of the Aeronautical Sciences, ICAS 2014*. International Council of the Aeronautical Sciences, 2014. doi:<https://doi.org/10.13140/2.1.5147.0721>.
- [33] Nicolosi F., Della Vecchia P., Ciliberti D., and Cusati V. Fuselage aerodynamic prediction methods, 2016. doi:<https://doi.org/10.1016/j.ast.2016.06.012>.
- [34] Nicolosi F., Della Vecchia P., and Corcione S. Design and aerodynamic analysis of a twin-engine commuter aircraft. *Aerospace Science and Technology*, 40:1–16, 2015. doi:<https://doi.org/10.1016/j.ast.2014.10.008>.
- [35] Nicolosi F., Corcione S., and Della Vecchia P. Commuter aircraft aerodynamic characteristics through wind tunnel tests. *Aircraft Engineering and Aerospace Technology*, 88(4):523–534, 2016. doi:<https://doi.org/10.1108/AEAT-01-2015-0008>.
- [36] Nicolosi F., Corcione S., Della Vecchia P., Trifari V., and Ruocco M. Aerodynamic design and analysis of an innovative regional turboprop configuration. 2018.
- [37] Nicolosi F., Corcione S., Della Vecchia P., Trifari V., Ruocco M., and De Marco A. Design and aerodynamic analysis of a regional turboprop innovative configuration. 2017.
- [38] Nicolosi F., Corcione S., Trifari V., Cusati V., Ruocco M., and Della Vecchia P. Performance evaluation and doc estimation of an

- innovative turboprop configuration. In *2018 Aviation Technology, Integration, and Operations Conference*. American Institute of Aeronautics and Astronautics, 2018. doi:<https://doi.org/10.2514/6.2018-3662>.
- [39] G. Paduano F. Nicolosi. Development of a software for aircraft preliminary design and analysis, 2011.
- [40] Vincenzo Giordano. *Alcune considerazioni sul downwash dell'ala*. PhD thesis, University of Naples Federico II, Department of Aerospace Engineering, University of Naples Federico II, Naples, Italy, 1966.
- [41] I.M. Goldsmith. *A Study to Define the Research and Technology Requirements for Advanced Turbo/Propfan Transport Aircraft*. NASA Ames Research Center, New York, 1981.
- [42] TXT Group. Pacelab apd. URL: <https://www.txtgroup.com/markets/solutions/pacelab-apd/>.
- [43] H. W. Hilton. *High Speed Aerodynamics*. Longmans, 1951.
- [44] D. Howe. *Aircraft conceptual design synthesis*. Aerospace Series. Professional Engineering Publishing, 2000. URL: <https://books.google.it/books?id=QJZTAAAAMAAJ>.
- [45] International Air Transport Association (IATA). Jet fuel price monitor. URL: <https://www.iata.org/en/publications/economics/fuel-monitor/>.
- [46] ICAO Annex 16 Environmental protection International Civil Aviation Organization. Aircraft engine emissions, pp. (iii-2-1) - (iii-2-5).
- [47] Berndt J and De Marco A. Progress on and usage of the open source flight dynamics model software library, jsbsim. *Proceedings of the AIAA Modeling and Simulation Technologies Conference, Chicago, Illinois,*.
- [48] Reed P. M. Kollat, J. B. Comparison of multi-objective evolutionary algorithms for long-term monitoring design. *Advances in Water Resources*, 2006.

- [49] Graham R.R. Koven, W. Wind tunnel investigation of high-lift and stall-control devices on a 37 sweptback wing of aspect ratio 6 at high reynolds numbers. *RM No L8D29*, 1948.
- [50] Pascale L. and Nicolosi F. Design and aerodynamic analysis of a light twin-engine propeller aircraft. In *26th Congress of International Council of the Aeronautical Sciences, ICAS 2008*. International Council of the Aeronautical Sciences, 2008.
- [51] David W. Levy. Prediction of average downwash gradient for canard configurations, 1992.
- [52] Drela M. Avl - athena vortex lattice. URL: <http://web.mit.edu/drela/Public/web/avl>.
- [53] B. W. McCormick. *Aerodynamics, Aeronautics, and Flight Mechanics*. John Wiley, 1995.
- [54] Walsh M.J. Riblets as a viscous drag reduction technique. *AIAA Journal*, 21(4):485–486, 1983. doi:10.2514/3.60126.
- [55] Marcello R. Napolitano. *Aircraft Dynamics: From Modeling to Simulation*. John Wiley, 2012. URL: <http://www.amazon.com/Aircraft-Dynamics-From-Modeling-Simulation/dp/0470626674>.
- [56] L.M. Nicolai and G. Carichner. *Fundamentals of Aircraft and Airship Design*. Number v. 1 in AIAA education series. American Institute of Aeronautics and Astronautics, 2010. URL: <https://books.google.it/books?id=qA0oAQAAMAAJ>.
- [57] Air Transportation Association of America. Com 2002/683; 2002; amended proposal com 2002/683 of the european parliament and the council for a directive on the establishment of a community framework for noise classification for civil subsonic aircraft of 29.11.2002. URL: <http://ec.europa.eu/transparency/regdoc/rep/1/2002/EN/1-2002-683-EN-F1-1.Pdf>.
- [58] Air Transportation Association of America. Standard method of estimating comparative direct operating costs of turbine powered transport airplanes.

- [59] Association of European Airlines. Aea requirements.
- [60] University of Manchester. Flight. URL: <http://www.flight.mace.manchester.ac.uk/index.html>.
- [61] MIT Technology Licensing Office. Mses. URL: <http://web.mit.edu/drela/Public/web/mses/>.
- [62] Oracle. Javafx: Getting started with javafx. URL: <https://docs.oracle.com/javase/8/javafx/get-started-tutorial/jfx-overview.htm#JFXST784>.
- [63] Della Vecchia P. and Nicolosi F. Aerodynamic guidelines in the design and optimization of new regional turboprop aircraft. *Aerospace Science and Technology*, 38:88–104, 2014. doi:<https://doi.org/10.1016/j.ast.2014.07.018>.
- [64] Della Vecchia P., Corcione S., Pecora R., Nicolosi F., Dimino I., and Concilio A. Design and integration sensitivity of a morphing trailing edge on a reference airfoil: The effect on high-altitude long-endurance aircraft performance. *Journal of Intelligent Material Systems and Structures*, 28(20):2933–2946, 2017. doi:<https://doi.org/10.1177/1045389X17704521>.
- [65] Airbus Canada Limited Partnership. A220-300 purpose built for efficiency. URL: <https://www.airbus.com/aircraft/passenger-aircraft/a220-family/a220-300.html>.
- [66] Airbus Canada Limited Partnership. Airbus family figures – farnborough 2018 edition. URL: <https://www.airbus.com/content/dam/corporate-topics/publications/backgrounders/Airbus-Family-Figures-booklet.pdf>.
- [67] Ciampa PD and Nagel B. The agile paradigm: the next generation of collaborative mdo. *8th AIAA/ISSMO Multidisciplinary Analysis and Optimization Conference, Denver, Colorado*.
- [68] J. D. Phillips. Approximate neutral point of a subsonic canard aircraft, 1985.

- [69] J. D. Phillips. Downwash in the plane of symmetry of an elliptically loaded wing, 1985.
- [70] J.D. Phillips. Downwash in the plane of symmetry of an elliptically loaded wing. Technical Report NASA-TP-2414, A-9871, NAS 1.60:2414, 1985.
- [71] García-Mayoral R. and Jiménez J. Drag reduction by riblets. *Philosophical transactions. Series A, Mathematical, physical, and engineering sciences*, 369:1412–27, 2011. doi:10.1098/rsta.2010.0359.
- [72] Horonjeff R. and McKelvey F.X. *Planning and Design of Airports*. McGraw-Hill, 1994.
- [73] L. Rasmussen, M. *The effect of a canard surface on the total lift of an unswept wing in subsonic flow*. Oregon State College, 1959.
- [74] J. Roskam. *Methods for Estimating Stability and Control Derivatives of Conventional Subsonic Airplanes*. published by the author, 1971.
- [75] J. Roskam. *Airplane Design*. Number pt. 8 in Airplane Design. DARcorporation, 2002. URL: <https://books.google.it/books?id=GIHFFkd829cC>.
- [76] Ciornei S. *Mach number, relative thickness, sweep and lift coefficient of the wing - An empirical investigation of parameters and equations*. Phd, Hamburg University of Applied Sciences, Department of Automotive and Aeronautical Engineering, 2005.
- [77] Corcione S., Nicolosi F., and Della Vecchia P. High lift aerodynamic characteristics of a three lifting surfaces turboprop aircraft. 2019. doi:10.2514/6.2019-2884.
- [78] Airbus S.A.S. Global market forecast 2018-2037. URL: <https://www.airbus.com/aircraft/market/global-market-forecast.html>.
- [79] OPEN CASCADE SAS. Open cascade. URL: <https://www.opencascade.com/>.

- [80] P.M. Sforza. *Commercial Airplane Design Principles*. Elsevier Science, 2014. URL: <https://books.google.it/books?id=knhHAgAAQBAJ>.
- [81] M. R. Sierra and C. A. Coello Coello. Improving pso-based multi-objective optimization using crowding, mutation and ϵ -dominance. *Evolutionary Multi-Criterion Optimization*, 2005.
- [82] Abe Silverstein and S. Katzoff. Design charts for predicting downwash angles and wake characteristics behind plain and flapped wings, 1939.
- [83] Abe Silverstein and S. Katzoff. Downwash and wake behind plain and flapped wings, 1939.
- [84] R. Slingerland. *Prediction of Tail Downwash, Ground Effect and Minimum Unstick Speed of Jet Transport Aircraft*. Phd, University of Technology (TU Delft), Aerospace Engineering, TU Delft, 2005.
- [85] E. Torenbeek. *Synthesis of Subsonic Airplane Design: An Introduction to the Preliminary Design of Subsonic General Aviation and Transport Aircraft, with Emphasis on Layout, Aerodynamic Design, Propulsion and Performance*. Springer, 1982. URL: https://books.google.it/books?id=NG2_qiSjmMEC.
- [86] E. Torenbeek. *Advanced Aircraft Design: Conceptual Design, Technology and Optimization of Subsonic Civil Airplanes*. Aerospace Series. Wiley, 2013. URL: <https://books.google.it/books?id=C0gUyoYewhoC>.
- [87] Cusati V. *Design activities for innovative turboprop aircraft with minimum economic and environmental impact*. Phd, University of Naples Federico II, Department of Industrial Engineering, University of Naples Federico II, Naples, Italy, 2020.
- [88] Cusati V., Nicolosi F., Corcione S., Ciliberti D., and Della Vecchia P. Longitudinal stability issues including propulsive effects on an innovative commercial propeller-driven aircraft. 2019. doi:10.2514/6.2019-2882.

- [89] Trifari V. *Development of Multi-Disciplinary Analysis and Optimization framework and applications for innovative efficient regional aircraft*. Phd, University of Naples Federico II, Department of Industrial Engineering, University of Naples Federico II, Naples, Italy, 2020.
- [90] Trifari V., Ruocco M., Cusati V., Nicolosi F., and De Marco A. Multi-disciplinary analysis and optimization java tool for aircraft design. 2018.
- [91] Trifari V., Ruocco M., Cusati V., Nicolosi F., and De Marco A. Automatic modeling of aircraft external geometries for preliminary design workflows. *Aerospace Science and Technology*, 2020. doi: 10.1016/j.ast.2019.105667.
- [92] Quagliarella D. Vitagliano, P. L. A hybrid genetic algorithm for constrained design of wing and wing-body configurations. *the Conference on Evolutionary methods for design, optimization and control applications to industrial and societal problems, Spain.*, 2003.
- [93] A.D. Young. The aerodynamic characteristics of flaps, 1947.

ManuelaRuocco

University of Study of Naples Federico II

home

80128 Napoli
Italy

languages

Italian native speaker
English

programming

♥ Java
C++, CSS3 & HTML5

who I am

creative, complex, dreamer. I have developed great technical skills in my career, the ability to work effectively, in my life. Passionate about every kind of art, addicted to sport.

Research and Engineering

- 2015-2019 **Ph.D. in Industrial Engineering** University of Naples Federico II
High lift and stability issues for innovative transport aircraft configurations in aerodynamic design
- 2016 **Research fellow** University of Naples Federico II
Aircraft design

experience

- Jan 2009 **SmartUp Engineering** Co-founder
Co-founder & Communication manager
- 2018-2019 **Teacher with contract** Protom Group s.p.a. for Accenture
Java programming language

education

- 2013-2016 **MSc in Aerospace Engineering** University of Naples Federico II
Thesis title: Development of a Java-Based Framework for Aircraft Preliminary Design
- 2019-2013 **BSc in Aerospace Engineering** University of Naples Federico II
Thesis title: Modellazion CAD del velivolo tecnam P92JS certificato CS / VLAA.
- 2004-2009 **Scientific certificate**

Total Production

Conferences and Journals papers

Conferences Proceeding

- ICAS 2018 – Belo Horizonte, V. Trifari, M. Ruocco, V. Cusati, F. Nicolosi, A. De Marco: *“Aerodynamic design and analysis of an innovative regional turboprop configuration”* - speaker - Speaker
- ICAS 2018 – Belo Horizonte, M. Ruocco, P. Della Vecchia, F. Nicolosi, A. De Marco: *“A comprehensive framework for high lift aerodynamic prediction based on an improved approach”* - Speaker
- ICAS 2018 – Belo Horizonte, V. Trifari, M. Ruocco, V. Cusati, F. Nicolosi, A. De Marco: *“Multi-disciplinary analysis and optimization java tool for aircraft design“*
- Aviation Technology, Integration, and Operations Conference 2018 – Georgia, F. Nicolosi, S. Corcione, V. Trifari, V. Cusati, University of Naples "Federico II"; Manuela Ruocco, University of Naples Federico II; Pierluigi Della Vecchia: *“Performance Evaluation and DOC Estimation of an Innovative Turboprop Configuration“*
- READ 2016 – Warsaw , M. Ruocco, V. Trifari, V. Cusati " A java-based framework for aircraft preliminary design - Wing aerodynamic analysis module, longitudinal static stability and control module." - Speaker
- READ 2016 – Warsaw, V. Trifari, M. Ruocco, V. Cusati: " Java framework for parametric aircraft design - Performance analysis module."
- CEAS 2017 – Bucuresti, P. Della Vecchia, F. Nicolosi, M. Ruocco, L. Stingo, A. De Marco: "An improved method for transport aircraft for high lift aerodynamic prediction" - Speaker

- CEAS 2017– Bucuresti, A. De Marco, V. Cusati, V. Trifari, M. Ruocco, F. Nicolosi, P. Della Vecchia: "A java toolchain of Computer Programs for Aircraft Design"

Journal Papers

- V. Trifari, M. Ruocco, V. Cusati, F. Nicolosi, A. De Marco; 2017; "*Java framework for parametric aircraft design – ground performance*"; Aircraft Engineering and Aerospace Technology, (SCOPUS Cite Score: 0.67; ISI Web of Science Impact Factor: 0.519), Vol. 89, Issue: 4; DOI 10.1108/AEAT-11-2016-0209; PUBLISHED
- P. Della Vecchia, F. Nicolosi, M. Ruocco, L. Stingo, A. De Marco "*An improved method for transport aircraft for high lift aerodynamic prediction*", CEAS Aeronautical Journal (SCOPUS Cite Score: 0.99) (2018). <https://doi.org/10.1007/s13272-018-0349-5>